BAM
Bundesanstalt für
Materialforschung
und -prüfung

Sicherheit in Technik und Chemie

Maximilian Franz-Arthur Sprengel

Study on the determination and the assessment of the residual stress in laser powder bed fused stainless steel structures

BAM-Dissertationsreihe | Band 173

M.Sc. Maximilian Franz-Arthur Sprengel

Study on the determination and the assessment of the residual stress in laser powder bed fused stainless steel structures

BAM-Dissertationsreihe · Band 173
Berlin 2023

Die vorliegende Arbeit entstand an der Bundesanstalt für Materialforschung und -prüfung (BAM).

Impressum

Study on the determination and the assessment of the residual stress in laser powder bed fused stainless steel structures

2023

Herausgeber:
Bundesanstalt für Materialforschung und -prüfung (BAM)
Unter den Eichen 87
12205 Berlin
Telefon: +49 30 8104-0
Telefax: +49 30 8104-72222
E-Mail: info@bam.de
Internet: www.bam.de

Layout: BAM-Referat Z.8

ISSN 1613-4249

Die BAM ist eine wissenschaftlich-technische Bundesoberbehörde im Geschäftsbereich des Bundesministeriums für Wirtschaft und Klimaschutz.

Study on the determination and the assessment of the residual stress in laser powder bed fused stainless steel structures

Dissertation

zur Erlangung des akademischen Grades

Doktoringenieur

(Dr.-Ing.)

von M.Sc. Maximilian Franz-Arthur Sprengel

geb. am 18.11.1989 in Herford

genehmigt durch die Fakultät für Maschinenbau der Otto-von-Guericke-Universität Magdeburg

Gutachter:

Univ.-Prof. Dr.-Ing. habil. Thomas Kannengießer

Univ.-Prof. Dr.-Ing. Uwe Reisgen

Promotionskolloquium am 29. März 2023

Abstract

Additive manufacturing processes offer extensive advantages for the design freedom of structures through layer-by-layer production. This enables high weight savings as well as the integration of functions such as cooling channels. This technology thus offers great potential to contribute to a sustainable future. The pioneer among these manufacturing processes is the powder bed fusion of metals with laser beams (PBF-LB/M). This process is characterised by high laser scanning speeds and highly localised heat input, which have a strong effect on the microstructure and thus also on the mechanical properties. For example, the austenitic steel 316L exhibits a cellular structure at the sub-grain level. This microstructure feature leads to higher yield strengths and comparable ductility to conventionally processed 316L. In addition to the traditional applications of 316L steel in the petrochemical and nuclear industries, this enables new applications such as medical stents or bipolar plates for fuel cells with proton exchange membranes. However, the layer-by-layer production with high scanning speeds and localised heat input induces cooling rates in the order of 10^6 $K.s^{-1}$. The large temperature gradients and the shrinkage restraints of each weld bead and layer lead to the development of complex residual stress fields. These reduce the material performance and can even lead to premature failure. Thus, the fatigue properties are severely affected by rapid crack growth or prematurely developing cracks. Furthermore, specimens may warp during PBF-LB/M or immediately when the components are separated from the build plate. Therefore, residual stress is one of the main disadvantages of PBF-LB/M, making it difficult for this technology to be more widely accepted in the industry. Based on the current state of the literature, the procedure for determining residual stress employing diffraction methods, the influence of the component geometry, as well as the inter-layer-time (ILT) on residual stress and, lastly, suitable heat treatment strategies for relaxing residual stress in PBF-LB/M/316L, were identified as insufficiently researched areas.

Determining residual stress is a major challenge. X-ray and neutron diffraction are particularly suitable for filigree structures, which can preferably be produced using PBF-LB/M. Here, the microscopic strain of the lattice planes is used to calculate the macroscopic residual stress. These methods are non-destructive and allow the spatial resolution of the bi-axial and tri-axial residual stress. In the present work, in-situ neutron diffraction tensile tests were performed to analyse the micromechanical behaviour of

PBF-LB/M/316L. The suitability of the lattice planes for calculating the macroscopic residual stress was investigated. The (311) lattice plane was found to be the best option for determining the macroscopic residual stress in PBF-LB/M/316L. Furthermore, it was shown that the Kröner model can be used to calculate the X-ray diffraction constants despite the texture. Currently, both aspects are common practices in the determination of residual stress. The results presented here support the validity of this approach and increase the confidence in the experimentally determined residual stress, which has a positive effect on the assessment of quality concerning the safety of a component manufactured by PBF-LB/M.

The geometry of a structure manufactured by PBF-LB/M determines the component stiffness and influences the thermal gradients during manufacture and ultimately the residual stress. The effect of smaller or larger dimensions (larger than 10 mm) on the residual stress is rarely considered. To investigate this aspect, representative test specimens with different thicknesses and lengths were produced. Hence, the influence of the geometry i.e., component stiffness on the residual stress was evaluated. The residual stress was determined using X-ray and neutron diffraction. The analysis of the residual stress showed that an increase in thickness leads to overall higher residual stress. In addition, it was shown that increasing the sample dimension leads to smaller residual stress gradients. Above a threshold value of a few millimetres, no significant change in the residual stress was observed.

The ILT is inherent in every PBF-LB/M construction job and influences the thermal gradients during production and thus the residual stress. A change in wall thickness in a geometrically complex structure or a variation in the number of specimens in the construction process leads directly to a change in the ILT. To simulate this, specimens with different ILT were produced. The residual stress was determined by X-ray and neutron diffraction. The use of a short ILT resulted in higher surface residual stress, but lower volume residual stress. Here, the surface residual stress and the residual stress in the volume showed contrary behaviour. This was attributed to the complex heat conduction during the process, as shown by the thermographic measurements.

To avoid distortion of the specimens or real components upon separation from the build plate or during post-processing steps, stress relief annealing is usually performed after the PBF-LB/M process. Based on standards for

heat treatment of welded austenitic steels, heat treatments were performed at low (450 °C for four hours) and high (800 °C and 900 °C for one hour) temperatures. The results show that the heat treatment at 450 °C relaxed the residual stress by only 5 %. This low relaxation is due to the stability of the cell structures. The high-temperature heat treatment showed that 900 °C is required to dissolve the cell structure and achieve a relaxation of about 85 %. This result is in good agreement with the standards for stress relief annealing of welded austenitic steels.

Kurzfassung

Additive Fertigungsverfahren bieten durch die schichtweise Herstellung weitreichende Vorteile für die Gestaltungsfreiheit von Strukturen und ermöglichen somit hohe Gewichtseinsparungen. Auch die Integration von Funktionen, beispielsweise Kühlkanäle, können unmittelbar während der Herstellung eingebracht werden. Damit bietet diese Technologie ein hohes Potential zu einer nachhaltigen Zukunft beizutragen. Der Vorreiter unter diesen Fertigungsprozessen ist das Pulverbettbasierte Schmelzen von Metallen mittels Laserstrahlen (PBF-LB/M). Dieser Prozess zeichnet sich durch hohe Laserscangeschwindigkeiten und eine stark lokalisierte Wärmeeinbringung aus, welche sich auf die Mikrostruktur und damit auch auf die mechanischen Eigenschaften auswirken. So weist der austenitische Stahl 316L eine zelluläre Struktur auf Subkornniveau auf, welche zu höheren Streckgrenzen jedoch nicht verringerter Duktilität im Vergleich zu konventionell verarbeitetem 316L führt. Dies ermöglicht, neben den traditionellen Einsatzgebieten des Stahls 316L in der petrochemischen und nuklearen Industrie, neue Anwendungen wie medizinische Stents oder Bipolarplatten für Brennstoffzellen mit Protonenaustauschmembran. Die schichtweise Fertigung mit hohen Scangeschwindigkeiten und lokaler Wärmeeinbringung bedingt jedoch Abkühlraten in der Größenordnung von 10^6 K.s^{-1}. Die hohen Temperaturgradienten im Zusammenspiel mit den Schrumpfbehinderungen jeder Schweißraupe und Lage sorgen für die Entstehung komplexer Eigenspannungsfelder. Diese verringern die Beanspruchbarkeit des Materials und können sogar zu einem vorläufigen Versagen führen. So sind die Ermüdungseigenschaften durch ein rapides Risswachstum bzw. ein vorzeitig entstehender Riss durch Eigenspannungen stark beeinträchtigt. Des Weiteren kommt es vor, dass sich die Proben während des PBF-LB/M oder unmittelbar bei der Trennung der Bauteile von der Bauplatte verziehen. Daher sind die Eigenspannungen eines der Hauptnachteile des PBF-LB/M, die eine breitere Akzeptanz dieses Verfahrens in der Industrie erschweren. Ausgehend vom aktuellen Literaturstand, wurde die Vorgehensweise bei der Bestimmung der Eigenspannungen mittels Beugungsmethoden, der Einfluss der Bauteilgeometrie bzw. Bauteilsteifigkeit sowie der Zwischenlagenzeit auf die Eigenspannungen und zuletzt geeignete Wärmebehandlungsstrategien zur Relaxation der Eigenspannungen in PBF-LB/M/316L als unzureichend erforschte Bereiche identifiziert.

Die Bestimmung der Eigenspannung ist eine große Herausforderung. Insbesondere bei filigranen Strukturen, welche vorzugsweise mittels PBF-LB/M hergestellt werden können, eignen sich die Röntgen- und Neutronenbeugung. Hierbei wird die mikroskopische Dehnung der Gitterebenen zur Berechnung der makroskopischen Eigenspannung verwendet. Diese Methoden sind zerstörungsfrei und ermöglichen die räumliche Auflösung der bi-axialen und tri-axialen Eigenspannungen. In der vorliegenden Arbeit wurden in-situ Neutronenbeugungszugversuche durchgeführt, um das mikromechanische Verhalten des PBF-LB/M/316L zu analysieren. Die Eignung der Gitterebenen zur Berechnung der makroskopischen Eigenspannung wurde untersucht. Die (311) Gitterebene erwies sich als die beste Option für die Bestimmung der makroskopischen Eigenspannung in PBF-LB/M/316L. Darüber hinaus wurde gezeigt, dass das Kröner-Modell trotz Textur zur Berechnung der Röntgenbeugungskonstanten verwendet werden kann. Derzeit werden beide Aspekte in der Bestimmung der Eigenspannungen standardmäßig angewandt. Die hier präsentierten Ergebnisse untermauern die Gültigkeit dieses Vorgehens und erhöhen das Vertrauen in den experimentell bestimmten Eigenspannungen, welches sich positiv auf die Beurteilung der Qualität hinsichtlich der Sicherheit eines durch PBF-LB/M gefertigten Bauteils auswirkt.

Die Geometrie einer durch PBF-LB/M hergestellten Struktur bestimmt maßgeblich die Bauteilsteifigkeit und beeinflusst die thermischen Gradienten während der Herstellung und letztendlich die Eigenspannungen. Die Auswirkung kleinerer oder größerer Abmessungen (größer 10 mm) auf die Eigenspannungen wird derzeit oft nicht berücksichtigt. Um diesen Aspekt zu untersuchen, wurden repräsentative Probekörper mit unterschiedlichen Dicken und Längen hergestellt. Damit konnte der Einfluss der Geometrie bzw. Bauteilsteifigkeit auf die Eigenspannungen gezielt bewertet werden. Die Eigenspannungen wurden mittels Röntgen- als auch Neutronenbeugung bestimmt. Die Analyse der Eigenspannungen ergab, dass eine Erhöhung der Dicke zu insgesamt höheren Eigenspannungen führt. Zusätzlich wurde gezeigt, dass eine Vergrößerung der Probenabmessung zu kleineren Eigenspannungsgradienten führt. Oberhalb eines Schwellenwerts von wenigen Millimetern ändern sich die Eigenspannungen nicht mehr signifikant.

Die sogenannte Zwischenlagenzeit (ILT) ist jedem PBF-LB/M-Bauauftrag inhärent und beeinflusst die thermischen Gradienten während der Herstellung und damit maßgeblich die Eigenspannungen. Ein Wanddickensprung in einer geometrisch komplexen Struktur bzw. einer Variation der Probenanzahl im Bauprozess führt unmittelbar zu einer Änderung der ILT. Um dies nachzubilden, wurden Proben mit unterschiedlichen ILT hergestellt. Die Eigenspannungen wurden mittels Röntgen- und Neutronenbeugung bestimmt. Die Verwendung einer kurzen ILT hat zu höheren Oberflächeneigenspannungen geführt, jedoch zu geringeren Volumeneigenspannungen. Hierbei zeigten die Oberflächeneigenspannungen und die Eigenspannungen im Volumen ein konträres Verhalten. Dies wurde auf die komplexe Wärmeleitung während des Prozesses zurückgeführt, wie die thermografischen Messungen zeigten.

Um den Verzug der hergestellten Probekörper oder realen Bauteile bei der Abtrennung der Bauplatte oder in Nachbearbeitungsschritten zu vermeiden, wird in der Regel ein Spannungsarmglühen nach dem PBF-LB/M Prozess durchgeführt. Basierend auf Standards für die Wärmebehandlung von geschweißten austenitischen Stählen, wurden Wärmebehandlungen bei niedrigen (450 °C für vier Stunden) und hohen (800 °C bzw. 900 °C für eine Stunde) Temperaturen durchgeführt. Die Ergebnisse zeigen, dass die Wärmebehandlung bei 450 °C die Eigenspannungen um lediglich 5 % relaxierte. Diese geringe Relaxation ist auf die Stabilität der Zellstrukturen zurückzuführen. Die Hochtemperatur-Wärmebehandlung zeigte, dass 900 °C erforderlich sind, um die Zellstruktur aufzulösen und eine Relaxation von etwa 85 % zu erreichen. Dieses Ergebnis steht in guter Übereinstimmung mit den Standards für das Spannungsarmglühen geschweißter austenitischer Stähle.

Foreword

This study was performed during my time as a doctoral student in the weld mechanics and micro non-destructive testing sections of the Bundesanstalt für Materialforschung und -Prüfung (BAM) in Berlin. The funding was provided by BAM as part of the materials project "Microstructure Development in Additively Produced Metallic Components: from Powder to Mechanical Failure".

I first would like to thank my supervisors Arne Kromm and Alexander Evans for their guidance and the excellent technical discussions on the topic of residual stress. At the start of my journey, I did not expect to perform so many experiments at various large-scale facilities in Europe. Each one of these experiments was an adventure and for each one of them, I had great colleagues surrounding me. I would like to thank my colleagues Alexander Ulbricht, Tatiana Mishurova, Tobias Fritsch, Itziar Serrano-Munoz for sharing their knowledge, for their excellent contributions to joint publications, engaging technical discussions and support through my research. A special thanks goes to Alexander Ulbricht, who always enjoyed a ride on the s-bahn after an eventful day to talk about life while enjoying a beer. A typical Berlin day.

I did my PhD to dive deep into a technical subject but also to challenge myself. The two goals were fully achieved. In a relatively short period, I had to become an expert in residual stress and diffraction. In my opinion, the main goal of research is to publish the results. It was an incredible challenge to publish, and I would like to thank Professor Giovanni Bruno to have guided me in this journey. Furthermore, I would like to express my gratitude towards Professor Thomas Kannengießer, who kindly accepted to become my supervisor. His technical advice and support during the difficult time of the pandemic helped me finishing my PhD. Moreover, I would like to thank both of my Professors for the great liberty they gave me throughout my time at BAM. Their trust gave me the opportunity to dive deeply in the field of residual stress and to build a successful collaboration with the University of Linköping. A special thank goes to Cheng-Han Yu, who I

met during a summer school and with whom I have performed excellent work and who I am happy to call a friend. I would like to also thank all my colleagues at BAM, who always provided good technical advice and with whom I have successfully published. A special thanks goes to Simon J. Altenburg and Gunther Mohr for the thermographic measurements and signal post processing.

Finally, I would like to thank my family for their support from the start until the end. The past years were difficult on all levels. Without this safety net, I would have had a difficult time finishing this one-in-a-lifetime project. Especially my brother, who himself was working on his PhD and had very good advice to help me through the moments where my motivation was challenged. Looking back, I agree with people saying that a PhD is not just work on a technical subject but also on yourself as a person. I equally gained knowledge on material characterization and on myself and I encourage anyone to go through this rollercoaster adventure.

"This planet has – or rather had – a problem, which was this: most of the people living on it were unhappy for pretty much of the time. Many solutions were suggested for this problem, but most of these were largely concerned with the movements of small green pieces of paper..." – Douglas Adams, 1979

List of abbreviations

AM	Additive Manufacturing
BD	Build Direction
BAM	Bundesanstalt für Materialforschung und -Prüfung
BCC	Body-Centred-Cubic
CAD	Computer Aided Design
CMM	Coordinate Measurement Machine
DEC	Diffraction Elastic Constants
DED	Directed Energy Deposition
DED-Arc/M	Directed Energy Deposition of Metals using an Arc
DED-LB/M	Directed Energy Deposition of Metals using Laser Beams
DIC	Digital Image Correlation
D10, D50, D90	Particle size distribution; 10 %, 50 %, 90 % below the values in µm
EBM	Electron Beam Melting
EDX	Energy Dispersive X-ray Spectroscopy

EBSD	Electron Backscattered Diffraction
FCC	Face-Centred-Cubic
FWHM	Full-Width-At-Half-Maximum
GSAS	General Structure Analysis System
HT1	Heat Treatment at 450 °C for 4 hours
HT2	Heat Treatment at 800 °C for 1 hour
HT3	Heat Treatment at 900 °C for 1 hour
HAGB	High Angle Grain Boundary
ILT	Inter-Layer-Time
IN625	Inconel 625
IN718	Inconel 718
ND	Neutron Diffraction
OM	Optical Microscopy
OPS	Oxide Polishing Suspension
PBF	Powder Bed Fusion
PBF-LB/M	Powder Bed Fusion of Metals with Laser Beams
SEM	Scanning Electron Microscopy

SCEC	Single Crystal Elastic Constants
SENB	Single-Edge Notch Bend
SALSA	Strain Analyser For Large Scale Engineering Applications
SXRD	Synchrotron X-ray Diffraction
TD	Transverse Direction
TGM	Thermal Gradient Mechanism
TIG	Tungsten Inert Gas
TOF	Time-Of-Flight
UE	Engineering Uniform Elongation
UTS	Ultimate Tensile Strength
VED	Volumetric Energy Density
WEDM	Wire Electric Discharge Machining
XRD	X-ray Diffraction
YS	Yield Strength
YS0.2	Yield Strength at 0.2 % strain

List of symbols

a	Lattice parameter
a_0	Stress free lattice parameter
C	Constant in the Larsson-Miller equation (empirical)
d	Lattice spacing
d_0	Stress free lattice spacing
E	Young's modulus
E_{hkl}	Lattice Young's Moduli
h	Hatching Distance
hkl	Miller Indices
P	Laser Power
$\vec{q}$	Scattering vector
Ra	Arithmetic mean height of profile height
Sa	Arithmetic mean height of surface height
s_1	Diffraction elastic constant
s_2	Diffraction elastic constant

t	Layer Thickness
T	Temperature
T_m	Melting temperature
T_E	Thermal effect/ Larsson-Miller parameter
v	Scanning Velocity
ε	Strain
ε_{hkl}	Lattice strain
$\varepsilon_{thermal}$	Thermal strain
θ	Diffraction angle
λ	Wavelength
ν	Poisson ratio
ν_{hkl}	Lattice poisson ratio
$\tilde{\sigma}^{\mathrm{I}}(\vec{x}))$	Macroscopic Residual Stress, type I Residual stress
$\tilde{\sigma}^{II}(\vec{x})$	Microscopic Residual Stress, type II Residual Stress
$\tilde{\sigma}^{III}(\vec{x})$	Microscopic Residual Stress, type III Residual stress
$\sigma_{compressive}$	Compressive residual stress

$\sigma_{tensile}$	Tensile residual stress
σ_X	Residual stress in the longitudinal direction X
σ_Y	Residual stress in the transversal direction Y
σ_Z	Residual stress in the build direction Z
$\Delta\sigma_X$	Residual stress range in X
$\Delta\sigma_Y$	Residual stress range in Y
$\Delta\sigma_Z$	Residual stress range in Z
$\sigma_{X,PC}$, $\sigma_{Y,PC}$, $\sigma_{Z,PC}$	Peak compressive residual stress in X, Y or Z
$\sigma_{X,PT}$, $\sigma_{Y,PT}$, $\sigma_{Z,PT}$	Peak tensile residual stress in X, Y or Z
φ, Ψ	Pair of angles relating the laboratory coordinate to the specimen coordinate system
Γ	Orientation parameter

Table of content

1 Introduction

The resolution of the "Green Deal" by the European Comission has marked the start to further push the boundaries of todays materials and processes to enable a sustainable future. The additive manufacturing (AM) technology has thereby been identified as a key enabler to reach multiple United Nations sustainable development goals [1]. In fact, when it comes to shifting the boundaries of design of freedom, functionalisation in manufacturing and tailored material properties, one cannot ignore the AM process powder bed fusion of metals with laser beams (PBF-LB/M). These advantages lead to novel applications such as the flow-optimized and reduced weight and dimension valve casing for hydrogen filling stations, see Figure 1.1 a). A key aspect was the introduction of sensors to monitor the structural health of the valve during its service life [2]. The alloy used to manufacture the valve was austenitic stainless steel 316L. The low-carbon stainless steel is a workhorse alloy for a wide range of industrial applications. Recently, a remarkable increase in yield strength was obtained when processing 316L by PBF-LB/M. The improved yield strength (2x increase in most reported cases) is balanced by comparable UTS and ductility to the conventionally manufactured counterpart [3-6]. This was found to be related to the subgrain solidification cellular structure, see Figure 1.1 b). This structure is composed by microsegregations, precipitates and dislocations, which prevent dislocation motion (pinning) [3, 4, 7, 8]. The versatility of austenitic steel 316L has been improved by the PBF-LB/M processing. It is one of the most investigated alloys in the field of PBF-LB/M and is the focus of this study.

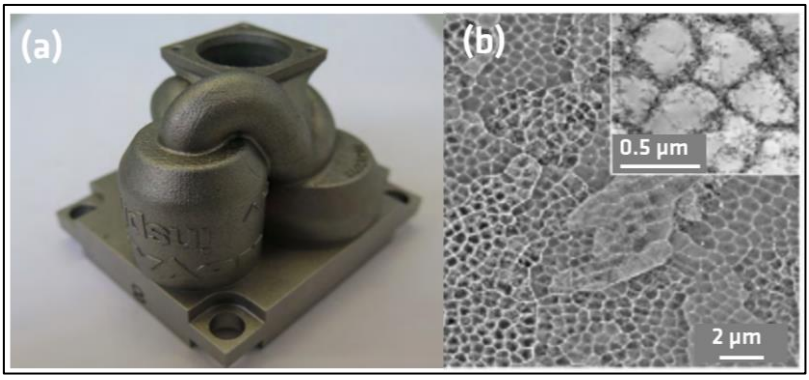

Figure 1.1: a) Redesigned 316L hydrogen pressure valve (developed by Nova Werke AG and inspire AG) manufactured using PBF-LB/M [9], b) cellular structure in PBF-LB/M/316L, reprinted from [6], with permission from Elsevier.

The PBF-LB/M processed 316L in the as-built state promises to overcome the strength-ductility trade-off generally encountered with austenitic steels i.e. high yield strength comes with low ductility [3]. One of the main challenges to overcome in PBF-LB/M manufactured parts is the residual stress. The PBF-LB/M process is used to manufacture parts in a layer-by-layer fashion using a localized heat source (in this case a laser), whereby each layer is scanned at high scanning velocities [10]. These manufacturing circumstances lead to very high cooling rates (see Figure 1.2 a) and ultimately lead to the formation of residual stress, which may be as high as the material yield strength [11]. It is essential to have knowledge of the residual stress, the distribution and the magnitude, so that critical parts such as the pressure valve shown in Figure 1.1 a) can be operated in a safe manner.

One of the advantages of PBF-LB/M is to produce complex structures, which pose novel challenges to the determination of the residual stress. Diffraction based residual stress assessment has unique advantages as it allows for the non-destructive determination of the bi-axial (at the surface) and tri-axial (in the bulk) residual stress with high spatial resolution. However, the rough surface (Figure 1.2 b) and the complex microstructure (Figure 1.2 c) of PBF-LB/M structures pose novel challenges.

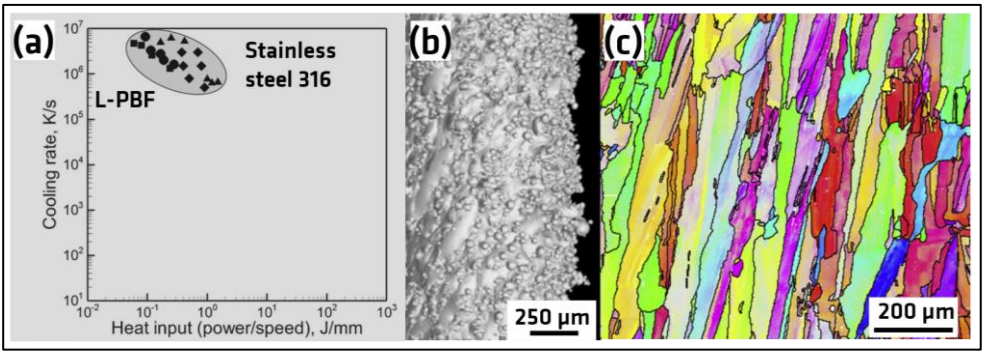

Figure 1.2: a) Cooling rates in PBF-LB/M, adapted from [12], b) surface roughness 1 mm diameter lattice struts manufactured by PBF-LB/M, reprinted from [13], with permission from IUCr Journals, and c) grain morphology of PBF-LB/M/316L microstructures, reprinted from [14], with permission from Elsevier.

Fundamental assumptions used to calculate the residual stress based on conventionally processed alloys are still used for PBF-LB/M structures. However, given the unique microstructure shown in (Figure 1.2 c) it is necessary to verify the commonly accepted approaches to ensure that they are valid for the residual stress analysis in PBF-LB/M parts. This study tackles this aspect by putting the focus on

the selection of an appropriate lattice plane to determine the residual stress in PBF-LB/M/316L.

The design of PBF-LB/M structures may involve changing wall thicknesses which in turn alter the heat input throughout the manufacturing. This simple example shows the inter connectivity of the geometry and the process. Similar to welding, assessing the residual stress requires the consideration of the link between the temperature field, the strain and the stress fields and the microstructure [15]. Therefore, the following aspects were investigated.

A geometrically complex part may include varying wall thicknesses and the hence varying restraint and its influence on the residual stress needs to be understood. Therefore, the influence of the geometry on the surface, subsurface and bulk residual stress magnitudes and distributions is investigated. The focus hereby lies on the characterisation of the triaxial through thickness residual stress and changes related to varying the thickness or length of a simple geometry. The choice of simple geometries is related to the necessity of deriving generalities concerning the residual stress that may be adapted to complex geometries.

Inherent to PBF-LB/M, a change in the component thickness will also affect the inter-layer-time. This is a measure for the time necessary for the recoating of a fresh powder layer and the illumination of the layer. This parameter influences the heat accumulation and as such the residual stress. Understanding this connection will give an insight on varying residual stress throughout complex geometries but also on how changing the number of parts on the build plate may affect the residual stress.

Finally, the aspect of the stress relieve heat treatment is analysed. The formation of residual stress is inherent to PBF-LB/M. Therefore, a post process stress relieve heat treatment is generally applied to avoid the distortion following the relaxation of macroscopic residual stress. The exceptional static mechanical properties are linked to the microstructural features which could be dissolved during the heat treatment. The investigated temperatures are therefore chosen to analyse the limit between the loss of the solidification subgrain cellular structure (see Figure 1.1 b) and the relaxation of the residual stress.

In this study, multiple diffraction techniques were combined to characterize the residual stress distribution in PBF-LB/M/316L components. The surface residual stress are determined by X-ray diffraction in knowledge of the surface roughness. In combination with electropolishing, the subsurface residual stresses are also characterized. To provide a full through thickness residual stress characterisation, multiple neutron diffraction experiments were carried out at large-scale-facilities.

The investigation of the lattice place choice was performed through a dedicated in-situ neutron diffraction tensile test. The experimental approach was chosen to answer the above highlighted aspects.

The work presented first starts with a state-of-the-art section highlighting the research gaps present to date on the topic of residual stress in PBF-LB/M (chapter 0). Besides the general introduction on the austenitic steel 316L and the AM processes, the formation of the residual stress in PBF-LB/M, the determination of the residual stress in PBF-LB/M structures, the influence of process parameters, and the stress relieve heat treatment of PBF-LB/M/316L are addressed. Second, the manufacturing of the test specimens is detailed as well as the calculation of the residual stress and the measurement procedure (chapter 3). Third, combined results and discussion chapters include the characterisation of the material, the micromechanical behaviour covering the choice of an appropriate lattice plane, the distribution and magnitudes of residual stress in simple geometries, the effect of process parameters on the residual stress, and the thermal relaxation of the residual stress (chapter 4). Finally, the conclusions from the experimental results are drawn (chapter 5).

2 State of the Art

2.1 Austenitic stainless steel AISI 316L

The following subchapters give an overview of the austenitic stainless steel 316L. First, the metallurgy and the industrial applications of the alloy are addressed in subchapter 2.1.1. Second, the influence of different additive manufacturing methods on the microstructure and the mechanical properties is detailed in subchapter 2.1.2.

2.1.1 Metallurgy and applications

Stainless steels are a material of choice when it comes to corrosion resistance and longevity in harsh environments [16]. A steel is referred to as stainless if a minimum of 10.5 % of chromium (Cr) is included in the alloy composition, which allows the formation of a passive surface oxide to prevent oxidation and corrosion [17]. The austenitic steels of the AISI 300 series are the most common stainless steels [17, 18]. Among the 300 series, the alloy 316L is a low-carbon type austenitic stainless steel with a nominal carbon (C) level of 0.03 weight % [16, 17]. The second largest alloying element is nickel (Ni), which is used to promote the formation and the stability of the austenitic phase. The third largest alloying element is molybdenum (Mo), which further improves the corrosion properties. Further alloying elements include manganese (Mn) and silicon (Si) [16]. The chemical composition of 316L is given in Table 2.1. The 316L alloy has improved resistance to intergranular attack in corrosive environments, as the low level of carbon reduces the formation of $M_{23}C_6$ carbides [17, 19]. This characteristic makes 316L particularly valuable in e.g. welding [19]. According to the chemical composition given in Table 2.1 and the Schaeffler diagram shown in Figure 2.1 a), the predicted microstructure of welded 316L lies in the field of austenite and ferrite.

The four solidification and solid-state transformation modes of austenitic stainless steel weld metals according to the Fe-Cr-Ni phase diagram are shown in Figure 2.1 b) [17]. Depending on the composition, the stainless steel either solidifies as primary austenite (face-centred-cubic FCC) or primary ferrite (body-centred-cubic BCC). Thereby, lower Cr/Ni ratios lead to primary austenitic solidification whereas higher Cr/Ni ratios lead to primary ferrite compositions [17]. Upon reaching room temperature, alloys that solidified primarily as fully austenitic remain austenitic. When the primary solidification is ferrite, the final microstructure may be a mixture of ferrite and austenite [17]. Besides the Cr/Ni ratio also the cooling rate plays a role on the phase content. For low Cr/Ni ratios the ferrite content decreases with increasing cooling rates (applicable to 316L, as the Ni content is

relatively high compared to other austenitic steels e.g. [20]). With high Cr/Ni ratios the ferrite content increases with increasing cooling rates [17]. Examples of a fully austenitic microstructure and an austenitic microstructure with remaining ferrite of electron beam welded stainless steels are shown in Figure 2.2 a) and b) respectively.

Table 2.1: Chemical composition in weight % of the stainless steel 316L [17]

Fe	C	Cr	Ni	Mo	Mn	P	S	Si
balance	0.03	16.0-18.0	10.0-14.0	2.0-3.0	2.0	0.045	0.03	1.0

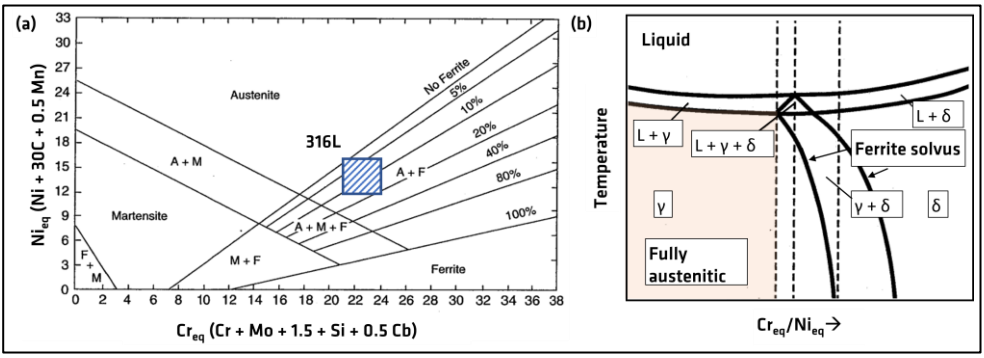

Figure 2.1: a) Schaeffler diagram and prediction of welded 316L microstructure (Adapted from [21] and [20]), b) Fe-Cr-Ni pseudo binary phase diagram showing the solidification types of stainless steels (Adapted from [17]). Calculation of the Cr equivalent (Cr_{eq}) and the Ni equivalent (Ni_{eq}) given in a).

The number of different phases in stainless steels is vast but common to almost all stainless steels is the carbide of type $M_{23}C_6$ (FCC), in which Cr is the predominant metallic element [17, 22]. Furthermore, Cr plays a major role in the formation of intermetallic phases such as the σ-phase $(Fe, Ni)_x(Cr, Mo)_y$. The two phases are of interest as they reduce heavily the ductility (the σ-phase is hard and brittle [17]) and the corrosion resistance i.e. depleting the matrix of Cr as precipitates accumulate on the grain boundaries [18]. This can be the case when welding austenitic steels, as the low heat conductivity can lead to the formation of carbides in the heat affected zone, which in turn reduces the corrosion resistance of the weld. Secondary phases such as the χ, the η, the G and the Laves phases may precipitate in stainless steels but typically after long exposure times [17, 22].

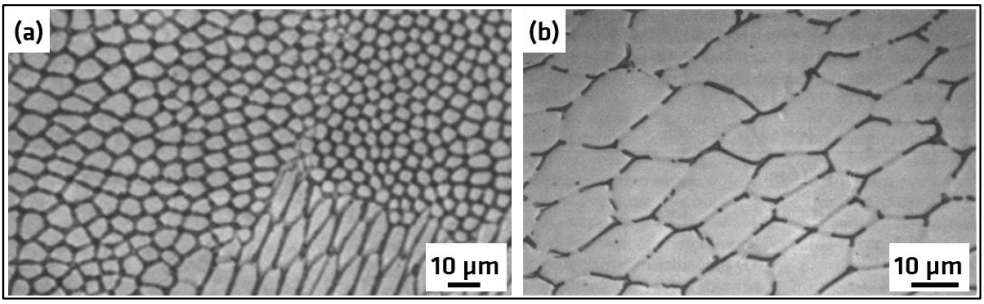

Figure 2.2: a) Fully austenitic microstructure of an electron beam welded stainless steel, b) intercellular ferrite [23], reproduced with permission from Springer Nature.

The 316L alloy has good ductility but relatively low strength, which is often overcome by increasing the amount of cold work [3]. This alloy can be employed at temperatures up to 540 °C [19], limited by the precipitation of various phases as previously mentioned. The mechanical and corrosion properties of 316L gives a lot of flexibility to design engineers, which is mirrored in the wide range of applications. Whilst this alloy is often used for the petrochemical and nuclear industry e.g. shield modules for the fusion system of the international thermonuclear experimental reactor, novel applications via additive manufacturing processing increased the applications to more filigree structures such as medical stents, bipolar plates in proton exchange membrane fuel cells or lattice structures [22, 24, 25]. The ability to tailor microstructures to improve mechanical properties, while enabling the manufacturing of unprecedented structures is a great benefit of the use of additive manufacturing [3, 16].

2.1.2 Additive manufacturing of stainless steel 316L

The additive manufacturing (AM) of metals can be divided in the direct energy deposition (DED) and powder bed fusion (PBF) technologies according to ISO/ASTM 52900 [26]. The DED refers to technologies that use thermal energy to melt material upon deposition and achieve fusion. For DED the metal powder is directly fed into the melt path using a carrier gas such as argon [10]. Common processes are the DED-LB/M (L standing for laser) and the gas metal arc DED-Arc/M, also commonly defined as wire-arc additive manufacturing (WAAM). The PBF refers to technologies that uses thermal energy to selectively fuse material in a powder bed, whereby depending on the orientation of the part the addition of support structures is necessary [10, 27]. The most prominent process is the PBF of metal with laser beam (PBF-LB/M) process. The process sketch of the PBF-LB/M and the DED-LB/M processes is shown in Figure 2.3). A common denominator of the AM processes is the layer-by layer manufacturing approach. Starting from a

digital model i.e. the input is a computer-aided-design file (CAD) of the part, which is subsequently sliced in layers of defined thickness which are typically between 20 µm and 1 mm depending on the AM process [27]. The part is manufactured track-by-track and layer by layer, whereby the scanning or deposition sequence is defined by the scanning strategy. The need for expensive tooling is avoided, which is a unique feature to the AM manufacturing processes [10]. There are multiple differences between PBF and DED. The PBF processes are limited in the part size manufactured (limited by the build chamber dimensions) and are often characterised by lower build rates. In contrast, the DED processes are characterised by their ability to produce much larger parts at higher deposition rates or even to be used to repair components such as turbine blades [27]. Nonetheless, the PBF process allows the manufacturing of intricate parts and the reduction or even elimination of multiple parts in an assembly, which is a major advantage [28, 29].

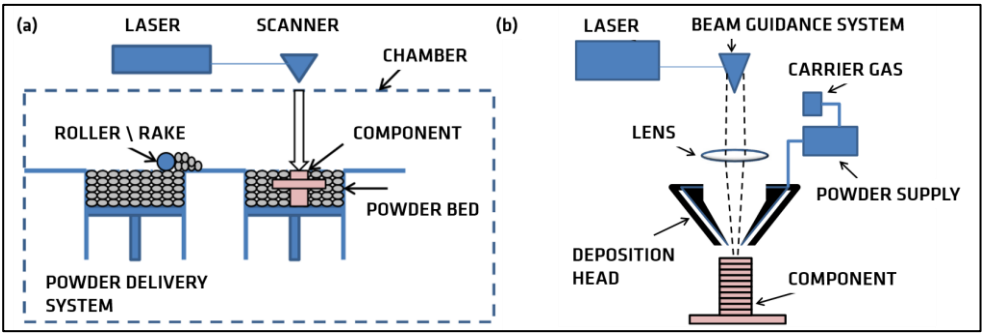

Figure 2.3: a) Schematic of the PBF-LB/M process and b) the DED-LB/M process [29], reproduced with permission from Springer Nature.

The use of rapid moving thermal sources, complex scanning strategies and the layer-by-layer manufacturing makes the AM processes prone for defect formation. The common defects for metal AM processes are porosity and lack of fusion defects, surface roughness, cracking and delamination, loss of alloying elements, residual stress and distortion [10]. The formation of porosity and lack of fusion defects for all PBF and DED processes has been reported for various alloys in the literature [27]. The susceptibility of these processes to produce porosity and lack of fusion remains generally in the use of non-optimal process parameters, which ultimately can be avoided by defining optimal process parameter windows [16, 30]. The printability of the three processes PBF-LB/M, DED-LB/M and DED-Arc/M was assessed by simulation in [31]. An analogy to the widely used weldability for the welding processes is proposed for AM. This analysis was performed to evaluate how the large difference in heat input between the three AM processes influences the processed alloy, to ultimately generate a printability database. To give an order

of magnitude, the heat input of DED-LB/M can be around ten times higher compared to PBF-LB/M [32]. The aspects of chemical composition change, lack of fusion defects, distortion and residual stress were assessed [31], thus regrouping some of the major challenges in metal AM. The residual stress and distortion analysis of the three processes is shown in Figure 2.4. The much larger σ_x, the residual stress in the direction of the wall length as shown in Figure 2.4 a), and distortion in the DED-Arc/M 316L part is correlated with the larger heat input. Both the residual stress and the distortion decrease for the DED-LB/M and PBF-LB/M, reaching a minimum in the PBF-LB/M. Furthermore, the higher ratio of the surface compared to the melt pool volume has been reported to induce a chemical composition change in the manufacturing of the PBF-LB/M, which is less the case for the DED-LB/M and DED-Arc/M [31].

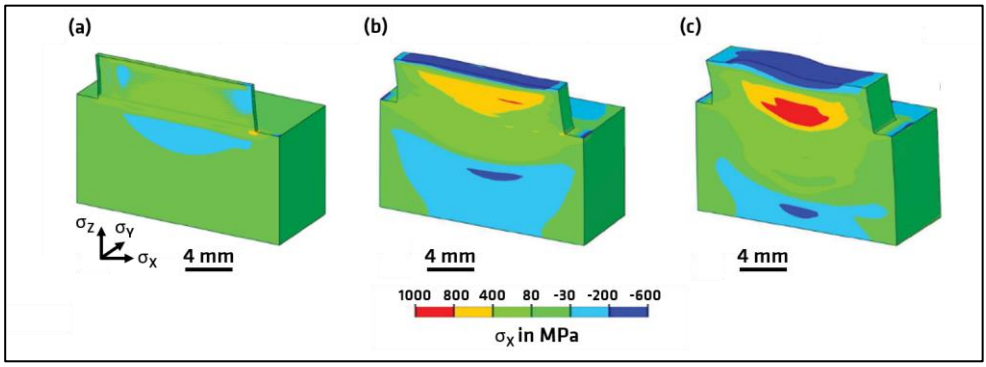

Figure 2.4: a) Residual stress and distortion in PBF-LB/M, b) in DED-LB/M and c) DED-Arc/M. Adapted from [31].

One further observation that can be deduced from Figure 2.4 is the difference in wall thickness. It appears clearly that depending on which AM process is employed, different wall thicknesses can be achieved. Much larger weld beads are deposited using DED-Arc/M and to a lesser degree DED-LB/M [31], which results in a much larger deposition rate of the DED processes [29]. The DED processes are limited when it comes to manufacturing complex parts. Thereby DED-Arc/M often requires post process machining to obtain the final part geometry, whilst PBF-LB/M is considered to be able to produce net-shape parts [10, 33]. Complex structures requiring small wall thickness such as lattice structures (see Figure 2.5 a and further examples in e.g. [13, 34]) cannot be manufactured to date using the DED process [10]. Nonetheless, as-built PBF-LB/M parts still have higher surface roughness (see Figure 2.5 b and c) compared to machined surfaces e.g. Sa (arithmetic mean height of 3D roughness) of 5 µm-6 µm for 316L PBF-LB/M compared to 1 µm Sa for machined and polished wrought 316L [35, 36]. Though the

dimensional accuracy of PBF-LB/M is high, the as-built surfaces may require post processing as it was found to lower the fatigue properties [35, 36].

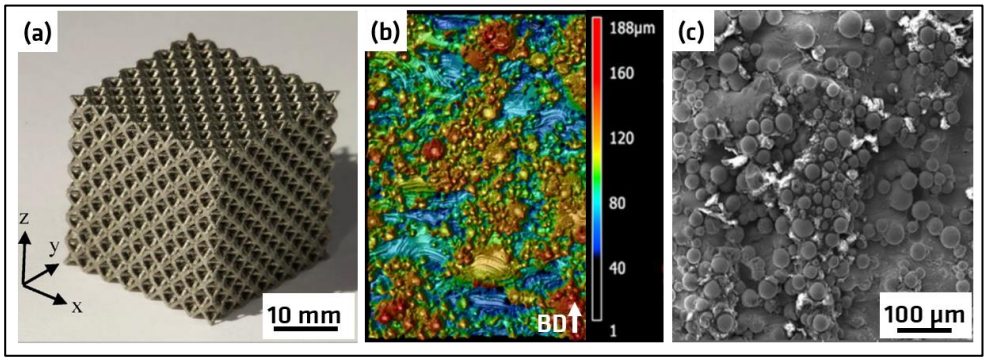

Figure 2.5: a) 316L PBF-LB/M lattice structure, reprinted from [25], with permission from Elsevier, b) surface roughness map (height map in µm) and c) SEM image of the surface of PBF-LB/M/Ti-6Al-4V [37], reproduced with permission from Springer Nature.

A short summary of the different attributes discussed herein with additional information on post processing options, the dimensional accuracy and tensile properties is given in Table 2.2. The PBF-LB/M is able to produce net-shaped parts with a much higher dimensional accuracy as well as manufacturing complex shapes and tailored microstructures, which explains why it has been in the focus of many research groups.

Table 2.2: Comparison of various attributes associated with the AM processes PBF-LB/M, DED-LB/M and DED-Arc/M.

Process	PBF-LB/M	DED-LB/M	DED-Arc/M
Solidification	fully austenitic [16]	austenitic, amounts of ferrite [41]	austenitic, amounts of ferrite [44]
Post-processing [38]	heat treatment, hot isostatic pressing, machining	heat treatment, machining, grinding	heat treatment, stress relieving, machining
Dimensional accuracy, average deviation in mm [38]	0.04-0.2	0.2-5	1-5
Yield Strength [MPa]	528 ± 10 [39]	469 ± 6, 429 [42, 43]	418 [45]
Ultimate Tensile Strength [MPa]	613 ± 10 [39] 638 ± 22 [40] 674 ± 9 [40]	649 ± 2, 567 [42, 43]	550 ± 6 [45]
Elongation [%]	30 ± 2, 39 ± 4 [39, 40]	23 ± 3, 76 [42, 43]	/

The PBF-LB/M is the technology of choice to produce parts with very complex, net shaped-geometries with internal features. These aspects are important as they may lead to the reduction of the weight. Moreover, improved mechanical properties compared to wrought counterparts and other AM processes were reported for PBF-LB/M. Since PBF-LB/M leads to fully austenitic microstructures which remain stable, the additional complexity of phase transformation or the presence of different phases can be avoided when analysing the resulting properties. Following metallurgy aspects covered in subsection 2.1.1, any remaining Ferrite (area enriched in Cr) could lead to a decrease of the corrosion properties as enhanced precipitation could occur. Overcoming the strength-ductility trade off via the use of PBF-LB/M is a promising field as compared to other manufacturing techniques, no tooling or surface mechanical treatment (except for functional surfaces) is required [3]. *Therefore, in the remaining of this chapter a focus will be placed on PBF-LB/M of 316L.*

Microstructure of PBF-LB/M/316L

The microstructure of the PBF-LB/M/316L was characterized in detail in [3] and is shown in Figure 2.6. A hierarchical microstructure was observed in PBF-LB/M/316L spanning several orders of magnitude, covering aspects of the grains having lengths up to 200 µm shown in Figure 2.6 a), fusion boundary and high angle grain boundaries (HAGB) shown in Figure 2.6 b), the presence of solidification subgrain cellular structures with the cell sized smaller than 1 µm and the cell walls thicknesses smaller than 160 nm as shown in Figure 2.6 c) and d). On the nanometre scale, the presence of precipitates sized between 10 to 150 nm and impurities such as nitrogen and hydrogen below 1 nm were observed [3]. The aforementioned improvement in the tensile response of the PBF-LB/M/316L is related to the collective effect of the hierarchical microstructure [3]. PBF-LB/M/316L was mostly observed to be fully austenitic due to the high cooling rates during the processing (see comment on low Cr/Ni ratios in subchapter 2.1.1) [16]. This is of particular importance as it directly affects the phases occurring in the material [46].

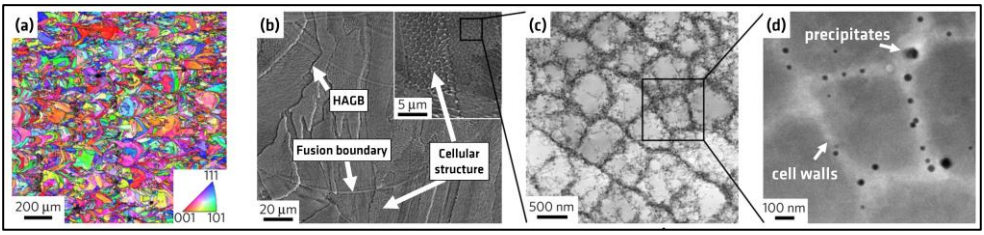

Figure 2.6: a) microstructure of PBF-LB/M showing the reverse-bell shaped grains, b) HAGB, fusion boundaries and cellular structure, c) cell structure and d) cell walls and precipitates [3], reproduced with permission from Springer Nature.

The texture in PBF-LB/M/316L has been reported to depend heavily on the process parameters and more specifically the scanning strategy [16, 33]. A predominant <200> texture was observed to change when to a <220> texture in the build direction when decreasing the laser power by 16 %. A similar effect was found when varying the scanning strategy. All other parameters were kept constant. Decreasing further the laser power was reported to lead to a random texture [33]. It is argued that as the <100> grains grow along the main thermal gradient as it is the fastest growing direction in the solidification of cubic materials [16, 47]. An increase of just the laser power leads to a stronger thermal gradient in the build direction, which results in a microstructure having a <200> texture in the build direction [33]. The values are between 1-3 multiple times random[48] and have a significant impact on the mechanical properties as shown in a study on the anisotropic tensile behaviour of PBF-LB/M/316L in [49-51]. The definition of multiple times random is a quantitative way of describing the texture by normalizing the intensity with the value 1 defining a random texture i.e. no intensity density accumulation as a function of direction [52].

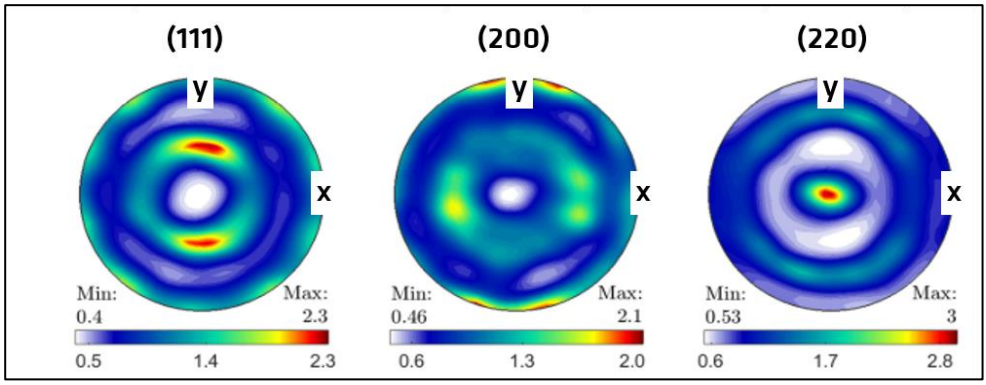

Figure 2.7: Pole figures of as-built PBF-LB/M/316 showing a <220> texture along the build direction (z) – out of plane direction in this representation. Adapted from [33].

The PBF-LB/M process offers the possibility to tailor the texture and hence adapt the material properties [53]. Thereby the solidification subgrain cellular structure (cellular structure) plays a major role [16]. Recently, multiple studies [4-6] were published on the origin and properties of the cellular structure, which is summarized in the following.

The solidification subgrain cellular structure

The formation of the solidification subgrain cellular structure is linked to the solidification mechanisms occuring during PBF-LB/M driven by the high cooling rate, which reaches up to 10^5 to 10^6 K/s [12]. The appearance of the cellular structure in the plane perpendicular to the build direction is shown in Figure 2.8 a) and b). The formation of these cells was mainly observed in face-centered-cubic Co-, Ni-, Fe- and Al-based alloys [54]. Knowledge acquired on the welding metallurgy of austenitic stainless steels attribute the formation of cells and dendrites to the solidification as primary austenite because of the segregation of elements with low diffusivity, in case of 316L the elements Cr and Mo, which consequently pin the shape of this solidification structure [17]. Indeed, in PBF-LB/M of 316L, the walls are comprised of Cr and Mo segregations and Mn-enriched SiO_2 precipiates and are decorated with forests of dislocations [3, 55] as shown in Figure 2.8 c) and d). The growth direction of the cellular structure with respect to the melt pool is shown in Figure 2.8 e). The schematic indicates the preferred nucleation of dendrites at the bottom of the melt pool with a growth direction tangential to the curvature of the next melt pool [55].

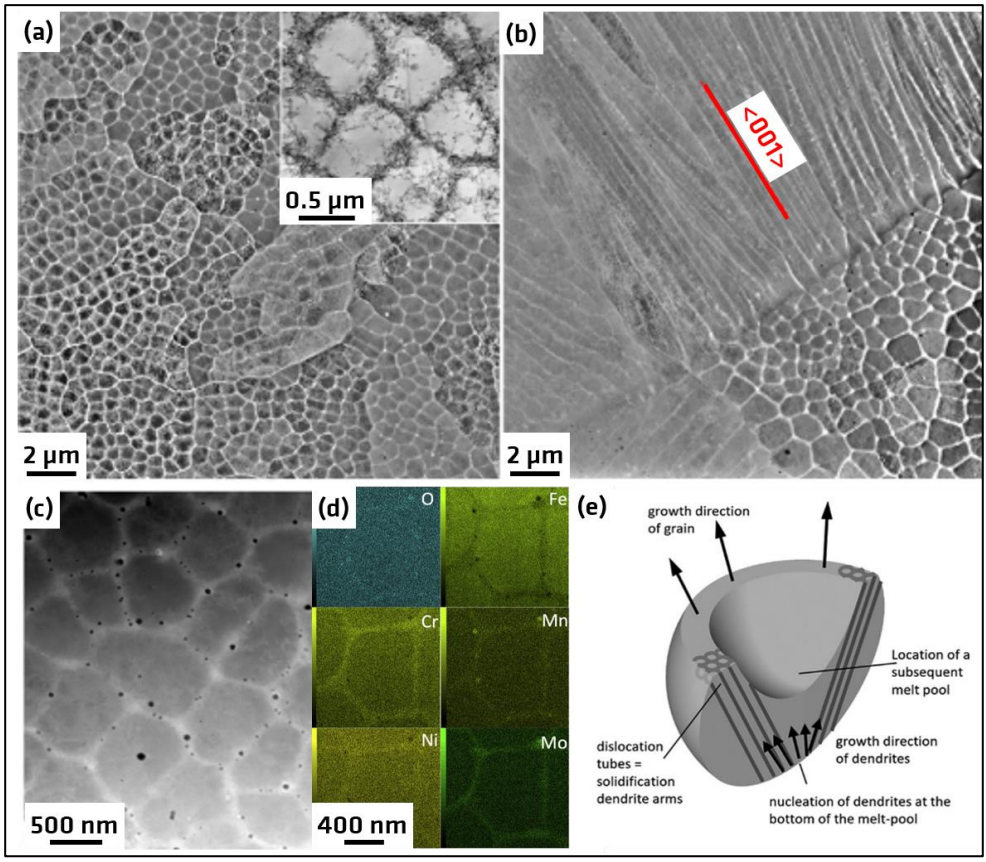

Figure 2.8: a) transmission electron microscopy acquisition of the cellular structure in PBF-LB/M/316L in the plane perpendicular to the build direction, b) of the elongated cellular structure at a grain boundary/ molten pool boundary , c) close up view of the cellular structure highlighting the presence of precipitates in the cell walls, d) Energy Dispersive X-ray Spectroscopy (EDX) analysis of the cell walls, and e) schematic of growth direction of the grain and cellular structure. a) to c) reprinted from [6], and d) to e) reprinted from [55], with permission from Elsevier.

A major difference to cells seen in welded specimens is the size. In Tungsten Inert Gas (TIG) welded 316L the cells are of one magnitude larger than in PBF-LB/M [6, 56]. A clear difference in cell size is also observed when comparing the microstructure of the fully austenitic electron beam welded stainless steel shown in Figure 2.2 a). There is an ongoing discussion on the formation mechanisms. A few theories on the formation of the cellular structure explain this phenomenon with the effects of micro-segregrations that create local misfits which are accomodated by dislocations [5]. In another study, the formation is linked to first

the arising of the dislocation structure resulting from the solidification and thermal shrinkage and corresponding residual stress development, which is then prone to act as sinks for solute diffusion [4]. Most recently, a study revealed that whilst the source of the dislocations is the deformation induced by a restrained thermal expansion or shrinkage, the shape of the structure is attributed to the influence of the micro-segregation [5]. Further studies have also revealed the presence of small precipitates in the cell walls [6]. The cell size and wall thickness i.e. the shape of the cellular structure are affected by the solidification conditions (thermal gradient, cooling rate and the solidification front velocity) [3].

The comparison of PBF-LB/M and their wrought counterpart alloy is often performed despite having differences in the chemical composition. A good example showing the differences between the PBF-LB/M, the cast and the forged stainless steel 316L was reported in [55]. The PBF-LB/M parts were subsequently molten in an arc furnace and then cast and forged (hot forged at 850 °C and recrystallization and solution treatment at 1050 °C for 30 mins) to achieve each condition. The microstructure resulting from the three processes is shown in Figure 2.9. The typical reversed-bell grain structure developing during the PBF-LB/M is shown in Figure 2.9 a). The inset further shows the characteristic melt pool boundaries with sizes corresponding to the hatch distance [55]. The overlay of the optical microscopy image shows that the grains grow through multiple layers as discussed previously. The presence of the colour gradients indicates the presence of low angle grain boundaries within the grains. The forged 316L microstructure is shown in Figure 2.9 b). Much larger grains are visible. Since the PBF-LB/M grains exhibit such a complex shape, it is difficult to compare grain sizes. However, the grain boundary density in the PBF-LB/M material is 1.5 times higher than the forged material [55]. A large number of twins is present in the forged material, contributing to 56 % of all large grain boundaries. In Figure 2.9 c) the microstructure of the cast 316L consist of large grains with inclusions (ferrite). The large difference in cooling behaviour leading to the smaller grains of the PBF-LB/M material compared to the cast material is evident from Figure 2.9 c) [27].

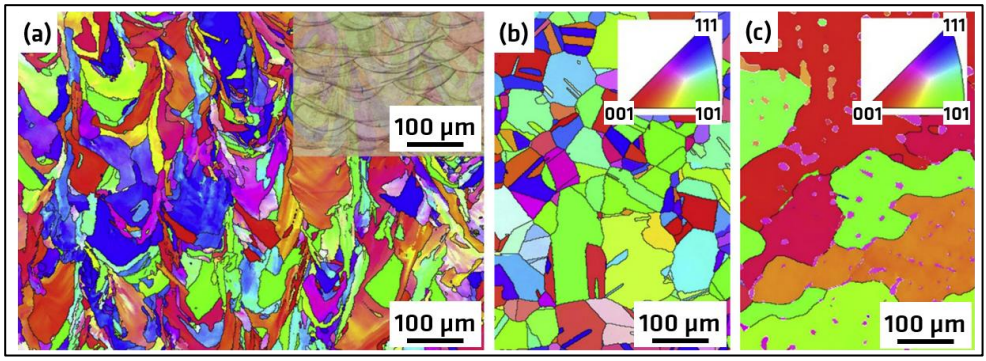

Figure 2.9: a) microstructure of 316L PBF-LB/M, b) forged 316L and c) cast 316L. Reprinted from [55], with permission from Elsevier.

The layer wise manufacturing, localised heat input and the generation of very high cooling rates through high scanning velocities leads not only to the complex microstructure of PBF-LB/M but also generates residual stress. The residual stress was reported to be ubiquitous in PBF-LB/M and one of the major challenges to overcome [57]. The notion of residual stress refers to the presence of a self-equilibrating stress in a body exempt of external forces, moments, or thermal gradients [58]. Residual stress affects the performance of a part e.g. compressive residual stress may delay fatigue crack propagation but tensile residual stress may increase the mean stress resulting in poorer fatigue lives [58]. For the wider use of AM parts in safety critical applications, knowledge of the residual stress formation and distribution is therefore crucial which is the topic of the next chapter.

2.2 Residual stress in powder bed fusion of steels with laser beams

The notion of residual stress as well as different methods, non-destructive and destructive, to determine them is introduced in subchapter 2.2.1. The diffraction-based assessment of the residual stress and related challenges is detailed in subchapter 2.2.2. Then the formation and distribution of residual stress in PBF-LB/M is detailed in subchapter 2.2.3 and 2.2.4. Finally, the influence of PBF-LB/M process parameters on the residual stress is presented 2.2.5.

2.2.1 Generalities of residual stress and determination methods

The residual stress is defined as stress retained in a body in absence of external forces and moments or thermal gradients [58]. The residual stress is classified by the length-scale over which it equilibrates. The residual stress types and their respective length scale is shown in Figure 2.10 a). The type I residual stress equilibrates over the length-scale of the component, the type II residual stress equilibrates over the length-scale of multiple grains and finally the type III residual stress equilibrates within one grain [59].

The type I residual stress ($\tilde{\sigma}^{\mathrm{I}}(\vec{x})$) is referred to as macroscopic residual stress and the type II ($\tilde{\sigma}^{\mathrm{II}}(\vec{x})$) and type III residual stress ($\tilde{\sigma}^{\mathrm{III}}(\vec{x})$) are referred to as microscopic residual stress [58, 60]. The summation of the type I -type III residual stress can be expressed by the total residual stress ($\tilde{\sigma}(\vec{x})$) in a volume, whereby integrating the total residual stress over this volume equals zero as shown in equation 1.

$$\tilde{\sigma}(\vec{x}) = \tilde{\sigma}^{\mathrm{I}}(\vec{x}) + \tilde{\sigma}^{\mathrm{II}}(\vec{x}) + \tilde{\sigma}^{\mathrm{III}}(\vec{x}), \int \tilde{\sigma}(\vec{x}) dV = 0 \qquad (eqn.\,1)$$

The underlying source for residual stress is the misfit between different regions or between different phases of the material [58]. This misfit can originate throughout the processing and post processing steps e.g. machining, heat treatment, welding [60]. The determination of the residual stress can be either performed by non-destructive or destructive methods [58]. Representative techniques are summarized in Figure 2.10 b). In each case, the residual stress is not directly determined but rather a physical material property is measured that can be linked to the residual stress e.g. when using diffraction the lattice spacing of a crystal is calculated from the measured diffraction peak position (angle, time-of-flight (TOF), energy) which is then used to calculate the stress (more details are given in subchapter 2.2.2) [61]. In case of the destructive techniques, material is removed,

and the contraction or expansion i.e. the deformation of the material is measured to calculate the initial residual stress [58]. The difference between the non-destructive and destructive techniques lies in the fact that the use of the destructive techniques results in the scrapping of the part investigated (especially in the case of the slitting and the contour method). Moreover, the destructive methods are independent of the microstructure of the material investigated [62]. These techniques also differ in the information retrieved from the experiment because of the underlying principle to determine the residual stress e.g. the contour method determines only the residual stress component normal to the cutting plane [63]. Another method often used in investigations on the residual stress in PBF-LB/M is based on the measurement of the deflection of a cantilever shaped specimen [64]. In fact, the determination of the surface residual stress via this method makes use of the tensile residual stress which causes the upward deflection of the specimen. This effect can also be captured by digital image correlation (DIC) techniques or a coordinate measurement machine (CMM) e.g. [65-67].

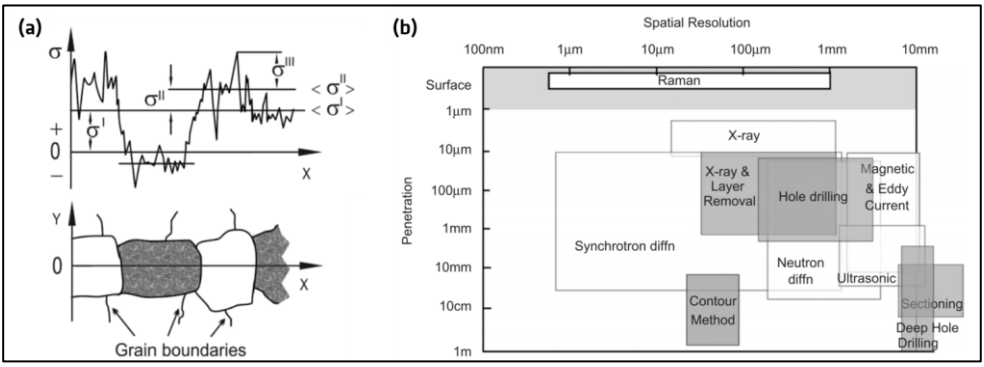

Figure 2.10: a) The different types of RS according to their respective length-scale in a single-phase material (reproduced with permission of De Gruyter) [59], b) Spatial resolution and penetration depth of non-destructive and destructive determination methods of residual stress, reprinted from [68], with permission from Elsevier.

An advantage of PBF-LB/M is the ability to manufacture complex shapes, such as the valve shown in Figure 1.1 a) or the lattice structure shown in Figure 2.5 a). Assessing the residual stress in these components is challenging and reduces the number of methods which can be used. For instance, using the hole drilling method requires to apply a rosette strain gage with a typical diameter of 5.13 mm (from [69] according to ASTM E837-13a [70]). This limits the use of this method for filigree AM components. Also the increased surface roughness of PBF-LB/M is an

issue for the application of a strain gage, which can be remedied by e.g. sanding as reported in [71]. *However, performing such surface treatment alters the residual stress.*

The diffraction methods are particularly suited to also determine the residual stress in complex structures e.g. PBF-LB/M lattice structures with 1 mm (diameter) struts [13] or curved PBF-LB/M 2.5 mm thick walls [72]. In contrast to the destructive methods hole drilling, slitting and contour there is no need for additional tooling or surface preparation. This is a great benefit as PBF-LB/M is often used for small part series [10]. *The inherently non-destructive determination of the residual stress via diffraction reduces the number of specimens for investigations, which can be of great benefit as the powder feedstock for PBF-LB/M is costly [38].*

As shown in Figure 2.10 b), either X-ray diffraction (XRD) or neutron diffraction (ND) can be used when determining the surface or bulk residual stress respectively. Synchrotron XRD (SXRD) also permits to determine the residual stress near the surface and at higher depths compared to the laboratory XRD sources [73]. Combining laboratory XRD (including layer removal by electropolishing), SXRD and ND either individually or complementing each other makes it possible to characterise the distribution of the residual stress from the surface to the bulk in a non-destructive manner (semi-destructive when using layer removal). In case of ND it is possible to calculate the triaxial bulk residual stress and the near surface residual stress (requires extensive data processing [74, 75]). Also, the evolution of residual stress in realistic environments and loading techniques can be monitored by ND or SXRD, whereby the spatial resolution can be tailored to the aim of the experiment [61]. Furthermore, phase specific and type II residual stress can be determined by ND or SXRD [61]. These aspects are not covered by destructive methods. However, a major drawback is the limited access to carry out ND or SXRD experiments.

When opting for diffraction based residual stress assessment, laboratory XRD combined with layer removal is the most practical option to investigate the surface and the subsurface residual stress. When it comes to determining the residual stress in the bulk, ND has the major advantage of higher penetration in metals e.g. up to 100 mm in aluminium [62]) and almost cubic gauge volume shapes over SXRD i.e. a better spatial resolution in the three dimensional space can be achieved. Both SXRD and ND measurement time is difficult to obtain (limited access, high competition and lengthy proposal and acceptance process). As ND can provide better spatial resolution, it is of great benefit to perform triaxial residual stress mappings. In

combination with laboratory XRD, the two methods enable to determine the through-thickness residual stress profile with a high resolution.

2.2.2 Diffraction-based residual stress assessment

The theory behind the diffraction based assessment of residual stress makes use of Bragg's law describing the relationship of the wavelength λ of either a X-ray or Neutron beam to the lattice spacing d via the diffraction angle θ as shown in Figure 2.11 a) and calculated from [76]:

$$n\lambda = 2d_{hkl}\sin(\theta) \qquad (eqn.2)$$

Whereby n is the order of interference and hkl are the Miller index labels corresponding to the respective crystallographic plane. The acquisition of a diffraction pattern in the direction of the scattering vector $\vec{q}$ (see Figure 2.11 a) is a measure of all crystallites within the gauge volume that fulfil Bragg's condition of a given reflection. In Figure 2.11 b) it is schematically shown how crystals fulfil Bragg's law in the monochromatic case ($\vec{q}_1$) and in the polychromatic case ($\vec{q}_1$ to $\vec{q}_3$) e.g. the orange arrows indicate crystals having their (220) lattice plane in reflection and the red and the pink arrows indicate crystals having their (311) and (200) lattice planes in reflection respectively. Each of the crystallites fulfilling Bragg's condition contribute to a diffraction peak. The resulting peak position (identified by 2θ or the time-of-flight in µs) is the average lattice spacing of these crystallites.

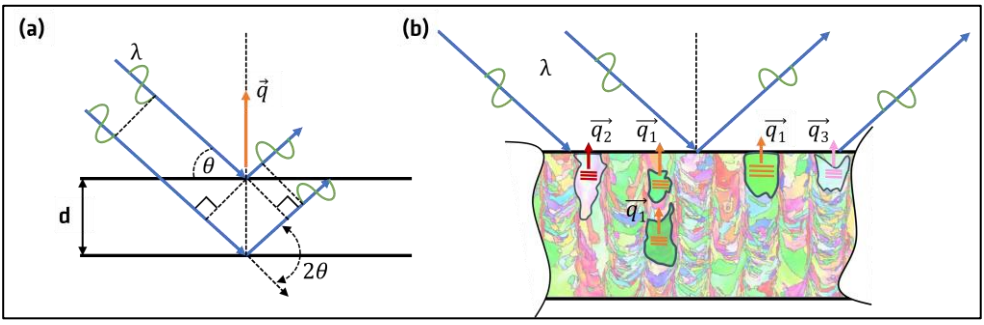

Figure 2.11: a) Schematic for the derivation of Bragg's law (adapted from [77]) and b) crystallographic planes in reflection. In b) $\vec{q}_1$scattering vectors indicate the monochromatic case whereas $\vec{q}_1$ to $\vec{q}_3$ scattering vectors are considered for the polychromatic or TOF case. Background image in b) taken from [78].

Generally, when using a monochromatic set-up, the diffraction peak of a single lattice plane will be acquired (in some cases the detector coverage is sufficiently large to acquire more than one peak). However, using polychromatic source i.e white beams, a larger number of diffraction peaks can be acquired with the same scattering vector [79]. From each reflection, information on the position, the intensity and the peak profile can be derived [77]. In case of diffraction based residual stress assessment (mostly type I residual stress), the targeted information is the peak position. However, each diffraction peak will also give information on the microstructure and microscopic residual stress through the full width at half maximum (FWHM) [77]. The subgrain dislocation structure may have local misorientation (mosaicity) which upon dissolution during annealing decreases the FWHM as reported in [80]. Also, larger FWHM resulting from higher dislocation densities may indicate plastic deformation as reported in [81]. *The FWHM is a convolution of the instrument characteristics, the microstructure, and the microscopic residual stress. It is important to both analyse the microstructure and the FWHM to have the possibility to extract deconvoluted information.*

The calculation of the residual stress depends on the diffraction method and set-up used. The calculation of the residual stress using laboratory XRD and ND (angular and energy dispersive) is further detailed in subsection 3.7, as the two methods are primarily used in this study. The reader is referred to [61, 73] for more details regarding SXRD. There are a number of challenges when using diffraction to determine the residual stress as discussed in [58, 82, 83]. One common aspect of diffraction based residual stress assessment is the necessity of using appropriate diffraction elastic constants (DEC). When using XRD, SXRD or ND, the lattice strains are determined with the aim to calculate the type I residual stress [61, 84]. This link is provided through the DEC. The DEC s_1 and s_2 are calculated from [52]:

$$s_1 = \frac{-\nu_{hkl}}{E_{hkl}} \;\&\; \frac{1}{2}s_2 = \frac{1+\nu_{hkl}}{E_{hkl}} \qquad (eqn.3)$$

Whereby ν_{hkl} and E_{hkl} are the Poisson ratio and Young's modulus of a specific (hkl) lattice plane respectively. These can be either determined experimentally via e.g. uniaxial tensile tests (see subchapter 4.2) or calculated from single-crystal data and modelling the elastic coupling of crystallites e.g. [85]. Since the diffraction pattern is closely associated to a set of grains, acquiring a second strain direction (for the calculation of the Poisson ratio) also means that another, independent set of grains is analysed. In practice the direct calculation of the Poisson ratio is difficult, especially for anisotropic materials. It was shown in [86] that the

calculation of the Poisson ratio from the diffraction data led to erroneous or highly scattered values, especially for textured material.

The DEC are a property of the lattice plane selected and used to calculate the type I residual stress from lattice strains. Therefore (most importantly when using monochromatic XRD or ND [87]), a suitable lattice plane needs to be selected for the residual stress analysis. It is advised to consider the following main aspects [83]: the accumulation of type II strains, the texture of the material and the crystal symmetry. From the crystal symmetry the multiplicity can be derived, which is a measure of the number of equivalent reflection peaks having the same lattice spacing [61]. This is a practical aspect in terms of reducing the measurement time but also to use better grain statistics and reduce intergranular effects.

Selection of the lattice plane

Following the definition of type II residual stress (see Figure 2.10 a) it can be deduced that when determining the type I residual stress, the resulting value is a superimposition of the two types of residual stress [88]. However, when selecting a lattice plane which does not accumulate type II strains, the resulting value is a better representation of the type I residual stress. Following suggestions and findings reported in [79, 89], the (311) lattice plane best describes the type I residual stress in FCC alloys. With ND as measurement technique for determining the residual stress, multiple in-situ experiments combined with simulation and texture analysis were carried out on austenitic stainless steels e.g. [79, 86, 90-92]. The aim was to understand the micromechanical behaviour but also to verify, which lattice plane best describes the macroscopic residual stress. Moreover, the diffraction Young's moduli were determined from the acquired data. An example of an in-situ tensile test using polychromatic ND from [79] is given in Figure 2.12 a). The lattice strain evolution of various lattice planes is shown when applying a tensile load to a polycrystalline, fully austenitic FCC stainless steel with a small rolling texture (<1.5 times random) [79].

The evolution of the lattice strain can be separated in the fully elastic regime and the plastic regime. The transition between these two regimes is the elastic-plastic regime. In the fully elastic regime, the slope of the lattice strain is dominated by the elastic anisotropy of the material. The result is a visible spread between each lattice planes as shown in Figure 2.12 a). A first important aspect to note is the vicinity of the (311) lattice plane evolution with the Rietveld refined lattice parameter and overall macroscopic material behaviour (here denoted as the macroscopic Young's modulus). The advantage when using polychromatic i.e. energy-dispersive ND is the possibility to determine the lattice parameter of the

alloy using multiple diffraction peaks based on least-squares approaches (Rietveld and Pawley refinement [79, 93, 94]). The lattice parameter is not affected by the accumulation of microstrain in single phase materials. It provides in theory the best approximation of the macroscopic elastic behaviour (note the similar slope of the macroscopic Young's modulus and the Rietveld data in Figure 2.12 a) and the type I residual stress. The onset of plastic deformation is indicated by the load shedding and the load accumulation of different lattice planes. In the case of austenitic steel, the lattice plane to yield first is the (220) lattice plane, which results in the strain accumulation of the (200) lattice plane (indicated by the arrow in Figure 2.12 a). When a lattice plane yields, no elastic lattice strain accumulation occurs and increasing the applied load leads to an upward deviation of the slope. *In both cases, a deviation from linearity occurs and when releasing the applied load this deviation is retained as a residual lattice strain.*

Performing the loading and unloading at various stages starting with the elastic-plastic regime and plastic regime leads to the plot shown in Figure 2.12 b). Following the predictions of microstrain accumulation of FCC material in [89], the (200) and the (311) lattice planes tend to accumulate tensile residual microstrain whereas the (220) and the (111) lattice planes tend to accumulate compressive residual microstrain. This behaviour is observed in Figure 2.12 b). The (311) lattice plane accumulates low values of microstrain as well as the (111) lattice plane.

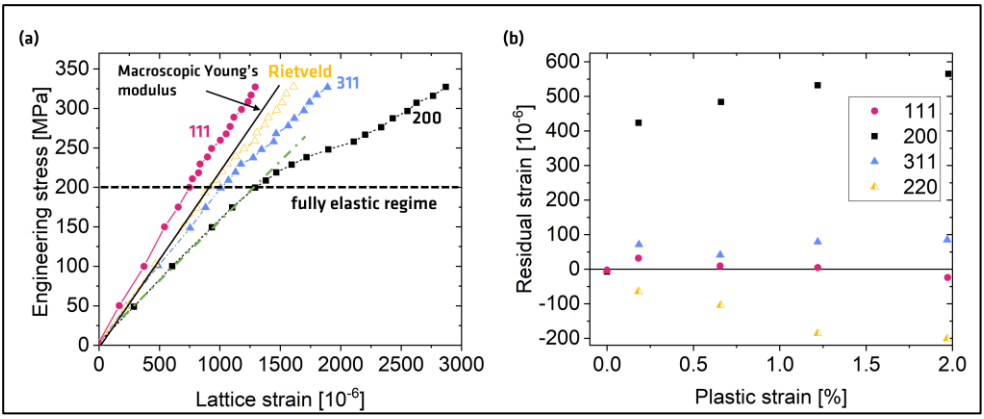

Figure 2.12: a) Evolution of the (111), the (311) and the (200) lattice plane strains under an applied tensile load compared to the lattice parameter (Rietveld refinement) and the macroscopic Young's modulus (Adapted from [79]). The dashed green line in a) denote the fully elastic regime limit and the onset of plasticity as the (200) lattice plane starts accumulating strain at a faster rate (deviation from linearity). b) Accumulation of residual strain of different lattice planes under an applied tensile load (Adapted from [90]).

The second aspect to consider is the prevailing texture. Following suggestions reported in [87] the lattice plane to best describe the type I residual stress should be chosen according to the texture e.g. if a strong <100> texture is present in the material, the (100) lattice plane should be used to calculate the residual stress. However, as observed in Figure 2.12 b) the (100) lattice plane accumulates the largest microstrains. Several studies were performed to investigate the suitability of various lattice planes for the determination of the residual stress on conventionally processed austenitic steels e.g. [79, 86, 87, 90]. For PBF-LB/M processed material, the investigations are scarce. The lattice strains in PBF-LB/M/316L under tension were investigated using SXRD in [48, 95]. The trends described by the lattice strains were similar to the ones shown in Figure 2.12 a), which may indicate that the PBF-LB/M austenitic steel has a similar micromechanical behaviour compared to wrought processed austenitic steels. *With regards to the selection of a lattice plane, a detailed analysis on which lattice plane to use to describe the type I residual stress in PBF-LB/M material was not performed i.e. the accumulation of microstrains was not investigated and no comparison was made between the elastic bulk behaviour (refinement using Pawley or Rietveld) and the lattice planes*.

Determination of the DEC

Once the lattice plane is selected, the appropriate DEC need to be known to calculate the residual stress. As mentioned previously, the DEC can be either tabulated from single-crystal-elastic constants (SCEC) using theoretical schemes or acquired through dedicated experiments [96, 97], which furthermore give indications on the choice of the lattice plane to correctly describe the macroscopic residual stress. The most important grain interaction theoretical schemes are the Voigt, the Reuss and the Kröner models [61]. In the Voigt model each grain in the polycrystal is assumed to be exposed to a uniform strain. This, however, violates the equilibrium of forces at the grain boundaries. In the Reuss model each grain is assumed to be exposed to an average stress. This assumption does not comply with the continuity of displacement at grain boundaries [52]. In the Kröner model the grains are assumed to be ellipsoids in a homogenous matrix, where each grain can experience different stresses and strains [61]. For FCC materials such as austenitic steel 316L, the Kröner model is generally used to derive the DEC [97]. The in-situ SXRD tensile tests of PBF-LB/M/316L showed that the diffraction Young's moduli along a single direction were in good agreement with the Kröner model [48]. These values were, however, not representative of the strongest texture in the material (up to 4 times multiple random in the build direction). In fact, the Kröner model works well with isotropic materials (texture free), whereas for textured materials the Reuss model may be applicable [52]. This was observed for a textured PBF-LB/M/IN718 [98]. Due to scarce PBF-LB/M specific DECs, the common approach used in residual stress investigations on AM is to use DECs determined for wrought and cast alloys to calculate the residual stress [83, 96].

Since the DECs are linked to the microstructure, the values used for wrought or cast alloys might not be appropriate to calculate the residual stress in PBF-LB/M alloys. Therefore, dedicated experiments such as the in-situ tensile ND test results shown in Figure 2.12 are required to investigate which lattice plane (including the DEC) can be used to describe the type I residual stress. In fact, several studies use the tabulated values using the Kröner model e.g., [99, 100]. As described in subchapter 2.1.2, the PBF-LB/M processed 316L is not texture free and raises the question of whether the Kröner model can still be applied to calculate the DEC needed for the subsequent calculation of the macroscopic residual stress.

Stress-free reference

Once the lattice plane is selected, an appropriate stress-free-reference d_0 is necessary for the calculation of the residual strains. While the value of d_0 is less important for the calculation of the surface residual stress via the $\sin^2\Psi$ method (see derivation of the method in subsection 3.7.1), it is of utter importance for the determination of the absolute residual stress via ND. The ISO 21432 standard suggests different approaches including: the measurement at a position inside the specimen containing negligible residual stress, measurement on a powder of the same chemical composition, the use of extracted geometries such as combs or cubes from the specimen to be investigated, imposition of force and moment equilibrium or using the boundary condition of zero stress perpendicular to a free surface [101]. Advantages and disadvantages to each approach are discussed in detail in [83]. A systematic study investigating the use of cubes, filings, powder and boundary conditions to determine the residual stress in PBF-LB/M/IN718 showed that the boundary conditions and cubes provided a more appropriate stress-free reference [81]. As mentioned in subsection 2.1.2, the PBF-LB/M process can lead to a chemical change over the build height of the component. This effect was observed in the DED-LB/M of IN625 [102]. Cubes or combs are the better choice to capture changes in the stress-free reference when chemical composition or phase distribution changes are expected [101]. This is also shown by studies in literature opting for this approach e.g. [14, 48, 103, 104]. Following the standard, the force or moment equilibrium approach should be mainly used for validation purposes [101]. *Therefore, using cubes or combs as stress-free reference appears to be a good choice for the determination of residual stress in PBF-LB/M specimens.*

2.2.3 Formation of residual stress in PBF-LB/M

The formation mechanism of residual stress during PBF-LB/M was first analysed in detail on stainless steel 316L and reported in [11]. The residual stress was determined experimentally using the crack compliance method and XRD, which were compared to simulations. The experimental results showed that the residual stress at the surface was tensile, and that compressive residual stress was present in the bulk of the specimen as shown in Figure 2.13 a). The depth investigated was 10 mm. Since the crack compliance method is not suitable for accurately determining the residual stress at the surface, additional XRD measurements were performed. Initial results revealed low residual stress in the order of the measurement uncertainty. The author's attributed this to the high surface roughness of PBF-LB/M structures [11]. The rough surface was processed by electric discharge machining (EDM) and polished. The additional measurements confirmed the presence of tensile residual stress at the surface reaching values around

150 MPa. On similar test specimens but using a different scanning strategy, the XRD measurements revealed that the highest tensile residual stress (~300 MPa) was found in the specimen with a height of 10 mm. The lowest residual stress (~40 MPa) was determined in the specimen with a height of 2.5 mm as shown in Figure 2.13 b).

The results shown in Figure 2.13 indicate that tensile surface residual stress is balanced by compressive residual stress in the bulk. The surface roughness results in lower residual stress values and parameters such as the scanning strategy and the geometry influence largely the residual stress. This is further discussed in the subchapters 2.2.3 and 2.2.5.

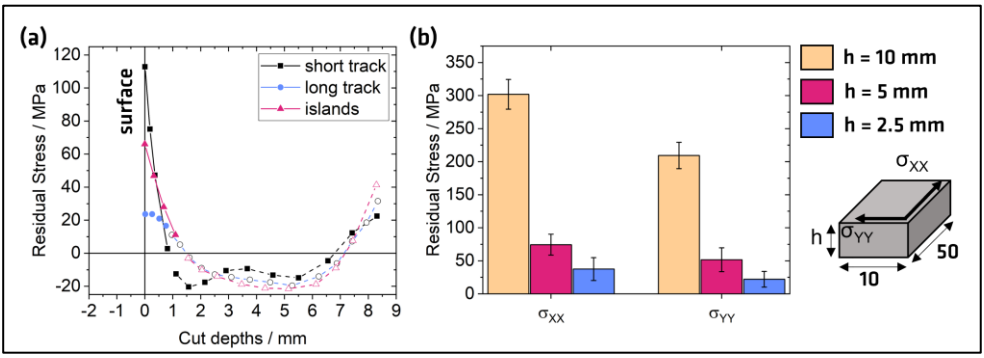

Figure 2.13: a) Residual stress distribution in a PBF-LB/M/316L sample as a function of different scanning strategies. b) Residual stress on the top surface of PBF-LB/M/316L specimens of 2.5 mm, 5 mm, and 10 mm height. Specimen dimensions in b) are in mm. Adapted from [11].

The authors in [11] coupled the experiments with simulations. The approach taken to describe the formation of the residual stress was the separation in two distinct mechanisms. The thermal gradient mechanism (TGM) and the cool-down phase or restraint shrinkage of the molten layers. A sketch of the two sources of residual stress formation in PBF-LB/M is shown in Figure 2.14. The TGM refers to a mechanism commonly used in laser bending of sheets. When rapidly heating a surface, a large thermal gradient is induced between the surface and the colder underlying material. Hence, the material at the surface is expanding faster than the colder surrounding material (see Figure 2.14 a). This expansion is limited by the material reaching the temperature dependent yield strength. Upon cooling, the thermal elastic strain is inhibited by the surrounding material, which results in tensile residual stress at the surface and compressive residual stress in the surrounding material. It is important to note that this mechanism does not require

the material to be molten. In PBF-LB/M, the melt pool depth is mostly larger than the layer thickness and the heat introduced acts on the underlying layers which are not in a molten state. The cool-down phase is referring to the restraint shrinkage of a molten layer by the surrounding material, introducing tensile residual stress in the surface and compressive residual stress in the surrounding material as shown in Figure 2.14 b). The model described in [11] simplifies the formation of residual stress to the process of scanning a track and to the process of melting a layer. *Both of these assumptions do not fully apply, since the scanning of a layer is a sequential process including the deposition of multiple tracks according to complex scanning strategies [57].*

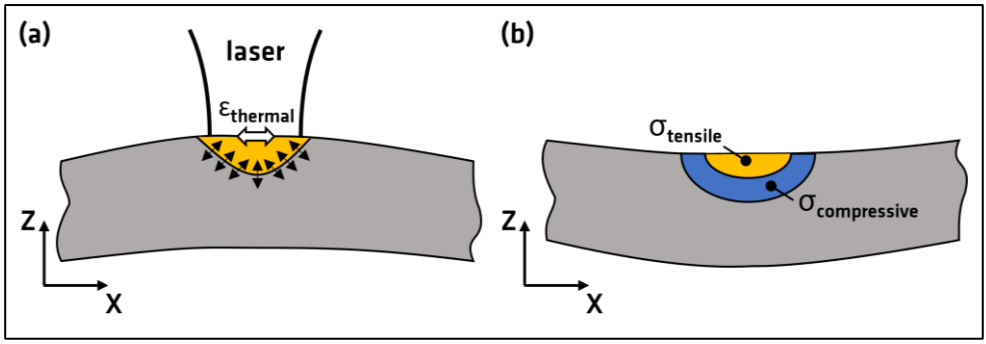

Figure 2.14: a) TGM mechanism and b) cool-down phase describing the formation of residual stress in PBF-LB/M. Adapted from [11].

The simulation results based on the model using the TGM and cool-down phase in [11] showed that the residual stress in the build plate are compressive to balance the tensile residual stress developing in the deposited material. It was further simulated that the residual stress in the last layer reach the material's yield strength. Increasing the amount of layers was reported to increase the residual stress in the build direction but to reduce the residual stress perpendicular to the build direction [11]. The findings reported in [11] were further supported by additional investigations on the in-situ synchrotron diffraction manufacturing of Ti-6Al-4V walls [105].

The results reported in [11] constituted the foundation of residual stress investigations in AM by first describing the formation and the distribution of the residual stress in PBF-LB/M parts as well as highlighting the influence of the scanning strategy and geometry. A major limitation to the results reported in [11] is the size of the investigated specimens. Moreover, the model predicted the presence of residual stress as high as the material's yield strength in the final layer, which did not correspond for any of the specimens investigated as yield strength values

between 500 and 700 MPa were found in PBF-LB/M/316L specimens [40, 51]. The formation of the residual stress is very complex and the analysis of the influence of process parameters on the residual stress requires determination techniques to both analyse the surface and the bulk, as the results show a marked difference between the two regions.

Welding and AM share many aspects and as such it is useful to build upon the many decades of knowledge on welding to describe the residual stress in AM. When welding, the residual stress appears as a result of a non-homogenous temperature field, external restrains, non-homogenous material properties and possible volume changes during phase transformations [15, 106]. The TGM and cool-down phase model include factors generally considered to describe the formation of residual stress in welded structures. An example is given in Figure 2.15. It becomes apparent, that the formation of residual stress when welding is complex. As detailed in subsection 2.1.1 and 2.1.2, no phase transformation occurs in stainless steel 316L when solidifying as primary austenite (fully austenitic case, see Figure 2.1 b). Thus, the interactions between the strain and stress field and the microstructure can be discarded at first. The temperature field is directly related to the process parameters, and both affects the microstructure and the thermal stress generated. The external restraints, which are given by geometrical factors of the welding structure and the clamping or fixture also affect the residual stress.

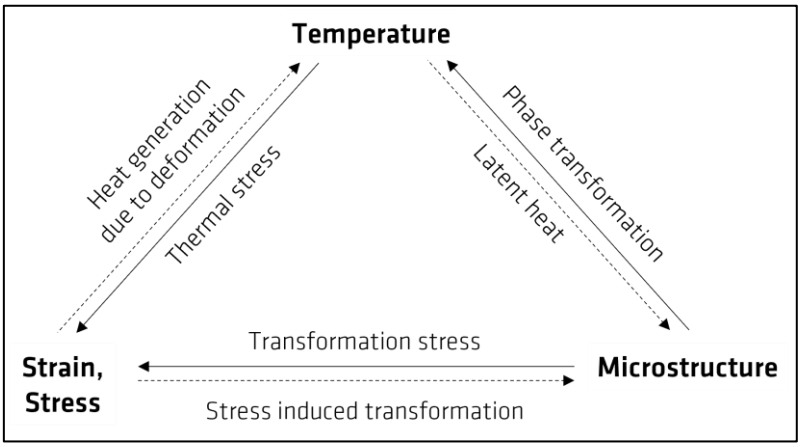

Figure 2.15: Interaction between the temperature, the strain and the stress fields with the microstructure. Adapted from [15].

Using a fixture may increase the resulting residual stress whilst reducing the deformation of the welded structure [15]. The formation of residual stress during welding can be explained by the three-bar or five-bar model [107]. In the five-bar

model (see Figure 2.16), the formation of residual stress is simplified by rigidly connected bars (at the top and the bottom) where the outer bars (C) remain at room temperature whilst the inner bars are at higher temperature (B) and the most inner bar reaching the fusion temperature (A). When heating the inner bar (A) to fusion, the adjacent bars (B) will expand and put the cold bars (C) under tension whilst being compressed by the rigid frame.

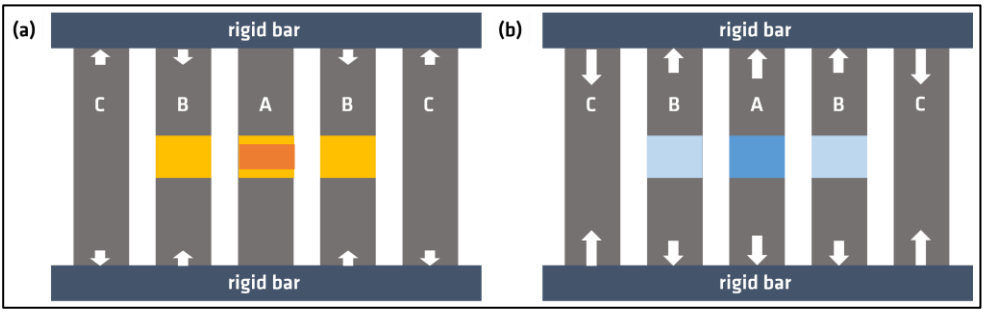

Figure 2.16: a) Five bar model showing the interaction during the heating of bar A to fusion temperature, b) cooling phase of the structure. The arrows indicate compression and tension in the respective bars. The arrow sizes qualitatively indicate the magnitude of the stress. Adapted from [107].

Upon cooling, the inner bars (A and B) will shrink. They are however hindered by the colder bars (C) and their own plastic deformation if during the heating the thermal stress surpassed the temperature dependent yield strength. Therefore, the inner bars (A and B) will be in tension leading to the stress profile shown in Figure 2.17 a). Following the description of the model in [107], the maximum stress value is then close to or higher than the materials yield strength (uniaxial) and for austenitic steel the stress values will decrease with increasing distances from the weld bead [106, 107]. The residual stress in tungsten inert gas welded 316L plates is shown in Figure 2.17 b). The longitudinal stress reaches positive values in the weld bead and compressive values at a greater distance from the weld bead.

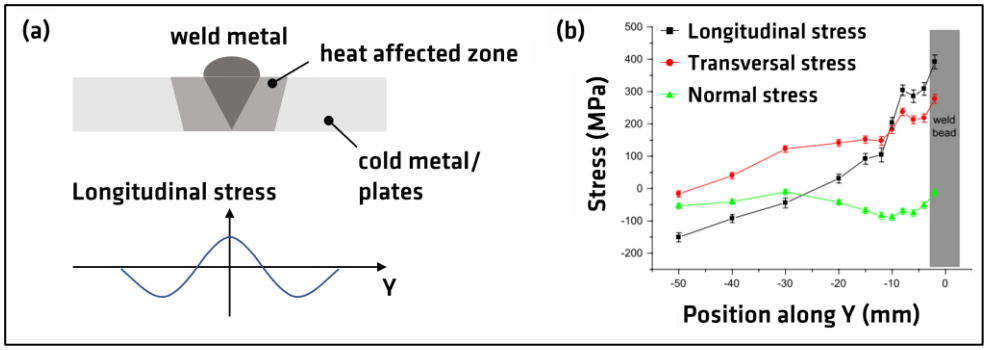

Figure 2.17: a) Thermal stress (longitudinal stress) in the direction of the weld bead (adapted from [107]), b) residual stress in tungsten inert gas (TIG) welded 316L plates determined 2 mm below the surface by ND (adapted from [108]).

The concepts for the formation of welding residual stress can be applied to a certain degree to the formation of residual stress during PBF-LB/M. The fact that the solidification during PBF-LB/M is of the order of 10^6 K/s even corresponds to assumptions taken that lead to the exemplary stress profile in Figure 2.17 a) [106]. Despite the similarities, many differences between the two processes prevail e.g. in AM a part is manufactured by depositing subsequently layers whereas in welding parts are joined, the size of a single weld bead (TIG weld bead in 316L) can be of the order of multiple mm whereas the weld bead of the PBF-LB/M is the size of the laser spot and in the order of tens of micrometre. These differences lead to different residual stress profiles in PBF-LB/M compared to welding, which is the subject of the next subchapter.

2.2.4 The distribution of residual stress in PBF-LB/M

There is currently no definition on how to separate the residual stress according to the area investigated. In this thesis, a practical approach is given. The surface residual stress refers to the values that are acquired when determining the residual stress at the surface with an XRD (penetration depth is around 5 µm to 10 µm). This may correspond to the first incremental drilling steps when using the hole drilling technique. The subsurface residual stress refers to the stress up to a depth of around 200 µm. This distance corresponds to the depth that was reached using the layer removal technique without having a strongly convex surface at the position of the layer removal. Beyond this depth, the residual stress is referred to as bulk residual stress.

Surface residual stress

The formation of residual stress in PBF-LB/M leads to tensile residual stress at the surface balanced by compressive residual stress beneath. The distribution of the residual stress over a PBF-LB/M body is the subject of this section. Tensile residual stress has been found at the surface of different PBF-LB/M processed alloys e.g. AISI 316L [109-111], AlSi10Mg [71, 112], Ti-6Al-4V [110, 113], IN718 [114, 115].

The residual stress at the top surface of 30 mm x 30 mm x 0.05 mm-1 mm (length x length x height) PBF-LB/M/316L was investigated by means of XRD in [110]. The residual stress parallel to the scanning direction was found to be higher compared to the residual stress perpendicular to the scanning direction, whereby the magnitudes reached values close to 500 MPa [110]. The residual stress in the specimens with heights of 0.05 mm and 1 mm was similar in magnitude. This is in contradiction with the effect of increasing residual stress values in the build height (2.5 mm, 5 mm and 10 mm in [11]). The surface residual stress sectioned net-shaped PBF-LB/M/316L tensile specimens (6.5 mm x 4 mm x 58.5 mm) was found to be around 350 MPa [14]. *However, similar to the analysis in [11] the surface electro polished to reduce the surface roughness. This procedure is however not commonly used, and the removal of material and related relaxation needs to be accounted for.*

The distribution of surface residual stress in PBF-LB/M/IN718 specimens sized 100 mm x 20 mm x 20 mm (length x length x height) determined by XRD revealed that the residual stress in the scanning direction was similar to the residual stress perpendicular to the scanning direction [81]. Moreover, it was also observed that the residual stress was similar at the surface centre and the edge (along with the length). This result suggests that the residual stress distributes homogenously, when using a uni-directional scanning strategy (see 2.2.5) as in [81]. Tensile surface residual stress were not only observed on the top surface of PBF-LB/M specimens but also on the lateral faces, with a tendency of lower stress magnitudes [111, 113, 116-118]. Several studies addressing the surface residual stress used the bridge-curvature or the cantilever-method [65, 66, 81, 119, 120]. As described in subchapter 2.2.1, these methods have the advantage to map the residual stress over the full size of the investigated specimen. The corners of various PBF-LB/M shaped parts (rectangular, triangular and disc shapes) were observed to deflect because of the tensile surface residual stress [81, 99, 119].

The distribution of the residual stress on the top of discs sized 20 mm to 28.5 mm in diameter and height of 6 mm (h_{part}) was investigated using DIC and XRD [66]. The discs were built with slanted side faces with different angles α, as shown in Figure 2.18 a). The results showed that the residual stress was mostly tensile but

that the distribution was heterogenous (see Figure 2.18 b). Furthermore, it was reported that discs with smaller angles α had more variation in the radial residual stress and exhibited higher magnitude residual stress, thus highlighting the influence of the geometry and resulting changes in the thermal equilibrium of the part during the manufacturing and cooling [66]. Similarly, the hoop residual stress was found to vary over the surface of the part, though the values were much lower. It was concluded, that the residual stress distribution and magnitudes are highly dependent on the geometry and the scanning strategy [66]. The dependency of the residual stress on the geometry and scanning strategy was simulated in [121]. The PBF-LB/M of Ti-6Al-4V triangle and rectangular shaped specimens (maximum cross section was 5 mm x 5 mm) with varying aspect ratios were found to exhibit higher residual stress in regions of accumulated heat, corresponding to short scan vectors (<2.5 mm, corners of a triangle) [121].

The PBF-LB/M process leads to tensile residual stress at the surface, which was observed for many different alloys. However, the investigations reported in literature are often performed on small scale specimens. The dimensions are mostly below 30 mm, which is only a fraction of the build height achievable with PBF-LB/M machines. The models detailed in subsection 2.2.3 correctly predict the presence of tensile residual stress in the top surface of PBF-LB/M processed alloys. Furthermore, the distribution and magnitudes of the residual stress appear highly dependent on the geometry and the scanning strategy.

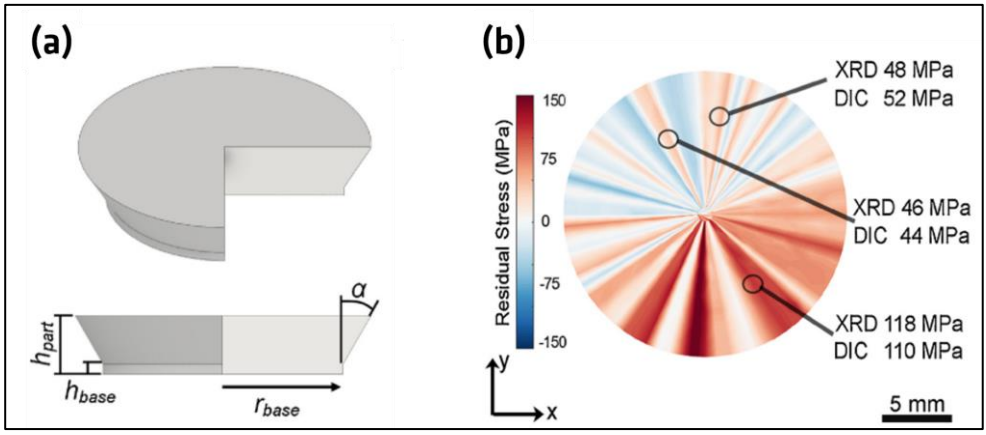

Figure 2.18: a) PBF-LB/M/316L discs of 6 mm height b) radial residual stress distribution calculated from DIC measurements and from XRD. Reprinted from [66], with permission from Elsevier.

Subsurface residual stress

As described by the residual stress formation models in subchapter 2.2.3, the surface tensile residual stress is balanced by compressive residual stress in the underlying layers. A few studies have investigated the subsurface residual stress. Residual stress depth profiles were performed on 316L PBF-LB/M specimens sized 100 mm x 9 mm x 3 mm (length x width x height) in [122]. Tensile residual stress in the two in-plane directions corresponding to the scanning plane (length x width) were observed at the surface, which remained at a constant magnitude up to a depth of about 120 µm. A similar observation was reported based on residual stress depth profiles performed on the top surface of 5 mm x 3 mm x 2 mm (length x width height) PBF-LB/M/316L specimens in [123]. In [111] the subsurface residual stress in the build direction of PBF-LB/M/316L specimens was determined using XRD and layer removal on the side surface of a specimen. The tensile residual stress at the surface was observed to increase at a depth of 100 µm before decreasing to lower tensile values at a depth of 500 µm.

The experiment reported in [124] was performed on PBF-LB/M net-shape compact tension 316L specimens with a thickness of 3 mm shown in Figure 2.19 a). The residual stress was determined at the surface and subsurface via XRD and the electropolishing of material on the lateral surfaces of specimens in the as-built condition and heat treated at 650 °C for 2 hours (the relaxation obtained from the heat treatment is subject of section 2.3). The σ_X shown in Figure 2.19 b) was of low magnitude (tensile residual stress) at the surface and became compressive (-150 MPa) at a depth of 200 µm. The σ_Y (residual stress in the building direction) shown in Figure 2.19 c) was much higher and remained tensile up to a depth of -200 µm, indicating the transition to compressive residual stress at greater depths. At the surface, the tensile residual stress was approximately 250 MPa and increased to about 430 MPa at a depth of 100 µm before decreasing again. These values are higher than the residual stress in the building direction at greater depth shown in Figure 2.21 d) but were not as high as the yield strength of this material [40, 51]. The authors in [11] reported that the high roughness of PBF-LB/M parts influenced the determined residual stress values. The surface of PBF-LB/M specimens exhibits a complex topology with partially melted powder particles and material bulges resulting from the layer-wise manufacturing (see Figure 2.5). The influence of the roughness on the residual stress determined by XRD has been investigated in [125]. It was observed that the residual stress increased with the depth of the measurement position. The authors further suggested to either post-process the surface, as performed in [11], or use non-destructive determination techniques which can determine the residual stress at an increased depth e.g. XRD in combination with layer removal, SXRD and ND.

The subsurface residual stress at a depth of 150 µm of the top layer of a 10 mm x 10 mm x 10 mm specimen was observed to reach 590 MPa determined by layer removal and XRD, which was correlated to the higher temperature at the melt pool bottom [126]. Similar values were observed in identically sized specimens but at a greater depth from the top surface at ~500 µm, whereby the depth residual stress profile starting from the top surface described a peak residual stress in contrast to a plateau when removing material from the lateral surface [127].

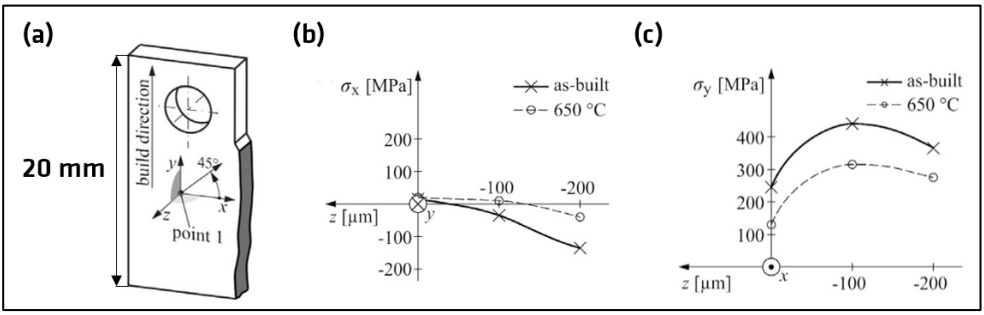

Figure 2.19: a) Geometry and measurement position, b) distribution and magnitude of the σ_X and c) of the σ_Y. Reprinted from [124], with permission from Elsevier.

The fact that the σ_Y decreased towards the surface (z = 0 µm) in Figure 2.19 b) is interesting, as this residual stress direction is not restrained by boundary conditions in this condition. This phenomenon was not described in the simulation models reported in [11] neither observed in other simulation results on PBF-LB/M/316L reported in [14]. However, the presence of a subsurface peak was further confirmed in the analysis of 12 mm x 14 mm x 10 mm (length x thickness x height) PBF-LB/M/316L specimens as reported in [117]. In this experiment, the in-plane residual stress (not further specified) were found to reach values between 280 MPa and 330 MPa, whereby the subsurface peak was observed to shift to a greater depth depending on the scanning velocity (the influence of process parameters on the residual stress is subject of 2.2.5) [117]. *It is noted that the residual stress values were calculated from averaged uni-axial strains, which influenced the absolute magnitudes reported in [117].* However, subsurface tensile residual stress peaks were also observed in PBF-LB/M of Ni-base superalloys, whereby the peak values were distributed over several hundreds of µm depth describing a plateau as reported in [114, 128].

To summarize, the results on the subsurface residual stress indicate the presence of greater residual stress magnitudes compared to the surface residual stress. The position and the magnitude of the peak residual stress appear to be affected by the

process parameters (e.g. scanning velocity) and the alloy analysed. Since the surface and subsurface residual stress is tensile, per definition compressive residual stress must be present in the bulk of the specimen. Therefore, it is important to use complementary methods to investigate the bulk residual stress.

Bulk residual stress

Many studies have performed the analysis of bulk residual stress in AM specimens using different methods. The distribution of the residual stress in PBF-LB/M/316L structures was reported in [119]. In this study, different geometries were manufactured with varying scanning strategies. The prism shaped specimens had a height of 60 mm (see Figure 2.20 a) whereas the L-shaped specimens had a height of 30 mm (see Figure 2.21 a). The residual stress was determined with ND and represents the bulk residual stress. The results of the residual stress investigation on the prisms are shown in Figure 2.20. The σ_{XX} in the centre of the specimen (blue line) was compressive with values around -170 MPa near the cut surface (area close to the build plate before the removal) which increase with the build height up to approximately -320 MPa before becoming tensile close to the surface. The same trend was observed for the two measurement lines close to the surface (green and red line), which were asymmetric with respect to the geometrical centre of the specimen. This asymmetry was attributed to the one-sided surface preparation and the distortion following the build plate removal [119]. Nonetheless, the σ_{XX} reached high values between -320 and 300 MPa. In contrast, the σ_{YY} and σ_{ZZ} were much lower with values oscillating between -100 MPa and 100 MPa and 0 MPa and 150 MPa for the two residual stress directions respectively. The sudden increase in σ_{YY} close to the surface further supports the presence of tensile residual stress near the last layer as modelled in [11].

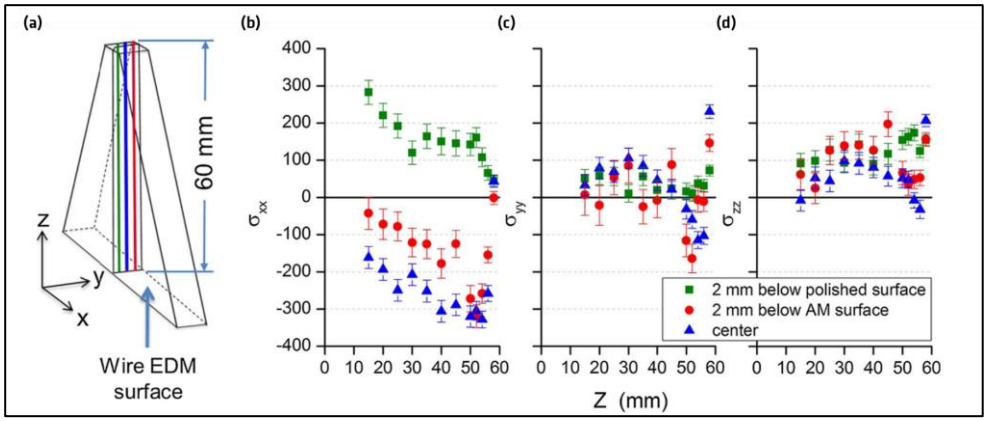

Figure 2.20: a) PBF-LB/M/316L prism and b) σ_{XX}, c) σ_{YY} and d) σ_{ZZ} distribution along the build height [119]. Reproduced with permission from Springer Nature.

The residual stress distribution in PBF-LB/M/316L was further investigated in L-shaped specimens (see Figure 2.21) and reported in [119]. This geometry was chosen to analyse how the different dimensions influence the residual stress. The L-shaped specimens were shorter compared to the prisms in Figure 2.20. Interestingly, the σ_{XX} exhibited lower values i.e. -50 MPa to 150 MPa compared to the residual stress range in the prisms (see Figure 2.21 a). A minor difference was observed in the σ_{YY} but a drastic change of the σ_{ZZ} was found (Figure 2.21 b and c). The values were between -400 MPa and 400 MPa, which is much higher compared to the σ_{ZZ} values in the prisms. The tensile values of 400 MPa were much closer to the material's yield strength (see subchapter 2.1.2). Furthermore, it appears that the bulk σ_{ZZ} was larger in the section of the L-shape with a thickness of 9 mm compared to the section with a thickness of 6 mm. This is, however, less the case for the σ_{XX} and the σ_{YY}. For both residual stress components the length of the dimension is similar for both sections. Thus, it appears that the geometry of the structure has a different influence on the residual stress magnitudes. *However, in the L-shape specimen the thin and the thick sections are connected, and it is not possible to separate the effect of a varying thickness.*

In comparison to the prisms, the residual distributes are broadly symmetric with respect to the geometrical axes of the L-shaped specimen. A similar observation was made in the investigation of the residual stress in PBF-LB/M Ni-alloy structures reported in [129]. Moreover, the influence of increasing structure heights was investigated. The following trends were observed with increasing build heights: the in-plane residual stress (σ_{XX} and σ_{YY}) is tensile and of highest magnitude along the largest dimension (40 mm) and becomes compressive when adding additional layers, the magnitude of the residual stress in the build direction (σ_{ZZ}) increases with the build height [129].

To summarize, the modelling and experimental validation of small sized specimens (up to 10 mm) reported in [11] are supported by findings related to the characterisation of the residual stress in much larger specimens reported in [119]. Moreover, the findings show that the bulk residual stress along the build height is of highest magnitude. The residual stress reaches values close to the material's yield strength towards the lateral surfaces. This was however not the case for the prism, which exhibited different trends: the residual stress in the build direction (σ_{ZZ}) was compressive, the highest residual stress was along the length of the prism (σ_{XX}) and the distribution of the residual stress in the prism was asymmetric. These observations can be attributed to the one-sided polishing of the prism surface as well as the distortion following the build plate removal. The distortion is thereby linked to the geometry and related stiffness Moreover, the effect of an increase in build height on the residual stress could not be shown in the prisms.

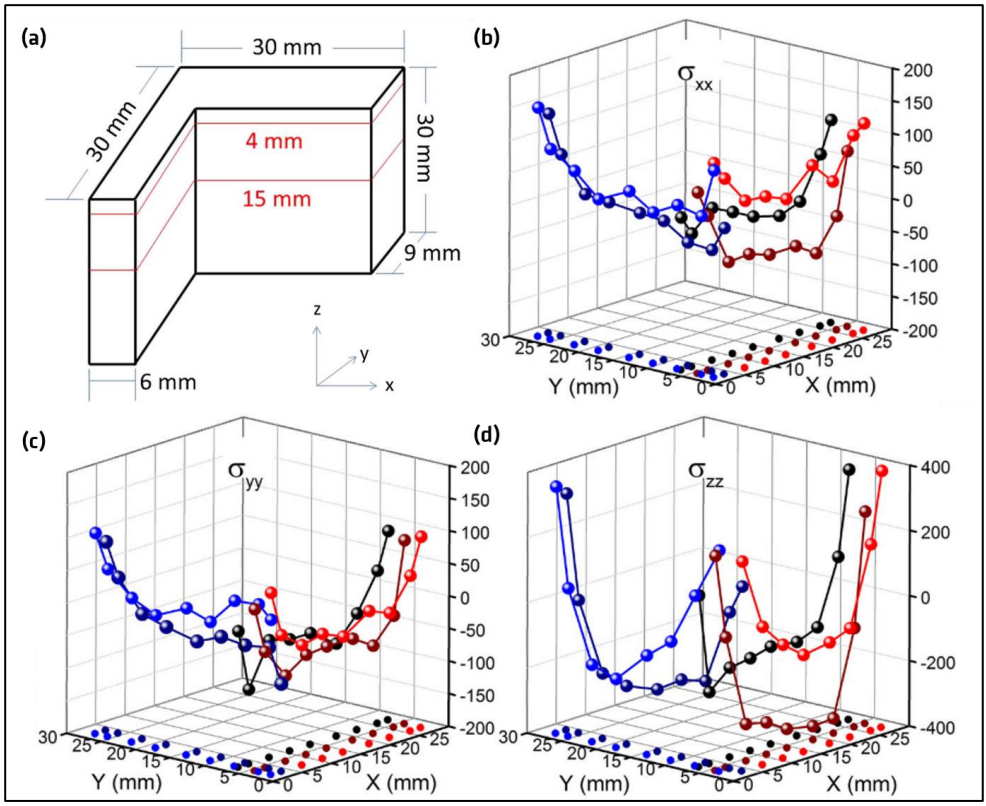

Figure 2.21: a) dimensions of the L-shaped 316 L PBF-LB/M specimens and distributions at 15 mm of height of the b) σ_{XX}, c) σ_{YY} and d) σ_{ZZ} [119]. Reproduced with permission from Springer Nature.

The distribution and magnitudes of the residual stress in 316L PBF-LB/M net-shaped tensile specimens was reported in [14]. The tensile specimens were sized 6.5 mm x 4 mm x 58.5 mm (length x thickness x height) and manufactured horizontally and vertically. The horizontal specimens distorted upon the removal from the build plate, which altered the residual stress distribution and magnitude. However, similar results to the findings shown in Figure 2.21 were reported for the vertically manufactured specimen. The σ_{ZZ} was of greatest magnitude at about - 500 MPa at the centre of the specimen. Towards the surface (the measurement position was at 1 mm from the surface), tensile σ_{ZZ} of roughly 100 MPa was observed. Along the build height, the results were in contradiction with the findings shown in Figure 2.20 (residual stress in the prisms reported in [119]) as the σ_{ZZ} was of greater magnitude compared to the other two direction as well as being compressive. Furthermore, the residual stress was also captured through the thickness of the specimen revealing a similar U-shaped distribution of the residual stress as shown in Figure 2.21.

Also cylindrical geometries manufactured by PBF-LB/M were analysed, such as the 316L discs reported in [99]. The dimensions of the discs used for the residual stress analysis varied between diameters of 45 mm to 80 mm with heights ranging from 5 mm to 15 mm. The discs were manufactured with and without support structures and the analysis was performed before and after the removal from the build plate. In the specimens with a height of 5 mm and a diameter of 80 mm, the σ_{ZZ} was lower compared to the σ_{XX} and the σ_{YY} with values between 0-100 MPa. The σ_{XX} and the σ_{YY} were similarly distributed and the values were between – 150 MPa, near the lateral surfaces, and close to 400 MPa at the centre. In comparison to the results shown in Figure 2.20 and Figure 2.21, depending on the geometry analysed the magnitudes of the residual stress change but seem to evolve in a similar range. Reducing the diameter from 80 mm to 70 mm did not have a significant impact on the residual stress. However, reducing the diameter to 45 mm was reported to increase the in-plane residual stress gradients by a factor of three. Increasing the height led to a very different distribution of the in-plane residual stress. The maximum residual stress was similar but interestingly the σ_{XX} and the σ_{YY} were less prone to decrease near the lateral surfaces [99]. This is questionable, as the two residual stress directions should decrease to fulfil the free-surface boundary i.e. the stress should be zero perpendicular to a free surface. Nonetheless, the study reported in [99] highlighted the influence of the geometry on the residual stress distribution. This was also observed for the PBF-LB/M processed Ni-based superalloys and Al-based alloys [112, 129].

The distribution of the residual stress found in 316L PBF-LB/M was also observed for Ni-based super alloys [128-131]. The following general trends can be drawn: the

residual stress in the build direction is of the highest magnitude, with lower values in the in-plane components. These findings are however dependent on the geometry and the manufacturing orientation (distortion upon removal of the build plate). Early models describing the residual stress in the PBF-LB/M process predicted well the presence of tensile surface and compressive bulk residual stress. The magnitudes are not as high as the materials yield strength in the last layer. However, it appears that the subsurface residual stress achieves this level. The knowledge on the residual stress in PBF-LB/M available in the literature (see review articles [10, 57, 83, 132-134]) is so far extensive for process parameter optimization. It is, however, limited in terms of geometry variations and geometry scaling as most of the literature reports residual stress values in small cubes. The question remains open whether the residual stress magnitudes in these cubes can be transferred to larger structures. A study on the fatigue behaviour and defect densities in PBF-LB/M/17-4PH (martensitic/ austenitic stainless steel) was performed to understand the geometry influence [135]. Dog bone shaped Ø 7 mm x 90 mm specimens (representing the witness specimen) and rectangular rod specimens (12 mm x 12 mm x 90 mm and 25 mm x 25 mm x 90 mm) were compared. Significant differences in defect distributions were observed and explained with different thermal histories [135]. A common PBF-LB/M qualification test artifact i.e. specimen designed to qualify the process – part performance was proposed in [136]. This specimen design has the dimensions 40 mm x 40 mm x 39 mm. Hence, it appears necessary to perform residual stress assessment on larger specimens than solely cubes with sizes between 10 mm and 20 mm. Moreover, most of the literature focusses the influence of process parameters and as shown in Figure 2.22, a multitude of parameters need to be considered. Unfortunately, the process-parameter space in AM is vast. There is a need to perform experiments which focus on varying a low number or ideally single parameters at once. The following subchapter discusses the main process parameters and their influence on the residual stress.

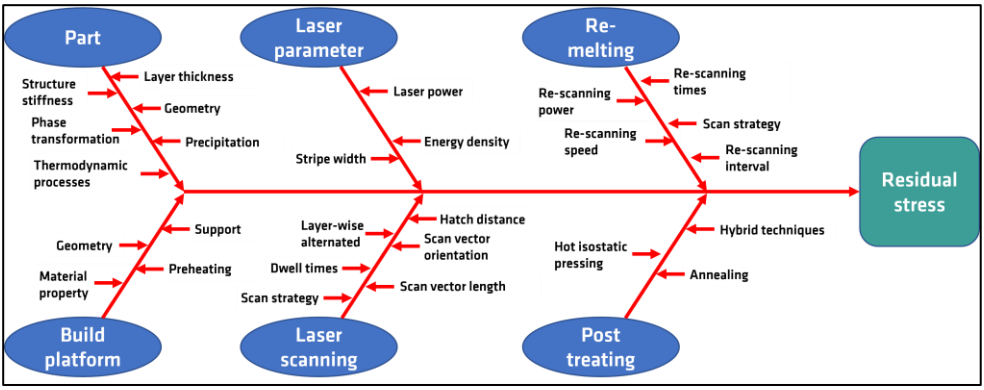

Figure 2.22: Ishikawa diagram showing the interdependency of part, process, and post-process parameters. Reprinted from [133], with permission from Elsevier.

2.2.5 Influence of PBF-LB/M parameters on the residual stress

The enumeration of different factors affecting the residual stress in PBF-LB/M shown in Figure 2.22 are divided in six major subjects. These can be further regrouped in three topics i.e. beam variables, scan strategy, process conditions and geometry according to [57]. Discussing all of these factors individually is not in the scope of this work and the reader is referred to the review articles [10, 57, 83, 132-134]. In subsection 2.2.4 the influence of the geometry was highlighted. As suggested in Figure 2.22 more factors attributed to the topic of the part and the build platform need to be considered. Some of these factors were already highlighted in the debut of residual stress analysis in AM [11]. The preheating of Ti-, Al-, Ni and Fe-alloys was observed to lead to residual stress relaxation of up to 90 % of a Ti-alloy and an Al-alloy when employing preheating temperatures of 570 °C and 200 °C respectively [133, 137, 138]. The preheating of the build platform at a temperature of 200 °C was found to decrease the residual stress in PBF-LB/M/316L specimens slightly [139]. The preheating of the build platform is often limited to 200 °C in commercial systems and higher temperature require specific adjustments to the PBF-LB/M machine [137]. Moreover, given the manufacturing times in the order of several hours e.g. 10 – 64 hours [140], using a preheating temperature at higher temperatures in the case of PBF-LB/M/316L can lead to the precipitation of detrimental phases (see subsection 2.1.1).

Another factor to be considered is the position of the specimens on the build plate. As observed in the PBF-LB/M of a Ti-alloy and a AISI 300 steel, the specimens exhibited varying surface and subsurface residual stress depending on their position on the build platform which was attributed to different heat dissipation mechanisms [141, 142]. *It is therefore advised to compare the residual stress in specimens with similar build positions or positions close to another. When only limited numbers of specimens are available, the use of non-destructive characterisation methods becomes a necessity.*

As denoted in subsection 2.2.4, the scanning strategy has a large influence on the residual stress. The main scanning strategies are the spiral, the raster, the zigzag, the island and the fractal scanning strategies [143]. Examples of these strategies are shown in Figure 2.23. The choice of the scanning strategy with a given geometry directly influences the length of the scanning vectors, which in turn influences the residual stress e.g. shorter hatch lengths were found to increase the surface residual stress perpendicular to the scanning direction compared to longer hatch lengths [81]. The scanning strategy defines the sequence in which the layer is molten and as such the distribution of the heat input and subsequently the residual stress distribution. The simulation study on the residual stress distribution in a single WAAM layer manufactured with various scanning strategies showed that the more homogenous heat distribution leads to lower residual stress [143]. This is also the idea when using island canning strategies (see Figure 2.23) [11, 64, 119].

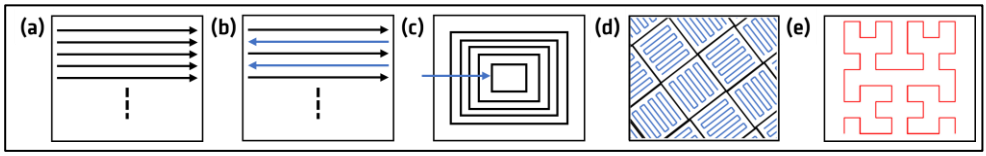

Figure 2.23: a) Stripe, b) Zigg-Zagg, c) Spiral, d) Island and e) Hilbert fractal scanning strategies. Adapted from [64, 143, 144].

It was observed that dividing the surface scanning in small sectors "islands" results in overall lower residual surface stress compared to Stripe scanning strategies (see Figure 2.23 a and b). The length of these islands, which define the scan vector length, also influence the residual stress. However, contradictory results were reported, either attributing an increase of the residual stress with larger scan vectors or the opposite [117, 119, 139, 145-147]. Various scanning strategies similar to the patterns described in Figure 2.23 a), b) and d) and their influence on the residual stress were investigated in [146]. The scanning vectors were generally found to be of highest magnitude along the direction of the scanning, whereby the Zigg-Zagg scanning strategy (see Figure 2.23 b) led to the lowest residual stress.

The length and orientation of the scan patterns on the bridge shaped PBF-LB/M/316L specimens was investigated in [64]. It was reported that decreasing the scan vector from 20 mm to 2 mm led to a decrease in the curling angle of 13 %, whilst reducing the scan vector length through the use of islands was observed to increase the surface tensile residual stress [119]. Interestingly, the compressive residual stress in the bulk was found to remain insensitive to the scanning strategy, whilst the tensile surface residual stress was found to be strongly affected [119]. The scanning of subsequent layers can also include a rotation between each layer, which further affects the residual stress as shown in [148]. The influence of the rotation of the scanning was observed to form microstructures that lead to a reduction in residual stress [149]. A few studies report on the correlation between the residual stress and the scanning strategies with different vector lengths. However, some of the results were affected by microstructural, surface roughness changes, higher porosity and cracks [113, 115, 119, 148]. A further aspect attributed to the scan strategy is the remelting or rescanning of a layer according to [57]. Remelting the layer with increasing scanning velocities was observed to reduce the residual stress [11]. Using the same laser beam parameters and scanning velocity did not, however, reduce the residual stress. Interestingly, this phenomenon was observed to be material dependent as the curling angle of PBF-LB/M/Ti-6Al-4V cantilever beams was observed to become smaller when remelting whereas no change was observed in PBF-LB/M/316L cantilever beams [64].

The influence of the scanning strategy on the residual stress remains unclear and contradicting findings are reported in the literature. Varying the scanning strategy is found to change the microstructure, affect the defects, the surface roughness and thus makes the comparison between specimens more difficult. Nonetheless, the scanning strategy has undoubtedly a large influence on the residual stress. The vast number of studies investigating its influence on the residual stress, however, shadow relations between other process parameters. To further the understanding of the PBF-LB/M process on the formation of residual stress, it is advised to select a single scanning strategy to understand the influence of other process parameters.

The volumetric energy density (VED) is calculated according to formula (1) using the laser power P (in W), the scanning velocity v (in mm/s), the layer thickness t (in mm) and the hatching distance h (in mm). This variable is one of the main metric used in process-structure-property investigations, as it regroups characteristic process parameters and is calculated from [57, 111, 150]:

$$VED = \frac{P}{vht} \qquad eqn.\,(4)$$

The influence of varying VED on the residual stress was analysed in [111] on PBF-LB/M/316L cubes. Although the VED has a direct influence on the heat input, the residual stress for varying VEDs was relatively constant. Perhaps the VED steps were too small (maximum variation was about three times). The investigation in [123] showed that an increase of the laser power tends to lead to an increase of the residual stress, when keeping the remaining parameters constant. The influence of the VED on the surface residual stress of PBF-LB/M/316L cubes was also investigated in [118], but reported no direct correlation between this metric and the resulting residual stress magnitudes. It was however observed, that below a certain VED, the resulting residual stress values were scattered. In fact, using identical VED but changing single process parameters (Laser power and scanning velocity) was observed to lead to very different distortions of PBF-LB/M cantilever beams [151]. By analysing single process parameters from the VED, it was found that increasing the laser power can lead to higher residual stress [118, 123, 126, 152, 153]. This is however greatly depending on the alloy investigated (see 2.2.3), as the contrary was observed for PBF-LB/M/Ti-6Al-4V [154]. Changes in the VED do not necessarily lead to homogenous results as an increase in hatch spacing was found to increase the surface residual stress in the top layer of a specimen whilst reducing the residual stress on the lateral surfaces [118]. At constant laser power and scanning velocity, an increase in hatch spacing was observed to decrease the residual stress [154]. In some cases, the changes in VED led to variations in residual stress within the error bar, which thus makes direct correlations difficult [147]. Nonetheless, further increasing the laser power can also lead to a significant number of pores, which may reduce the residual stress in the part [119, 126]. Furthermore, it was also shown that increasing the laser power reduces the melt pool aspect ratio, with deeper melt pools resulting from higher laser power [126]. In PBF-LB/M/Ti-6Al-4V, an increase of the scanning velocity increased the residual stress [125] which was also observed for PBF-LB/M/316L [117]. However, this trend appears to be also depending on the location of the measurement position (top or lateral face) [117].

The VED includes process parameters which directly influence the thermal history of a part. In fact, changing the VED results in variations of the residual stress magnitudes and distribution but also have a significant impact on the microstructure and defects [57, 113]. From research in welding, it is known that the heat input has a large influence on the residual stress [12], which is mirrored as shown by the above enumerated results reported in the literature. However, the VED

as metric doesn't seem to well describe the influence of changing parameters on the residual stress as shown by the contradicting results reported in the literature. A multitude of different metrics are proposed in [155] to better correlate the residual stress and the process parameters. These are, however, not yet established. Furthermore, these metrics are always affected by the residual stress determination method employed as well as the part geometry. Simulation models reasonably predict the residual stress formed in PBF-LB/M and account for variations in the process parameters. The simulation models employed either focus on the laser and powder bed interaction or the interaction of a thermal field in a larger component [57, 133]. In both cases, also valid for analytical models, some aspects cannot be simulated accurately, which leads to discrepancies between the simulated and experimental values [11, 14, 64, 154, 156].

The formation of residual stress is largely driven by the heat input. So far, the influence of the scanning vector, scanning strategy and the process parameters laser power, scanning velocity, layer thickness and hatching spacing were discussed. When manufacturing specimens using PBF-LB/M, the time between the start of melting a layer and the recoating, also called inter-layer-time (ILT), depends on the number of specimens manufactured [157]. Moreover, changes in the geometry can also affect the ILT and therefore makes this parameter of great interest when manufacturing complex shaped specimens with varying cross sections. When reducing the ILT a reduction in hardness and increased depths of the melt pools were observed in PBF-LB/M/316L [157]. Changes in the microstructure, defects and resulting properties due to varying ILT were also observed in PBF-LB/M and DED-LB/M of a Ti-alloy, and DED-LB/M 316L [158-160].

The influence of different ILTs on the temperature in the part and the resulting microstructures are shown in Figure 2.24. When using short ILTs (18 s), the temperature in PBF-LB/M/316L specimens reached values between ~500-580 °C in the final layers as shown in Figure 2.24 a). Increasing the ILT drastically reduces the temperature in the specimen, as the temperature in the specimen was maintained below 200 °C when applying an ILT of 116 s [140]. The grain size and the texture were also found to change because of the variation in the thermal history of the specimen. Shorter ILT (18 s) favored the growth of longer grains and more [100] oriented grains in the build direction (see Figure 2.24 b) compared to the specimens manufactured with an ILT of 65 s. The different thermal history of DED-LB/M specimens due to varying ILT was found to also affect the residual stress, whereby longer ILT led to higher residual stress in a Ti-alloy specimen compared to no effect in a Ni-alloy [161].

The ILT affects the heat accumulation within the specimen, similar to the preheating of the build platform. As discussed above, the preheating temperature range is often limited by the machine. The ILT here promises a larger degree of freedom to tailor the heat accumulation within the specimen and as a result the microstructure. However, as the thermal history is directly influenced by this parameter, also changes in the residual stress are expected. Knowledge on the influence of the ILT on the residual stress formed during PBF-LB/M is lacking. It is however a key parameter, as it is inherently linked to the geometry of the part manufactured as well as the number of parts on the build plate. Therefore, it is crucial to understand this link to further increase the wider application of the PBF-LB/M process in industry.

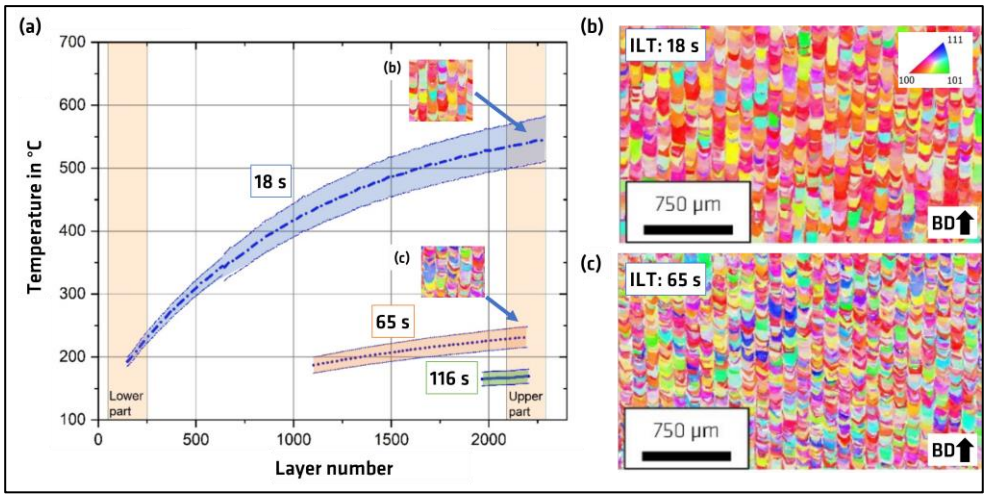

Figure 2.24: a) Temperature evolution of PBF-LB/M/316L specimens built using ILTs of 18 s, 65 s and 116 s, b) ESBD picture of the microstructure for an ILT of 18 s and c) for an ILT of 65 s. Adapted from [140].

2.3 Stress-relieve heat treatment of PBF-LB/M/316L

One of the post-processes mentioned in Figure 2.22 influencing the residual stress in PBF-LB/M parts is the heat treatment of the specimens. Generally, a heat treatment is performed before the removal of the part from the build plate to avoid any distortion [162]. The distortion is, thereby, directly linked to the relaxation of macroscopic residual stress (type I). The following subchapters details the state of the art regarding the thermal stability of the microstructure and selected mechanical properties as well as the relaxation of the residual stress following different heat treatments.

2.3.1 Evolution of the microstructure and mechanical properties

The evolution of the microstructure and tensile properties with heat treatment has been investigated in several studies reported in the literature [6, 7, 14, 51]. The microstructure of PBF-LB/M/316L has been observed to show resilience to grain growth up to temperatures around 1000 °C [51]. However, changes in the microstructure were reported to occur before reaching 1000 °C on a smaller length scale [51].The evolution of the cell structure with various heat treating temperatures is shown in Figure 2.25. The solidification subgrain cellular structure in PBF-LB/M/316L remained stable at temperatures below 600-700 °C [6, 7, 51]. A temperature range is given as different starting temperatures were reported in the literature, which may be related to the various chemical compositions employed [6]. Temperatures above 800 °C were reported to be a tipping point [7], from which the cellular substructure rapidly starts dissolving (see Figure 2.25 b) [8, 51, 163-165]. Findings in [8, 51] showed that the cellular structure is barely visible when heat treating at 900 °C for 1 hour (see Figure 2.25 c). At temperatures above 1000 °C the cellular structure was reported to have fully vanished (see Figure 2.25 d) [6, 7].

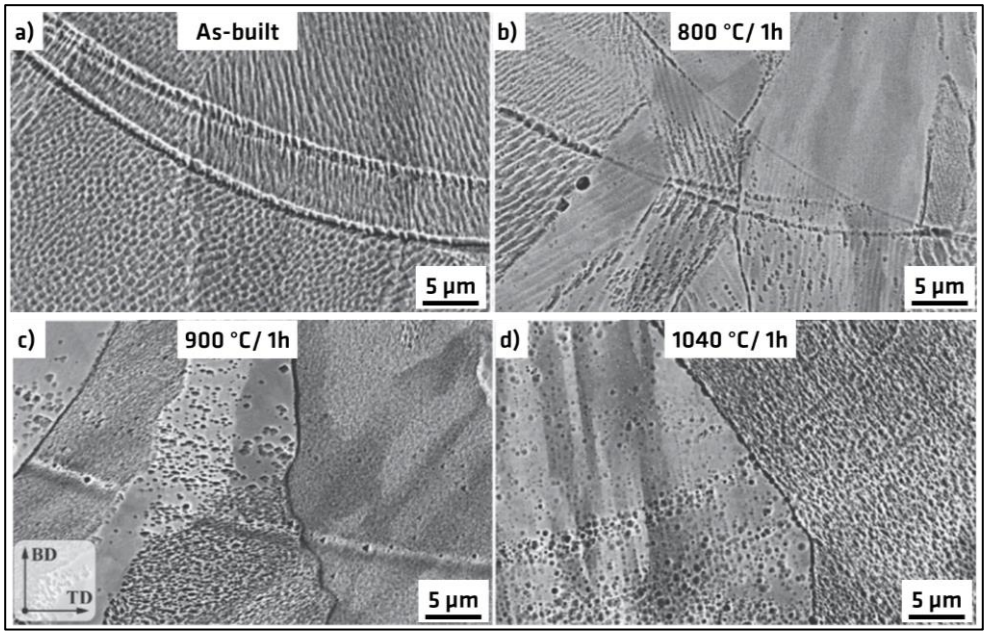

Figure 2.25: a) As-built and post heat treatment cellular structure of PBF-LB/M/316L after b) 800°C for 1 hour, c) 900 °C for 1 hour and d) 1040 °C for 1 hour. BD and TD denote the build direction and transverse direction respectively. Adapted from [51].

Stable tensile properties and hardness values were observed in conjuncture with the evolution of the cellular structure. In Figure 2.26 the yield strength was found to remain stable after applying a heat treatment at 600 °C for 1 hour [6]. A similar evolution of the hardness of PBF-LB/M/316L with increasing heat treatment temperatures was reported in [8]. Nonetheless, the material maintains a higher $YS_{0.2}$ compared to conventionally processed 316L even when heat treated at temperatures initiating recrystallization [6, 51].

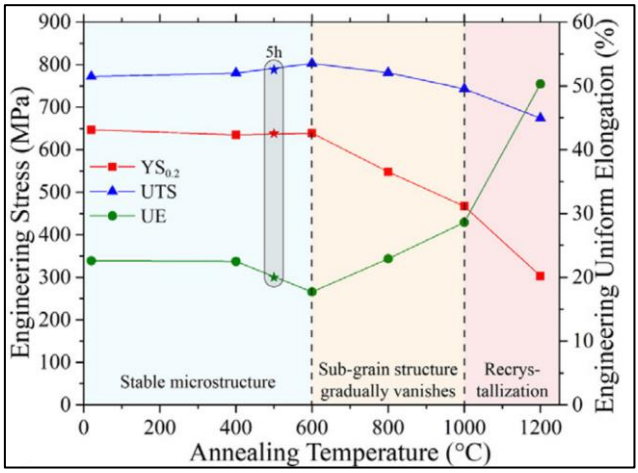

Figure 2.26: Dependence of the yield strength at 0.2 % strain ($YS_{0.2}$), the ultimate tensile strength (UTS) and the engineering uniform elongation (UE) of PBF-LB/M/316L on the heat treatment employed, reprinted from [6], with permission from Elsevier.

The temperature range in which the cellular structure starts dissolving also corresponds to increased precipitation (see 2.1.1), which may be deleterious to the material properties e.g., yield strength, elongation, corrosion properties. According to [8, 51], the material undergoes the following stages; recovery as the dislocation density is reduced, homogenisation of the austenite solid solution and recrystallization. The temperature ranges do not coincide fully between the two studies. However, both research groups observed a reduction in dislocation density in the temperature range in which the cellular structure dissolves. This is substantiated by the simulation of the diffusion of Cr and Mo in PBF-LB/M/316L in the cell walls as reported in [6]. This study showed that these elements exhibit reduced diffusion until approximately 650 °C but that major dissolution is achieved when applying 800 °C for 1 hour. At temperatures of 850 °C and greater, only minor Cr and Mo content was found in the cell walls after holding times of a few minutes.

These microstructural changes also affect the broadening of the diffraction peaks i.e. FWHM (see 2.2.1). Changes of the FWHM were observed in PBF-LB/M/316L microstructures with increasing heat treatment temperatures; a decrease in lattice strain and FWHM was reported when heat treating at 800 °C and above [6]. This change was related to increased defect mobility, chemical homogenization and changes in the residual stress. Similar observations were reported in [8]. *In both studies, the change in residual stress or strain was not quantified. As the cellular structure is known to affect the dislocation mobility [3, 48], it can be hypothesized*

that this microstructural feature also affects the residual stress relaxation. When manufacturing a geometrically complex component, retaining of the designed shape is of critical importance. Understanding how the residual stresses relax and avoiding distortion is crucial to reduce the number of scrapped parts.

2.3.2 Residual stress relaxation

The mechanisms leading to stress relaxation through heat treatments are defined as thermally activated processes, whereby the time and the temperature of the heat treatment are interchangeable within limits [166]. When the temperature is below 0.5 T_m (melting temperature), relaxation is occuring through so called recovery processes [166]. During recovery, the dislocation density is reduced and depending on the dislocation distribution, either diffusion driven or dislocation climb and movement drive the relaxation. Dislocation arrangements in cells (such as seen in PBF-LB/M/316L) are stable and favour a relaxation driven by volume/bulk diffusion [166, 167]. Above 0.5 T_m the relaxation will occur through the very strong reduction of the dislocation density as a result of the growth of new grains. This however leads to significant changes in microstructure and associated mechanical properties [166]. In case of PBF-LB/M/316L, heat treating temperatures above ~1040 °C were observed to recrystallize the microstructure [6, 51]. Moreover, the residual stress relaxation is inherently correlated to the temperature dependent yield strength. Upon reaching this limit, plastic deformation occurs which in turn relaxes the residual stress (similar mechanism described in subchapter 2.2.3). The yield strength as a function of temperature is shown in Figure 2.27 a). It can be observed that a strong reduction of the yield strength occurs at temperatures above 600 °C.

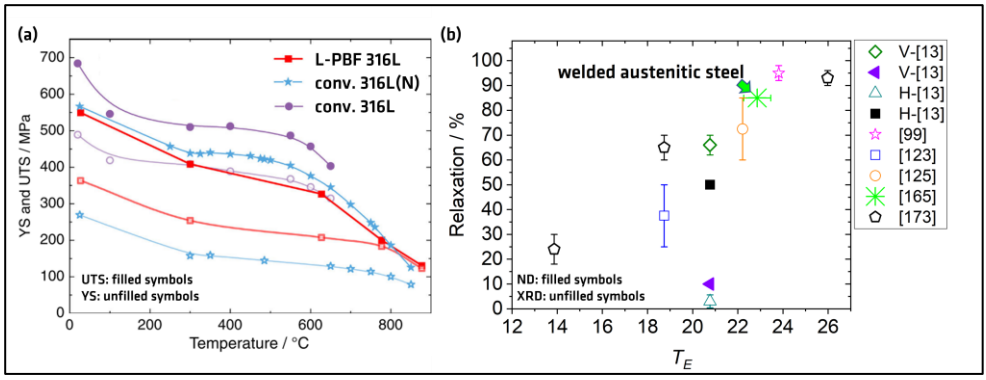

Figure 2.27: a) Ultimate tensile strength (UTS) and yield strength (YS) of conventional 316L [168], 316L(N) – (nitrogen alloyed 316L) [169] and PBF-LB/M/316L [170] (Adapted from [170]). b) Residual stress relaxation as a function of thermal effect of PBF-LB/M/316L compared to relaxation values obtained from welded austenitic steel [171]. Adapted from [172]. In b), V and H denote the relaxation obtained in vertically and horizontally manufactured 316L specimens respectively.

Since the microstructure and residual stress in PBF-LB/M are not comparable to e.g., welded microstructures or cast microstructures (see Figure 2.9), it could be hypothesized that the stress relaxation behaviour is affected. This was observed when comparing the relaxation of residual stress in ground, shot peened and milled steel surfaces and related to the different dislocation densities and structures related to the post-processes [167]. *The aim of the heat treatment should be: to sufficiently reduce the residual stress to prevent distortion upon the removal of the build plate, to reduce the residual stress to a known level, and to maintain the benefits from an as-built PBF-LB/M microstructure. Only a few systematic studies were performed to investigate the influence of the heat treatment on the relaxation of the residual stress in PBF-LB/M/316L. These are discussed in the following (see summary in Table 2.3).*

The Larson-Miller equation can be used to describe the time-temperature dependency of the stress relaxation [173] whereby the thermal effect T_E is calculated from:

$$T_E = T \times (\log(t) + C) \times 10^{-3} \qquad eqn.\ (5)$$

with the temperature T (in Kelvin), the time t (in hours) and the material constant C (~20 [46, 174]). The time and temperature component are here interchangeable, which highlights the two components of the stress relaxation. Plotting the residual stress relaxation against the T_E retrieved from the literature summarized in Table 2.3 highlights the scatter of the available data as shown in Figure 2.27 b).

When applying 400 °C for 4 hours, 650 °C for 2 hours and 1100 °C for 5 mins to PBF-LB/M/316L, a relaxation of around 24 %, 65 % and 90 % was obtained [175]. The relaxation was calculated using the compressive residual stress of 250 MPa at the surface of 2 mm slices extracted from 90 mm x 30 mm x 30 mm (height, length, thickness) specimens. This approach is similar to extracting a smaller volume from a larger part to create a stress-free reference (see subchapter 2.2.1). The goal of this approach is to relax the macroscopic residual stress. The rate of relaxation strongly depends on the velocity of dislocations, which depends on the residual stress magnitudes. Therefore, lower residual stress leads to a lower relaxation rate [176], which has an influence on the relaxation behaviour [167]. Therefore, the relaxation values reported in [175] need to be used with care. Heat treatments performed below 480 °C are reported to reduce peak residual stress in austenitic steels according to ASM International [46]. This indication corresponds well with the findings reported in [175]. However, this temperature is much lower than the temperature range of 550 °C to 650 °C given for post weld heat treatments in [17]. *Additional measurements should be performed to verify and validate this finding as the microstructure was reported to remain stable at these temperatures (see subchapter 2.3.1).*

In another investigation, applying 650 °C for 2 hours led to a relaxation of 50 % at the surface and ~30 % of the subsurface residual stress [124]. Furthermore, a heat treatment at 700 °C for 2 hours was observed to relax the surface residual stress by ~65 % [14]. However, for the same specimen a relaxation of ~10 % was reported when using the bulk residual stress for the analysis [14]. *The relaxation at the surface and bulk appears to differ. This reduces the amount of relaxation data available and adds to the complexity of which heat treatment to employ for the stress relaxation.*

Applying 800 °C for 5 hours was observed to reduce residual stress magnitudes from around 120-220 MPa (this range is probably related to the specimen-to-specimen scatter but is not further discussed in the reference given) to 50 MPa, which is equivalent to a relaxation of ~60-80 % [126]. Further increasing the temperature to 900 °C and holding for 2 hours was observed to fully remove the surface residual stress [100]. Based on the data available in the publication [100], the relaxation was about ~90 %. *This corresponds broadly with the indication given by ASM Internation of 85 % relaxation of the residual stress in welded austenitic stainless steels using a temperature range of 840 °C-900 °C [171]. However, for both studies reporting relaxation values at 900 °C and 1100 °C the surface residual stress was affected by the specimen preparation (extracted from a larger body [175]) and the surface machining of the specimen (machining, polishing [100]). The relaxation of the residual stress using 900 °C for 45 minutes was around 40 % in DED-LB/M 316L [177]. This is an indication, that potentially the surface post-processing and specimen manufacturing did affect the relaxation resulting from heat treating in this temperature range.*

Table 2.3: Residual stress relaxation in PBF-LB/M/316L reported in the literature.

Temperature in °C	Time in hours	Method	Relaxation in %	Ref.
400	4	XRD	23	[175]
650	2	XRD + layer removal	25-46	[124]
650	2	XRD	~63	[175]
700	2	XRD	3 - 66	[14]
700	2	ND	10 - 50	[14]
800	5	XRD	60-85	[126]
900	2	XRD	~90	[100]
1100	1/12	XRD	~92	[175]

According to ASM International, heat treating austenitic steels is not advisable unless the part is used in environments that may promote stress corrosion [46]. Now the dilemma becomes clear as the PBF-LB/M process induces residual stress close to the yield strength of the material (see subchapter 2.2.4). Changing the process parameters may reduce the magnitudes (see subchapter 2.2.5) but still high residual stress remains in the part. Performing stress relieve heat treatments is one option to reduce the residual stress but it needs to be balanced against the microstructural and the related mechanical property changes. A few studies reported relaxation values of the surface and subsurface residual stress in PBF-LB/M/316L [14, 100, 124, 126, 175]. The approach taken often involved determining the residual stress in small specimens or extracted volumes from larger parts. In both cases, the residual stress magnitudes are low compared to the as-built condition. Since the relaxation depends on the stress magnitude, the impact of the specimen preparation must be considered. Moreover, most of the relaxation data reported is related to heat treatment temperatures below the 900 °C indicated by ASM International for the full stress relief for welded austenitic steels [46]. Especially the range between 800 °C and 900 °C is of interest, as it correlates with a faster dissolution of the cellular structure. Additional measurements, ideally performed in the volume (bulk residual stress relaxation data remains scarce) and within the same specimen (avoid

specimen to specimen scatter) should be performed to validate and extend the current state of knowledge.

2.4 Conclusions from the state of the art

The following gaps were identified based on the state of the art:

1. The diffraction-based assessment of the residual stress in the PBF-LB/M austenitic steel 316L is still based on the approach related to conventionally processed 316L. The (311) lattice plane is assumed to best describe the macroscopic residual stress as it is expected to accumulate minor levels of microstrain. This has however not been shown for PBF-LB/M/316L.

2. The determination of the residual stress requires the diffraction elastic constants to link the lattice strains to the macroscopic residual stress. These are currently calculated using single crystal elastic constants from conventional austenitic steel and tabulated using the Kröner grain interaction model. Since the diffraction elastic constants are closely linked to the microstructure further experiments need to be undertaken to show the degree of agreement between experimental data and model.

3. The results reported in the literature show that the residual stress at the surface is lower than the simulated values, which were predicted to be as high as the material's yield strength. This effect may be attributed to the surface roughness. The high roughness tends to result in underestimated residual stress values. However, many studies addressing the influence of process parameters or post processes use surface residual stress values. Thereby, the influence of the surface roughness is not yet widely considered or understood. It is key to include systematically surface roughness measurements when performing experiments.

4. The residual stress is clearly affected by the geometry. The geometry of the part defines its stiffness, the restraint to shrinkage and the thermal gradients. These aspects affect the residual stress formation. Most of the studies reported in the literature do not address the part geometry. In several cases too many part dimensions are changed at once, which makes it difficult to allow clear conclusions regarding the residual stress to be drawn. A systematic study showing the influence on the residual stress by changing just one dimension i.e. varying the restraint to shrinkage e.g. the thickness, the length or the height has not yet been performed.

5. Most of the residual stress studies were performed on small geometries (cubes with an edge length of 10 mm to 20 mm). The question remains unanswered whether this design allows the transfer of the findings to

larger components. In fact, findings in the literature show that the geometry influences the thermal history and as such it appears necessary to analyse the residual stress in larger structures. A guideline to be used can be the 40 mm height of a recently proposed process-part performance qualification artifact specimen.

6. The influence of process parameters and scanning strategies on the residual stress has been heavily investigated in the literature. Thereby, the importance of the heat input has been highlighted. A factor yet only scarcely understood and investigated is the ILT, which defines the time to illuminate a powder layer and the recoating of a fresh layer. The ILT is inherently linked to the PBF-LB/M process. When building parts with varying thicknesses or changing the number of specimens manufactured in a build job, the ILT changes and consequently the heat input. Therefore, the residual stress may also be altered. No studies to date investigate the relation between the ILT and the residual stress in PBF-LB/M/316L.

7. The PBF-LB/M process is characterised by a vast process parameter space, which influences the residual stress. Optimizing the process parameters (e.g., scanning strategy, powder bed preheating) may reduce the residual stress. Nonetheless, adequate post-process stress relief heat treatments remain necessary as additional option to reduce the residual stress.

8. The influence of stress-relieve heat treatments was analysed in a broad temperature range (400 °C – 1100 °C). The key temperature range between 800 °C and 900 °C corresponding to the dissolution of the characteristic cellular structure was, however, sparsely investigated. The solidification subgrain cellular structure may influence the thermally activated stress relaxation mechanisms. The link between the cellular structure dissolution and the residual stress relaxation needs to be understood to permit a read across to the stress relieve heat treatments employed for welded austenitic steels.

9. The relaxation results reported to date are based on the relaxation of surface residual stress. The few studies available performed relaxation tests on post processed surfaces and extracted volumes from larger specimens. The two approaches alter the residual stress as well as the dislocation structures. A relaxation of ~30 % was reported for a heat treatment at a temperature at which no microstructure nor mechanical property changes were observed. These values need to be taken with care as the relaxation of a post processed surface residual stress may not be

representative of the as-built PBF-LB/M residual stress. Furthermore, a discrepancy between the relaxation values obtained from the surface and from the subsurface or bulk values was reported. The relaxation of bulk residual stress remains scarcely investigated but is necessary to validate the surface relaxation values.

The following objectives and tasks have been derived based on the above summarized gaps in the literature.

2.5 Objectives and tasks

The overarching goals of this study are: (I) to verify which lattice plane to use for the calculation of the macroscopic residual stress, (II) to provide the full through thickness characterisation of PBF-LB/M structures, (III) to analyse the influence of the process parameters ILT, and (IV) to analyse the effect of stress-relieve heat treatments.

The study is carried out using the austenitic stainless steel 316L. The formidable gain in yield strength and retention of high levels of ductility and the versatility through the good corrosion properties explain the large amount of research performed on this alloy processed by PBF-LB/M. However, based on the literature review fundamental questions regarding residual stress remain unanswered which are targeted by the goals (I)-(IV). The large elastic anisotropy, good scattering properties, and large residual stress make the alloy 316L suitable to analyse the impact of the following aspects on the residual stress: the variations of the residual stress due to geometrical changes and the influence of process parameters and post processes. The residual stress is assessed by X-ray and neutron diffraction. These methods possess the advantages being non-destructive and enabling the through thickness characterisation of the residual stress in a structure.

The necessity to consider metallurgical, structural and process parameter aspects when assessing the residual stress leads to the identification of the following tasks (see Figure 2.28).

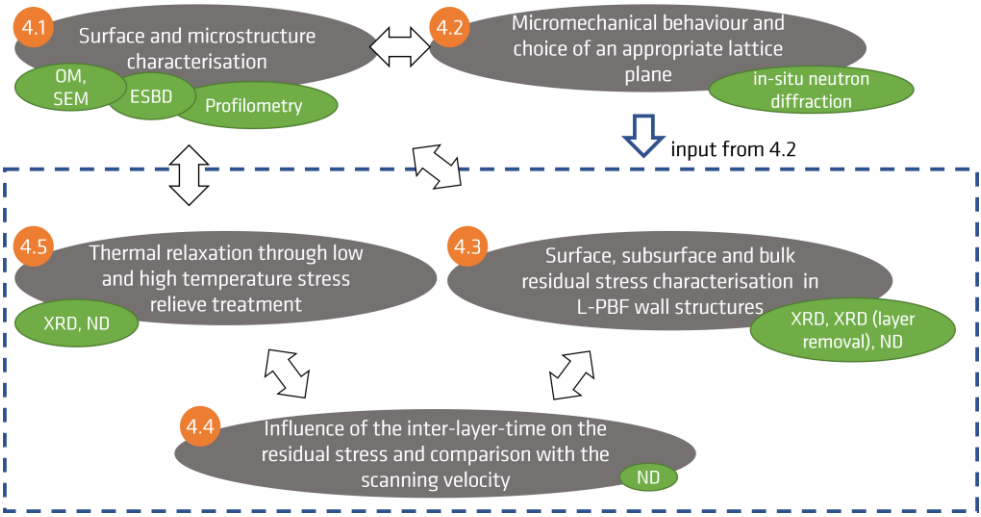

Figure 2.28: Overview of the result chapters, their interactions (indicated by arrows), and the employed experimental methods. The blue frame highlights the outcome of chapter 4.2, which gives indications on the determination of the residual stress.

First, the surface and the microstructure of the PBF-LB/M/316L specimens are assessed (subchapter 4.1). The surface measurements hereby allow the comparison of surface residual stress values by avoiding the influence of the surface roughness. This analysis also provides the degree of transferability with the available literature on PBF-LB/M/316L. The microstructure and the surface analysis are important for the interpretation of the in-situ tensile neutron diffraction test (subchapter 4.2), to link the microstructure with the residual stress (subchapter 4.3), and for the comparison of the surface residual stress to assess the relaxation potential of the low temperature heat treatment (subchapter 4.5).

Second, the micromechanical behaviour of PBF-LB/M/316L is assessed to provide a guideline on which lattice plane should be used to calculate the residual stress (subchapter 4.2). The outcome of this analysis impacts the subchapters 4.3 - 4.5 (see the frame in Figure 2.28) as the choice of the lattice plane includes the diffraction elastic constants, which directly influence the magnitude of the residual stress. In connection with the microstructure and the surface analysis results, indications will be given to the wider residual stress community on how to assess the residual stress in PBF-LB/M structures.

Third, the full characterisation of geometrically simple PBF-LB/M structures i.e. walls and prisms is performed (subchapter 4.3). These geometries are chosen as

there is currently no standard geometry (test artifact) that displays the complexity of PBF-LB/M designs. Therefore, to avoid the use of non-realistic geometries it is opted to use wall and tower shaped specimens. The change of individual dimensions and their influence on the surface, subsurface and bulk residual stress are analysed non-destructively. Moreover, the results are compared to the larger tower specimens (within subchapter 4.3 and with subchapter 4.4). This analysis will help to understand the size effect of the residual stress in PBF-LB/M structures.

Fourth, the influence of the ILT on the residual stress is analysed (subchapter 4.4). The ILT defines the time necessary to recoat a fresh powder layer and the illumination of the layer. The heat input and the thermal gradients are affected by this parameter and, therefore, the resulting residual stress. The variation of the ILT is compared to the change of the scanning velocity, which is more widely studied. The outcome of this subchapter will indicate how the residual stress changes when manufacturing complex geometries with varying wall thickness or when changing the number of specimens in the build job.

Fifth, the thermal relaxation of the residual stress is analysed (subchapter 4.5). Low and high temperature heat treatments are applied, which retain and dissolve the solidification subgrain cellular structure (subchapter 4.1). The influence of conventional heat treatments and their stress relaxation potential will be assessed. The cellular structure affects the relaxation mechanisms but is also the underlying source for the exceptional gain in yield strength of PBF-LB/M/316L. A key outcome is to give the wider scientific and industrial community knowledge on the stress relieving potential of various heat treatments.

3 Specimen Manufacturing and Characterisation Methods

3.1 PBF-LB/M manufacturing parameters and specimen build positions

All specimens were manufactured on the SLM Solutions 280HL (SLM Solutions Group AG, Lübeck, Germany) PBF-LB/M machine available at BAM. The build envelope of this machine is 280 mm × 280 mm × 360 mm and the machine is equipped with a single 400 W continuous wave ytterbium fibre laser.

Figure 3.1: The PBF-LB/M machine SLM Solutions 280HL (SLM Solutions Group AG, Lübeck, Germany) used for the manufacturing of the 316L specimens.

The AISI 316L specimens were manfuactured using commercial AISI 316L powder. The spherical powder was produced by gas atomization and the particle size distribution was D10 = 18 µm, D50 = 31 µm, and D90 = 18 µm. The chemical composition is given in Table 3.1.

Table 3.1: Chemical composition of the AISI 316L powder in weight % measured by the manufacturer

Cr	Ni	Mo	Mn	Si	C	P	S	N	Fe
17.7	12.6	2.35	0.92	0.60	0.017	0.012	0.004	0.1	balance

The specimens were manufactured using a meander stripe scanning strategy. The scanning vectors were aligned with the geometrical axes of the specimens. Each layer was offset by 90°. A schematic of the scanning strategy is shown in Figure 3.2.

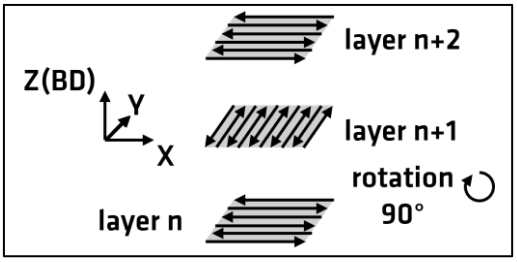

Figure 3.2: Meander stripe scanning strategy. The scanning vectors were aligned with X and Y and the rotation between each layer was set to 90°.

The specimens characterised in this study were manufactured using either a layer thickness of 30 µm or 50 µm. The corresponding process parameters are listed in Table 3.2. The wall specimens used for the investigation on the influence of the geometry on the residual stress were manufactured using the process parameters for a layer thickness of 50 µm.

Table 3.2: PBF-LB/M process parameters used to manufacture the AISI 316L specimens

Layer Thickness in µm	Laser Power in W	Laser Spot in mm	Scanning Velocity in mm/s	Hatch Distance in mm
30	200	0.08	800	0.12
50	275	0.08	700	0.12

The 50 µm specimens were also manufactured with variations in the ILT and the scanning velocity. This induces a change in the VED. The hatch distance and the scanning strategy remained constant. The different parameters are summarized in Table 3.3. Tower_65s_AB denotes the as-built condition of a twin specimen of Tower_65s.

Table 3.3: Specimens built with variations in inter-layer-time and scanning velocity

Specimen ID	Build job ID	Laser Power in W	Scanning Velocity in mm/s	VED in J/mm^3	Inter-Layer-Time in s
Tower_18s	10I02f	275	700	65	18
Tower_65s_AB	012P18f	275	700	65	65
Tower_65s	012P08f	275	700	65	65
Tower_116s	011M05f	275	700	65	116
Tower_116s_HV	011N03f	275	900	49	116

The build positions of the Tower specimens on the build plate are shown in Figure 3.3. The scanning of the specimens started at the top left corner and finished and the bottom right corner. The same approach was used for the manufacturing of the SENB and wall specimens shown in Figure 3.4.

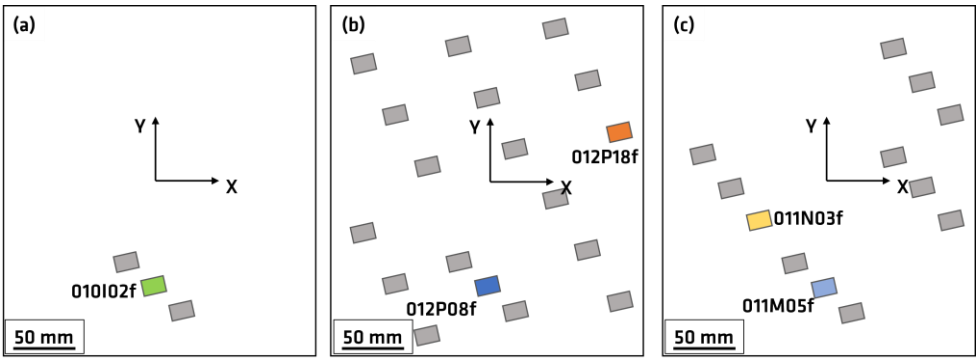

Figure 3.3: a) Build position of the specimens Tower_18s (ID: 010I02f), b) Tower_65s_AB and Tower_65s (IDs: 012P18f and 012P08f respectively), c) Tower_116s and Tower_116s_HV (IDs: 011M05f and 011N03f respectively).

The build positions of the SENB specimens (see dimensions in subchapter 3.2) and the build positions of the wall specimens from which the tensile specimens were extracted for the in-situ ND test (see subchapter 3.2) in Figure 3.4 a) and b) respectively.

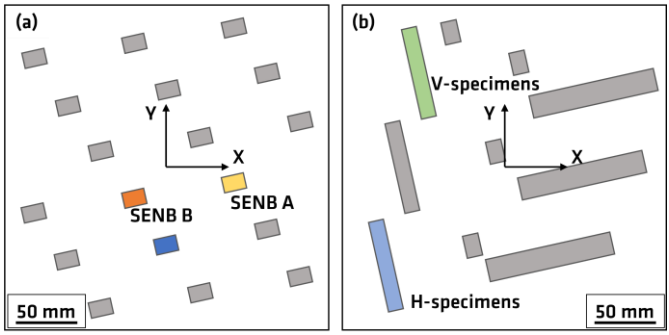

Figure 3.4: a) Build positions of the SENB A and SENB B specimens, and b) the walls for the in-situ ND tensile specimens.

The build positions of the wall specimens are shown in Figure 3.5. The walls were manufactured on a build plate with larger specimens. The larger specimens were scanned first. Then, first the 9 mm specimens, second the 5 mm specimens and

third the 2 mm specimens were scanned. The red arrows indicate both the specimens, on which the subsurface residual stress was investigated and also the surface where the depth profiles were performed on Figure 3.5.

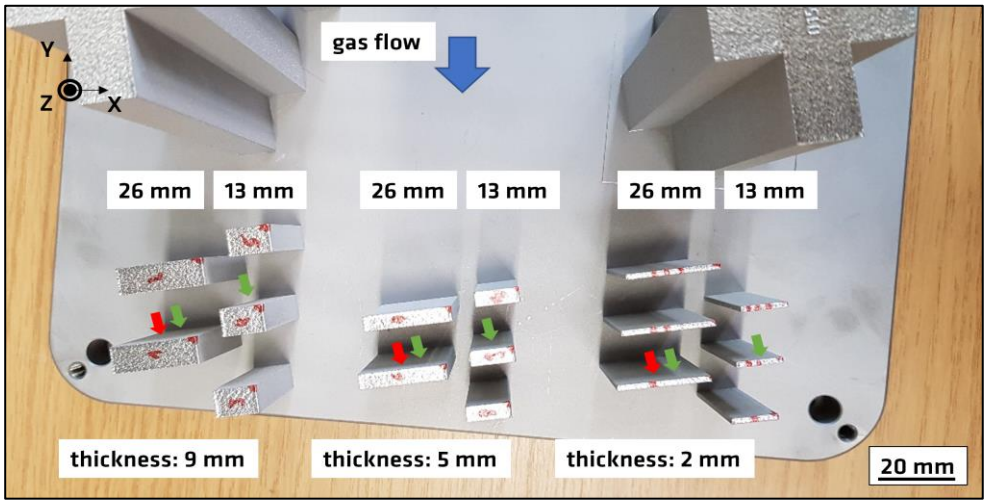

Figure 3.5: Build positions of the wall specimens. The green arrows indicate the specimens in which the bulk residual stress was investigated, and the red arrows indicate the specimens in which the subsurface residual stress was investigated (more details are given in subchapter 3.9.2).

Once the specimens were built and reached room temperature, the specimens were removed from the build plate by saw cutting. Three different geometries analysed in this study are exemplarily shown in Figure 3.6. The dimensions of the walls (Figure 3.6 a) and b) are detailed in Table 3.4. The Tower shaped specimens had the dimensions shown in Figure 3.6 c).

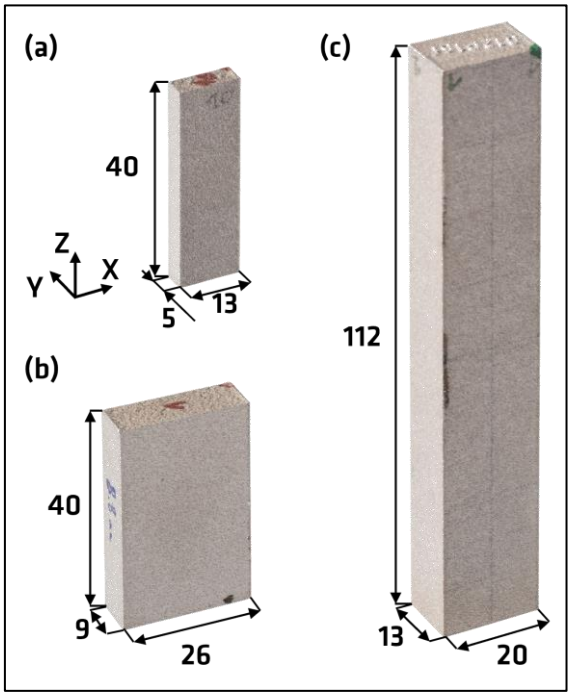

Figure 3.6: a) and b) wall specimens 5mm_13mm and 9mm_26mm, and c) large as-built specimen. All dimensions are in mm.

Table 3.4: Wall dimensions and ID

Specimen ID	X in mm	Y in mm	Z in mm
2mm_13mm	13	2	40
2mm_26mm	26	2	40
5mm_13mm	13	5	40
5mm_26mm	26	5	40
9mm_13mm	13	9	40
9mm_26mm	26	9	40

The specimen shown in Figure 3.6 c) was used with no further post-processing (as-built) for the comparison of the residual stress with the walls (see subchapter 4.3.2). Furthermore, a set of specimens was heat treated (see subchapter 3.3) for the extraction of the Tower specimens and the single edge notch bend (SENB) specimens. The geometry of the SENB specimen is shown in Figure 3.7. The SENB specimens are used to investigate the crack propagation behaviour. While this test was not performed in this study, it was part of the cross-cutting initiative on the aging of PBF-LB/M/316L at BAM. In this study, this geometry was chosen to analyse the subsequent post-process heat treatments detailed in subchapter 3.3.

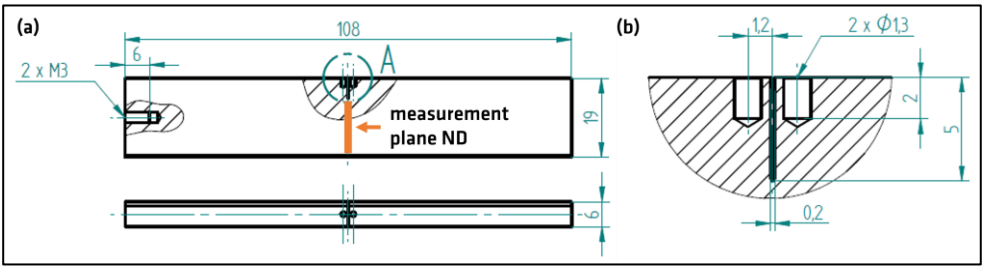

Figure 3.7: a) Technical drawing of the SENB specimens with the position of the ND measurement plane and b) detail A showing the location of the WEDM notch. All dimensions are in mm.

The Tower specimens were extracted by wire-EDM (WEDM) from the specimen shown in Figure 3.6 c). The height was reduced to 74 mm for the Tower_65s_AB and the Tower_65s specimens through multiple cuts (see Figure 3.16). The

Tower_18s, the Tower_116s, and the Tower_116s_HV specimens height was reduced to 68 mm, as two additional 3 mm slices were removed by WEDM to retrieve the stress-free reference cubes (see subchapter 3.7.2).

The tensile test specimens used for the in-situ diffraction test were extracted from 80 mm x 80 mm x 80 mm PBF-LB/M walls using a layer thickness of 30 µm (see process parameters in Table 3.2). The dimensions of the tensile test specimen are shown in Figure 3.8.

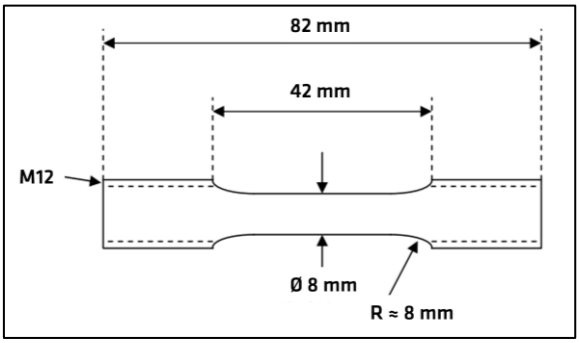

Figure 3.8: Dimensions of the tensile test specimens for the in-situ tensile test neutron diffraction experiment. The dimensions were taken from the sample environment of the ENGIN-X instrument [178].

3.3 PBF-LB/M post-processing

As mentioned before, the specimens were heat treated at 450 °C for 4 hours on the build plate (except the specimens for the investigation in as-built condition i.e., the walls and one large specimen, see Figure 3.6 c). This step is performed to avoid the distortion of the specimens upon the removal from the build plate. According to ASM International, this temperature and holding time followed by slow cooling can be used to reduce peak residual stress [46]. Additionally, the heat treatment temperatures 800 °C and 900 °C were subsequently used on the SENB specimens. Gas quenching was used to reduce the risk of extensive carbide precipitation. The summary of the heat treatments is shown in Table 3.5. The HT2 and HT3 were applied to the SENB specimens already having received HT1.

Table 3.5: Investigated heat treatment (HT) strategies and associated heating and cooling rates

ID HT	Time in h	Temperature in °C	Heating rate in °C/min	Cooling rate in °C/min	HT atmosphere
HT1	4	450	4	2	argon
HT2	1	800	10	gas quenched	vacuum
HT3	1	900	10	gas quenched	vacuum

3.4 Optical and scanning electron microscopy

The microsections for the optical microscopy (OM) and scanning electron microscopy (SEM) were cut from the specimens using a gravity saw. The samples were then cold embedded using the epoxy resin Epofix (Struers GmbH, Willich, Germany). The preparation of the microsections for the optical and SEM investigations followed the sequence as detailed in Table 3.6. The polishing steps were performed using diamond and oxide polishing suspension (OPS).

Table 3.6: Microsection preparation steps for OM and SEM

Investigation	Grinding/ Grit	Polishing	Etching
OM	320, 500, 800, 900, 1200	6 µm, 3 µm, 1 µm, OPS	Beraha II (800 ml H_2O, 400 ml HCl, 48 g NH_4HF_2)
SEM	180, 320, 600, 1200	3 µm, 1 µm, OPS	Bloech & Wedl II (50 ml H_2O, 50 ml HCl, 0.6 g $K_2S_2O_5$)

The SEM was performed on a Leo Gemini 1530 VP (Carl Zeiss Microscopy GmbH, Jena, Germany) system equipped with a EBSD detector e-FlashHR+ (Bruker Corporation, United States). The acquisition, indexing and post-processing was accomplished in the software package ESPRIT 1.94 (Bruker Corporation, Billerica, Massachusetts, United States). The acquisition parameters were: 16.5 mm working distance, 20 kV acceleration voltage, 70° cross section tilt (EBSD), 2 µm pixel size, approximately 10 nA beam current and a pattern size of 160 × 120 pixels. The EBSD investigation of the 30 µm layer specimens was carried out using a step size of 3.89 µm.

3.5 Surface roughness measurements

The surface roughness was measured in alignment with the standard ISO 11562 [179]. The contact profilometer Hommel T8000 equipped with a TKL300 probe was used and the results were assessed with the Turbo Wave V7.59 software (Jenoptik Industrial Metrology GmbH, Villingen-Schwenningen, Germany). The measurements were performed along four lines of 10 mm length along X and Y at Z = 37 mm (see Figure 3.16 c) and d). The spacing was 133 µm. The surface roughness measurements were performed on the specimens Tower_18s, Tower_65s, Tower_116s, and Tower_116s_HV.

The surface roughness of the 2mm_26mm, the 5mm_26mm and the 9mm_26mm specimens was measured using a MarSurf CM expert confocal microscope (NanoFocus AG, Oberhausen, Germany) at 10 mm along the BD from the position of the layer removal (see Figure 3.15).The images were taken at a magnification 20× with the objective 800XS. The arithmetic mean height (Sa) was calculated using the software µsoft (NanoFocus AG, Oberhausen, Germany) according to ISO 4288 [180]. The area used for the calculation was 2 mm × 2 mm.

3.6 In-situ thermography measurement

The in-situ thermography measurements were performed using the ImageIR8300 camera (InfraTec GmbH, Dresden, Germany). The camera has a spectrum covering the mid-infrared spectral region. The objective used had a focal length of 25 mm. The set-up was positioned above the PBF-LB/M machine. The view path is guided via mirrors. The resolution was 420 µm/pixel and the acquisition frame rate was 600 Hz. The subwindow size was 160 x 200 pixels. Further details of the set-up were reported in [157].

The region of interest was set in the middle of the specimen (X=Y= 0 mm) at Z = 34 mm of the Tower_18s, the Tower_116s, and the Tower_116s_HV specimens (dimensions of the specimens shown in Figure 3.16 c). The calculation of the temperature using the infrared signal is detailed in [181] and used the parameters shown in Table 3.7. An average temperature was calculated based on 40 layers (corresponds to the size of the gauge volume used in the ND experiment, see Table 3.9). The average of all layers was calculated by first filtering the raw data using a running average filter of 50 ms for each layer and second normalizing the time (peak temperature in each position in the gauge volume at the time t = 0 s).

Table 3.7: Calibration parameters used for the temperature calculation using the infrared signal.

Specimen	Black body calibration range [K]	Integration time [µs]	Surface emissivity	Build chamber temperature [°C]	Converted calibration range [K]
Tower_18s	573 - 873	46	0.23	37.0	721 - 1221
Tower_116s, Tower_116s_HV	473 – 673	186	0.23	41.7	575 - 877

3.7 Diffraction based residual stress assessment

As described in subchapter 2.2.2, the diffraction based residual stress assessment makes use of Bragg's law to calculate the lattice spacing and subsequently the lattice strain and the stress. The connection between the lattice strain and the differences in the residual stress determination using laboratory X-ray and neutron diffraction is the focus of the following subchapter.

3.7.1 X-ray diffraction based residual stress assessment

The equations 2. and 3. describe the connection between an arbitrary direction of strain $\varepsilon_{\varphi,\Psi}$ and the components of the stress tensor describing the stress in a volume. The reader is referred to [182] for a detailed derivation of the above-mentioned equations. The strain $\varepsilon_{\varphi,\Psi}$ along the measurement direction defined by the angles $\varphi \; and \; \Psi$ can be calculated from:

$$\varepsilon_{\varphi,\Psi} = \varepsilon_{11} cos^2\varphi sin^2\Psi + \varepsilon_{12} \sin 2\varphi \, sin^2\Psi + \varepsilon_{13} \cos\varphi \sin 2\,\Psi + \varepsilon_{22} sin^2\varphi sin^2\Psi + \varepsilon_{23} \sin\varphi \sin 2\Psi + \varepsilon_{33} cos^2\Psi \qquad (eqn.6)$$

When applying the generalized Hooke's law, the relationship between stress and strain is obtained from:

$$\varepsilon_{\varphi,\Psi} = \frac{1}{2} s_2(\sigma_{11} cos^2\varphi sin^2\Psi + \sigma_{22} sin^2\varphi sin^2\Psi + \sigma_{33} cos^2\Psi) + \frac{1}{2} s_2(\sigma_{12} \sin 2\varphi \, sin^2\Psi + \sigma_{13} \cos\varphi \sin 2\Psi + \sigma_{23} \sin\varphi \sin 2\Psi) + s_1(\sigma_{11} + \sigma_{22} + \sigma_{33}) \qquad (eqn.7)$$

whereby the strains $\varepsilon_{i,j}; i,j = 1,2,3$ and stresses $\sigma_{i,j}; i,j = 1,2,3$ describe the symmetric 2nd rank strain and stress tensor in a homogenous and isotropic material. The relationship between strain and stress assumes isotropic properties in a homogenous material (depth of X-ray penetration). Assuming that *no shear* stresses are present $eqn.2$ can be reduced to:

$$\varepsilon_{\varphi,\Psi} = \frac{1}{2} s_2\big((\sigma_\varphi - \sigma_3) sin^2\Psi + \sigma_3\big) + s_1(\sigma_1 + \sigma_2 + \sigma_3) \qquad (eqn.8)$$

The stress component normal to the surface σ_3 is assumed *to be zero* based on the low depth of penetration of the laboratory X-rays (see subchapter 2.2.1). The formula $eqn.4$ is furthermore simplified for the azimuth $\varphi = 0°$ and $\varphi = 90°$ to:

$$\varepsilon_{0,\Psi} = \frac{1}{2} s_2 \sigma_1 sin^2\Psi + s_1(\sigma_1 + \sigma_2) \qquad (eqn.9)$$

$$\varepsilon_{0,\Psi} = \frac{1}{2} s_2 \sigma_1 sin^2\Psi + s_1(\sigma_1 + \sigma_2) \qquad (eqn.10)$$

using the DEC s_1 and s_2 (see definition in subchapter 2.2.2). When measuring the lattice spacing d for different $sin^2\Psi$ values, one obtains

$$\sigma_\varphi = \frac{1}{d_0} \frac{1}{\frac{1}{2} s_2} \frac{\partial d_{\varphi,\Psi}}{\partial sin^2\Psi} \qquad (eqn.11)$$

The distribution of the lattice spacing against $sin^2\Psi$ is linear for quasiisotropic materials. The slope of this line is proportional to the residual stress Shear stress, σ_3 gradients along the depth, texture or plastic deformation may affect the linearity [52].

3.7.2 Neutron diffraction based residual stress assessment

One of the major differences between neutrons and laboratory X-rays is the large difference in penetration depths. Neutrons are suited to determine the residual stress in the bulk, as they interact with the atom nuclei instead of the electron shells in case of the X-rays. Moreover, the use of neutrons permits to define cubic gauge volumes (provided a suitable reflection is chosen) i.e., the same material volume will be analysed for each measurement directions.

The stress tensor ($\bar{\bar{\sigma}}$) and the strain tensor ($\bar{\bar{\varepsilon}}$) are related via the stiffness tensor ($\bar{\bar{C}}$) and the elastic compliance tensor ($\bar{\bar{S}}$). The strain tensor has six unknown components, which need to determined using at least six measurement directions [61]. The calculation of the strain ε_i along three orthogonal directions (X, Y, and Z) from:

$$\varepsilon_i = \frac{d_i - d_0}{d_0} \; ; i = X, Y, Z \qquad (eqn.12)$$

with the lattice spacings d_i in the corresponding directions is necessary to subsequently calculate the respective stress using equation 13. However, this approach does not consider any shear components i.e., the orthogonal directions chosen are *assumed to correspond to the principal stress directions*.

Furthermore, the stiffness and the elastic compliance tensors can have up to 36 independent components, which would make the calculation of the stress from measured strains a difficult task [61]. Therefore, in most engineering applications isotropic material properties are assumed, which renders the simplified form to calculate the residual stress using equations 13 [61]. The residual stress is then calculated using Hooke's law for triaxial stress according to:

$$\sigma_i = \frac{E_{hkl}}{(1+\nu_{hkl})(1-2\nu_{hkl})}\left[(1-\nu_{hkl})\varepsilon_i + \nu_{hkl}(\varepsilon_j+\varepsilon_k)\right]; i,j,k = X,Y,Z \qquad (eqn.13)$$

When using Time-of-Flight (TOF) sources, the wavelength of each neutron can be related to its TOF t_{hkl}. This is the time elapsed after passing the choppers (system to define a neutron pulse with a defined range of wavelengths) until the detection at the detector. Using Bragg's Law $(eqn.2)$ the lattice spacing d_{hkl} can be calculated from:

$$d_{hkl} = \frac{ht_{hkl}}{2\,sin(\theta_D)\,mL} \qquad (eqn.14)$$

In knowledge of h Planck's constant, m the mass and L the path length from the choppers to the detectors. When averaging over multiple diffraction peaks e.g. Pawley refinement, the lattice parameter is calculated [61]. The calculation of the residual stress is analogue to using the lattice spacing but uses the lattice parameter a and the lattice parameter corresponding to the stress-free reference a_0 (see $eqn.12$ and $eqn.13$). However, analysing the residual stress using the lattice parameter provides an approximation of the bulk residual stress and avoids the influence of remaining type II residual strains [61]. A diffractogram of a TOF neutron source is shown in Figure 3.13 b).

The stress-free reference d_0 is of major importance when calculating residual stress using neutron diffraction. In contrast to the $sin^2\Psi$ approach using laboratory X-ray diffraction, errors in the order of 10^{-4} nm in the d_0 values increase the residual stress magnitudes by 170 MPa in the principal stress directions [52]. When assuming $\sigma_3 = 0$ (e.g. $sin^2\Psi$ method using laboratory X-ray diffraction) the d_0 values can vary in the order of 10^{-3} nm without inducing significant errors in the residual stress values. In case of neutron diffraction, various approaches to obtain d_0 are detailed in [101]. In general, the aim is to extract a small material volume from the specimen which has dimensions aligned to the gauge volume used. It is

then assumed, that the macroscopic residual stress (type I) has been relaxed and that the chemical and phase distribution is comparable to the material investigated. This means that neutron diffraction is not fully non-destructive and often twin specimens are used to obtain a d_0 value. The reader is referred to [82, 83] for more details. The strategies to obtain appropriate d_0 values in this study are summarized in Table 3.16.

In this investigation the residual stress directions will be defined as shown in Figure 3.9: σ_X refers to the residual stress direction along the length of the specimen (in X), σ_Y refers to the residual stress direction along the thickness of the specimen (in Y), and σ_Z refers to the residual stress direction along the BD of the specimen (in Z).

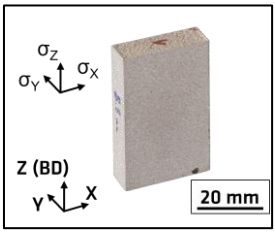

Figure 3.9: Definition of the residual stress directions with respect to the geometry of the PBF-LB/M structures.

Throughout the experiments, the measurement orientations were aligned with the geometrical axes of the specimens (Figure 3.10). To obtain a diffraction peak in each direction and a total of three measurement orientations, the specimens needed to be rotated accordingly. The measurement directions and orientation of the specimen during the experiment is given in Figure 3.10.

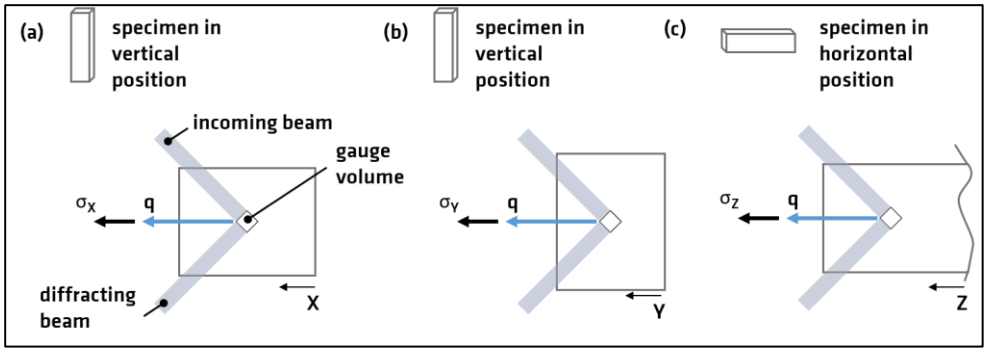

Figure 3.10: a) orientation of the specimen and scattering vector and corresponding direction of σ_X, b) of σ_Y, c) and of σ_Z.

3.8 X-ray and neutron diffractometers

This chapter details the different X-ray and neutron diffractometers used for the non-destructive determination of the residual stress in the laser powder bed fused stainless steel 316L.

3.8.1 Xstress G3 mobile X-ray diffractometer

The surface residual stresses were determined using the Xstress G3 mobile diffractometer (StressTech Oy, Vaajakoski, Finland). A photograph of the instrument is shown in Figure 3.11. The G3 diffractometer is equipped with position sensitive line detectors. The measurement is performed according to the $\sin^2\chi$ method. The X-ray tube and apparatus thereby rotates instead of the specimen. The measurements and the calculation of the residual stress is performed using the software XTronic (StressTech, Oy, Vaajakoski, Finland).

Figure 3.11: Xstress G3 mobile diffractometer (StressTech Oy, Vaajakoski, Finland).

Depth profiles can be performed by electropolishing material layers and subsequently determining the residual stress. The electropolishing systems MovilPol-3 (Struers GmbH, Willich, Germany) and Kristall 650 (ATM Qness GmbH, Mammelzen, Germany) were used to perform the layer removal. The initial thickness of the specimen was set as Z = 0 mm and after each layer removal, the depth was measured using a dial indicator (Digimatic dial indicator ID-C series 543-471 B, Mitutoyo Deutschland GmbH, Berlin, Germany). Thereby a voltage of 20 V or 30 V (depending on the system) was applied for a duration of 10 seconds. The

electropolishing solution is composed of 550 ml saturated saline solution (NaCl 359g/l at room temperature), 150 ml H_2O, 200 ml Ethylene glycol $C_2H_6O_2$ and 100 ml Ethanol C_2H_6O. Due to the nature of the measurement approach (manual system), each electro polishing step did not lead to identical material removal steps.

The parameters for the acquisition of the diffraction peaks and the calculation of the surface and subsurface residual stress are shown in Table 3.8. The position sensitive detectors were set at an angle of 152° corresponding to the diffraction angle of the (311) lattice plane. The corresponding DECs were calculated using the Kröner model with the XEC software [183]. The parameters were kept constant throughout the investigation.

Table 3.8: XRD diffractometer acquisition and residual stress calculation parameters.

Measurement mode	$\sin^2\Psi$	Collimator diameter in mm	2
Current in mA	6.7	Young's modulus E (311) in GPa	184
Voltage in kV	30	Poisson's ratio ν (311)	0.294
Radiation	MnKα	Acquisition time in s	5
Reflection / 2θ in °	Fe – 311 / 152	Background fitting	hyperbola
Ψ – angle range in°	-45 to 45	Peak fitting	Pearson VII
Ψ – tilt in steps	19	Background reduction in %	20

3.8.2 Residual stress assessment with angular-dispersive neutron diffractometers

The characterisation of the residual stresses (subchapters 4.3, 4.4 and 4.6) was performed on the angular-dispersive neutron diffractometers E3 at the Helmholtz Zentrum Berlin (Berlin, Germany) and strain analyser for large scale engineering applications (SALSA) at the Institut Laue-Langevin (Grenoble, France) [184, 185]. General information on the instrument set-up for this study is given in Table 3.9.

Table 3.9: General information of the measurements at the angular-dispersive neutron diffractometers E3 and SALSA

Instrument	Target reflection	Diffraction angle 2θ in °	Wavelength in nm	Gauge volume in mm^3	Counting time in min
E3	311	86	0.1471	8 (cubic)	12-20
SALSA	311	103	0.16	8 (cubic)	4-12

The collimation depends on the set-up and whilst a combination of slits and one collimator is used for E3, only collimators were used for SALSA. The counting times depend heavily on the specimen geometry and the neutron source and instrument set-up. The two set-up sketches and a picture of SALSA are shown in Figure 3.12.

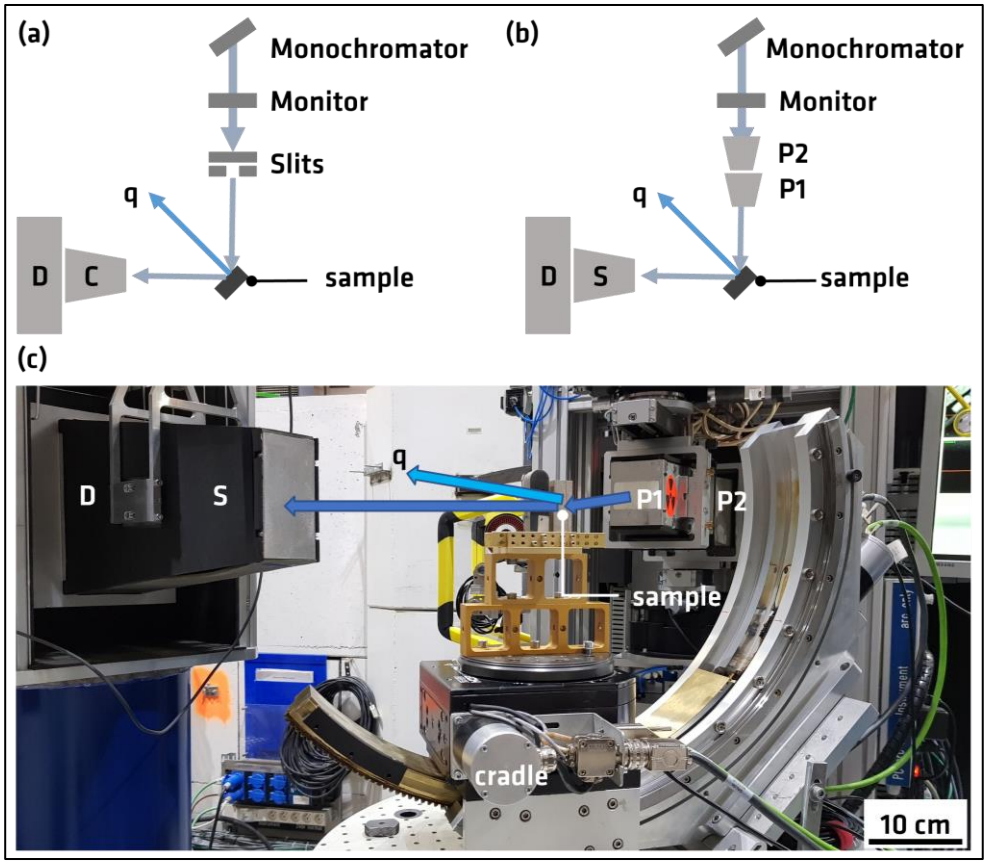

Figure 3.12: a) Set-up E3, b) Set-up SALSA and c) picture of SALSA with mounted specimens. The set-up sketches highlight the position of the area detectors (D), the collimators (C, S, P1 and P2) and the scattering vector q.

The analysis of the diffraction pattern acquired at E3 is performed using the software StressTextureCalculator [186]. For the correct fitting of the lattice spacing, the sample-detector distance was set to 1120 mm and the pixel size to 1.17 mm. When fitting the diffraction peak, the background area (angular range) needs to be extracted from the full diffraction peak. The angular range used was 82° to 89°. The extracted background was set as linear and subtracted from the diffraction pattern. The peaks were fitted using a gaussian profile. Additionally,

due to a small crack in the monochromator of E3, the resulting shoulder in the diffraction peak was fitted as individual peak. This step was necessary to not affect the position of the diffraction peak used for the subsequent residual stress calculation.

The analysis of the neutron diffraction data acquired at SALSA is done using the software suite LAMP [187]. Each experiment requires a calibration file provided by the instrument scientist. The calibration of the instrument ensures that the optics are aligned with the centre of diffraction (centre of mass of the gauge volume). The individual peaks were then fitted using a gaussian profile and by assuming a flat background (subchapter 4.4) and a background file (subchapter 4.5). The background was fitted using a reduced angular range of approximately 99° to 107°.The residual stress was calculated using the diffraction elastic constants given in Table 3.8.

3.8.3 Residual stress assessment with the Time-of-Flight diffractometer ENGIN-X

The characterisation of the residual stress (subchapters 4.3, 4.6.2) was performed on the TOF diffractometer ENGIN-X at the ISIS Neutron and Muon Source (Harwell, United Kingdom). General data of the experiment and the software used for the data are summarized in Table 3.10.

Table 3.10: ENGIN-X experiment general information on the set-up.

Wavelength range in nm	TOF window in µs	Counting time in min	Data analysis
0.1-0.3	19000-40000	15-30	Open Genie [188]

The ENGIN-X set-up is shown in Figure 3.13 a. The position of the detector banks is fixed in this experimental set-up. An example of a TOF diffractogram is shown in Figure 3.13 b).

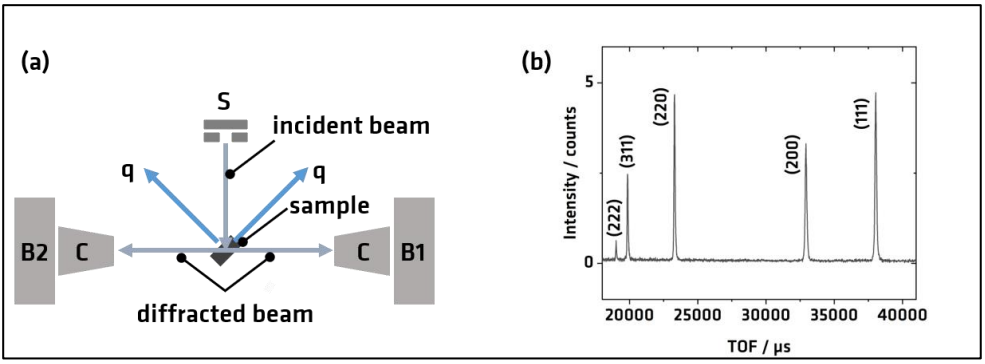

Figure 3.13: a) ENGIN-X sketch showing the detector banks B1 and B2, the collimators C, the slits S, and the diffraction vector q; b) TOF diffractogram.

The analysis of the TOF diffractograms was performed using the open source software tool Open Genie [188]. This software calculates the lattice parameter (call function: *analyze_scan*) or the individual peaks (call function: *analyze_scan/peaks*). The software Open Genie makes use of the GSAS calculation routine whereby the lattice parameter is obtained from a Pawley refinement [93, 94]. When fitting the individual peaks, the shape of the diffraction peak is fitted using the convolution of an exponential and Voigt function [93].

The residual stress was calculated using as Young's modulus 196 GPa and 0.282 as Poisson ratio for the residual stress calculated using the lattice parameter (values reported in [189]).

3.9 Measurement positions for the determination of the residual stress

The following subchapters detail the measurement set-up and sequence for the in-situ tensile test performed at ENGIN-X (subchapter 4.2).

3.9.1 In-situ tensile testing at the Time-of-Flight diffractometer ENGIN-X

The in-situ tensile tests were performed on ENGIN-X using the uniaxial hydraulic rig (INSTRON® 100 kN). The instrument set-up shown in Figure 3.14 a) is similar to the one in Figure 3.13 a). However, to analyse the evolution of the lattice parameter and individual lattice planes the gauge volume was set to 4 mm x 4 mm x 4 mm.

Table 3.11: ENGIN-X in-situ tensile experiment general information on the set-up.

Wavelength range in nm	TOF window in µs	Counting time in min	Data analysis/ Pawley refinement
0.1-0.3	12500-40000	10	Open Genie [188]

In contrast to using a cube as stress-free-reference, the reference lattice parameter and lattice spacing to calculate the residual strain was acquired prior to the test at a load of 5 MPa. The strain was measured using an extensometer (INSTRON® 12.5 mm gauge length). The set-up and picture of the experiment is shown in Figure 3.14.

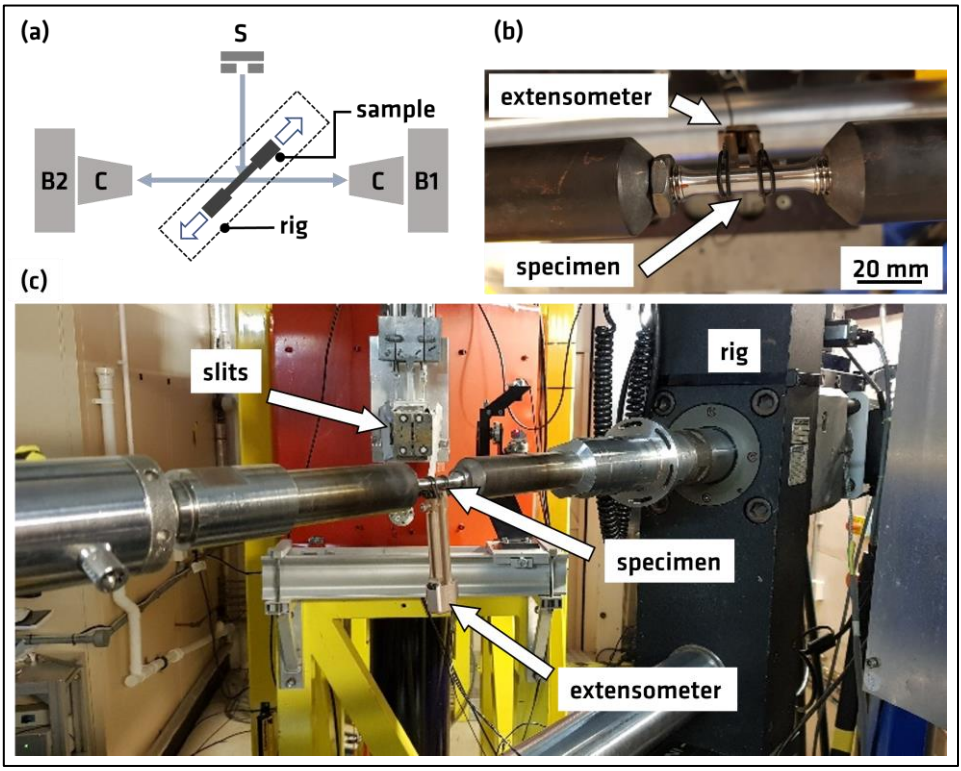

Figure 3.14: a) Sketch of the ENGIN-X in-situ tensile test set-up (arrows denote the loading direction during the experiment). b) Mounted tensile specimen with attached extensometer. c) Picture of the ENGIN-X set-up for the in-situ tensile test.

The test sequence for the in-situ tensile tests is summarized in Table 3.12. In the elastic regime a diffraction pattern was acquired at each increment of 30 MPa. The experiment was switched from load control to displacement control after reaching the transition load (see Table 3.12). These load levels account for the different elastic behaviour of the vertically extracted specimen (V-specimen) and horizontally extracted specimens (H-specimen). The time to reach each increment was 10 seconds and the counting time of each diffraction pattern was 10 minutes. The unloading ramp was 120 seconds. The acquisition of the diffraction pattern started once the increment (either load or displacement) was reached.

Table 3.12: Test sequence showing the transition load level indicating the switch from load to displacement control and the load before each unloading step.

Specimen	Transition load MPa	Unload no.1 in MPa	Unload no.2 in MPa	Unload no.3 in MPa	Unload no.4 in MPa	Unload no.5 in MPa
V-specimen	355	482	523	538	552	608
H-specimen	390	540	564	580	595	670

The diffraction elastic constants were calculated using the linear fitting tool in the OriginLab OriginPro 2019 software (OriginPro 2019, Version 9.6, OriginLab Corporation, Northampton, MA, USA). To compare the Young's modulus values with simulation results, the fitting range was set to 0.15 % strain. The error of the Young's modulus values is given by the error of the linear fit.

3.9.2 Surface and subsurface residual stress: measurement positions and depth profiles

The measurement points for the determination of the surface and subsurface residual stress on the wall specimens are shown in Figure 3.15 and given in Table 3.13.

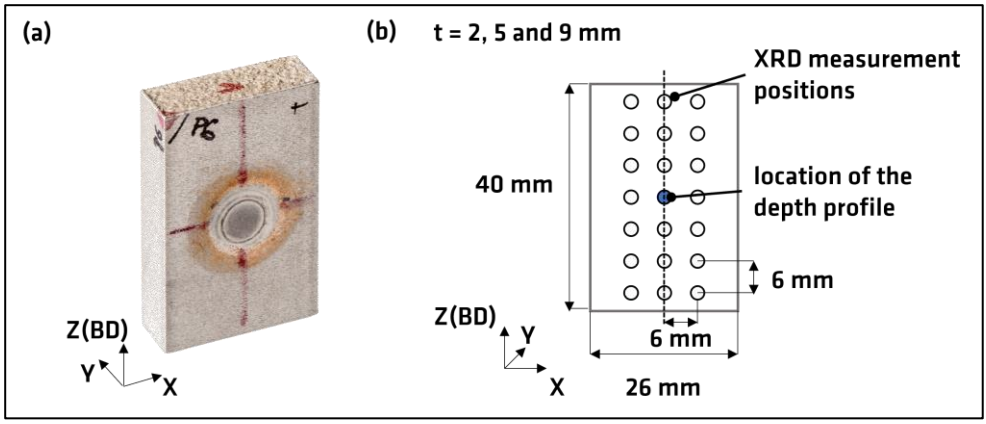

Figure 3.15: a) Picture of the 9mm_26mm specimen highlighting the position of the depth profile, b) measurement positions of the surface and subsurface residual stress in the 2mm_26mm, 5mm_26mm and 9mm_26mm specimens.

Table 3.13: Measurement positions and directions on the wall specimen.

Specimen	Measurement	Step size	Measurement directions
2mm_26mm, 5mm_26mm, 9mm_26mm	surface	6 mm (X and Z)	σ_Z
2mm_13mm, 2mm_26mm, 5mm_26mm, 9mm_26mm	subsurface	10-15 µm (Y)	σ_Z, σ_X

The measurement position for the determination of the surface residual stress were positioned on the lateral surfaces S1 to S4 as shown in Figure 3.16 a). The measurement points for the determination of the surface residual stress on the as-built specimen (see Figure 3.6 c) were positioned at the centre line and evenly distributed along Z as shown in Figure 3.16 b). General information on this measurement is given in Table 3.14.

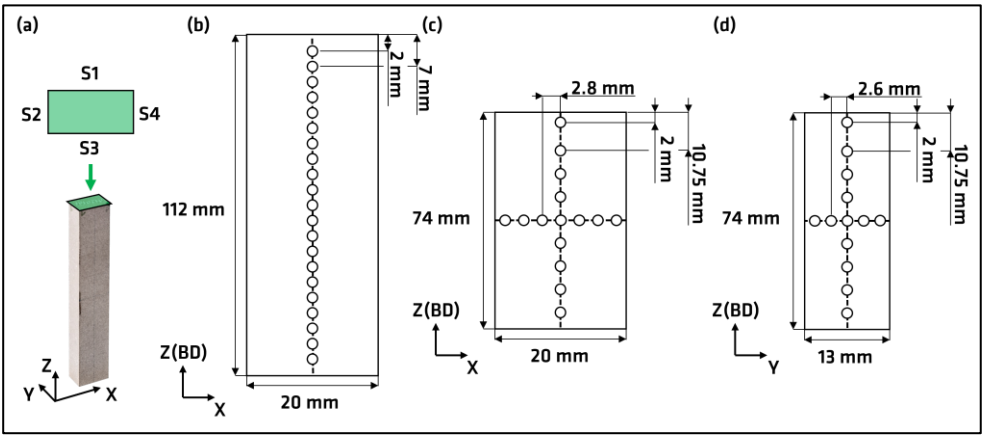

Figure 3.16: a) Blank specimen and description of the lateral surfaces, b) measurement positions along the build height, c) measurement on surface 1 (S1), d) measurements on surface 2 (S2) of the Tower specimens.

Table 3.14: Measurement positions and residual stress determination on the surface of the as-built Blank specimens.

Step size in mm	Measurement points	Measurement directions
5	21	σ_Z

The residual stress in the Tower specimens was determined on the positions shown in Figure 3.16 c) and d) corresponding to the surfaces S1 and S2. The summary is given in Table 3.15. The surface measurements for the investigation on the influence of the ILT (Tower_18s, Tower_116s, Tower_116s_HV) were only carried out on the position along X shown in Figure 3.16 c) and d). The influence of the low temperature heat treatment on the surface residual stress was determined using the measurement positions along Z in Figure 3.16 c) and d) as well as in X in Figure 3.16 d).

Table 3.15: Residual stress determination on the surface of the Tower specimens.

Specimen	Step size in mm	Measurement directions
Tower_65s_AB, Tower_65s	8.75	σ_X or σ_Y, σ_Z
Tower_18s, Tower_65s, Tower_116s, Tower_116s_HV	2.6-2.8	σ_X or σ_Y, σ_Z

3.9.3 Measurement positions for the bulk residual stress

The characterisation of the walls was performed on SALSA (results in subchapter 4.4). To characterize the walls, a smaller gauge volume was opted for compared to the other investigations. This decision was made to better describe the residual stress profiles. A trade-off between gauge volume size and counting times was made. The dimensions in which the strain was assumed to be nearly constant correspond to the gauge volume dimensions that were increased e.g. if the strain is homogenous in the build direction, the gauge volume in this direction can be increased. This approach results in the gauge volumes shown in Figure 3.17. The size of the gauge volume in Figure 3.17 b) and c) is identical but the specimen was rotated by 90° to maintain the resolution of the 0.6 mm collimator in the direction of the largest strain gradient (through the thickness, in the Y direction).

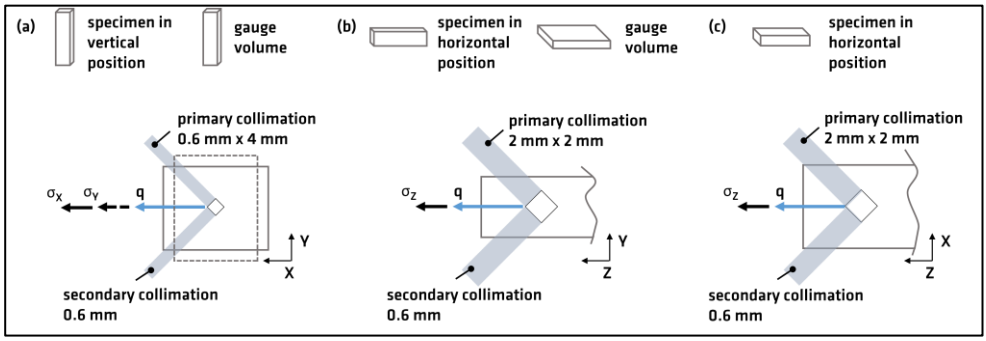

Figure 3.17: a) Tailored gauge volume when orienting the specimen in the vertical direction, b) in the horizontal direction (Z-Y plane) and c) in the horizontal position with a rotation by 90° (Z-X plane).

In the 2mm_13mm specimen only the centre point (X=Y= 0 mm, Z= 20 mm) was fully immersed. Hence, the triaxial residual stress was only measured in this position. When the gauge volume is partially immersed data correction needs to be performed. Depending on the measurement orientation and the position of the gauge volume with respect to the surface, the correction of the position (location of the centre of mass of the gauge volume) and strain needs to be performed. The approach is detailed in the appendix A.I. This procedure was initially performed for the 5 mm and the 9 mm thick specimens, to ensure that the measurement positions and resulting strains were not affected by having a portion of the gauge volume outside of the specimen. The measurement positions for the 5 mm thick specimens are shown in Figure 3.18. The size of the diagram corresponds to the specimen cross-section.

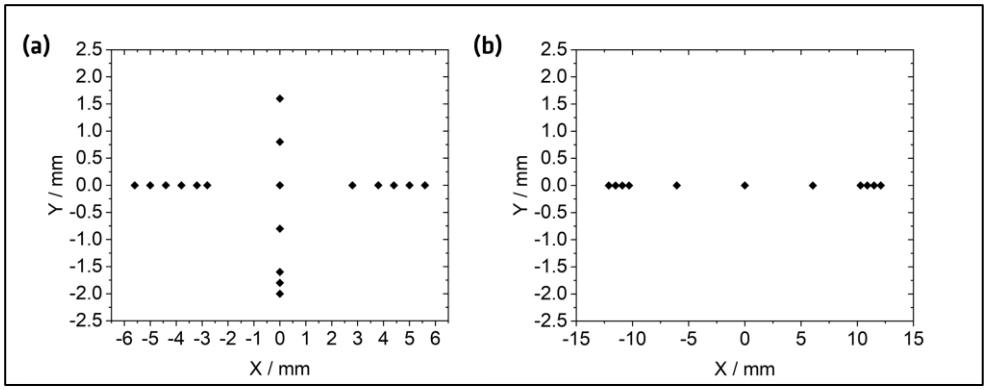

Figure 3.18: a) Neutron diffraction measurement position in the 5mm_13mm specimen, b) in the 5mm_26mm specimen. The measurement height was Z= 20 mm. The gauge volume is not shown to scale.

The measurement positions for the 9 mm thick specimens are shown in Figure 3.19.

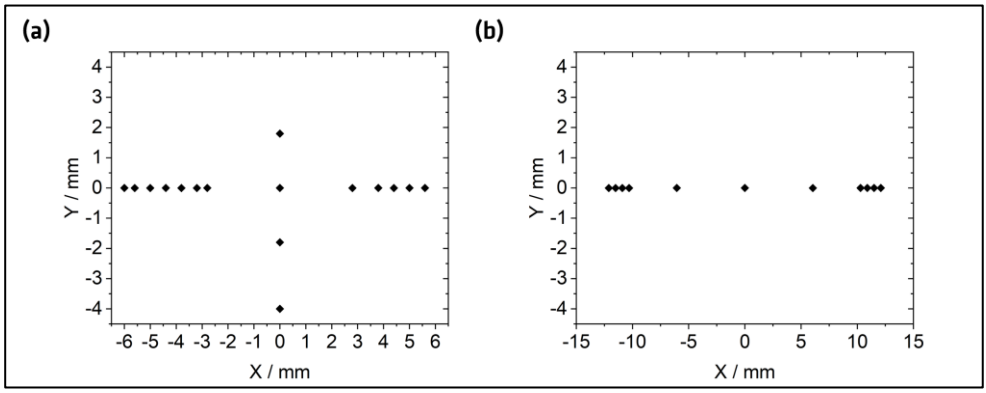

Figure 3.19: a) Neutron diffraction measurement position in the 9mm_13mm specimen, b) in the 9mm_26mm specimen. The measurement height was Z = 20 mm. The gauge volume is not shown to scale.

The characterisation of the full sized as-built blank specimen was performed on E3 (results in subchapter 4.3.3). Five measurement lines with each six measurement positions were distributed in the specimen (see Figure 3.20 a). The gauge volume was 2 mm x 2 mm x 2 mm. The first measurement position for each measurement line was positioned 3.4 mm from the surface. A distance of 25 mm was set between the first and second measurement point (see Figure 3.20 b). The subsequent step size in Z was 15 mm. The step size in X was 6.5 mm.

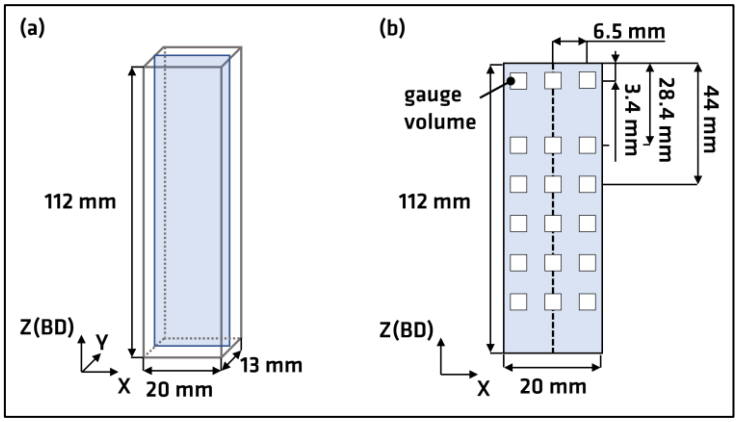

Figure 3.20: a) Dimensions of the as-built blank and the measurement plane, b) measurement positions for the determination of the bulk residual stress.

The characterisation of the Tower_65s_AB was performed on ENGIN-X. The measurement positions are shown in Figure 3.21. The general experimental settings are given in Table 3.10. The gauge volume was 2 mm x 2 mm x 2 mm. The measurement points were positioned so that the gauge volume edge along the diagonal would touch the free surface.

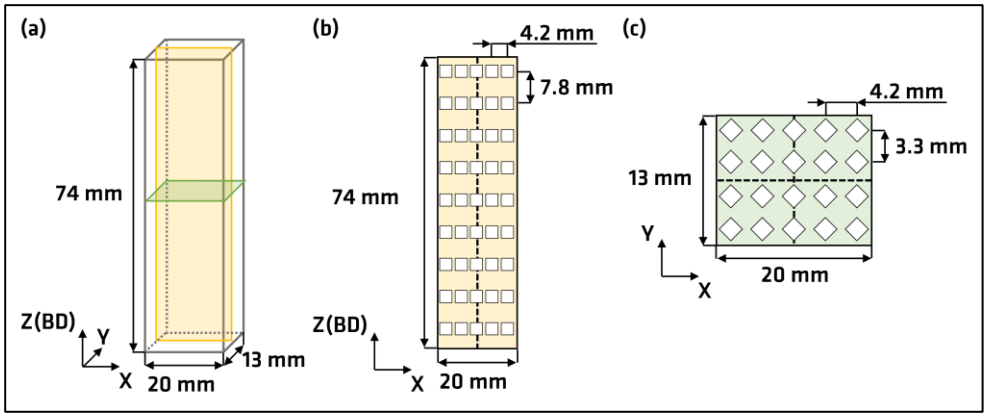

Figure 3.21: a) measurement planes in Tower_65s_AB and Tower_65s, b) measurement positions in the ZX plane, and c) in the XY plane.

The measurement positions related to the characterisation of the specimens Tower_18s, Tower_116s and Tower_116s_HV are shown in Figure 3.22. The residual stress profile along the build direction was captured using a total of 13 (14 for Tower_116s_HV) measurement positions (see Figure 3.22 b). The step size in

Z was 5.2 mm. In the Z-direction, the distance from the top and bottom surfaces was 2 mm (Figure 3.22 b).

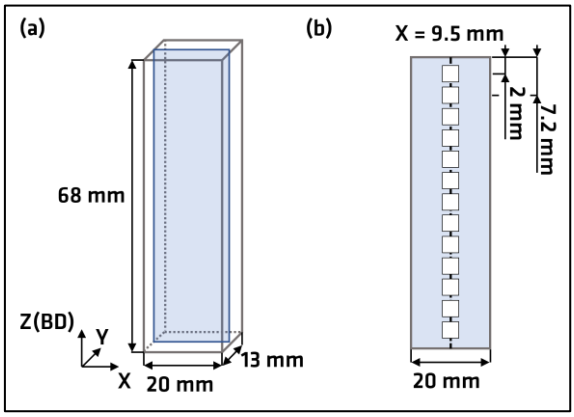

Figure 3.22: a) Dimensions of the as-built blank and position of the measurement plane, b) ND measurement positions along the height. The drawings are not to scale.

3.9.4 Measurement positions for the stress relieve analysis

The analysis of the stress relaxation after applying HT1 was performed using the residual stress distribution in Tower_65s (see Figure 3.21). The experiment settings are given in Table 3.10. The gauge volume was 2 mm x 2 mm 2.8 mm. The gauge volumes were positioned to touch the surfaces at the diagonal tip.

The investigation of the influence of the stress-relieve treatments in the SENB specimens (results in subchapter 4.5.2) was performed on the two measurement lines with each four measurement positions (see Figure 3.23). The measurement lines were positioned in the notch plane of the SENB specimens. The experiment settings are given in Table 3.9. The gauge volume was 2 mm x 2 mm x 2 mm. The distance in Y between the two measurement lines was 2.8 mm. The step size in X between the measurement points was 3.6 mm. The gauge volume edges were at a distance of 0.2 mm from the surfaces.

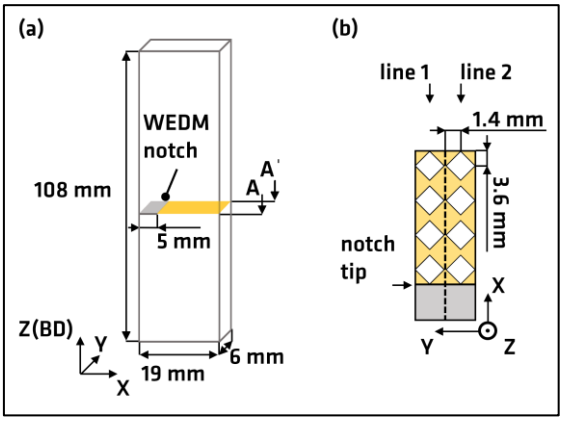

Figure 3.23: a) Simplified schematic of the SENB geometry and measurement plane A-A' and c) ND measurement positions in plane. More details on the SENB geometry are shown in Figure 3.7.

3.10 Stress free reference strategy

The stress-free-references d_0 used for the neutron diffraction beamtimes are shown in Table 3.16. In most cases, the d_0 was taken from parent or twin material i.e. specimen from the same build job and identical manufacturing parameters. These cubes were extracted using WEDM and no additional post-processing was undertaken. The cubes are therefore assumed to represent the chemistry and phase distribution of the investigated specimens. Furthermore, the residual stress in the cubes is assumed to be very low. In addition, the cube dimensions were chosen according to the gauge volume used for the residual stress determination. Therefore, any remaining residual stress gradient is averaged. It is therefore assumed that the cubes are an appropriate representation of the stress-free material investigated. For the investigation of the influence of the additional HT1-3, the d_0 was calculated from $(eqn. 13)$ assuming zero residual stress in the Y-direction ($\sigma_Y = 0\ MPa$).

Table 3.16: Stress free references used for the neutron diffraction beamtimes

Subchapter	Specimen	d_0 approach	d_0 reference material	Neutron Diffractometer
4.2	HT1 tensile samples	5 MPa load	Parent material	ENGIN-X/ in-situ
4.4.1	As-built walls	Cubes - 3 mm edge length & 1 mm edge length	Twin-specimen/ as-built	SALSA
4.4.1	As-built tower	Cubes - 3 mm edge length	Twin-specimen/ as-built	ENGIN-X
4.4.3	As-built blank	Cubes - 3 mm edge length	Twin-specimen/ as-built	E3
4.5.1	HT1 tower	Cubes - 3 mm edge length	Parent material	SALSA
4.5.2	HT1 tower HT1-3 SENB	Cubes - 3 mm edge length Cubes - 3 mm edge length	Twin-specimen/ HT1	ENGIN-X E3

4 Results and Discussion

4.1 Material characterisation

The aim of this chapter is to show that the microstructure of the PBF-LB/M/316L specimens is comparable with findings in the literature. Ultimately, the transfer of the knowledge acquired on the approach on how to determine the residual stress in PBF-LB/M/316L (chapter 4.2) as well as how to stress-relieve this material (chapter 4.5) is targeted. The microstructure investigation includes optical microscopy, scanning electron microscopy (subchapter 4.1.1) and electron backscattered diffraction in subchapter 4.1.2. Furthermore, results of the roughness variations depending on the specimen surface investigated are shown in subchapter 4.1.3.

4.1.1 Optical and scanning electron microscopy

In the optical microscopy pictures shown in Figure 4.1, the melt pool boundaries (orange arrows and lines) and layer boundaries (white dotted lines) are clearly visible and further highlighted in Figure 4.2 a). These microstructural features are typical of this manufacturing process [16]. In Figure 4.1 a) and b) the etching revealed a few features such as elongated grains and equiaxed grains forming a checkerboard pattern (green arrows in Figure 4.1 b). The former is typical for PBF-LB/M microstructures, and the latter is a feature of the scanning strategy employed [190]. The two features will be further discussed in subsection 4.1.2. Moreover, a change in roughness depending on the surface is observed in Figure 4.1 b). Whilst one side of the specimen features a wavy but smooth surface, the other surface appears very rough as partially molten powder particles and material bulging outwards are observed. The resulting surface roughness is further investigated in subchapter 4.1.3.

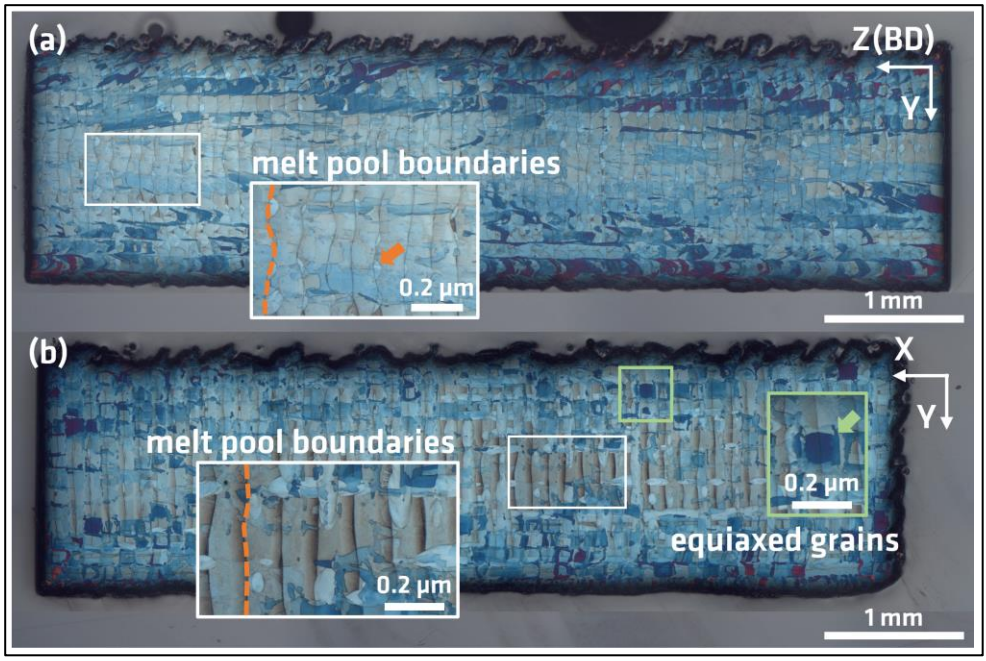

Figure 4.1: a) microstructure of the 2mm_13mm specimen (see subchapter 3.1) in the build direction and b) in the cross section (X-Y plane). The orange arrows and dotted lines indicate melt pool boundaries. The green arrows indicate equiaxed grains.

The microstructure displayed in Figure 4.2 a) and b) is a magnified view of the microstructure shown in Figure 4.1. The non-homogenous etching is a result of the microsection not being within one plane. A single plane can be defined by the track width, which is about the size of the laser spot ~80 µm (see process parameters in Table 3.2). Therefore, the melt pools appear in different shapes and sizes as indicated by the orange arrow in Figure 4.2 a). Moreover, a fine pattern is visible within the grains, which is further investigated by SEM in Figure 4.3. The etching of the microstructure gives insights on the elongated grains along the build direction in Figure 4.2 a), while equiaxed grains in the X-Y plane can be distinguished in Figure 4.2 b) . These features and a large <100> oriented grain (in Figure 4.2 b) are substantiated by the EBSD images in Figure 4.4 b). The equiaxed grains form a checkerboard pattern, which was also observed in other studies for PBF-LB/M/316L [6] as well as for PBF-LB/M/IN718 [98].

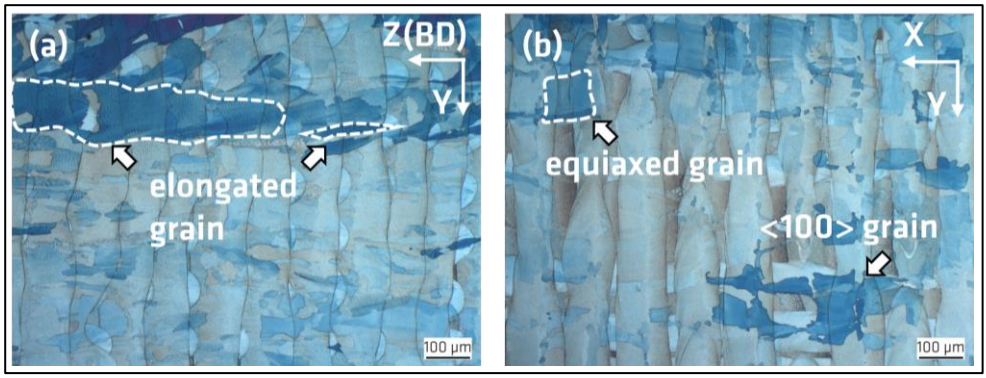

Figure 4.2: a) Magnified microstructure in build direction and b) in the X-Y plane. In a) arrows show grains growing through multiple layers. In b) equiaxed grain and <100> grains (validated in Figure 4.4 b) are highlighted.

As detailed in chapter 2.1, the grains and subgrain cellular structure of PBF-LB/M austenitic steel 316L grow along the main heat flow (approximately the BD). Depending on how the microsection is oriented with respect to the grain orientation, the cellular structure inside the grains appears either as fine elongated lines or as polygons (see BD cells in Figure 4.3 a) and b). This aspect is well described in [6]. This gives the characteristic microstructure shown in Figure 4.3 a) and b). Elongated grains in some cases grow through the melt pool boundaries (see Figure 4.3 a). Besides the cellular substructure and melt pool boundaries, also a few pores (entrapped gas as indicated by the circular shape) are visible in Figure 4.3 b). The porosity in these specimens is very low (optical images of the wall specimens and porosity reported in [49] and [157]). Additional optical microscopy images confirm this observation (see A. 2).

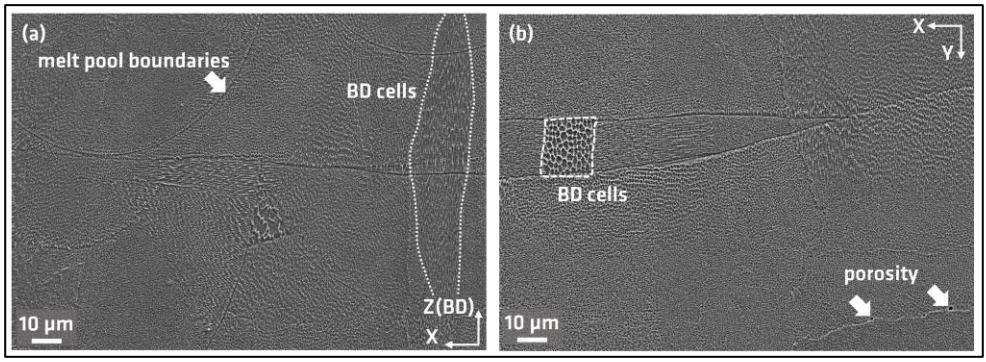

Figure 4.3: a) cellular structure in the Z-X plane and b) in the X-Y plane. BD cells either appear as fine lines in the Z-X plane or polygons in the X-Y plane.

4.1.2 Electron backscattered diffraction

The microstructure of the 2mm_13mm specimen was analysed along and perpendicular to the building direction using EBSD as shown in Figure 4.4 a). The colour code for the grain orientations is shown in Figure 4.4 a). The observations on elongated grains in the building direction and a checkerboard pattern in the plane perpendicular to the building direction are confirmed via EBSD in Figure 4.4. The grains grow through several layers (the layer thickness is 50 µm) as shown in Figure 4.2 a) and in Figure 4.4 a). Moreover, the continuous colour gradients in the grains indicate intragranular misorientation within the grains, which is linked to the solidification and the resulting cellular substructures. This observation was also reported in [5, 78]. Besides the elongated and large grains, smaller grains also occur between the laser tracks as shown in Figure 4.4 b).

The pole figures in Figure 4.4 c) and d) indicate that the grains exhibit a preferred orientation in the <110> direction along the build direction. Furthermore, <100> grains tend to align with the scan vector in the Y-direction and to a lesser degree in the X-direction. This is in agreement with observations made in [49]. Furthermore, the (100) pole figure in Figure 4.4 d) agrees to some extent to the Goss texture characterised by <100> grains aligned with the scanning directions and at 45° of the building direction as described in [78]. The pole figures showing the microstructure of the specimens manufactured with a layer thickness of 30 µm (see A. 5) have better statistics as the data used was taken from much larger maps (one map of 1 mm x 0.75 mm for the wall specimens against four maps of 4 mm x 3 mm for the 30 µm material). The indication of a Goss texture is substantiated whereas for the <110> a fibre texture in the build direction (see A. 5

e) is observed. In the <111> direction, the grains are rotated by 45° from the poles in the wall specimens but aligned with the poles in the 30 µm material (see A. 5 e).

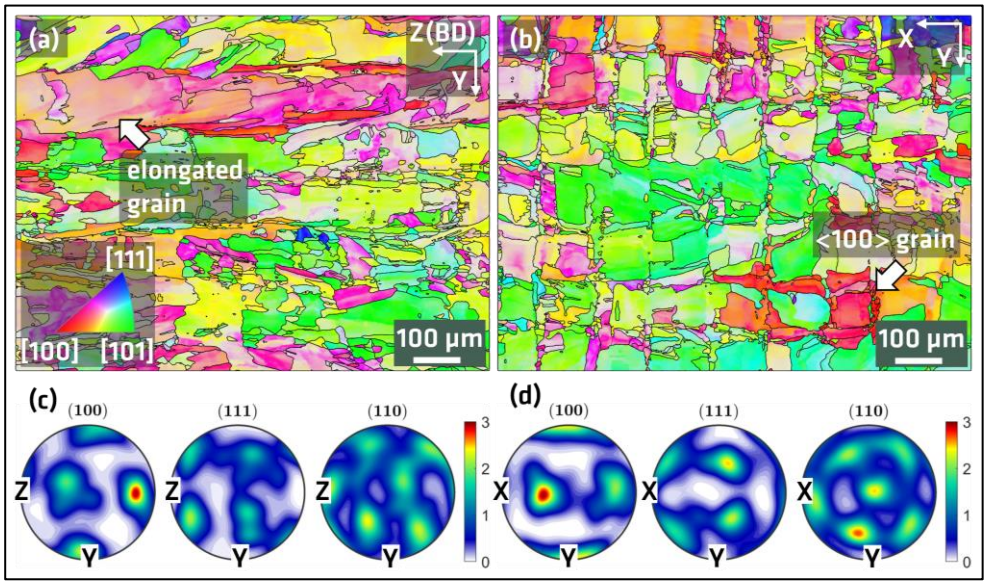

Figure 4.4: a) EBSD image of the 2mm_13mm microstructure in build direction and b) in the X-Y plane and associated pole figures in c) and d). A grain with a preferred <100> orientation is highlighted in b).

The ESBD images in Figure 4.5 correspond to the 9mm_13mm specimen. The same acquisition settings were employed. In both cases, the microstructure corresponds to the bulk of the specimen (the distances from the surface were ~700 µm for the 2mm_13mm specimen and 1600 µm for the 9mm_13mm specimen). The increase in thickness affects the microstructure as the grains appear more ordered and exhibit a slightly more characteristic shape (reversed bell as also shown in [78]) in the building direction as shown in Figure 4.5 a). Though this may be an artefact of the microsection preparation, the grains in the 2mm_13mm specimen are much coarser and less randomly oriented than in the 9mm_13mm specimen. This may be resulting from different thermal gradients as observed in [191]. An increase of the thickness of PBF-LB/M/316L walls was found to lead to a larger number of coarse <110> oriented grains away from the surfaces [192]. The near surface texture was observed to be random and grains were observed to nucleate at partially molten powder particles at the surface [27, 192]. This may explain the subtle indication that the grains appear to grow at an angle to the build direction in the optical microscopy images in Figure 4.1 a).

In 316L the primary growth directions are the <100> directions, which tend to align with the thermal gradient [10, 78]. For the PBF-LB/M of 316L and IN718 (bidirectional scanning pattern), <100> grains were observed to lie 15° from the thermal gradient and creating a 90° angle between the layers [47]. Thus, the grain growth orientation is approximately at an angle of 45° degrees which leads to the "chevron" type of features in Figure 4.5 a). This microstructural feature was well described in [78, 193].

The microstructures corresponding to the 316L PBF-LB/M specimens with a layer thickness of 50 µm and 30 µm (see A.II) agree well with findings reported in the literature [6, 49, 140]. The results describe the hierarchical microstructure, going from the molten pool boundaries, complex shaped grains to the cellular substructures. The elongated grains along the build direction and almost equiaxed grain shape (checkerboard pattern) perpendicular to the building direction are characteristic for PBF-LB/M/316L manufactured using a bi-directional scanning strategy [98]. The material does not exhibit a strong texture and the main findings <110> in the build direction and <100> perpendicular to the build direction and along with the scanning vectors agree as well with reported findings in the literature [6]. In addition, the presence of the cellular structure observed is a further indication that the PBF-LB/M/316L in this study is comparable to other findings reported in the literature. This also means that the results of this study are transferable in a broader sense and that to some degree, that the processing of 316L PBF-LB/M leads to repeatable microstructures with this scanning strategy. It is important to note that the cellular substructure is composed by entangled dislocations, precipitates, and chemical segregation (see the details in 2.1). The cellular structure is one part of the motivation of this study, as the aim is to understand whether the presence of this feature in combination with the complex grain shapes influences the micromechanical behaviour and subsequently the approach on how to determine the residual stress (see chapter 4.2). Furthermore, this feature is also expected to act on the residual stress relaxation (see chapter 4.5).

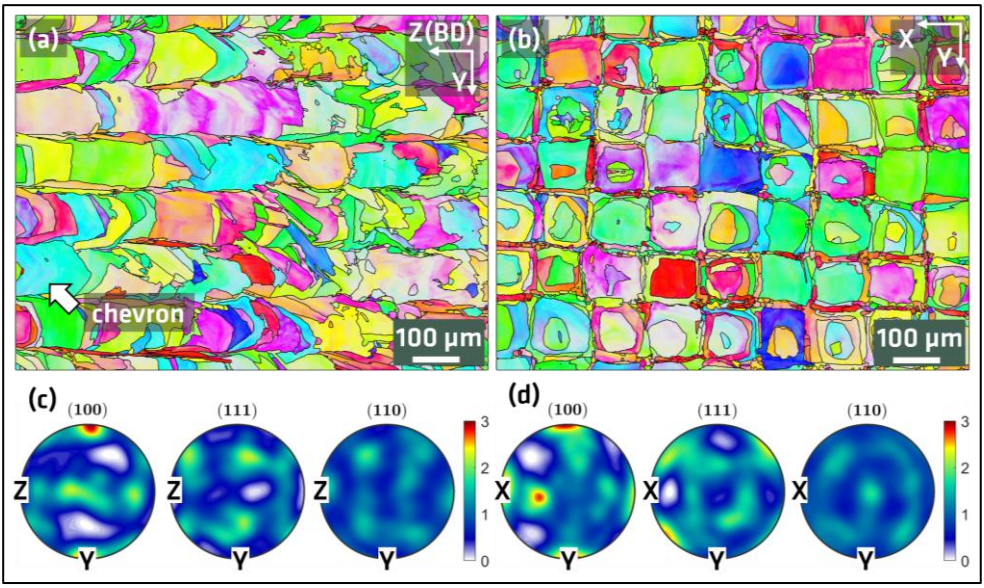

Figure 4.5: a) EBSD image of the 9mm_small microstructure in build direction and b) in the X-Y plane and associated pole figures in c) and d).

4.1.3 Surface roughness analysis

The surface roughness of the 2mm_26mm, the 5mm_26mm, and the 9mm_26mm specimens is shown in Figure 4.6. The corresponding area roughness parameter is shown in Table 4.1. Though the specimens were manufactured with identical process parameters, the surface exhibits different topologies between the 5mm_26mm specimen compared to the 2mm_26mm and the 9mm_26mm specimen. In Figure 4.6 a) and b), the step effect from the layer-by-layer manufacturing is clearly visible. The surface of the 5mm_26mm, however, does not exhibit similar features. In fact, the surface has features aligned with the build direction. The roughness parameter *Sa* of the 5mm_26mm specimen is thus two times higher than the 2mm_26mm and the 9mm_26mm specimens (see Table 4.1).

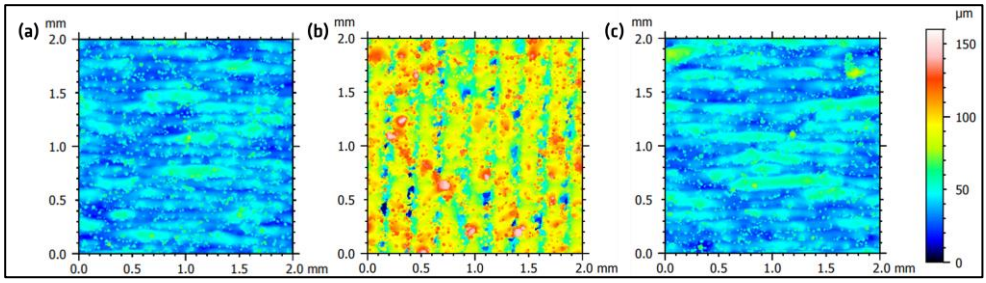

Figure 4.6: a) Surface roughness map of the 2mm_26mm specimen, b) of the 5mm_26mm specimen, and c) of the 9mm_26mm specimen (Adapted from Adapted from [194]).

At the current stage it is not clear why the 5mm_26mm specimen exhibits a higher surface roughness. The position of this specimen (see Figure 3.5) was more central with respect to the build platform compared to the 2mm_26mm and the 9mm_26mm specimen. This might have affected the laser inclination, which can change the local heat input. This effect was observed to affect the residual stress [142]. Since the process parameters, the scanning strategy, the inclination of the surface (towards the build platform) remained identical (these parameters were observed to affect the surface roughness [35]), no obvious reason apart from the different laser beam incidence angle was found to explain the difference in the roughness. Nevertheless, this result means that the surface residual stress of the 5 mm thick specimens cannot directly be compared with the other two specimens due to the penetration depth of the X-rays.

Although the specimen surface orientations are identical with respect to the build platform, changes in the position of the specimen on the build platform may influence the resulting surface roughness. The influencing variables are thereby manyfold. The PBF-LB/M process parameters build position, gas flow orientation, inclination of incident laser beam, scanning sequence, spattered powder [125, 142, 195] are reported to influence the surface roughness.

Table 4.1: Surface roughness *Sa* in µm of the PBF-LB/M/316L wall specimens.

2mm_26mm	5mm_26mm	9mm_26mm
7	14	7

The roughness of the Tower_18s as a function of the surface investigated is shown in Figure 4.7. The roughness profiles along two lines at half the height of the

specimen are shown in Figure 4.7 a) and b). The average roughness *Ra* changes drastically from 6.4 µm to 15.3 µm. The results in Table 4.2 summarize variations of the surface roughness on the Tower specimens. *The results show that each side of a specimen has a different surface roughness*.

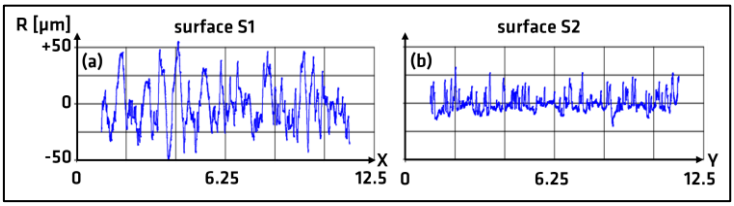

Figure 4.7: a) Roughness measurement on the Tower_18s specimen, b) and c) show the roughness profiles of one measurement line on the surfaces S1 and S2. Refer to Figure 3.16 for surface definition.

On Tower_18s and Tower_116s the *Ra* values vary significantly. In case of Tower_18s, these changes are a multiple of the penetration depth of X-rays in austenitic steel 316L [60]. In Figure 4.7 b) the surface peaks and valleys go from +50 µm to -50 µm. This roughness profile shows that when determining the residual stress via XRD, the calculated values are an average of the residual stress in the roughness peaks. These roughness peaks in case of surfaces of PBF-LB/M parts are in some cases partially molten powder particles [125]. Though the roughness peaks contribute to the diffracted signal, they are assumed to be mostly free of macroscopic residual stress as they are less restrained compared to the bulk material. Hence the residual stress values are lower. Therefore, when probing the residual stress at higher depths an increase in the stress values is observed, independently of the processed alloy [125, 191]. The large number of different effects affecting the surface may explain the variation in roughness of the Tower_65s in as-built and heat-treated condition. Interestingly, increasing the scanning velocity from 700 mm/s to 900 mm/s leads to similar values on all surfaces as shown for Tower_116s_HV in Table 4.2.

No general trend was found based on the roughness measurements on the small (walls) and larger specimens (towers). However, since it is known that a higher roughness can lead to lower residual stress values in accordance with [11] (when using diffraction to determine the surface residual stress see subchapter 2.2.3), it is important to pair surface residual stress determination with surface roughness measurements. In the subchapters 4.3, 4.4, and 4.5 the surface residual stress in the wall and Tower specimens is investigated on surfaces having similar Ra values where applicable.

Table 4.2: *Ra* in µm at mid height of the Tower specimens. Standard deviation is below 1 µm.

Specimen	Surface 1	Surface 2	Surface 3	Surface 4
Tower_18s	15.3	6.4	8.3	13.2
Tower_65s_AB	13.4	10.3	19.5	9.9
Tower_65s	10.3	7.9	10.9	16.7
Tower_116s	9.4	7.1	11.5	12
Tower_116s_HV	11	11.6	11.1	13.2

4.2 Micromechanical behaviour of the laser powder bed fused 316L stainless steel

This chapter aims at understanding in which way longstanding results concerning the determination of residual stress can be applied to the complex microstructure shown in chapter 4.1. In subchapter 4.2.1 the evolution of the lattice plane strains of the V-specimen and the H-specimen is analysed. In subchapter 4.2.2 the accumulation of intergranular strain is determined. In subchapter 4.2.3 the diffraction elastic modules are presented and compared to grain interaction models. Based on the results of this chapter, suggestions on how to calculate the residual stress in PBF-LB/M/316L and possible errors are given in subchapter 0.

4.2.1 Lattice strain evolution during uniaxial tensile testing

The strain evolution of four lattice planes versus the engineering stress are compared to the bulk behaviour as described by the Pawley refinement of the lattice parameter parallel to the loading direction of the V-specimen and H-specimen as displayed in Figure 4.8 and Figure 4.9 respectively. In the elastic regime, the spread of the lattices reflects the strong mechanical elastic anisotropy of austenitic stainless steel governed by the single crystal anisotropy (see Figure 4.8 a) [89]. All lattice planes evolve between the most compliant (200) and the stiffest (111) plane. This is the typical behaviour observed in conventionally processed FCC alloys [89, 90]. The evolution of the (220) lattice plane and the bulk (lattice parameter) is within the error bar of each other in the elastic regime. This corresponds to the fact that a <110> texture prevails in the loading direction (see A. 5).

When reaching approximately 420 MPa and 530 MPa for the V-specimen and the H-specimen respectively (see Figure 4.8 b) and Figure 4.9 b), a strong redistribution of the load is observed which marks the initiation of plastic deformation. Since not all grains undergo plastic deformation simultaneously, the material undergoes an elastic-plastic transition. The variation of the slopes of the lattice strains indicates the change from elastic to the plastic accommodation of strain, as described in [196]. The upward inflection of the (220) lattice plane strain is an indicator for plastic deformation, as the increase in engineering stress does not lead to an accumulation of elastic strain. The (220) plane starts yielding (increase in load but constant or “curling” evolution of the lattice strain i.e. inflection of the strain as the lattice plane carries no additional elastic strain [85]). At the same load the (200) lattice plane strain experiences a strong increase in the lattice strain.

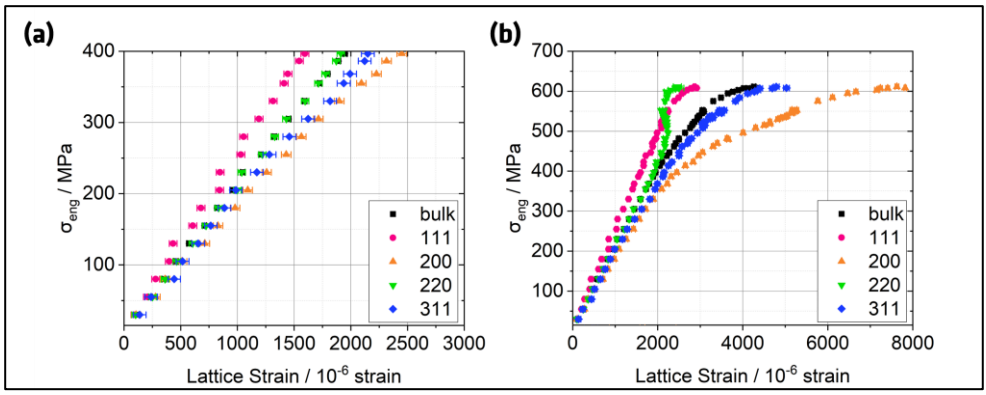

Figure 4.8: a) Elastic regime of the b) evolution of the lattice strains and bulk elastic behaviour (Pawley refined lattice parameter) of the V-specimen.

The evolution of the lattice strains in the axial direction of the H-specimen shown in Figure 4.9 is very similar to the V-specimen. This can be ultimately related to the low texture (2x random). The (220) plane and the bulk (Pawley refined lattice parameter strain) evolve similarly in the elastic regime (see Figure 4.9 a). An offset of the upward deflection of the (220) plane and the accumulation of the strain in the (200) plane occurs at a higher load (approximately 530 MPa vs. 420 MPa).

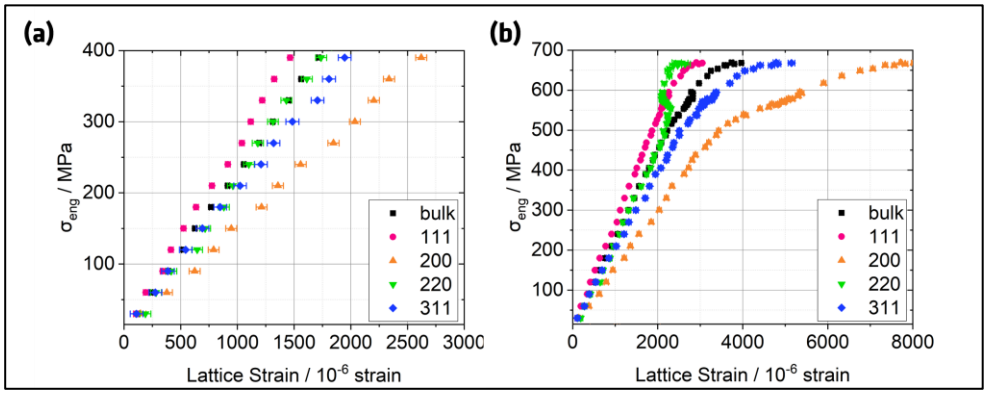

Figure 4.9: a) Elastic regime of the b) evolution of the lattice strains and bulk elastic behaviour (Pawley refined lattice parameter) of the H-specimen.

To further compare the V-specimen and the H-specimen, the lattice strain evolution of the (220) and the (200) lattice planes are plotted against the normalized applied stress using the respective yield strength. The result is shown in Figure 4.10 a). The (220) lattice strains of the two specimens are very similar.

The elastic behaviour of the V-specimen is slightly stiffer compared to the H-specimen. This is likely due to the more pronounced <220> texture in the loading direction of the V-specimen (see Figure 4.10 b). Furthermore, the similar behaviour of the V-specimen and the H-specimen also shows that it is unlikely that defects affected the macroscopic tensile behaviour (defects were found to have an influence on the anisotropic behaviour of PBF-LB/M alloys [51]). Indeed, the porosity can be assumed to be less than 0.01 % as reported in [49] (see A. 3).

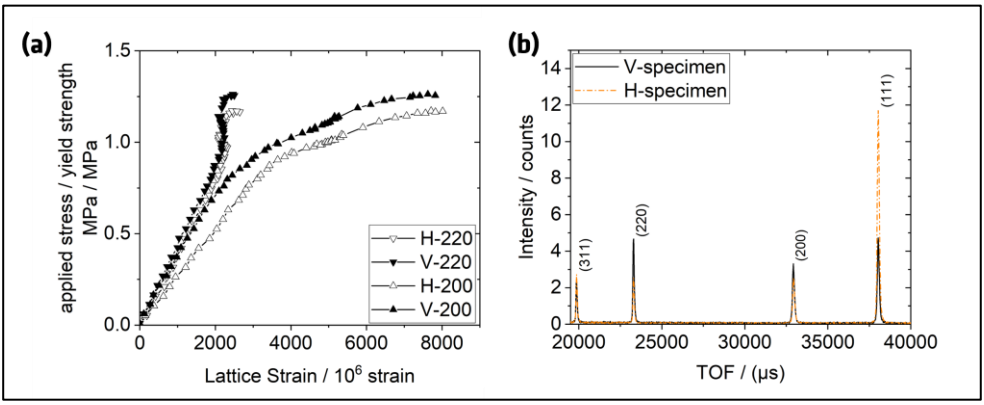

Figure 4.10: a) (220) and (200) lattice plane strains in the V and H-specimen, b) comparison of the diffraction patterns before the start of the in-situ tensile test.

When analysing the (200) lattice plane evolution in the two specimens, a notable difference is observed in the elastic regime. The departure from linearity in the (200) lattice plane strain occurs much earlier in the H-specimen than in the V-specimen (Figure 4.8 a) and Figure 4.9 a) respectively). Various sources, individually or in combination, could lead to this observation. The deviation from linearity of the (200) lattice plane is an indication of load transfer from the (111) or the (220) lattice planes. This might result from room temperature creep (small amount of plasticity) resulting in an increase of strain at a low applied stress (see A. 7 in Annex A.I). This phenomenon can occur during in-situ tensile tests, as reported in [90, 92]. Furthermore, a change in slope could be evidence for the presence of type II residual stress, which leads to the material undergoing small amount of plastic deformation. This observation was also reported for a rolled austenitic steel in [86].

The yield strengths of the V-specimen and the H-specimen differ by approximatively 100 MPa (484 MPa and 571 MPa for the V-specimen and the H-specimen respectively). The yield strength was calculated using a self-written Python code detailed in the appendix A.IV). This result is in good agreement with

findings in the literature [49, 51]. It is noted that the bulk values agree well with the values of specimens manufactured using the identical stainless steel AISI 316L powder but adapted PBF-LB/M parameters to a layer thickness of 50 µm as reported in [49] (~500 MPa and ~580 MPa for horizontally and vertically built specimens respectively).

The comparison of the V-specimen and the H-specimen with conventional 316L data is more complex, as it is not possible to ensure identical chemical composition. In Figure 4.11 a), the evolution of the (200) and the (220) lattice plane strains of a conventional 316L are compared against the V-specimen. The conventional 316L exhibited a low texture (not specified) after the annealing at 1050 °C for 10 hours [92]. Up to a true stress of ~160 MPa the two materials evolve similarly as shown in Figure 4.11 b). The yielding of the (220) lattice plane and simultaneous elastic strain accumulation in the (200) lattice plane occurs much earlier in the conventional material compared to the PBF-LB/M material. Moreover, both phenomena are more pronounced in the PBF-LB/M material. This is possibly due to the difference in texture and the larger amount of strain at the onset of plasticity.

At strain levels below 3 % (according to Figure 4.12), the dislocation slip is the dominant deformation mechanism [3]. The interaction of the dislocations with the cellular structure is an additional explanation for the more pronounced load shedding and strain accumulation effect of the additively manufactured specimen. The dislocations are pinned when interacting with the cellular structure as shown in [3]. Therefore, the accumulation of the dislocations requires higher applied stresses to permit them to further move i.e. the material needs higher stress to plastically deform. It can be therefore hypothesized that the higher loads then lead to larger lattice strains in the more compliant lattice planes once the plastically soft lattice planes deform. Furthermore, the in-situ tensile test of the PBF-LB/M material included several unloading steps to analyse the accumulation of intergranular strain. Unloading from high applied stress values can result in dislocation recombination that may affect the elastic response in the subsequent evolution [86, 90], which was also observed to occur in PBF-LB/M/316L [3].

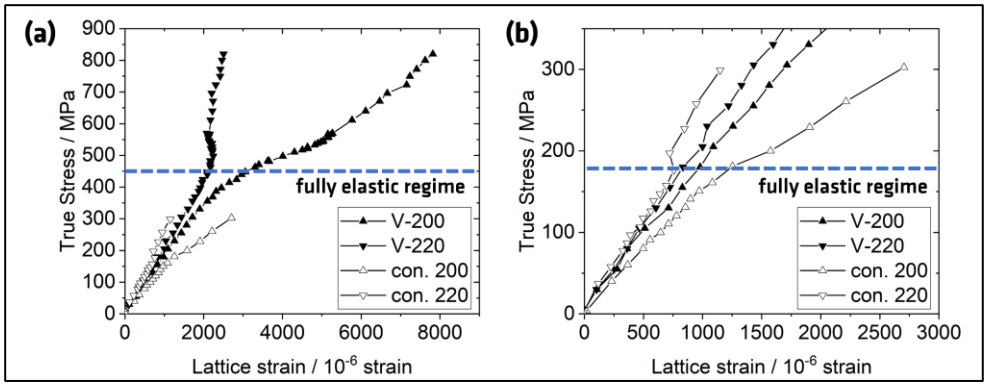

Figure 4.11: a) Comparison of the (200) and the (220) lattice plane strain under an applied tensile load of the V-specimen to a conventional 316L specimen (conv). b) Close up view with axis limits adapted to the conv. material. The conventional material was annealed at 1050 °C for 10 hours as reported in [92].

The evolution of the lattice strains in the V-specimen and the H-specimen differ due to the prevailing texture in the loading direction. The non-linear behaviour of the H-specimen in the elastic regime might be a convolution of room temperature creep and remaining type II residual stress leading to small amounts of plastic deformation. The comparison of the V-specimen to a conventional 316L material (results taken from [92]) shows that the material behaves similarly up to a true stress of 160 MPa. This level marks the initiation of the plastic deformation for the conventional material. The load shedding of the (220) lattice plane and the strain accumulation of the (200) lattice plane is more pronounced in the PBF-LB/M specimen. Given the similarity of the conventional and the PBF-LB/M material, it might be assumed that the (311) lattice plane is also the best suited crystallographic plane to link the microstrains to the macroscopic residual stress. This is further analysed in the next subchapter.

4.2.2 Lattice strain accumulation

The lattice strain accumulation of the PBF-LB/M/316L shown in Figure 4.12 follows the general tendency of strain accumulation in FCC materials as described in [89]: compressive microstrain accumulation in the (111) and the (220) planes and tensile microstrain accumulation in the (200) and the (311) planes. The behaviour of the bulk (Pawley refined lattice parameter) and the (311) strain accumulation are within the error bar until 3 % plastic strain for the H-specimen. However, this is not the case for the V-specimen, as a difference of up to 250 microstrain is observed at a macroscopic strain of about 1 %. The lowest microstrain accumulation is observed

for the (111) plane up to 3 % plastic strain for both specimens, which is in agreement with findings in [87]. The strain accumulation of the (220) plane in both specimens also evolves within the error bar. Interestingly, the Pawley refined lattice parameter accumulates lattice strain (see subchapter 2.2.1). This is unlikely to be resulting from sampling an insufficient number of reflections as ten reflections were used [79]. A much higher strain accumulation takes place in the (200) and the (311) planes of the V-specimen compared to the H-specimen for comparable plastic strain levels. The trend is however similar; the strain accumulation rapidly increases before reaching a plateau. The plateau indicates that no additional elastic strain can be accommodated i.e. the material deforms plastically. At larger strain levels, all grains underwent plastic deformation, and the accumulation of strain is defined by the elastic and plastic anisotropy [90]. When comparing the residual lattice strain of the PBF-LB/M/316L with the conventional austenitic steel described in subchapter 2.2.2, it can be noted that the accumulated microstrains are much greater in the PBF-LB/M material. For the (311) lattice plane, the accumulation of microstrain around 1 % macroscopic strain is close to 500×10^{-6} strain compared to approximately 80×10^{-6} strain (see Figure 2.12 b). As discussed in 4.2.1, this may be attributed to the higher strains at the onset of plasticity, the texture and the cellular structure. This result, however, challenges the general assumption that the (311) lattice plane accumulates no residual lattice strain [89].

To summarize, the PBF-LB/M material follows the general trends of FCC alloys as described in 2.2.2. A notable microstrain accumulation is observed in the (311) plane, which challenges the results for conventional austenitic steel. The microstrain accumulation in the V-specimen and the H-specimen is broadly similar for the (220) and the (111) lattice planes. However, there is a significant difference in the (200) and the (311) planes of the two specimens. The texture difference and type II residual stress may explain the different behaviour in strain accumulation at lower strains. The strain accumulation in the (200) and the (311) occurs when a stiffer lattice plane e.g. the (220) lattice plane yields. The load is transferred to the elastic more compliant lattice planes. Therefore, the texture plays a major role as it defines the number of grains which will yield and thus shed the load to the other lattice planes. The stress level at which the lattice planes yield is affected by the initial residual stress (superimposition of applied stress and type I and type II residual stress). The residual stress may lead to microyielding, which in turn affects the strain accumulation in the first unloading.

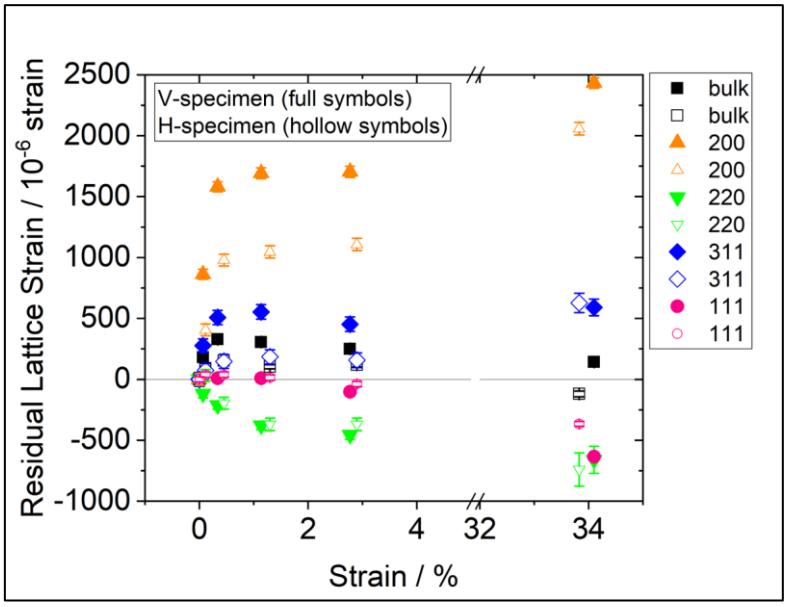

Figure 4.12: The accumulation of microstrains in the V-specimen and the H-specimen during the subsequent unloading steps in the in-situ tensile test.

4.2.3 Diffraction elastic constants

The diffraction elastic moduli of the (111), the (200), the (220) and the (311) planes and macroscopic values (Pawley refinement) are summarized in Table 4.3. These values were calculated using the data up to 0.15 % strain (to remain in the fully elastic regime i.e. below the onset of plastic deformation). The experimental values are compared to the values calculated using the Kröner and the Reuss model (tabulated from single-crystal elastic constants of austenitic steel using the software XEC [183]). The macroscopic anisotropy of the V-specimen and the H-specimen is also observed on the microscopic scale. The difference between the V-specimen and the H- specimen is most prominent for the (220) lattice plane and is about 13 %. The (220) lattice plane elastic modulus is similar to the macroscopic value (Pawley refinement) for the V-specimen. This may be expected as the V-specimen has a (220) texture in the loading direction. For the H-specimen, the lattice specific and bulk values differ by about 5 %, which is attributed to the lower (220) texture in the loading direction (see A. 5).

The elastic moduli of the different lattice planes and the Pawley refined bulk behaviour (E_P) summarized in Table 4.3 are similar to the ones found in the SXRD in-situ tensile test of PBF-LB/M AISI 316L reported in [48]. However, some

discrepancies are observed, which can be related to the different texture compared to the texture of the V- and the H-specimens and to small differences in the chemical composition. The largest difference between the elastic moduli is observed between the values of the (200) lattice plane. This is to be expected, as this crystallographic reflection is the most compliant and is heavily affected by the surrounding grains [197]. The other values are within 20 GPa from each other, which can be explained by the texture difference and different chemical compositions.

Table 4.3: The elastic moduli of specific reflections in the PBF-LB/M specimens compared to the Reuss and the Kröner model.

Specimen	E_{111} in GPa	E_{200} in GPa	E_{220} in GPa	E_{311} in GPa	E_P in GPa
V-specimen	247 ± 5	172 ± 3	206 ± 3	194 ± 4	206 ± 6
H-specimen	263 ± 3	148 ± 5	238 ± 7	195 ± 3	224 ± 2
Reuss [183]	287.5	101.2	196.9	145.7	n.a.
Kröner [183]	241.5	151.8	210.4	184	n.a.
Vertical [48]	264.1 ± 1.6	139.1 ± 1.1	219.1 ± 1.6	179.6 ± 1.2	n.a.

The elastic moduli calculated from the initial linear strain region (up to 0.15% strain) as a function of the orientation parameter are shown in Figure 4.13. The orientation parameter Γ is calculated from:

$$\Gamma = \frac{h^2k^2 + k^2l^2 + h^2l^2}{h^2 + k^2 + l^2} \qquad (eqn. 15)$$

and is a function of the Miller indices (*hkl*) (see subchapter 3.8). The elastic moduli of the V-specimen and the H-specimen are best described by the Kröner model compared to the Reuss model, see Figure 4.13 (corresponding values of the Kröner and the Reuss model are given in Table 4.3). Although the material is textured (up to 2 × random), the DECs correspond well to the tabulated DECs using Kröner (isotropic material, see subchapter 2.2.2). This result substantiates the findings on

the DECs reported for PBF-LB/M/316L in [48]. Furthermore, the observation is in good agreement with results on conventionally processed FCC materials reported in the literature [97]. However, as mentioned in 2.2.2, it is not always the case that the elastic moduli of lattice planes in FCC alloys are best described by the Kröner model. In fact, the DECs of a PBF-LB/M IN718 (texture up to 3 × random) were better described with the Reuss model, which was attributed to the crystallographic texture and to the elongated grain shape [98].

The very good agreement of the (311) lattice plane with the Kröner model of the two different loading directions (two distinct textures) is a considerable advantage over e.g., the (111) lattice plane (also considered as appropriate lattice plane to describe the macroscopic residual stress). Since the calculation of the residual stress often assumes isotropic material properties (3.7), using the (311) lattice plane may reduce the resulting error. The good agreement between the Kröner model and the experiments also gives the possibility to avoid determining the Poisson ratio experimentally. As described in *subchapter 2.2.2, these values are difficult to determine in textured materials.*

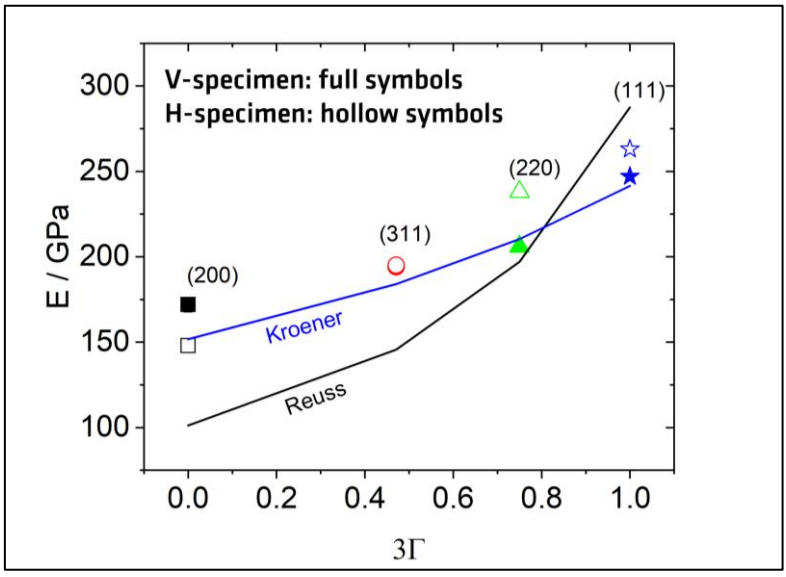

Figure 4.13: Comparison of the experimental diffraction Young's moduli to the Kröner and the Reuss models.

4.2.4 Choice of reflection for the determination of the residual stress

Following the suggestions in [87], it is stipulated to use the lattice plane most representative of the texture in the material. As shown in 4.1.2 (including Figure A. 5), the PBF-LB/M/316L specimens produced in this investigation exhibit a <220> texture. This result may suggest using the (220) lattice plane for monochromatic XRD and ND experiments. The findings in subsection 4.2.1 show that the (220) plane evolves similarly to the bulk for both specimens in the purely elastic regime. However, the (220) plane is also the first crystallographic plane to yield. This results in a strong deviation from linearity and an accumulation of compressive microstrains as discussed in subsection 4.2.2. The microstrains need to be accounted for, when the aim is to deduce the macroscopic residual stress (type I). Furthermore, the results also confirm that the (200) plane is not suitable to be used to describe the bulk elastic behaviour as it strongly deviates from linearity and accumulates very large intergranular strains. The (311) plane and the (111) planes stay the longest linear with a modulus close to the bulk behaviour in case of the (311) lattice plane. The (111) lattice plane accumulates the lowest residual lattice strain, which agrees with observations reported in [87]. However, considering the low multiplicity of the (111) lattice plane of 8 compared to 24 for the (311) lattice plane [85], it is not a practical approach to determine the residual stress using this reflection as it would increase the counting times. Moreover, it is further suggested in [87] that the (111) plane should only be considered in case the manufacturing history and induced stresses are known. This is, however, difficult to quantify given the complexity of the PBF-LB/M process. The (311) plane appears to be a good choice as it remains linear in the elastic regime and during the beginning of the plastic deformation, whilst evolving in a similar manner to the bulk elastic behaviour. The (311) plane accumulates intergranular strains between approximately 100 - 500 $\times 10^{-6}$ strain. Adding this range of additional strain to the calculation of the type I residual stress leads to an increase of up to 20-90 MPa (following a simplified approach of transferring the lattice strain to stress using Hooke's law for a uniaxial case as suggested in [90]).

To summarize, this result validates that the (311) lattice plane is the most suited lattice plane to be used to calculate the macroscopic residual stress. Nonetheless, the accumulation of residual lattice strain is not negligible (between 20 MPa and 90 MPa). Furthermore, the comparison of the experimentally determined and calculated Young's moduli shows that the Kröner model is well adapted to describe the elastic behaviour in this material. This result demonstrates that the assumptions for the diffraction based residual stress assessment usually applied to conventionally manufactured 316L (311 reflection, Kröner grain interaction model) also apply to the PBF-LB/M/316L material.

4.3 Residual Stress in laser powder bed fused 316L

The following chapter details the characterisation of the residual stress in PBF-LB/M/316L structures. In subchapter 4.3.1 the influence of increasing the specimen thickness and the specimen length is investigated. In subchapter 4.3.2 the residual stress is assessed in a larger structure.

4.3.1 Influence of single dimensional changes on the residual stress

Influence of the specimen thickness on the residual stress

The first part of this chapter investigates the influence of a change in thickness, while the other dimensions are constant. The surface, the subsurface and the bulk residual stress are investigated keeping the definition as detailed in subchapter 2.2.4.

Surface residual stress

The influence of the thickness on the surface σ_Z in specimens sized 40 mm x 26 mm (height and length) and a thickness of 2 mm, 5 mm, and 9 mm is shown in Figure 4.14 a-c). The σ_Z tends to increase with the thickness. To fulfil free surface boundary conditions, a lower σ_Z close to the cut surface is expected. Moreover, increasing residual stress with the build height corresponds well to the results reported in [11].

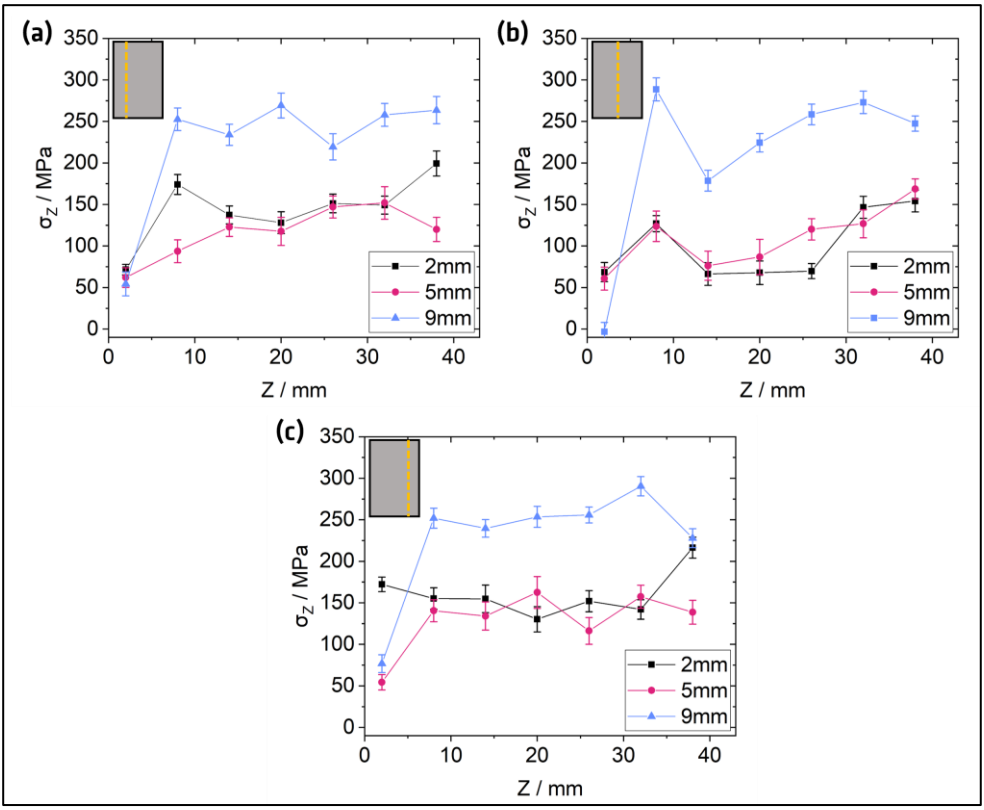

Figure 4.14: a) Surface σ_Z along the height at X= -6 mm, b) at X=0 mm c) at X=6 mm from the centre line respectively.

The surface σ_Z of the 2 mm and the 5 mm specimens are broadly similar and remain mostly between 50 MPa and 200 MPa. In comparison, the surface σ_Z of the 9 mm specimen is higher with values between 220 MPa and 300 MPa. Additionally, the surface σ_Z of the 9 mm specimen remains at a constant level except for the measurement line at X = 0 mm (Figure 4.14 b). The second measurement position was at approximately 8 mm from the cut surface. As mentioned, the residual stress does not vary with increasing heights. Hence, it can be assumed that the residual stress reaches its maximum value rapidly (within the first 10 mm). *This means that producing specimens greater than this measure may yield to larger residual stress with constant process parameters.*

For the three specimens a decrease in the residual stress values at X=0 mm is observed at approximately half the height of the specimen (Figure 4.14 b). The tensile surface residual stress increases towards the edges to some extent at X=-

6 mm and 6 mm (Z= 13 mm) as shown in Figure 4.14 a) and c). This effect was also observed in horizontally manufactured PBF-LB/M/316L specimens, where the edges of a prism bent upwards leading to lower residual stress in the centre of the part [119].

A change of the thickness from 2 mm to 9 mm results in much higher surface σ_Z. Only small differences are observed when comparing the 2mm_26mm to the 5mm_26mm specimen. As discussed previously, this may be the result of the different surface roughness (see Figure 4.6 and the roughness values in Table 4.1). The removal of the specimens from the build plate may have led to the distortion of the 2mm_26mm specimen. However, the measurement of the surface using a coordinate measurement machine showed that the displacement was in the order of the surface roughness (see A. 6). The use of scanning vectors in the direction of the thickness was reported to reduce the distortion [198]. The meander scanning strategy alternates the scanning vector along the length and the thickness. Thus, the distortion is assumed to be minor. Moreover, the measurement of the displacement following the removal of vertically oriented specimens resulted in deformations in the order of a few µm that were limited to the lower part of 60 mm tall PBF-LB/M/316L specimens as reported in [119]. Therefore, it is assumed that the expected variation in surface residual stress when increasing the thickness from 2 mm to 5 mm is a result of the different surface roughness (see Table 4.1). This is further proven with the subsurface measurements in the next section.

The surface residual stress σ_Z is tensile and increases with the build height as shown in Figure 4.15. This corresponds to the findings in the literature described in 2.2.3. Analysing the residual stress with knowledge of the roughness shows that the surface residual stress increases by a factor of ~3 when increasing the thickness from 2 mm to 9 mm. A comparison of the surface residual stress using the 5 mm thick specimen yields no additional insight, as the difference in roughness is much higher. Nonetheless a small increase of the average surface residual stress is observed. The fact that the values do not reach the yield strength is most probably related to the surface roughness as will be shown in the next section.

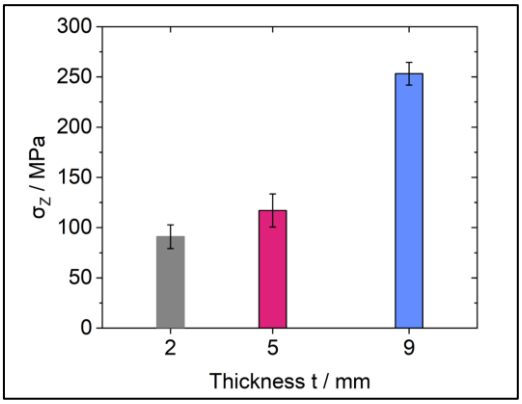

Figure 4.15: Average surface σ_Z at Z = 8 mm from the build plate as function of the thickness. The length of all specimens was 26 mm.

Subsurface residual stress

The subsurface σ_Z increases in all three specimens as shown in Figure 4.16 a). The gradient is, however, steeper in the 9mm_26mm specimen compared to the other two specimens. In the 2mm_26mm specimen a tensile peak value around 150 MPa is reached at a depth of 30 µm. From this position onwards the σ_Z descends steadily until reaching 70 MPa at a depth of 130 µm. In the 5mm_26mm and the 9mm_26mm specimens the σ_Z reaches values around 300 MPa at a depth of ~80 µm. While the σ_Z of the 5mm_26mm specimen then remains around this value, a small increase of the stress values is observed in the 9mm_26mm specimen around 170 µm.

Interestingly, the σ_X have similar values around 60 MPa in the 2mm_26mm and the 9mm_26mm thick specimens in a depth range between 25-75 µm. The σ_X in the 5 mm thick specimen remains low up to a depth of 30 µm before reaching a comparable level to the other two specimens. At greater measurement depths, the σ_X abates in the 2 mm_26mm specimen while it intensifies in the 5mm_26mm and the 9mm_26mm specimens to 170 MPa. Again, the trend between these two specimens is similar. The progression of the σ_Z in the 9mm_26mm is almost constant compared to the sudden increase at a depth of 130 µm in the 5mm_26mm specimen.

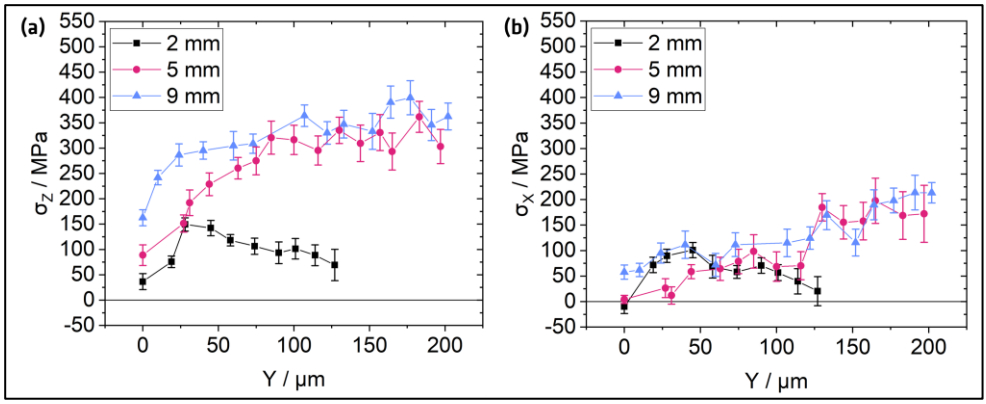

Figure 4.16: a) Influence of the thickness on the subsurface σ_Z and b) σ_X in the 26 mm length specimens (Adapted from [194]).

The trend of higher residual stress at a greater depth shown in Figure 4.16 may be related to the influence of the roughness. As discussed in 2.2.3, higher residual stress magnitudes were observed when removing the as-built PBF-LB/M surface roughness. The roughness of PBF-LB/M structures is extremely complex (see Figure 4.1). The layers create bulges and a multitude of powder particles remain attached, such as observed in [13, 35]. These features cannot retain high stress and as the grains in these features contribute to the diffraction pattern, the resulting residual stress is lower such as experimentally determined in [125]. From a mechanical engineering approach, an applied stress cannot be supported by features perpendicular to the stress direction. Thus, a material bulge perpendicular to the surface contributes to the diffraction signal. However, it retains a lower stress and the caculated residual stress will be low. This effect was also observed in [11]. The stress retained in partially fused powder particles or other features may, therefore, not be a representation of the residual stress in the subsurface. Specimens manufactured with different process parameters or at different positions on the build plate have different surface topologies [35, 150]. This means that the comparison of the residual stress between those specimens cannot be compared without the knowledge of the surface roughness.

This observation needs to be balanced with the residual stress formation mechanisms. The sudden increase of the σ_X occurs at approximately 130 µm. This corresponds to a measurement depth inside the second laser track (one laser track is about the width of the laser spot ~80 µm, see A. 4). In the first laser track, the material is restrained when shrinking by the underlying material. However, when depositing the second laser track, the restraint is induced by material both below and at the side (first laser track). The addition of material by producing PBF-

LB/M/316L structures composed of a rod (1D structure), a wall (2D structure) and a prism (3D structure) resulted in the decrease of the cooling rate [5]. *It can be hypothesized that a variation in the cooling rate may affect the misfit generated by the restrained shrinkage. Hence, next to the influence of the roughness it is also conceivable that the local changes of the restraint against the shrinkage evolve with the depth and thus also influence the residual stress.*

Finally, it appears that the σ_Z is more affected by the increase in thickness compared to the σ_X. Following the argumentation reported in [116], the σ_Z is driven by the TGM (see 2.2.3). As mentioned above, the increase of the geometry changes the thermal gradients. Therefore, the σ_Z is more affected by the increase in thickness. The magnitude of the surface σ_X or the σ_Y is often related to the length of the scanning vector of a PBF-LB/M structure (in the last layer). It was observed that longer scanning vectors lead to larger residual stress [81, 121]. However, for the wall specimens the length of the scan vectors did not change. Perhaps this may explain the fact that the σ_X is comparable (to a certain depth) although the thickness is changed.

To summarize, it becomes clear that the specimen having a 2 mm thickness retains lower residual stress in the subsurface. This trend is more pronounced for the σ_Z in the first 30 µm to 40 µm depth whereas for the σ_X the lower magnitudes are only observed when reaching a depth of 130 µm. In all specimens the σ_Z reach a subsurface maximum. The position of this maximum is well defined in the 2mm_26mm specimen. In the 5 mm and the 9 mm thickness specimen the subsurface σ_Z remain broadly similar and describe a plateau.

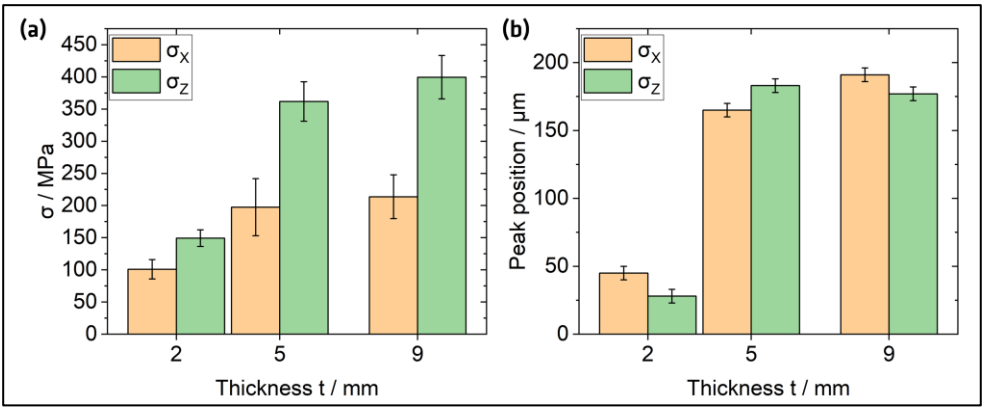

Figure 4.17: a) Subsurface peak magnitude of the σ_X and the σ_Z and b) their position as a function of the thickness in the 26 mm length specimens.

Bulk residual stress

The influence of the thickness on the bulk residual stress in structures sized 40 mm x 13 mm and thicknesses of 2 mm, 5 mm and 9 mm is shown in Figure 4.18. The distribution of the σ_Z is shown in Figure 4.18 a). The through-thickness σ_Z increases with the thickness. In the 2mm_13mm specimen, the σ_Z reaches a compressive peak residual stress close to -390 MPa. The compressive residual stress peak in the centre of the 5mm_13mm and the 9mm_13mm specimen is around -530 MPa and -620 MPa. The σ_Z magnitudes near the surface in the 5mm_13mm specimen reach approximately 250 MPa compared to 490 MPa in the 9mm_26mm specimen. This magnitude is close to the material's tensile yield strength and validates partially the residual stress formation models [11, 49]. The models predict the in-plane residual stress (on top of the specimen) to reach the material's yield strength in the last layer. However, the measurements show this is also the case for the residual stress in the build direction in the lateral subsurface region. In the 9mm_13mm specimen the σ_Z appears to be bound by the tensile and compressive yield strength (540 MPa and 600 MPa respectively according to [48]).

A similar trend is observed for the σ_X in Figure 4.18 b) as the tensile and compressive magnitudes increase with the thickness. The compressive σ_X at the centre is similar between the 2mm and the 5mm specimen. However, the σ_X reaches -100 MPa on both sides of the centre of the 5mm_13mm specimen and describe local minima. In the 9mm_13mm specimen the compressive peak σ_X at the centre is approximately twice as large compared to the other specimens. The σ_Y remain low through the thickness in all specimens as shown in Figure 4.18 c). This may permit to describe the residual stress as bi-axial in the wall specimens. This is

not the case for the 9mm_13mm specimen as the σ_Y is at -100 MPa in the centre. Nonetheless, it appears that the through-thickness residual stress cannot fully develop in this geometry. A similar observation was reported for the 6 mm PBF-LB/M/316L prisms (see 2.2.4).

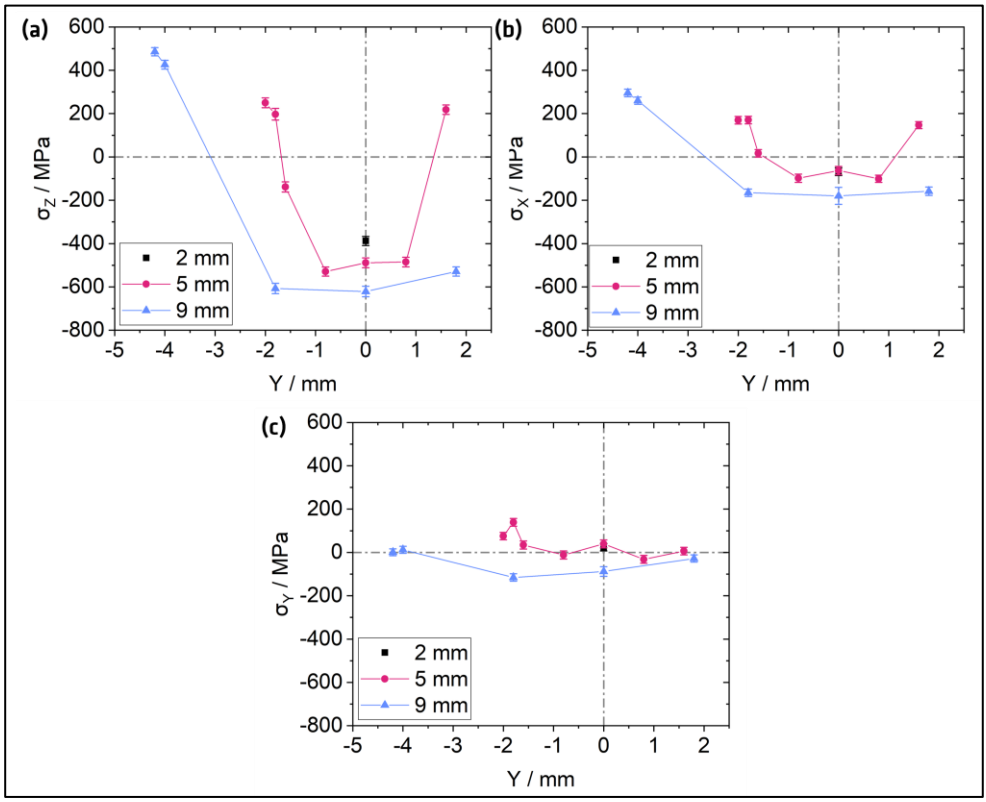

Figure 4.18: a) Through-thickness distribution of the σ_Z, b) the σ_X and c) the σ_Y in the specimens with a length of 13 mm.

The peak tensile residual stresses $\sigma_{X,PT}$, $\sigma_{Y,PT}$, and $\sigma_{Z,PT}$ and the peak compressive residual stresses $\sigma_{X,PC}$, $\sigma_{Y,PC}$, and $\sigma_{Z,PC}$ are summarized in Table 4.4.

Table 4.4: Changes of the peak residual stress through the thickness of the wall specimens. The stress error is < 25 MPa.

Specimen	$\sigma_{X,PT}$/ $\sigma_{X,PC}$ in MPa	$\sigma_{Y,PT}$/ $\sigma_{Y,PC}$ in MPa	$\sigma_{Z,PT}$/ $\sigma_{Z,PC}$ in MPa
2mm_13mm	n.a./-60	40/ n.a.	n.a./-390
5mm_13mm	170/-100	140/ -30	250/-530
9mm_13mm	295/-180	10/ -120	490/-620

The increase in thickness clearly leads to larger peak tensile and peak compressive residual stress. This effect is visualized in Figure 4.19 a) for the peak tensile residual stress ($\sigma_{X,Y,Z,PT}$) and in Figure 4.19 b) for the peak compressive residual stress ($\sigma_{X,Y,Z,PC}$).

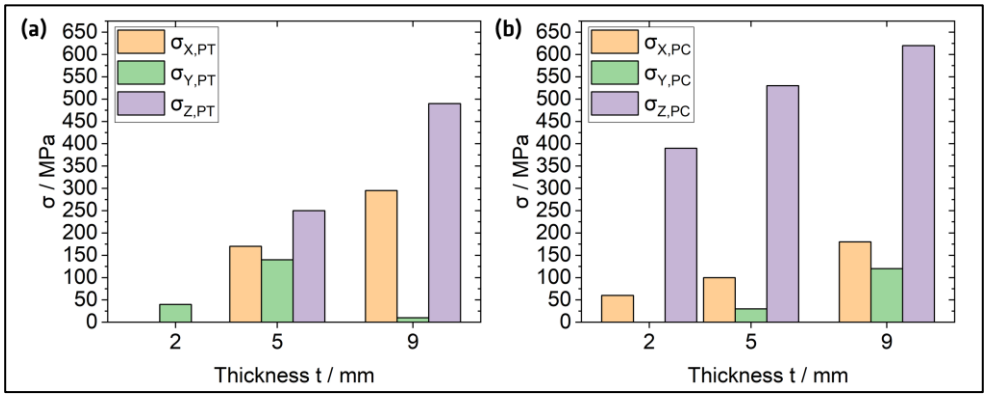

Figure 4.19: a) Bulk $\sigma_{X,PT}$, $\sigma_{Y,PT}$, $\sigma_{Z,PT}$ and b) $\sigma_{X,PC}$, $\sigma_{Y,PC}$, $\sigma_{Z,PC}$ as a function of the specimen thickness at a constant specimen length of 13 mm.

The σ_Z describes a U-shaped distribution in the 5mm_13mm and the 9mm_13mm specimens. This distribution was observed through the length of 316L L-shaped and Ni-alloy walls (see subchapter 2.2.4) but not through the thickness (insufficient point density). The distribution of the σ_Z through the thickness of a net-shape tensile specimen with a wall thickness of 4 mm was reported to describe a V-shape distribution with similar $\sigma_{Z,PC}$ at ~500 MPa [14]. However, the low number of measurement points was insufficient to verify whether already a U-shape distribution was present (see subchapter 2.2.4).

The σ_X describes in the 5mm_13mm and the 9mm_13mm specimens a U-shape distribution as well but the magnitudes are lower compared to the σ_Z (~45 %). As discussed above, the σ_Y remain low throughout the thickness. The residual stress gradients in MPa/mm of the 5mm_13mm and the 9mm_13mm specimens are summarized in Table 4.5.

Table 4.5: The residual stress gradients with the increase of the specimen thickness at a constant length of 13 mm.

Specimen	σ_X in MPa/mm	σ_Y in MPa/mm	σ_Z in MPa/mm
5mm_13mm	220	70	650
9mm_13mm	190	50	460

The gradients are influenced by the measurement point distribution. Nonetheless, it can be deduced that the residual stress gradients are larger in smaller structures. This effect is visualized in Figure 4.20.

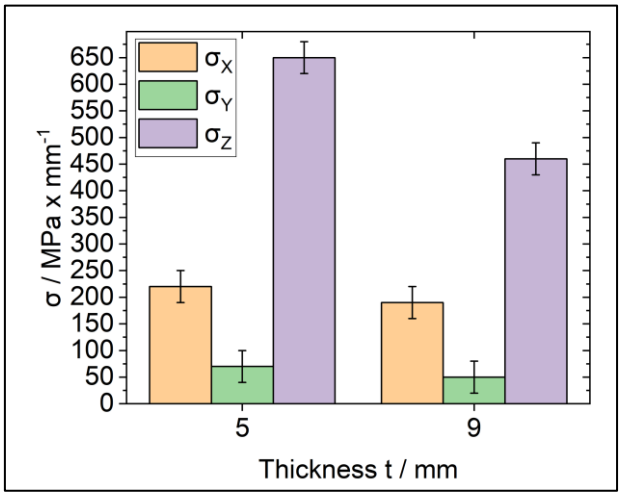

Figure 4.20: The bulk residual stress gradients through the thickness of the 5mm_13mm and the 9mm_13mm specimens.

To summarize, the analysis of the residual stress at the surface, the subsurface and the bulk of 2 mm, 5 mm and 9 mm thick specimens shows that the geometry has multiple effects:

- *A change in thickness from 2 mm to 9 mm increases the maximum surface residual stress values from less than 200 MPa to 250 MPa. The surface residual stress in the 9 mm thick specimen reaches a plateau over the build height within 8 mm from the cut surface, which is not the case for the other two specimens. The surface residual stress analysis, however, requires a detailed knowledge of the surface roughness. A change from 2 mm to 5 mm*

in thickness did not significantly change the surface residual stress. This was attributed to the ~two times higher average surface roughness. It is advised to couple the determination of surface residual stress using XRD with roughness measurements when e.g., analysing the influence of process parameters or for quality assurance.

- *The distribution of the subsurface residual stress strongly suggests that the tensile subsurface $\sigma_{Z,PT}$ (position, shape, and magnitude) also scales with the geometry. In the specimen with a thickness of 2 mm, the $\sigma_{Z,PT}$ position is at a depth of ~25 µm. A larger thickness results in a shift of the position of $\sigma_{Z,PT}$ to greater depths. A plateau forms in the specimens with a thickness of 5 mm and 9 mm at roughly 325 MPa and 350 MPa over a depth of 80 µm to 200 µm. The tensile subsurface σ_X is similar in all specimens up to 70 µm depth. Interestingly, while the σ_X decrease in the 2mm_13mm specimen an increase of the residual stress magnitudes is observed in the 5mm_13mm and the 9mm_13mm specimen. The distribution and magnitudes of the subsurface residual stress are assumed to be affected by the surface roughness and the local thermal gradients. The investigation of the subsurface residual stress in Ni-alloy PBF-LB/M tensile specimens with a thickness of 1 mm and 4 mm showed that the σ_Z increased at a smaller rate in the 1 mm thick specimen compared to the 4 mm thick specimen. However, at a depth of approximately 100 µm, the σ_Z were alike [191]. The roughness was comparable in both specimens. A similar result was found in this study although the thickness of the specimens was 5 mm and 9 mm.*

- *In the bulk the σ_Z and the σ_X describe U-shaped distributions through the thickness whereby the residual stress is tensile near the surface and compressive in the centre. These results agree with the findings summarized in 2.2.4. The largest tensile and compressive σ_Z are found in the 9mm_13mm specimen (490 MPa and -620 MPa). A change to larger thicknesses while maintaining the length and the height constant led to higher residual stress magnitudes. Interestingly, the σ_Z gradients close to the lateral surfaces are steeper in the specimen with a thickness of 5 mm compared to the specimen with a thickness of 9 mm. This difference is 30 MPa/mm in the σ_X and 210 MPa/mm in the σ_Z.*

- *The σ_Y remain low through the thickness. In the 9mm_13mm specimen the σ_Y reach -100 MPa. The presence of low σ_Y was also reported for 316L PBF-LB/M specimens with a thickness of 4 mm [14]. This allows to approximate the residual stress state as bi-axial for specimens with a thickness below*

9 mm. This information can be used when no d0 reference can be extracted from the specimen and to avoid specimen-to-specimen scatter (when using a twin specimen). This approach was taken for the calculation of the residual stress in DED-LB/M Ni-based walls and 316L walls with a thickness of 1.5 mm and 5 mm manufactured by DED-LB/M [189, 199]. This strategy was used in subchapter 4.5.2 to monitor the relaxation of the residual stress at the same measurement positions within the same specimens, thus unlocking the full non-destructive potential of ND as well as also reducing the necessary beamtime.

This analysis revealed the link between the geometry and the residual stress in PBF-LB/M/316L structures. The influence is observed at the surface, the subsurface and in the bulk of the specimens. It can be stated that increasing the dimensions of the specimen will increase the restraint and affect the heat inside the specimen. Assuming a single-track (one scan vector) wall manufactured by PBF-LB/M and at a distance from the build plate, the restraint to shrinkage will be directed by the underlying material. Since there is no material on the side of the weld beads, the weld bead can freely shrink in the direction of the thickness. Hence, the residual stress (σ_Y) will be low. The addition of scan vectors to increase the thickness of the wall will limit this contraction and thus influence the residual stress magnitudes. As described in the results of the subsurface residual stress, the restraint is also increased for the residual stress direction along the length. Hence, the triaxial residual stress will increase (see the calculation of the residual stress in 3.7). Also, it may be assumed that the heat inside the body will also change and thus increase the material volume that shrinks upon cooling to room temperature. The sequential scanning of a layer introduces the heat in a non-uniform way [121]. Hence, the material will cool in a heterogenous way leading to additional mismatch and higher residual stress.

Influence of the specimen length on the residual stress

The effect of the length on the surface and the subsurface σ_Z and σ_X is shown in Figure 4.21 a) and b) respectively. At the surface, the σ_Z in both specimens is broadly similar considering the error as shown in Figure 4.21 a). However, the σ_X is much higher in the 2mm_13mm specimen compared to the 2mm_26mm specimen (~40 MPa compared to values close to zero).

In the subsurface, the peak $\sigma_{Z,PT}$ is approximately three times larger in the 2mm_26mm specimen compared to the 2mm_13mm specimen. The σ_Z in the 2mm_13mm rapidly abates compared to the 2mm_26mm specimen. The σ_Z gradient appears similar in the two specimens once the peak position is reached

(~10 µm and ~30 µm). The length of the specimen affected the peak position, which agrees well with the findings in 4.3.1. The $\sigma_{Z,PT}$ is found closer to the surface in the 2mm_13mm specimen compared to the 2mm_26mm specimen. Interestingly, the σ_X distribution is very similar in both specimens as shown in Figure 4.21 b). When increasing the thickness, the σ_X increased in the 5mm_13mm and the 9mm_13mm specimen. This is not the case when changing the length of the 2mm_13mm specimen as shown in Figure 4.21 b).

The approximately three times higher peak $\sigma_{Z,PT}$ when increasing the length from 13 mm to 26 mm substantiates the findings in subchapter 4.3.1. The geometry of the specimen directly influences the magnitude of the subsurface σ_Z. However, the change in length has no effect on the subsurface σ_X. Hence, it may be assumed that the subsurface σ_X magnitude is governed by the thickness and not the length.

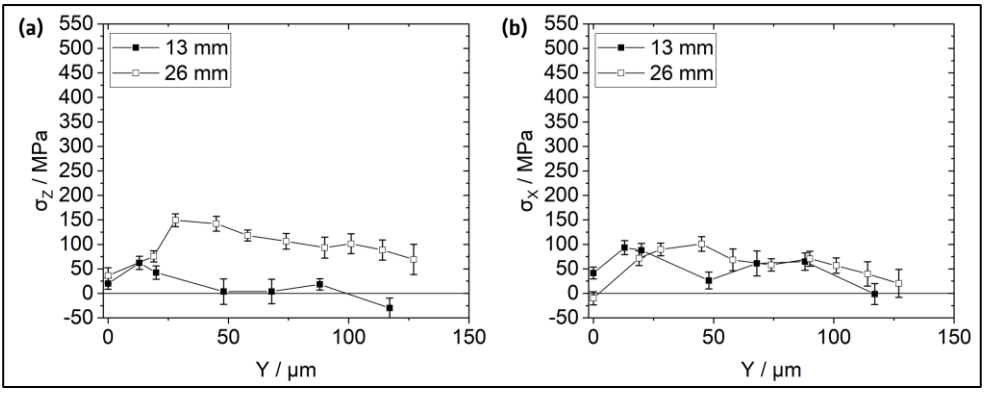

Figure 4.21: a) σ_Z distribution and b) σ_X distribution in the 2mm_13mm and 2mm_26mm specimens. See Figure 3.15 for more details on the measurement positions.

The influence of the length on the σ_Z in the 5mm_13mm and the 5mm_26mm specimens is shown in Figure 4.22 a). The σ_Z magnitudes reach approximately 490 MPa to 530 MPa (tensile) close to the surface and -400 MPa to -440 MPa (compressive) in the centre. The compressive residual stress is larger at the centre of the short specimen compared to the long specimen. Overall, a U-type distribution is observed. The compressive plateau is longer by ~45 % in the 26 mm long specimen. Steeper σ_Z gradients are observed in the 5mm_13mm specimen compared to the 5mm_26mm specimen. This agrees well with the findings on the through-thickness residual stress distributions (see 4.3.1). The magnitudes and distributions of the σ_Z of the 9mm_13mm and the 9mm_26mm specimens are shown in Figure 4.22 b). The $\sigma_{Z,PT}$ is around 540 MPa for both specimens and the

$\sigma_{Z,PC}$ is -630 MPa and -500 MPa for the short and the long specimen respectively. The distribution of the σ_Z is similar to the specimens with a thickness of 5 mm. Two observations resulting from the analysis on the 5 mm thick specimens are reinforced namely: larger compressive values in the shorter specimen and steeper σ_Z gradients in the shorter specimen. Interestingly, the distribution in the 9mm_13mm does not describe a plateau.

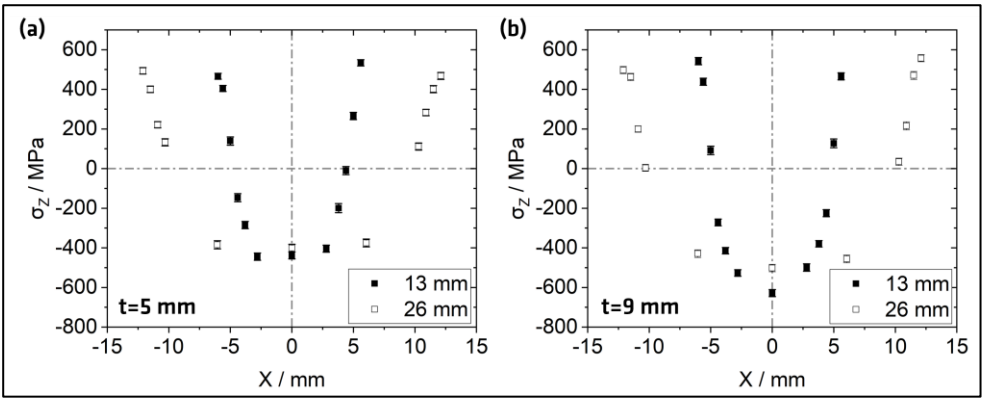

Figure 4.22: a) Influence of length on the bulk σ_Z in the 5mm_13mm and 5mm_26mm specimens, and b) in the 9mm_13mm and the 9mm_26mm specimens.

The σ_Z gradients were calculated using the measurement points between 1.5 mm and 2.7 mm from the surface for all specimens. The values in Table 4.6 show that increasing the length of the specimen while keeping the thickness constant at 5 mm reduces the σ_Z gradient by approximately 37 %. This reduction is around 12 % in the specimens with a thickness of 9 mm.

Table 4.6: σ_Z gradients in MPa/mm in the specimens with a thickness (t) of 5 mm and 9 mm showing the influence of a change in length.

t in mm	13 mm	26 mm
5	370 ± 24	232 ± 14
9	422 ± 5	373 ± 14

The influence of the length on the σ_X in the 5mm_13mm and the 5mm_26mm specimens is shown in Figure 4.23 a). The σ_X magnitudes reach approximately

60 MPa (tensile) close to the surface and -80 MPa (compressive) in the centre. Larger σ_X is found in the shorter specimen which agrees well with the previous results. The σ_X remain mostly compressive in the 5mm_26mm specimen. The σ_X tend to decrease towards the centre and increase slightly towards the surface. According to the boundary conditions the σ_X should be zero at the surface. The σ_X evolves in a range of approximately 140 MPa and 100 MPa (absolute values) for the 5mm_13mm and the 9mm_26mm specimens respectively. The small discrepancy with regards to the boundary conditions i.e., $\sigma_X \neq 0$ MPa at the surface may be attributed to either the d0 (shift of the profile) or the combination of a small gauge volume with possible variations of the microstructure near the surface. The change in thickness seems to heavily influence the σ_X distributions in the 9mm_13mm and the 9mm_26mm specimens as shown in Figure 4.23 b). The σ_X is mainly compressive and decreases towards the surfaces to fulfil the free surface stress boundary. A V-shape is observed, which scales with the increase in length. The peak $\sigma_{X,PT}$, however, remains at a similar level for both specimens at approximately -200 MPa.

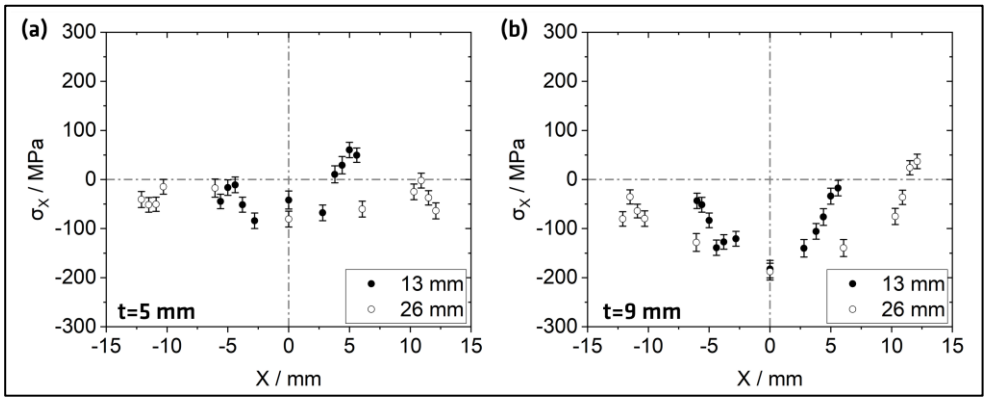

Figure 4.23: a) Influence of the length on the bulk σ_X in the 5mm_13mm and 5mm_26mm specimens, and b) in the 9mm_13mm and 9mm_26mm.

The σ_X gradients were calculated using the measurement points between 1.5 mm and 2.7 mm from the surface for all specimens. The values are summarized in Table 4.7. The σ_X gradients are larger in the shorter specimen with a thickness of 5 mm. However, since the values are scattered a distinct trend is not derivable (indicated by positive and negative gradients). The σ_X gradients are similar in the specimens with a thickness of 9 mm.

Table 4.7: σ_X in MPa/mm gradients in the specimens with a thickness of 5 mm and 9 mm showing the influence of a change in length.

t in mm	13 mm	26 mm
5	-35 ± 26	17 ± 39
9	62 ± 22	60 ± 28

The influence of the length on the σ_Y in the 5mm_13mm and the 5mm_26mm specimens is shown in Figure 4.24 a). No distinct trend of the distribution of the residual stress is observed, which is partially owed to the much lower magnitudes. However, this result agrees with the through thickness bulk σ_Y shown in Figure 4.18 c). The σ_Y do not form in the specimens with a thickness of 5 mm along the length of the specimen. This is however not the case for the 9mm_13mm and the 9mm_26mm specimens. As no free surface boundary applies for this residual stress direction towards the surfaces, a strong increase up to approximately 130 MPa is observed. The σ_Y distributes as U-shape in the 9mm_13mm specimen. In the 9mm_26mm specimen, the σ_Y first reduces and then reaches values close to zero MPa. A W-shaped distribution is observed.

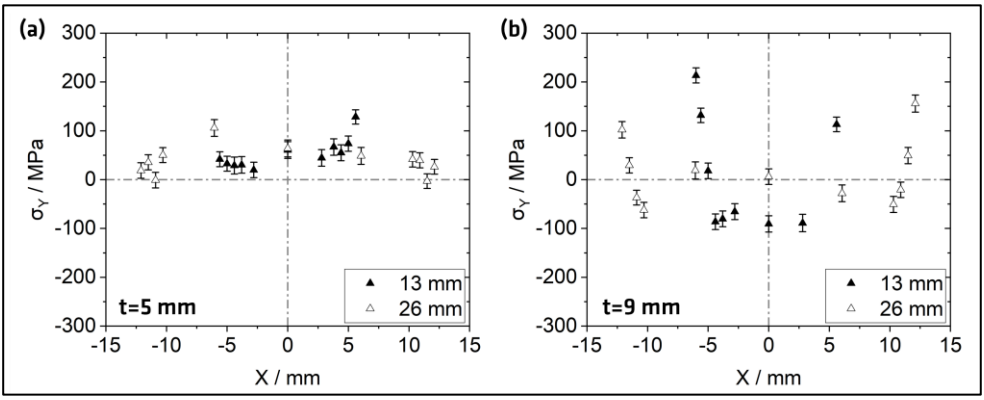

Figure 4.24: a) Influence of the length on the bulk σ_Y in the 5mm_13mm and 5mm_26mm specimens, and b) in the 9mm_13mm and 9mm_26mm.

The σ_Y gradients were calculated using the measurement points between 1.5 mm and 2.7 mm from the surface for all specimens. The values are summarized in Table 4.8. As mentioned before the σ_Y remain low in the specimens with a thickness of

5 mm, which results in small gradients. In the specimens with a thickness of 9 mm, the σ_Y are larger by ~35 % in the short specimen compared to the long specimen.

Table 4.8: σ_Y gradients in MPa/mm in the specimens with a thickness of 9 mm and length of 13 mm and 26 mm.

t in mm	13 mm	26 mm
5	19 ± 17	14 ± 17
9	110 ± 56	80 ± 30

The gauge volume in this experiment was 2 mm x 0.6 mm x 0.6 mm (shape of a matchstick, see Figure 3.17 a) for the acquisition of the lattice spacing in the X- and the Y-direction. However, the acquisition of the lattice spacing in the Z-direction was performed with a gauge volume sized 2 mm x 2 mm x 0.6 mm (see Figure 3.17 b). This means that for the σ_Z, an average lattice spacing of 2.82 mm (diagonal of the gauge volume) at the centre of the specimen (thickness approximately 5 mm) is taken. It is expected that the gradient of the σ_Z (see Figure 4.22) is partially averaged, which would lead to lower magnitudes. However, in the X-direction and the Y-direction the gauge volume diagonal is roughly 1 mm. Therefore, it is assumed that the gauge volume did correctly capture the values along the centre of the specimen. From the σ_X and the σ_Y in Figure 4.22 c) and d) it is possible to deduce that there is no strong gradient along the length.

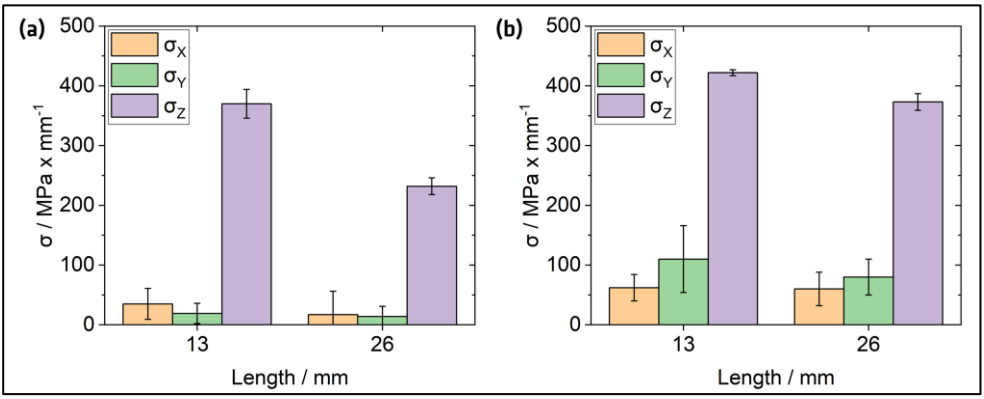

Figure 4.25: a) Residual stress gradients as a function of the specimen length in the specimens with a thickness of 5 mm and b) with a thickness of 9 mm.

To summarize, the analysis of the residual stress at the subsurface and the bulk of 2 mm, 5 mm and 9 mm thick specimens with varying lengths of 13 mm and 26 mm has shown the following results:

- *A greater length affected the subsurface $\sigma_{Z,PT}$ (magnitude and distribution) similar to an increase in thickness. The position of the $\sigma_{Z,PT}$ was at a greater depth and had a larger magnitude in the longer specimen. The σ_X and its distribution remained mostly unaffected.*

- *In the bulk, the $\sigma_{Z,PT}$ and the $\sigma_{Z,PC}$ were higher in the shorter specimen. The values were limited by the material's yield strength, which corresponds well to the models describing the residual stress formation in PBF-LB/M [11]. However, these models describe how the residual stress attains these magnitudes in the last layer (on the top of the specimen). This study reports on the lateral residual stress. So, despite the somehow stress relieving factor of adding layers (described in [11, 105]) the lateral residual stress still reach the level of the material's yield strength. Interestingly, the σ_Z did not reach the yield strength close to the surface of the thickness but close to the surface of the length in the 5mm_13mm specimen (compare Figure 4.18 a to Figure 4.22 a). In the 9mm_13mm specimen, close to both the surface of the thickness and the length the yield strength is reached. Therefore, it seems that when a dimension exceeds 9 mm the tensile residual stress near the surface will reach the material's yield strength (combined with the results of the through-thickness residual stress in 4.3.1). It is noted that this measure may be influenced by the process parameters.*

- *Besides the magnitudes of the σ_Z also the distribution was affected by the geometry. The σ_Z gradients were around 230-420 MPa/mm in the PBF-LB/M/316L specimens. These values are much higher compared to e.g. ~150 MPa/mm as reported in [119]. This may be resulting from the different scanning strategies and the geometries of the specimens. However, it may also be the case that the use of a tailored gauge volume allowed to observe these gradients. The set-up used in this study permitted to determine the residual stress with a spatial resolution of up to 0.6 mm. In comparison the gauge volumes generally used have a cube edge length of 1 to 2 mm [14, 99, 116]. This result highlights the necessity to choose gauge volumes that are able to capture the near surface residual stress gradients for a better comparison with simulation models.*

- *The increase of one dimension reduces the stress gradients close to the surface and changes the length of the plateau described by the compressive*

residual stress. This can be attributed to the thermal gradients during the process. Smaller cooling rates were observed in a bulky structure compared to a wall structure as reported in [5]. In PBF-LB/M the limited contact of the surface to the surrounding powder particles limits the heat flow from the surface to the powder bed [200]. When increasing the part dimensions, the ratio of the surface divided by the area decreases e.g., from 55 % to 30 % for the 5mm_13mm to the 9mm_26mm specimen respectively. The higher the ratio the more the heat is conducted through the specimen towards the build plate. The change of the geometry therefore not only changes the heat inside the structure but also how the thermal gradients align. This may affect how the residual stress distributes. From welding it is known that increasing the heated volume results in a greater range in which stresses are generated. The residual stress magnitudes remain the same [107]. This seems to be the similar case in PBF-LB/M. In the 9 mm thick specimens, the magnitudes are similar, but the gradients are less steep in the longer specimen.

- *The σ_X has generally lower magnitudes compared to the σ_Z. While an increase in the thickness leads to larger σ_X, the length has no apparent influence (magnitudes and gradients are mostly in the error bar). The σ_Y has as well lower magnitudes compared to the σ_Z. A change in length with a thickness of 5 mm had minor effects (values are mostly in the error bar). However, at a thickness of 9 mm the shorter specimen had larger σ_Y gradients and magnitudes. This corresponds to the observations made in subchapter 4.3.1. The σ_X and the σ_Y were found to have similar peak magnitudes in 45 mm, 70 mm, and 80 mm Ø disc shaped PBF-LB/M/316L specimens while still attached to the build plate [99]. This may be explained by the similar vector length along each axis. The in-plane residual stress was reported to be mainly influenced by the restrained shrinkage and by the geometry of the structure [116]. The results presented herein are based on the lateral residual stress whereas most of the literature analyses the surface residual stress of the last layer of the build (perpendicular to the lateral surfaces). Hence, the results include the stress relieving effect of adding additional layers. Nonetheless, the σ_X are larger compared to the σ_Y which validates the statement that longer scanning vectors lead to larger residual stress. The underlying concept is that shorter scan vectors reduce the temperature gradient generated as the previous weld bead has still a higher remnant heat as described in [64]. Overall, the findings correspond well with models described in the literature although the study focussed on residual stress on the lateral surfaces and within the structures.*

- *The model describing the formation of the residual stress in [11] does not explain the presence of the tensile residual stress in the lateral surfaces. The residual stress in the bulk is mostly compressive based on the results in 4.3.1. Hence, one could attribute the tensile surface residual stress as a reaction to fulfil the equilibrium condition. An alternative description of the formation of the residual stress based on DED-LB/M was given in [189]. The distributions of the residual stress in thin and bulky DED-LB/M 316L structures were similar to the results in 4.3.1. The magnitudes were, however, lower. The presence of the tensile residual stress at the surface and the compressive residual stress in the bulk was explained with the dissimilar cooling behaviour of the surface and the bulk. A simplified explanation is as follows: The cooling rate is lower at the surface compared to the bulk. This effect decreases with time. Once the surface and the core reach the room temperature a difference between the length of the core and the length of the surface remains. Thus, the surface residual stress remains tensile, and the bulk residual stress remains compressive. Following this description, a reduction of the thickness leads to lower residual stress, as the difference in cooling rate of the surface and the bulk is smaller. This again corresponds well to the findings in this chapter.*

Additionally, the transferability of the results from small walls to larger structures need to be addressed. The goal is to verify whether small structures (witness specimens) can be used to give a representative value of the residual stress in lager structures.

4.3.2 Influence of geometrical change on the residual stress

The surface σ_Z along with the height of a specimen sized 112 mm x 20 mm x 13 mm (height x length x thickness) is compared against the σ_Z for the 9mm_13mm and the 9mm_26mm specimens as shown Figure 4.26 a). The manufacturing parameters are identical for all three specimens. Based on Figure 4.26 a), the surface residual stress is at a comparable level between the small wall and the large prism. Furthermore, the analysis shows that the σ_Z reaches a plateau as well in the prism. Thus, this result is a first hint that the surface σ_Z remains largely unaffected by the size of the specimen, when surpassing a certain size threshold. The plateau residual stress is reached at the first measurement position (Z = 8 mm) from the cut surface. This value agrees well with the observation that a thickness of 9 mm needs to be reached to observe the development of the σ_Y (distribution and larger magnitudes, see Figure 4.24). The results reported in the literature are often based on structures with build heights around 10 mm to 15 mm e.g. [64, 126, 146, 152]. These structures were built to perform process optimization. However, the results

of this study show that the residual stress in PBF-LB/M requires ~10 mm to develop. The comparison of the lateral surface residual stress in the walls with the large specimen shows that the residual stress is similar. Therefore, it is advised to build larger specimens to ensure the transferability of the results between small and large structures.

In the bulk, the σ_Z ranges from 300 MPa near the surface to -500 MPa at the centre. These values are smaller compared to the σ_Z range in the 9mm_13mm specimen. The difference in range could be due to the different gauge volume sizes i.e. different regions are probed. In fact, the gauge volume for the characterization of the small walls permitted to obtain a much better spatial resolution of the residual stress gradient toward the surfaces. As a peak of the tensile residual stress is observed in the subsurface (see Figure 4.16), the lower σ_Z range might be caused by a greater averaging of the subsurface peak residual stress in the characterization of the large specimen compared to the small walls. However, the $\sigma_{Z,PC}$ at the centre of the large specimen corresponds well to the $\sigma_{Z,PC}$ found in the walls (see Figure 4.22 b).

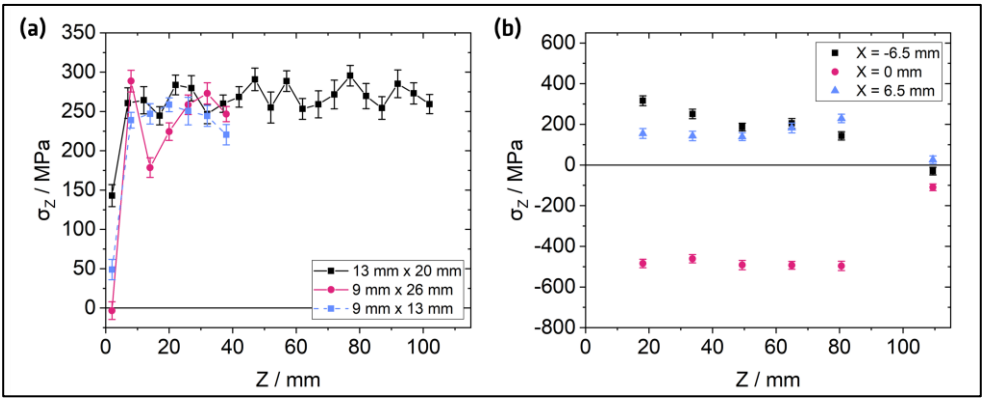

Figure 4.26: a) Surface σ_Z in the large PBF-LB/M/316L specimen compared to the small walls with 9 mm thickness, and b) evolution of the bulk σ_Z with the height at the centre (Y = 0 mm) of the large specimen. See Figure 3.20 for the measurement positions in the specimen.

The σ_X and the σ_Y along with the build height in the large specimen are shown in Figure 4.27. As observed in subsection 4.3.1, the bulk σ_X and σ_Y are lower compared to the σ_Z. For Z = 50 mm, the σ_X is compressive at around -100 MPa to -150 MPa in the centre. These values are slightly smaller (-200 MPa) compared to the centre of the 9 mm thick specimen (see Figure 4.23 b). The σ_X is mostly compressive, which agrees well with the observations made on the 9 mm thick specimen. The σ_Y is

mostly tensile, which also conforms with the previous results (see W-shape in the 9mm_26mm specimen in Figure 4.24 b).

The σ_X at the top of the specimen (Z = 112 mm) is tensile at the centre. This is an agreement with findings reported in the literature that the residual stress is tensile in the final layers [129, 201, 202]. Furthermore, the last layer was manufactured with scan vectors along the length of the specimen (in X). This may explain the larger σ_X (longer scan vector length) compared to the σ_Y (shorter scan vector length) in absolute values [64]. The distribution of the bulk residual stress along the build height is asymmetric. This was also observed in the wall specimens or results reported in the literature [119]. This can be explained with the convolution of the scanning strategy and related thermal history as further described in the chapter 4.4.

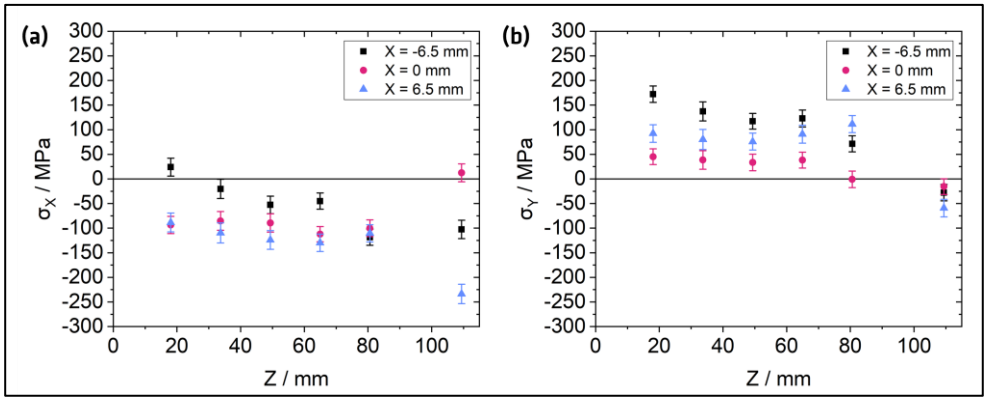

Figure 4.27: a) Evolution of the bulk σ_X and b) the σ_Y with the height at the centre (Y = 0 mm) of the large specimen.

The σ_X at X= -6.5 mm and 6.5 mm were expected to be closer to zero stress to fulfil the boundary conditions. This is not the case which may be related to an erroneous d0. The approach to use d0 values led to residual stress distributions broadly fulfilling the boundary conditions in the subchapters 4.3.1. Perhaps, the larger height led to a change of the chemical and phase distribution in the last layers which may have affected the d0. A change of the chemical composition was modelled in [31] (see subchapter 2.1.2).

The comparison of the large specimen with the smaller specimen detailed similar distributions and magnitudes of the surface and the bulk residual stress. Hence, these results show that small structures represent the residual stress in a much larger structure. The height should at least be twice the length needed for the

residual stress to build up and reach a plateau i.e. approximately 30-40 mm. This statement assumes that the process parameters are identical. The chapter 4.5 will further substantiate this observation with more detailed residual stress distributions in large specimens. While simplified models may explain the way the residual stress forms and distributes in different geometries, the PBF-LB/M process is too complex to fully decouple effects related to the restrained shrinkage and the thermal gradients. Nonetheless, a clear correlation between the geometry and the residual stress was found. To further understand the residual stress in PBF-LB/M, the next subchapter will focus on the influence of varying process parameters using constant specimen geometries.

4.4 Influence of selected process parameters on the residual stress

This chapter details the link between the heat accumulation and the formation of the residual stress in the PBF-LB/M/316L. The influence of the ILT and the scanning velocity on the residual stress is detailed in subchapter 4.4.1. The results are then correlated to the thermal history of the specimens using thermographic data from in-situ monitoring in subchapter 4.4.2. The analysis of the residual stress using the thermographic data was published in [181].

4.4.1 Influence of the ILT and the scanning velocity on the residual stress

Surface residual stress

The influence of the ILT on the surface residual stress is shown in Figure 4.28. The σ_Z reach values up to 375 MPa (75 % of the yield strength for PBF-LB/M/316L [49]). The largest surface σ_Z is observed in the specimen manufactured with an ILT of 18 s. The increase of the ILT reduces the surface σ_Z (see Figure 4.28 a). When changing the ILT from 18 s to 65 s, the $\sigma_{Z,PT}$ decrease by 100 MPa. The $\sigma_{Z,PT}$ in the Tower_65s (~240 MPa) is comparable to the $\sigma_{Z,PT}$ in the Tower_116s.

The σ_Y is much lower compared to the σ_Z as shown in Figure 4.28 b). However, the σ_Y reaches values up to 225 MPa (55 % of the yield strength for PBF-LB/M/316L [49]). These values are much higher than the surface residual stress magnitudes of a PBF-LB/M/316L part manufactured using the helix scan strategy [116] but comparable with the values from specimens built with various scanning strategies as reported in [117, 145]. The surface residual stress tends to decrease near the free surfaces. The distribution is largely symmetrical except for one measurement point in Tower_116s (see Figure 4.28 a).

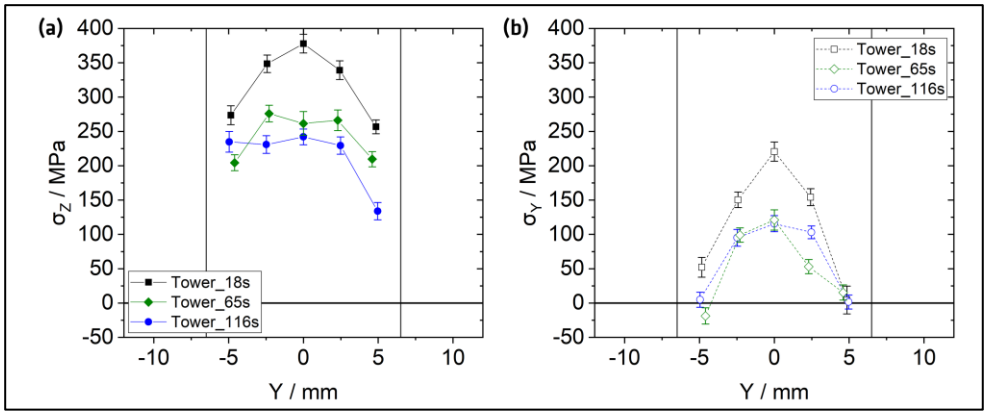

Figure 4.28: a) Influence of the ILT on the σ_Z, and b) on the σ_X on surface S2 (see Figure 3.16 a). Vertical lines represent the edges of the specimen.

The influence of the scanning velocity on the surface residual stress is shown in Figure 4.29. This analysis was performed on the surface defined by the length of the specimen (20 mm). The comparison of the Tower_65s and the Tower_116s substantiates the observation that the increase in ILT has only a minor effect beyond a value of 65 s (see Figure 4.29 a). However, increasing the scanning velocity heavily reduces the surface residual stress magnitudes as the $\sigma_{Z,PT}$ in the Tower_116s_HV decreases to 85 MPa (see Figure 4.29 a). The σ_X in the Tower_116s_HV is as well lower than the σ_X in the Tower_116s as shown in Figure 4.29 b). It is argued that a low scanning velocity leads to a larger volume of heated material and therefore reduces the thermal gradients and the resulting thermal stress [64]. The melt pool sizes of the Tower_116s and the Tower_116s_HV were analysed and reported in [157]. Indeed, larger melt pools were found in the Tower_116s compared to the Tower_116s_HV (from 300 µm to 200 µm). However, the surface residual stress is lower in Tower_116s_HV. This corresponds with results showing that an increase in scanning velocity reduced the surface residual stress in PBF-LB/M/316L specimens [109]. It can be argued that a larger melt pool leads to a larger restrained volume upon cooling which increases the residual stress as discussed in [203].

The surface residual stress *is higher in the specimen manufactured with a short ILT by approximately 100 MPa. The surface residual stress decreases with longer ILT. The magnitudes agree well with the surface residual stress shown in 4.3. The surface*

residual stress abates in the specimen manufactured at high velocity, which may be related to the smaller melt pools and therefore less restrained shrinkage.

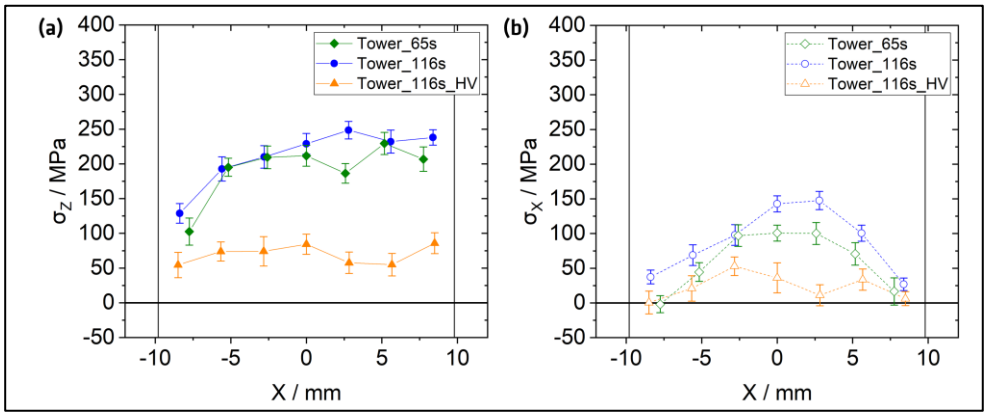

Figure 4.29: a) Influence of the scanning velocity on the σ_Z, and b) on the σ_X on surface S1 (see Figure 3.16 a). The Tower_65s data is plotted for statistical reasons. Vertical lines represent the edges of the specimen.

Bulk residual stress

The σ_X, the σ_Y and the σ_Z along the build height of the specimen (X=Y= 0 mm) are shown in Figure 4.30. The residual stress at the centre of the PBF-LB/M specimens is mostly compressive. The residual stress profiles are similar, and the stress values reach a plateau at about 10-15 mm of the WEDM cut surfaces. The σ_Z of all specimens reach a plateau between -400 MPa and -590 MPa. The $\sigma_{Z,PC}$ is -590 MPa and close to the compressive yield strength of PBF-LB/M/316L, as reported in [48]. Following the stress boundary conditions, the σ_Z decrease towards the free surfaces. The σ_X and the σ_Y are much lower compared to the σ_Z. The values are around -150 ± 10 MPa and -70 ± 30 MPa at the plateau respectively. These values are about 14-30% of the yield strength reported in [49].

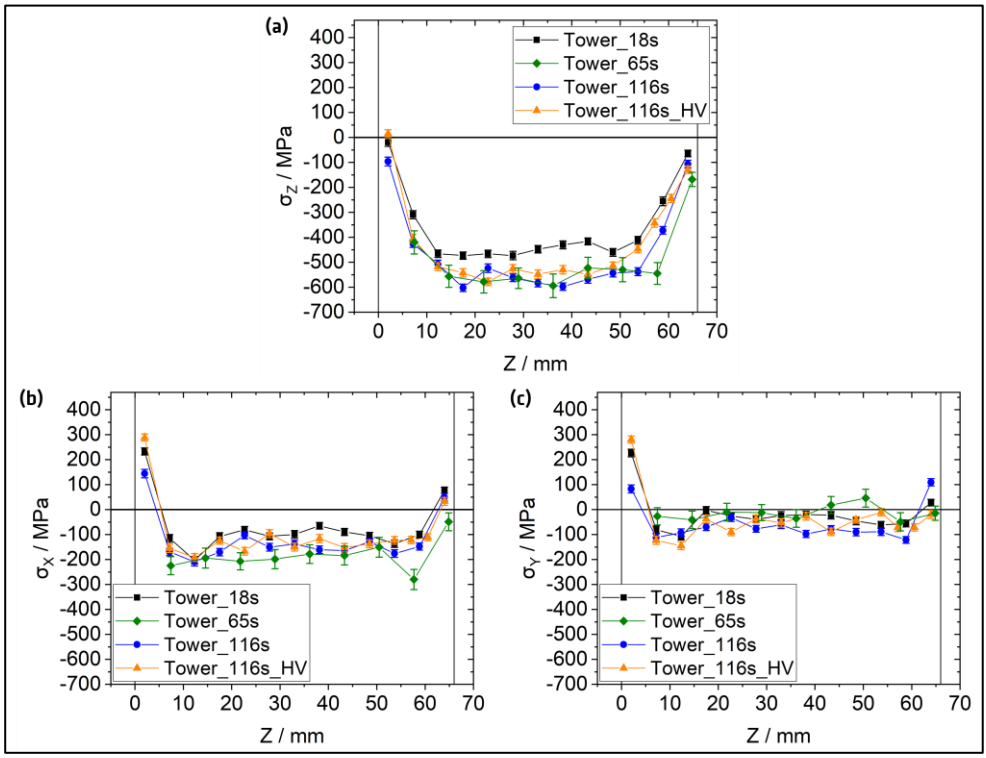

Figure 4.30: a) σ_Z, b) σ_X, and c) σ_Y along the height of the Tower specimens at X=Y= 0 mm. See Figure 3.21 b) and Figure 3.22 b) for the measurement positions.

The residual stress gradients towards the cut surfaces are very steep. While steep gradients were observed towards the as-built surfaces of the wall specimens (see subchapter 4.3), the stress gradients shown in Figure 4.30 are related to the WEDM

surfaces. The shift from compressive to tensile residual stress near the cut surfaces may be the result of a stress redistribution due to the relaxation of the residual stress.

The σ_Z, the σ_X, and the σ_Y were further analysed along the build direction at multiple positions in the bulk of the Tower_65s in Figure 4.31. The σ_Z is approximately 300 MPa near the surface and -600 MPa close to the centre of the specimen (X = 4.23 mm) as shown in Figure 4.31 a). The tensile σ_Z is lower compared to the values found near the surface shown in Figure 4.22. This can be attributed to the smearing of the steep residual stress gradients due to the larger gauge volume employed for this investigation. A relaxation of the residual stress due to the thermal heat treatment is not the cause of the lower residual stress values, as will be shown in subchapter 4.5.1. The σ_Z reaches a plateau at about 12 mm from the cut surface. The σ_X is mostly compressive and lies between 0 MPa and -200 MPa. The $\sigma_{X,PC}$ at -200 MPa corresponds well to the findings in the walls (see Figure 4.23). The σ_Y reaches values between approximately 50 MPa and -120 MPa. For all residual stress directions, a degree of asymmetry is observed when comparing the measurement points near the surfaces i.e. X = ± 8.46 mm to the values at the centre. This is an indication of a bending moment in the specimen resulting from the manufacturing on the build plate. During the manufacturing, the residual stress in the build plate becomes compressive while being mostly tensile in the specimen. This leads to a bending moment inside the specimen as described in [11, 129, 204]. The redistribution and relaxation of the residual stress as detailed in the model described in [11] has been extensively observed in specimens manufactured horizontally [14, 81, 119]. This is, however, less the case for vertical specimens [14, 119], which explains the large residual stress found in the Tower specimens.

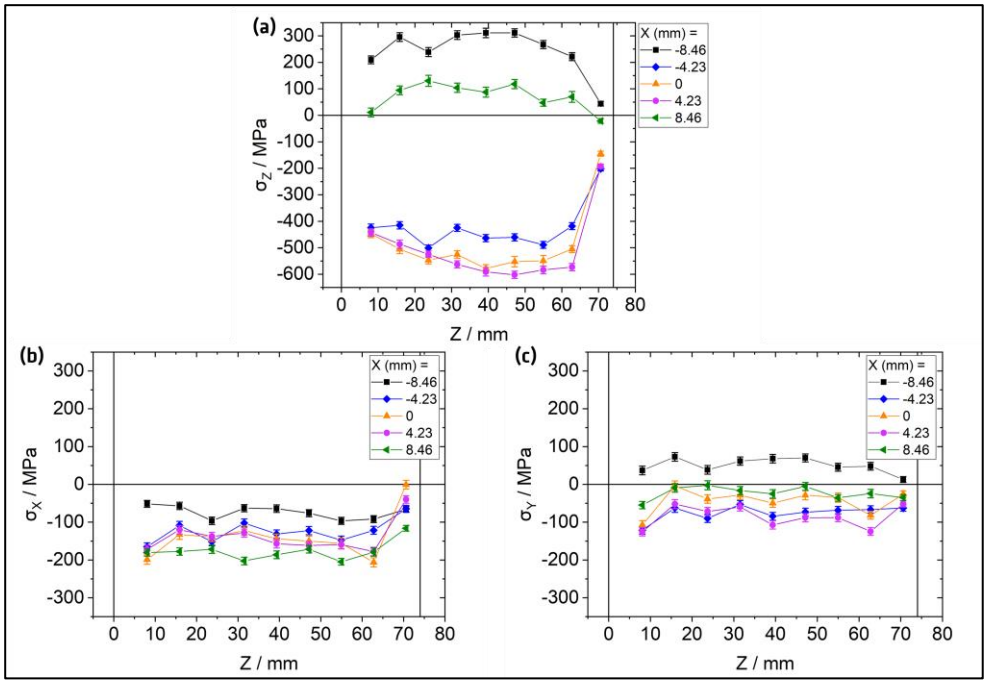

Figure 4.31: Distribution of the σ_Z, b) the σ_X, and c) the σ_Y along the build height Z of the Tower_65s specimen. See Figure 3.21 b) for the measurement positions.

The lowest bulk σ_Z was observed in the Tower_18s with a peak compressive magnitude of -470 MPa (see Figure 4.30 a). For all other specimens, this value is around -550 ± 10 MPa which is an increase by ~15 %. The results indicate that longer ILT lead to larger bulk compressive residual stress as shown in Figure 4.32. This effect is less discernible in the σ_X and the σ_Y due to the lower magnitudes. The higher scanning velocity led to much lower surface residual stress but the change in bulk residual stress is within the boundaries for the Tower_116s_HV and the Tower_116s.

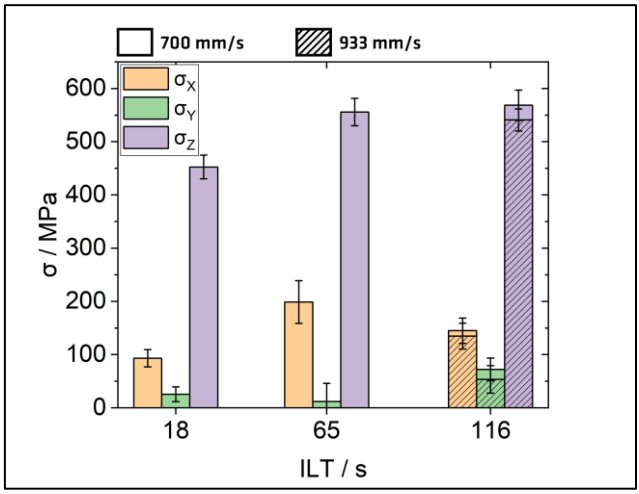

Figure 4.32: Influence of the ILT and the scanning velocity on the average residual stress in the Tower specimens. The average residual stress was calculated using the values 15 mm from the cut surfaces (plateau of the residual stress).

It appears that the change in process parameters has a different influence on the surface and the bulk residual stress. Following the summary of the literature on the influence of process parameters in subchapter 2.2.5 it is possible to assume that the ILT leads to a larger heat accumulation in the specimens. This may explain why the bulk residual stress is smaller in the Tower_18s compared to the other specimens manufactured with longer ILT. However, to understand this effect as well as the contradicting surface and bulk results in-situ process monitoring is necessary. This is the subject of the following chapter.

4.4.2 Thermal history of the manufacturing and its influence on the residual stress

The temperature evolution at the centre of the specimen is shown in Figure 4.33. The differences in the temperature evolution between Tower_18s, Tower_116s and Tower_116s_HV are clearly visible in the first 2.5 s following the passing of the laser spot (X, Y = 0 mm, and Z = 40 mm). The cooling rate is reduced in the Tower_18s compared to Tower_116s and Tower_116s_HV. This is an indication for a greater heat accumulation when using a short ILT. It is noted that the temperature in Tower_18s appears higher. In all cases, the material is melted and therefore, the temperature should be the same. However, this temperature is not properly captured by the in-situ monitoring and through the smoothing algorithm, a different maximum temperature is then obtained. Nonetheless, a measured temperature of

approximately 550 °C, 235 °C, 170 °C and 140 °C was reached for the Tower_18s, the Tower_65s, the Tower_116s and the Tower_116s_HV in the last layers (Z = 114.5 mm) as reported in [140].

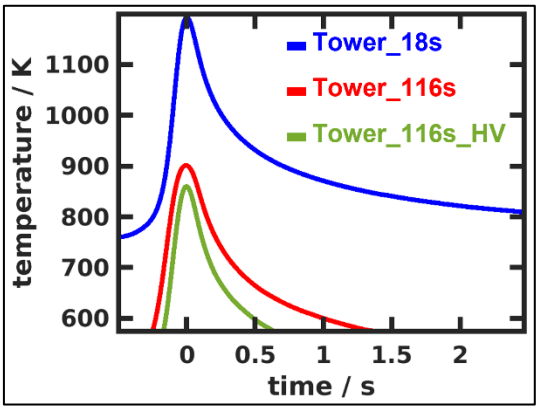

Figure 4.33: a) In-situ process monitoring data showing the temperature distribution during the manufacturing of a layer, b) temperature evolution at the measurement position, adapted from [181].

The higher temperature in Tower_18s may have acted as stress-relieve treatment and thus reduced the residual stress magnitudes compared to Tower_116s. During this type of heat treatment, the residual stress is affected by the heating, the soaking time at temperature and finally the cooling phase [205]. When heating, the temperature dependent yield strength reduces. If the stress is as high as the yield strength, a relaxation occurs through plastic deformation (see subchapter 2.3.2). Consequently, the stress distribution and magnitude change within the part. As an indication, the yield strength for PBF-LB/M/316L was about 190 MPa at a temperature around 520 °C, as reported in [170]. The temperatures during the manufacturing were much lower (see Figure 4.33 a) in specimen Tower_116s compared to specimen Tower_18s. Therefore, the stress in specimen Tower_116s might have achieved higher magnitudes compared to Tower_18s. Since Tower_18s was kept at high temperatures during manufacturing (around 12 hours), recovery can occur which reduces the stress [166]. The recovery of the material reduces the inelastic strains in the material through enhanced dislocation mobility and diffusion processes (see 2.3.2). Thus, it can be assumed that the stress in specimen Tower_18s was more prone to relax throughout the manufacturing compared to Tower_116s.

The ILT can be compared to a certain degree with other parameters that lead to higher temperatures in the specimens. These approaches increase the temperature

from which the part cools down homogenously but also reduce the TGM (see subchapter 2.2.3). A base-plate heating of 200 °C was reported to reduce residual stress in PBF-LB/M/316L by approximately 8 to 17 % according to [139]. A similar effect was also reported for PBF-LB/M of Ti-6Al-4V in [137]. The residual stress in Hastelloy-X (Ni-based superalloy) processed by PBF-LB/M and electron beam melting (EBM) were compared in [206]. It was reported that the preheating temperature of 750 °C in the EBM process was the main cause for the very low residual stress compared to the PBF-LB/M processed counterpart [206]. Similarly, the short ILT increases the temperature of the Tower_18s during the manufacturing. This leads to lower thermal gradients and upon reaching room temperature to lower residual stress.

Influence of the scanning velocity

The greater scanning velocity used to manufacture Tower_116s_HV resulted in a lower heat accumulation and higher cooling rates (see Figure 4.33). While the surface residual stress was the lowest (see subchapter 4.4.1), the bulk σ_Z are comparable to the other specimens. Additionally, the surface residual stress was the highest in the Tower_18s although the bulk residual stress was the lowest. As mentioned before, the bulk residual stress and surface residual stress are in contradiction. Since the scanning strategy was found to have a large influence on the residual stress [11, 119, 121, 123] a possible explanation may lay in the sequence of the scanning strategy and the resulting thermal history (see Figure 4.34 a).

The sequence of the scan vectors results in varying average temperatures distributed over the cross-section at the end of each layer as shown in Figure 4.34 b) and c). As discussed in 4.3, the heat dissipates less in the surrounding powder bed (low convection) [207]. The increased heat accumulation at the end of the exposure of a layer or scanning vector (surfaces S1 and S2) show this effect. It can be argued that the cooling difference between the surface and the bulk of the Tower_18s was greater compared to the other specimens, which may have led to higher surface residual stress. Moreover, the asymmetric profile of the surface σ_Z may also be related to the scanning strategy (see Figure 4.29 a).

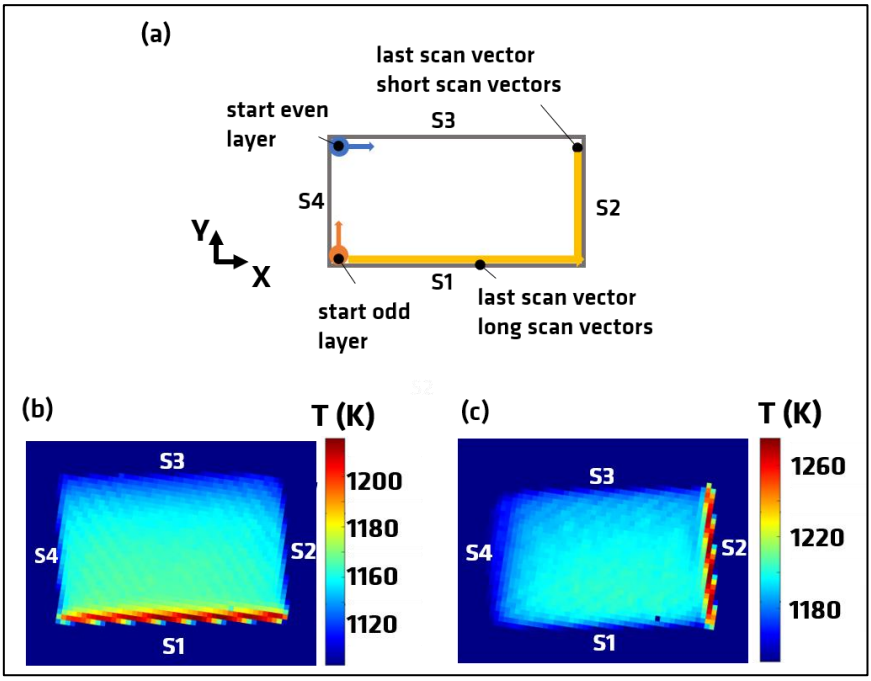

Figure 4.34: a) Start and end position of the scan vectors of the meander stripe scanning strategy with respect to the surfaces of the Tower specimens (surface details are given in Figure 3.16), b) temperature distribution in odd and c) in even layers. Figure adapted from [181].

It is conceivable that the asymmetric profile of the bulk residual stress shown in Figure 4.31 is also related to the scanning strategy. However, the distribution could also be due to varying d_0. A detailed study on the d_0 in PBF-LB/M/IN718 was reported in [128] revealing that in a cross-section at a given height in the build direction, the d_0 values remained constant. But, the d_0 values did change along the build height according to findings in DED of IN625, attributed to the accumulation of heat [102]. This can be explained by the increased mobility of the alloy elements to diffuse in a more homogeneous way at higher temperatures. Also, the PBF-LB/M process is more prone to the vaporisation of elements compared to other AM processes, which might further influence the variation of d_0 in a PBF-LB/M part [31]. Moreover, the cubes (when using this approach to determine a reasonable stress free reference) can retain type II residual stress [208]. The peak positions from which the d_0 values were calculated from for the investigation on the Tower specimens are shown in Figure 4.35 a). Though most of the values are constant, it seems that the peak position deviates from close to the surface (ce) comparing to the centre (cc) for Tower_116s_HV. The d_0 values

(indicated by arrows) used in the investigation on the effect of the ILT stem from two three-millimetre-thick slices taken from the top and bottom of the specimen as shown in Figure 4.35 b). The distance between the extraction distance of the cubes is small but already a variation in peak position is observed. This difference amounts to ~100 x 10^{-6} strain which is approximately twice the strain error of each measurement. In a uniaxial stress state, this difference would change the residual stress by approximately 20 MPa.

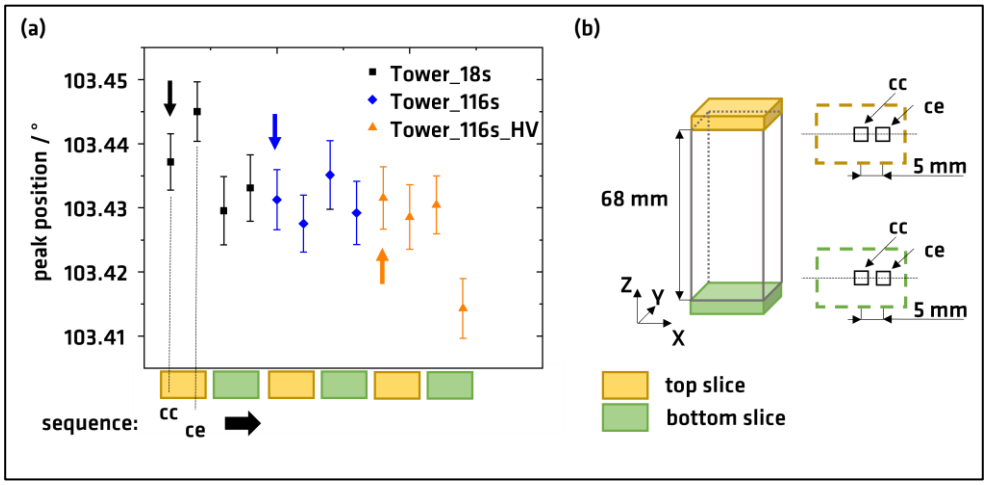

Figure 4.35: a) average peak positions calculated using the three measurement orientations of the cubes extracted from the top (yellow slice) and the bottom (green slice) of the specimen. b) location of the cube center (cc) and cube edge (ce) in the specimen and the cross-section. Adapted from [181].

To summarize, a short ILT increases the surface residual stress but reduces the bulk residual stress. This effect reaches a threshold above 65 s. A higher scanning velocity led to low surface residual stress but did not alter the bulk residual stress. The results show the close connection between the ILT and the residual stress in PBF-LB/M/316L. As described in the subchapter 2.2.5, a different heat accumulation in the specimen was expected. However, the herein reported results not only show this heat accumulation but more importantly quantify its effect on the residual stress. The use of in-situ process monitoring enabled to relate the 15 % lower bulk residual stress to the heat accumulation when using short ILT. The reduced residual stress is resulting from the heat accumulation, which reduces the thermal gradients in the part and leads to recovery. Short ILT are encountered in e.g. a low number of specimens in the build job or to a complex geometry with a sudden reduction of the scanning area. This can be the case for one part series in highly specialised fields e.g.

space industry. Moreover, the sequence of the scanning strategy leads to a heterogenous temperature field in each layer. The heat accumulates near the surfaces of the last scanning vectors. The resulting complex cooling gradients may explain the contradicting trends of the surface and the bulk residual stress and the asymmetric bulk residual stress.

The results show that high magnitude residual stress is locked in PBF-LB/M/316L structures. Thereby, the residual stress fields distribute asymmetrically. It has been shown that even smaller structures exhibit high residual stress (chapter 4.3). Tuning the process parameters that directly influence the heat input can lead to lower residual stress, but the values are still high (~50 % of the yield strength for PBF-LB/M/316L). Therefore, the next subchapter details different heat treatment strategies to reduce the residual stress based on standard heat treatment approaches [17, 171].

4.5 Thermal relaxation of the residual stress

In this chapter, the influence of a low temperature (see subchapter 4.5.1) and two high temperature stress relieve treatments for 316L are investigated (see subchapter 4.5.2). Furthermore, the influence of the heat treatment on the microstructure is analysed (see subchapter 4.5.3). The results of the high temperature stress relieve heat treatment and related change of the microstructure and the residual stress was published in [172].

4.5.1 The residual stress after the low temperature heat treatment

The surface residual stress measurement positions and results of Tower_65s_AB and Tower_65s are shown in Figure 4.36. The general trend shows that the residual stress values are higher towards the centre of the surfaces (Figure 4.36 a-c). At the corners the residual stress values tend to be lower. For the σ_X and the σ_Y this is expected, as these stress directions need to decrease to fulfil boundary conditions. Lower σ_Z values near the specimen corners were also observed. In Figure 4.36 b) the σ_Z of the two specimens are mostly within the error bar. In fact, the σ_Z and the σ_X in Tower_65s are higher compared to Tower_65s_AB despite the stress relieve treatment. The opposite trend is, however, observed on surface S2 in Figure 4.36 c) and d). The σ_Z remain at a similar level independently of the heat treatment. Lower σ_Y are observed in the stress relieved Tower_65s.

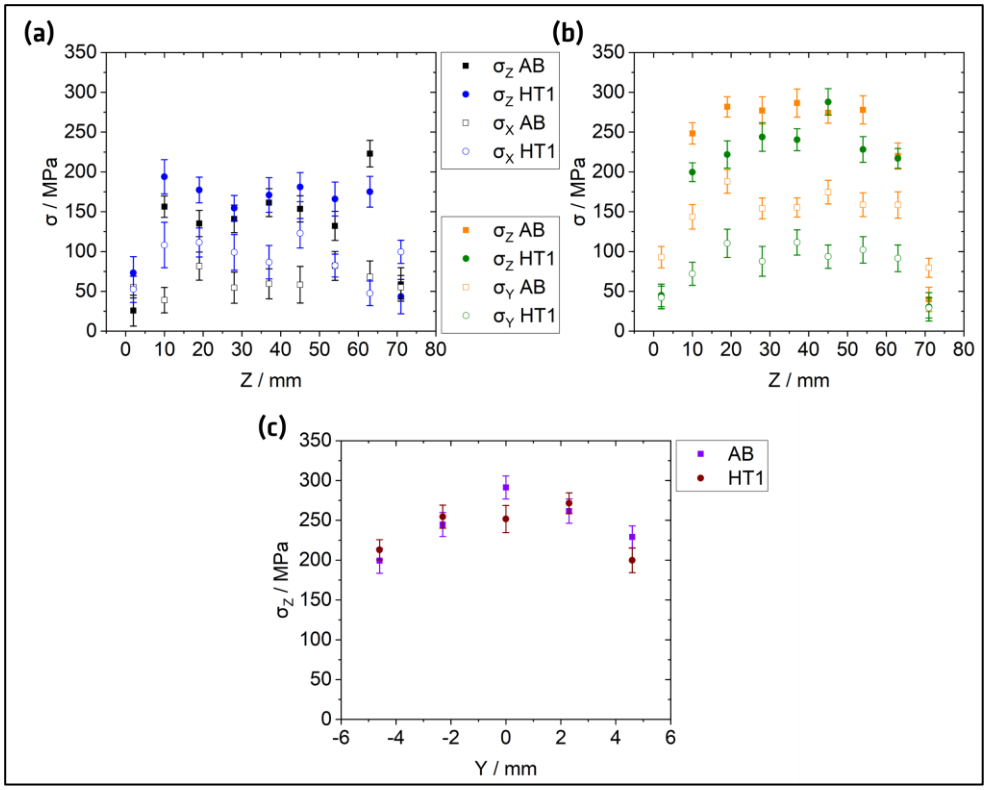

Figure 4.36: a) σ_Z and σ_X along the build direction on S1, c) σ_Z and σ_X along the build direction and c) across the thickness on S2. See Figure 3.16 c) and d) for the measurement positions.

Although higher residual stress values in the Tower_65s_AB is observed, it appears to be dependent on the surface and stress direction investigated. A relaxation of 31 % was reported for a heat treatment performed at 400 °C for 4 hours in [175]. Therefore, following the stress relieve mechanisms described in subchapter 2.3.2 a similar relaxation could have been expected for the heat treatment at 450 °C for 4 hours. In Figure 4.36 c) the residual stress values are lower after the heat treatment. The average residual stress values are shown in Table 4.9.

Table 4.9: Average residual stress values in the Tower specimens before and after the low temperature heat treatment.

Specimen	σ_Z in MPa	σ_X in MPa	σ_Y in MPa
Tower_65s_AB	198 ± 64	61 ± 13	145 ± 36
Tower_65s	192 ± 57	90 ± 26	82 ± 29

The relaxation (using the average residual stress values shown in Table 4.9) of the σ_Z and σ_Y is 12 % and 43 % respectively. These values are to some extent in agreement with findings in the literature. However, the roughness measurements showed that none of the surfaces had similar roughness values (see Table 4.2). Since in Figure 4.36 b), no difference in the residual stress values is observed between both specimens, no clear conclusion can be drawn from the surface measurements. Therefore, the bulk residual stress was investigated. The distribution of the residual stress in the cross section at half the height of the Tower specimens is shown in Figure 4.37 and Figure 4.38. Peak tensile σ_Z are present at the corners and remain tensile along each subsurface. The tensile residual stress is balanced by compressive σ_Z at the centre of the specimen. The σ_Z reach 510 MPa at the corners, which is in the order of the yield strengths in Table 2.2. The maximum compressive residual stress is -540 MPa. These values are similar to the magnitudes found in the walls analysed in subchapter 4.3.2.

The σ_X and the σ_Y are much lower compared to the σ_Z as shown in Figure 4.37 b) and c). The scale was readjusted for better visualisation of the following observations. The distributions of σ_X and σ_Y follow the boundary conditions. For each direction, peak values are obtained at the centre of a surface and low values are obtained where the free surface condition for stress applies (σ_X or σ_Y = 0 MPa when normal to the surface).

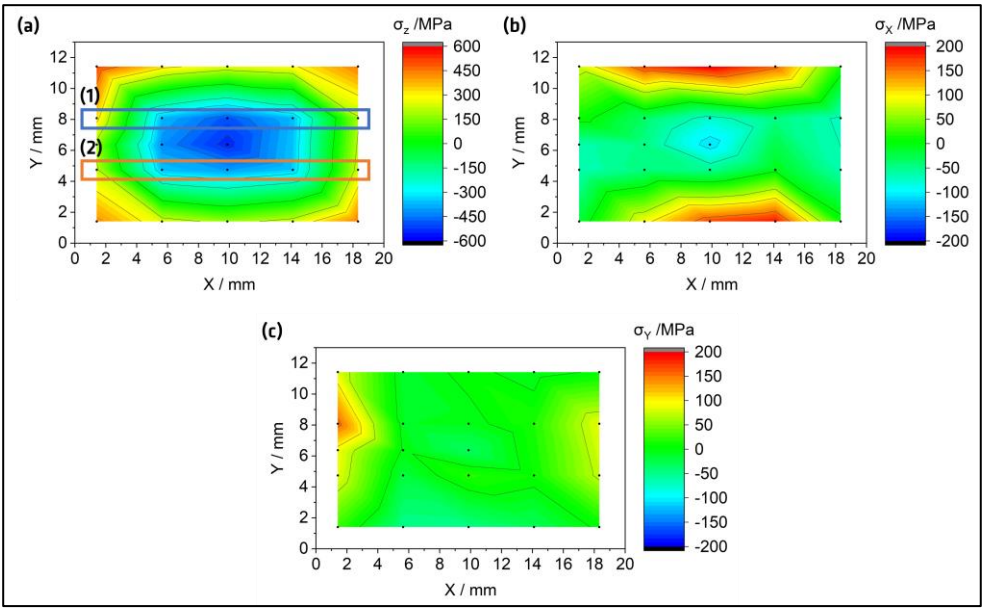

Figure 4.37: a) σ_Z, c) σ_X and d) σ_Y distributions in the Tower_65s_AB (as-built). The location of the measurement points is shown in Figure 3.21 c).

The distribution of the triaxial residual stress in Tower_65s shown in Figure 4.38 is similar to Tower_65s_AB. The main difference appears to be a higher stress range in the σ_X and a shift of the σ_Y to overall lower stress values. Moreover, the distribution of the residual stress corresponds well to findings in the literature [119, 130, 209, 210].

Both Figure 4.37 b) and Figure 4.38 b) show that the σ_X is compressive near the free surface with values between -50 MPa and -200 MPa. This may be resulting from a variation of the stress-free reference d_0 in e.g. X = 18.3 mm in Figure 4.38 c). As described in subsection 2.2.1, d_0 changes were observed to change with the build height [102] but not along the thickness or length at a fixed height [128]. Another explanation is that the extraction of 3 mm x 3 mm x 3 mm cubes may not have fully relieved the type I residual stress in PBF-LB/M material. Therefore, a shift to compressive residual stress values is observed.

The σ_X and the σ_Y along the central line (Y = 6 mm) for both specimens (see Figure 4.37 and Figure 4.38 b) and c) respectively) are similar to the distribution observed in the 9mm_26mm specimen (see Figure 4.23 and Figure 4.24). The σ_X remain mostly in compression below -200 MPa whereas the σ_Y increase towards the free surfaces. Interestingly, for both residual stress directions much lower values are

observed in the Tower specimens compared to the wall specimens near the surface. This is a result of the size of the gauge volume averaging of the maxima of the stress gradients (see subsection 2.2.1 and 3.7)

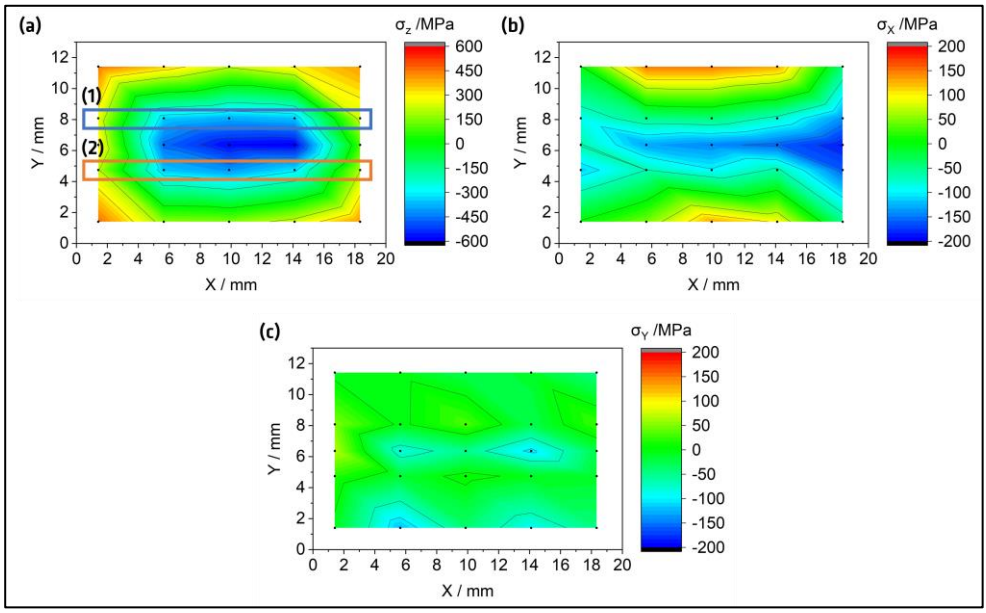

Figure 4.38: a) σ_Z, c) σ_X and d) σ_Y distributions in the Tower_65s (heat treated at 450 °C for 4 hours). The location of the measurement points is shown in Figure 3.21 c).

The σ_Z are further analysed along the two measurement lines (1) and (2). Similar to the approach taken to evaluate the influence of the thickness on the surface residual stress in 4.3.1, analysing the higher magnitude residual stress should give insights on whether relaxation occurred. The σ_Z along lines (1) and (2) in Tower_65s_AB and Tower_65s are plotted in Figure 4.39. The σ_Z values are mostly within the error bar.

The analysis of the surface and bulk residual stress shows that very little relaxation occurred when applying the heat treatment at 450 °C for 4 hours. This is also in line with observations showing no changes in the microstructure nor in mechanical properties such as the hardness or the yield strength [6, 7, 51]. As discussed before, type I residual stress in the d0 stress free-reference may have been retained.

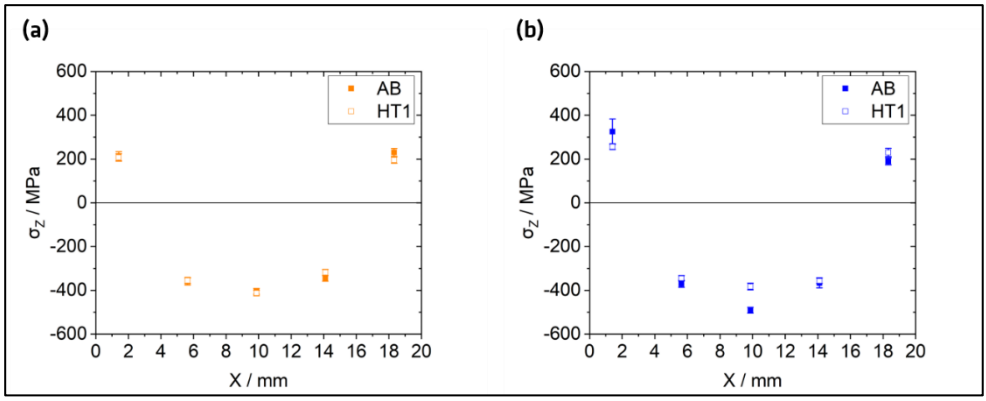

Figure 4.39: a) σ_Z along line 1 and b) along line 2 in the Tower_65s_AB and Tower_65s.

Two additional aspects need to be considered to assess the relaxation of the residual stress. As introduced in the subchapters 2.2.1 and 3.7, the residual stress values are a function of the gauge volume. The analysis on the wall specimens shows the residual stress distribution (chapter 4.3) and highlights the steep residual stress gradients towards the surface (around 400-600 MPa/mm, see Table 4.8).

It is possible that peak residual stress values were reduced by the heat treatment but not captured by the measurement positions and the choice of the gauge volume. The use of 2 mm x 2 mm x 2 mm gauge volumes induces a smearing of the near surface stress maxima. In fact, the relaxation and redistribution of the peak residual stress could lead to the very similar values between the Tower_65s_AB and the Tower_65s specimens. The relaxation obtained from the heat treatment at 450 °C for 4 hours using the residual stress ranges (maximum to minimum residual stress value) and an average error of 20 MPa is summarized in Table 4.10. The results clearly show that for the σ_Z very little relaxation is observed whereas for the two other residual stress directions, the maximum relaxation is 5 % and 26 % for the σ_X and the σ_Y respectively.

Table 4.10: The σ_Z, the σ_X and the σ_Y ranges in the Tower_65s_AB and the Tower_65s.

Specimen	$\Delta\sigma_Z$ in MPa	$\Delta\sigma_X$ in MPa	$\Delta\sigma_Y$ in MPa
Tower_65s_AB	1060	310	210
Tower_65s	1050	340	190
Relaxation in %	0 ± 4	-9 ± 14	7 ± 19

The second aspect, as discussed previously, is the fact that there is no clear trend of how the surface residual stress relax. Ideally, a clear trend should be visible independently of the surface analysed. Since this is not the case, one can conclude that the residual stress relaxation is below the resolution of the combined XRD and ND approach.

To summarize, the temperature heat treatment (450 °C for 4 hours) employed to relieve the residual stress in PBF-LB/M/316L did result in a minor relaxation of the residual stress. This result does not correspond with the relaxation of the compressive residual stress reported in [175]. The authors determined the σ_X and the σ_Y on 3 mm slices extracted from a larger structure. They reported a relaxation around 31 %, which is much higher than the values found for the heat treatment employed in this study. It is noted that the temperature employed for the low temperature heat treatment is 50 °C higher than the temperature employed in [175]. However, the relaxation of residual stress largely depends on the initial magnitude (see subchapter 2.3.2). Therefore, it can be assumed that the results in [175] do not display the relaxation of the residual stress in the PBF-LB/M AISI 316L. This observation is substantiated by the reduced diffusion and the dislocation mobility at these temperatures (see 2.3.1). The microstructure of PBF-LB/M/316L is reported to remain stable up to a temperature range between 600 °C and 700 °C. The relaxation may be driven by local plastic deformation if the residual stress is above the temperature dependent yield strength or time dependent relaxation mechanisms (see 2.3.2). The yield strength at 450 °C is between 200 MPa and 250 MPa as derived from the study reported in [170], which is lower than the σ_Z shown in Figure 4.37. Therefore, some relaxation may have occurred due to plastic deformation. In the directions of σ_X and σ_Y the magnitudes are lower than the yield strength at 450 °C. Therefore, the relaxation would have been predominantly driven by time dependent processes which, given by the relatively close stress ranges, did not occur (within the limitations of the characterisation method). Based on the findings presented the

relaxation of the residual stress using the low temperature heat treatment is below 5 %. Depending on the part thickness, the residual stress after this heat treatment may lead to distortion upon the removal of the part from the build plate.

4.5.2 The residual stress after high temperature heat treatment

The investigation on the influence of high temperature heat treatments was conducted on the SENB specimens (the geometry is shown in Figure 3.23). The triaxial bulk residual stress was determined before and after the respective heat treatment, at the same measurement positions. The residual stress before and after the two different heat treatments (800 °C and 900 °C for 1 hour respectively) is shown in Figure 4.41. The values are overplotted for comparison. The triaxial residual stress in the SENB specimen distributes similarly to the observations made on the distribution of the residual stress in the Y-direction (through the thickness, see Figure 4.18). The σ_Z describe a U-type profile. In this case the profile is asymmetric as the introduction of the WEDM notch leads to a redistribution and a relaxation of the residual stress (see details in [211, 212]). Furthermore, the σ_Z in the two measurement lines differ which is also attributed to the machining of the specimens. An increase of the σ_X close to the notch tip is observed, which can be as well related to the WEDM processing step [213]. The σ_Y are low in the two SENB specimens. The residual stress ranges remain high ≤~50 % compared to the ranges in the Tower_65s_AB (Table 4.10).

The influence of HT2 on σ_Z is shown in Figure 4.41 a). The values are reduced after exposing the specimen to 800 °C for 1 hour compared to those found after HT1. The presence of a residual stress gradient indicates that the residual stress does not fully relax. Furthermore, the stress values along the two measurement lines still differ by approximately 50 MPa (constant along the cross-section). A similar trend is observed when analysing the σ_Z after the heat treatment at 900 °C for 1 hour, whereby greater relaxation is observed. This trend is as well seen for σ_X. Peak stress values near the notch decrease until comparable values along the ligament are observed after the additional heat treatments as shown in Figure 4.41 c). After HT2, a small relaxation of the σ_X is observed. Nonetheless, a stress gradient is still visible which vanishes when applying HT3 (see Figure 4.41 d). The σ_Y in both specimens are shown in Figure 4.41 e) and f). The residual stress before and after the heat treatment are within the error bars.

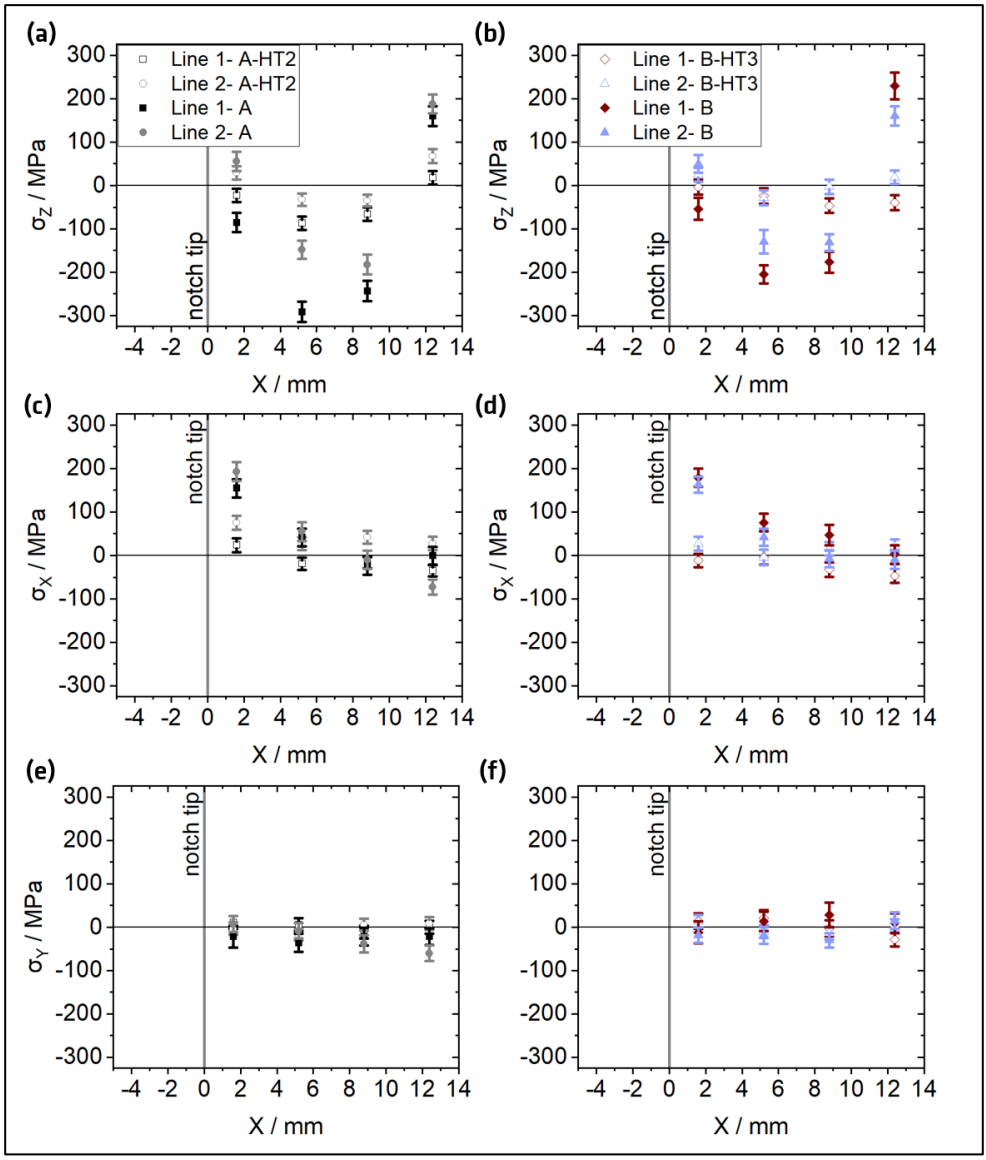

Figure 4.40: a) σ_Z, c) σ_X, and d) σ_Y along line 1 and 2 before after and after HT2; b) σ_Z, d) σ_X, and f) σ_Y along line 1 and 2 before and after HT3. The legend in a) and b) applies to c) through f). Adapted from [172].

The approach to infer the d_0 is applicable due to the low through thickness residual stress (σ_Y). The relaxation values calulcated using the residual stress ranges are summarized in Table 4.11.

Table 4.11: Relaxation after HT2 and HT3 for each stress direction.

Heat Treatment	$\Delta\sigma_X$ in %	$\Delta\sigma_Y$ in %	$\Delta\sigma_Z$ in %
HT2 (800 °C/ 1 h)	75 ± 7	8 ± 56	75 ± 2
HT3 (900 °C/ 1 h)	79 ± 3	9 ± 31	86 ± 4

The degree of relaxation determined depends on the residual stress direction. The much lower σ_Y led to erroneous values. However, the relaxation values using σ_X and σ_Z agree well for the respective heat treatment.

The relaxation obtained after HT2 and HT3 is compared with findings reported in the literature (summarized in Table 2.3) in Figure 4.41. A baseline is necessary to calculate the relaxation. In subchapter 4.5.1 it was concluded that the heat treatment at 450 °C for 4 hours gave rise to minimal stress relaxation (0±4 % as shown in Table 4.10). Therefore, the residual stress in the SENB specimens after HT1 can be used as baseline for the calculation of the residual stress relaxation when applying a subsequent heat treatment at 800 °C and 900 °C for 1 hour respectively. The discrepancy of the relaxation values obtained at a T_E smaller than 16 is detailed in 4.5.1. The residual stress relaxation resulting from HT2 and HT3 is in good agreement with the relaxation values for PBF-LB/M/316L from the literature as shown in Figure 4.41. The relaxation obtained by HT3 agrees well with results for welded austenitic steels i.e. relaxation of 85 % with a T_E between 22.4 – 23.5 [46, 171]. Cellular structures are also found in welded austenitic steels, although the size is different to the ones found in PBF-LB/M/316L (see 2.1). At 900 °C these cells mainly dissolve, which may explain the good agreement of the relaxation values between the welded and PBF-LB/M austenitic steel.

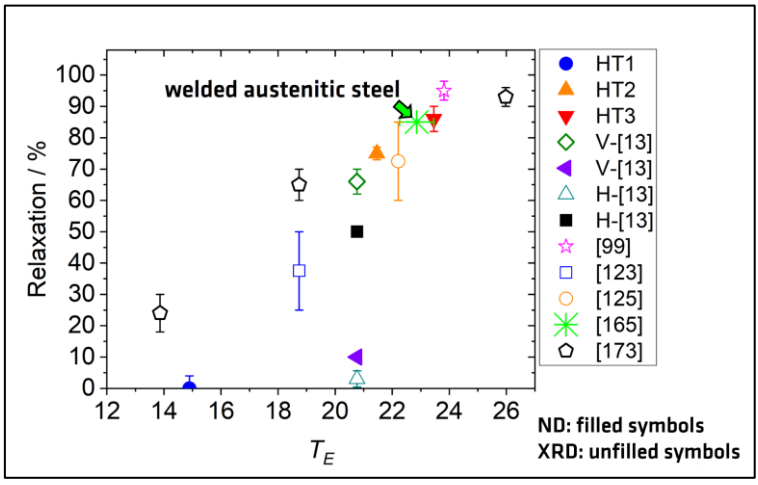

Figure 4.41: The relaxation of σ_z as a function of the T_E calculated using the averaged residual stress in specimen A and B as reference and comparison to findings reported in the literature; H (horizontally built specimen) and V (vertically built specimen). Adapted from [172].

4.5.3 Analysis of the microstructure and residual stress changes

The microstructure of an as-built (9mm_13mm) and a heat-treated specimen (SENB specimen) is shown in Figure 4.42. From literature it is known that no changes in the texture, the grain growth or in the cellular structure occurs at this temperature [6, 7, 51, 214]. Analysing just the cellular substructure of the two specimens reveals similar features in the two microstructures. The grain boundaries and melt pool boundaries remain clearly visible, as well as the cellular substructure.

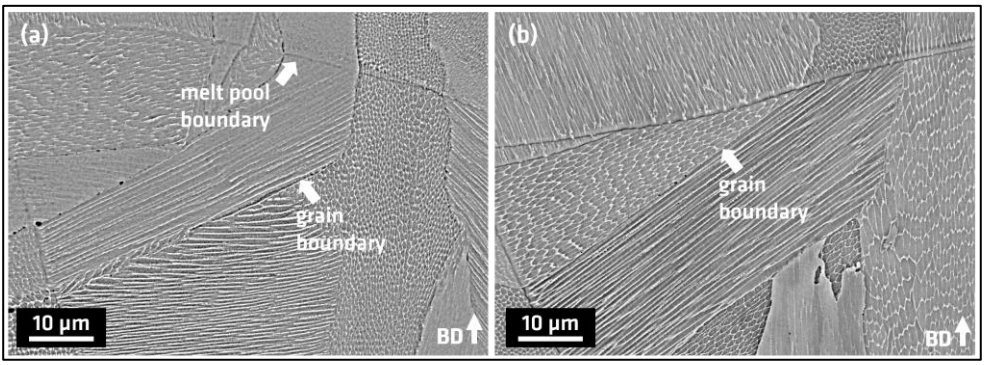

Figure 4.42: a) as-built microstructure of the 9mm_13mm specimen, and b) heat treated (450 °C/ 4 hours) microstructure of the Tower_65s_AB specimen.

Through the analysis of the FWHM it is possible to obtain information on the microstructure (mosaicity and crystallite size) changes. These can then be linked to the residual stress (type II and type III) changes (see 2.2.2). The mosaicity describes the misorientation at a subgrain level such as induced by the cellular structure in PBF-LB/M/316L. This misorientation induces peak broadening and as such a larger FWHM. In the case of cellular substructures, it is assumed that the cells have small misorientations. The dissolution of the cellular sub-structures therefore leads to the homogenization of the subgrain orientations and thus a decrease of the FWHM [80]. Grain growth may also lead to a reduction of the FWHM. However, only minor grain growth was observed when heat treating the specimens at 800 °C and 900 °C for 1 hour respectively (see Figure 4.43). Therefore, it is assumed that the influence of the grain size is negligible on the FWHM.

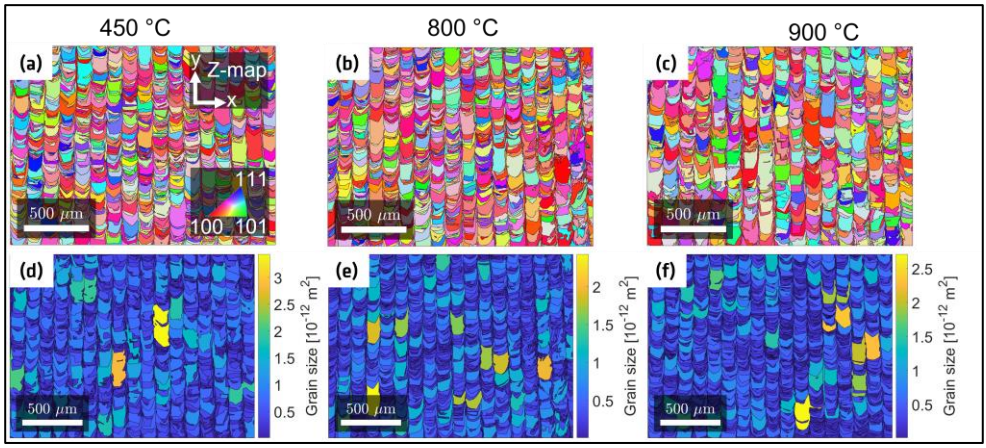

Figure 4.43: a) EBSD of the microstructure after the low temperature heat treatment, b) when applying 800 °C for 1 hour, c) when applying 900 °C for 1 hour, d)-f) associated grain sizes. a) through c) are adapted from [172].

Increasing the heat treating temperatures to 800 °C and 900 °C leads to significant changes in the cellular structure as shown in Figure 4.44 a and b. The cells are stable up to temperatures around 800 °C [7] and indeed, though the dissolution appears to have started i.e. contrast between cell wall and matrix less prominent, it is still visibile after HT2 (see Figure 4.44 a). The heat treating temperature 900 °C leads to the dissolution of the cells [7, 215] which agrees well with the microstructure shown in Figure 4.44 b. The cellular structure is composed of forests of dislocations, precipitates and segregation (mostly Cr and Mo) as described in 2.1. These features induce microstrains, which as well lead to a diffraction peak broadening and thus larger FWHM values. The FWHM profiles before and after HT2 and HT3 are shown in Figure 4.44 c and d respectively. The FWHM values decrease gradually when applying 800 °C and 900 °C for 1 hour. The FWHM varies with the location after HT2 and describe a profile which becomes flat after HT3. The non-homogenous reduction of the FWHM after HT2 indicates that minor misorientations (either induced by mosaicity or residual stress of type II or type III) are still present i.e. the cellular structure is still prevailing. This is indeed the case as shown in Figure 4.44 a. After HT3, the profile is flat which points out at the dissolution of the cellular structure, which is shown in Figure 4.44 b. As described in 2.1.2 the cellular structure is the main source for the increased mechanical properties. Therefore the loss of this microstructural feature and hence reduction in mechanical properties needs to be balanced against the relaxation of the residual stress. Applying HT2 and HT3 reduce the residual stress by a minimum of 75 % (up to 85 % for HT3) [172]. For indication, these heat treatments are

reported to reduce the hardness by 8 %-12 % [7] and the yield strength by 8 % - 17 % [6, 51] and 13 % - 25 % [51] respectively. Nonethelss, the yield strength (about 390 MPa when applying 900 °C [51]) remains much higher compared to wrought 316L (approximately 170 MPa in hot finished and annealed bars [171]).

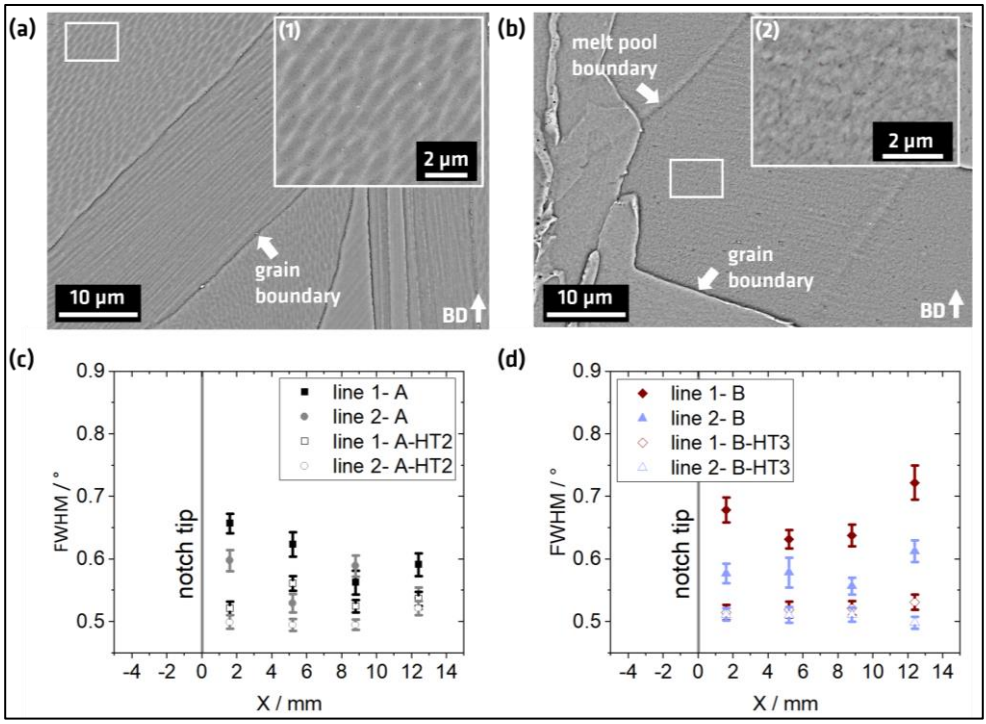

Figure 4.44: a) cellular structure after HT2 and b) HT3, highlighted in insets (1)-(2). The yellow arrows indicate melt pool boundaries, and the green arrows highlight grain boundaries. c) Evolution of the FWHM after HT2 and d) after HT3. All images are adapted from [172].

The thermal relaxation of the residual stress seems to broadly follow the indications given for welded austenitic steels. The heat treatment at 450 °C for 4 hours leads to a relaxation lower than 5 %. Findings in the literature suggest that ~30 % relaxation can be obtained [175, 216], which is however very unlikely given the results shown in 4.5.1. Setting the heat treatment temperature to 900 °C is one option to relax up to 85 % of the residual stress. Given the generalised argument that residual stress reaches magnitudes close to the yield strength, the specimens can end up with residual stress about 100 MPa (based on a yield strength around ~550 MPa, see Table 2.2). This needs to be accounted for in the design of the specimens as the residual stress is superimposed to any additional external load (either static or dynamic). When designing the part or performing a topology optimization, the thinnest part sections need to be analysed considering the residual stress after the heat treatment to prevent premature failure.

5 Summary and Conclusions

In this study the residual stress formed in stainless steel 316L specimens manufactured by laser powder bed fusion (PBF-LB/M) was investigated. This additive manufacturing process induces large thermal gradients. The layer-by-layer manufacturing leads to complex residual stress fields. The PBF-LB/M processing of the austenitic stainless steel 316L has shown that the strength-ductility trade-off normally encountered with this alloy can be overcome. Moreover, given the freedom of design of the PBF-LB/M process this alloy has seen its application range expand to include safety critical and crucial components for sustainable technologies.

Several gaps regarding the residual stress in PBF-LB/M/316L were identified in the literature. (I) The (311) lattice plane is commonly used to calculate the residual stress in PBF-LB/M/316L. However, it has not been shown if analogue to conventionally processed 316L this approach can be used. (II) The influence of the geometry on the residual stress is unclear as most of the studies to date investigate process parameter optimizations and their influence on the residual stress. (III) The impact of the process parameter inter-layer-time (ILT) on the residual stress has not been investigated for PBF-LB/M although it was found to significantly alter the residual stress in other additive manufacturing processes. Moreover, the ILT is known to influence the heat accumulation, which directly affects the residual stress. (IV) Stress relaxation heat treatments are employed, which rarely consider the indications given in available standards for welded austenitic steels. Thereby, the temperature range between 800 °C and 900 °C is scarcely investigated although it leads to the dissolution of the cellular structure, which is the source for the improved static mechanical properties.

This study used X-ray (XRD) and neutron diffraction (ND) to determine the surface residual stress, the subsurface (using the layer removal technique) residual stress and the bulk residual stress. The complex surface of PBF-LB/M structures poses challenges to the diffraction-based assessment of the residual stress. This was overcome by systematically measuring the roughness of the specimens. The diffraction findings were substantiated by the analysis of the microstructure using optical and scanning electron microscopy and thermographic measurements.

The results show that the (311) lattice plane is the most suitable lattice plane to calculate the macroscopic residual stress. Nonetheless, the (311) lattice plane was found to accumulate type II strains, which can induce an error between 20 MPa and 90 MPa. Moreover, the experimental results were well described by the Kröner grain interaction model despite the texture. The geometry was found to play a

major role on the residual stress. The residual stress changes with the geometry and an increase of the dimensions leads to higher magnitudes but lower residual stress gradients. These changes were explained by the variation of the restraint to the shrinking material and thermal gradients. When maintaining the process parameters constant, the residual stress has similar magnitudes in small and large structures. Increasing the ILT leads to an increase of up to 15 % of the peak compressive residual stress. Using a short ILT leads to a higher heat accumulation, which reduces the thermal gradient within the part und subsequently to lower residual stress magnitudes. This effect was observed to have a threshold at an ILT of 65 seconds. Heat treatment at 450 °C resulted in a relaxation of approximately 5 %. The use of 800 °C and 900 °C resulted in the relaxation of the residual stress by 75 % and 85 % respectively. The nearly full relaxation of the residual stress (900 °C) indicated by flat residual stress profiles needs to be balanced with the dissolution of the cellular structure.

The following conclusions can be drawn:

1. The roughness of the lateral surfaces of the PBF-LB/M/316L specimens differed strongly from each other. No trend was observed due to the large number of influencing factors. When analysing solely the surface residual stress, it is advised to ensure that the surface roughness is measured for comparison purposes.

2. The in-situ neutron diffraction tensile test in two measurement orientations (different textures) showed that the lattice strains describe a similar trend but differ due to the prevailing texture. A comparison with conventional 316L showed that there is good agreement in the fully elastic regime. In the plastic regime, the load shedding of the (220) lattice plane and the strain accumulation of the (200) lattice plane is more pronounced in the PBF-LB/M material compared to the conventional material. This was attributed to the texture, the large amount of strain at the onset of plasticity and the pinning of the dislocations due to the cellular structure.

3. The unloading sequences during the in-situ neutron diffraction tensile test permitted the analysis of the lattice strain accumulation in the material. The lattice strain accumulation behaviour of the two different loading directions (textures) was similar. However, the specimen with a <220> texture along the loading direction had larger tensile strain accumulation of the (200) and the (311) lattice planes. This was attributed to the prevailing texture. The (311) lattice plane is generally assumed to accumulate no residual strain, which is one reason why it is used for the residual stress assessment. However, at approximately 1 % macroscopic strain the lattice strain accumulation was as high as 500×10^{-6} strain (up to 90 MPa in idealized uniaxial stress), which needs to be considered when evaluating the residual stress magnitudes.

4. The diffraction Young's moduli (two textures) were found to be well described by the Kröner model. The values of to the (311) lattice plane were within the error bar, which may reduce the error of the resulting stress when using Hooke's law for triaxial stress. The good agreement between the model and the experimental results permits to avoid using Poisson values from diffraction experiments, which are difficult to accurately determine in textured materials.

5. The in-situ neutron diffraction tensile test showed that the (311) lattice plane is an appropriate choice for the calculation of the macroscopic

residual stress according to the lattice strain accumulation and the multiplicity.

6. High tensile residual stress at the surface of the rectangular PBF-LB/M/316L specimens was found to be balanced by compressive residual stress in the bulk. At the surface the residual stress in the build direction (σ_Z) was larger than the residual stress along the length (σ_X) and along the thickness (σ_Y). The maximum surface residual stress was located at the centre of the surface. In the subsurface, the σ_Z was higher compared to the σ_X. The residual stress in the subsurface reached a peak, which was affected by the geometry. The bulk residual stress was tensile near the surface and was compressive in the centre of the volume. The peak compressive (σ_Z) was generally located at the centre of the specimen.

7. The increase in thickness leads to larger surface residual stress along the build direction (σ_Z) but this effect reaches a threshold around 9 mm for this material and geometry. Moreover, the subsurface tensile residual stress peak (build direction) shifts to greater depths when increasing the thickness. This is, however, not the case for the in-plane residual stress. In fact, the residual stress along the length (σ_X) was observed to increase in the thicker specimens, which was attributed to the higher degree of restraint to shrinkage. In the bulk, the residual stress (σ_Z and σ_X) was found to increase with the thickness and to reach the material's yield strength (just σ_Z) close to the lateral surface of the specimens. The bulk through thickness σ_Y remained low, which allows to approximate the residual stress as bi-axial (up to a thickness of 9 mm).

8. The increase of the specimen length led to larger surface and subsurface σ_Z, similar to the increase in thickness. The bulk σ_Z were limited by the material's yield strength, which is in good agreement with the simplified residual stress models given in [11]. Increasing the length in fact reduced the σ_Z gradients, which was explained with the different heat conduction as a result of smaller surface to area ratio in larger specimens. The bulk σ_X and the bulk σ_Y and were found to be lower than the σ_Z. The σ_X were larger than the σ_Y corresponding to the longer scanning vectors and resulting thermal history.

9. The overall larger residual stress in specimens with greater dimensions was explained with the higher restraint to shrinkage and the heterogenous cooling. When increasing the dimensions, the restrained shrinkage of each weld bead becomes larger. Moreover, the surrounding powder acts as

insulation and when increasing the specimen dimensions, the cooling of the surface and the bulk are affected: the surface remains at a higher temperature while the bulk cools faster. Changing the dimensions leads to a more heterogenous cooling of the structure and induces additional mismatch in the material. This ultimately gives rise to larger residual stress, which is ultimately bound by the material's yield strength. For this material and this scanning strategy, the dimension from which the changes are minor when further increasing the specimen size was 9 mm. In fact, the analysis of the residual stress in a structure much larger (up to a factor of 2.5 mm greater dimensions) showed that the surface and bulk residual stress remained largely similar. This is essential when evaluating the residual stress on witness specimens to evaluate the residual stress in a much larger and more geometrically complex part. The results show that the residual stress observations may be transferred to assess larger structures and as such reduce manufacturing costs as the witness specimens can be smaller in height.

10. The analysis of the residual stress using the tailored gauge volume revealed very high σ_Z gradients near the surface and small σ_Y through the thickness. When performing ND experiments, the residual stress gradients need to be considered when choosing the gauge volume. Near the surface, a large gauge volume will average out the peak residual stress. Additionally, the approach to infer d0 values assuming small σ_Y may be used, which gives the full non-destructive potential of ND. This is especially useful when the aim is to capture the evolution of the residual stress following post processes.

11. The influence of the ILT on the residual stress was determined using XRD and ND. The analysis was substantiated by in-situ thermography. At the surface, short ILT led to higher surface residual stress. The use of long ILT reduced the surface residual stress and a threshold was reached at 65 seconds. The surface residual stress abates when using higher laser scanning velocities, which was related to the smaller melt pools and reduced shrinking volume. The analysis of the bulk residual stress shows how longer ILT results in ~15 % higher residual stress magnitudes in the bulk. Decreasing the ILT reduced the bulk residual stress as more heat is accumulated. High temperatures during the manufacturing reduce the thermal gradients and combined with long manufacturing times, the stress is reduced by recovery processes. Therefore, lower residual stress is found when decreasing the ILT. Variations in the ILT can be compared to a change in thickness of a geometrically complex structure or to a variation

of the number of specimens built during the same build job. Therefore, variations in the residual stress need to be accounted for in such scenarios.

12. The investigation on the influence of the ILT also showed that the surface and the bulk residual stress did not coincide when analysing the influence of process parameters. This effect was attributed to the heterogenous cooling of the surface and the bulk, which was affected by the heat accumulation. Ideally, the influence of process parameters should be performed using surface and subsurface or bulk residual stress.

13. The relaxation of residual stress by applying different heat treatments was investigated using ND. The findings indicate that a heat treatment at 450 °C for four hours yields a relaxation below the 5 %. The low relaxation of this heat treatment coincides with the stable microstructure and mechanical properties. This study also shows that heat treatment temperatures of 800 °C and 900 °C held for 1 hour are required to achieve a relaxation of 75 % and 85 % respectively. These results agree well with the indication for stress relieving welded austenitic steels. The relaxation obtained when applying 900 °C for 1 hour led to a strongly dissolved cellular structure. This needs to be accounted for when choosing the stress relieve heat treatment, as the loss of the cellular structure also reduces the static mechanical properties.

Throughout the study two aspects related to the residual stress in PBF-LB/M/316L were highlighted which can be the focus of future studies. The first aspect concerns the influence of the surface roughness on the determination of the surface residual stress via X-ray diffraction. The surface residual stress in the build direction increases with the depth. The experiment results provide no certainty on whether this increase is a result of a change of the restraint during the solidification or if the residual stress magnitudes are low due to the surface roughness. Because most of the results reported in the literature report surface values without indications on the surface roughness, it remains difficult to draw conclusions on correlations of residual stress magnitudes and process parameters.

The second aspect of interest is the connection between the subgrain solidification cellular structure and the residual stress relaxation. It can be assumed that keeping the subgrain solidification cellular structure in laser powder bed fused alloys prevents the residual stresses to relax during heat treatment. This structure is composed of a high density of tangled dislocations, precipitates, and segregated elements. Each of these constituents present an obstacle for dislocation motion, which is one driver for the residual stress relaxation. It is key to retain this

microstructural feature in view of maintaining the higher yield strength in LPBF processed alloys to enable efficient lightweight designs. Therefore, it can be hypothesized that understanding the link between the residual stress relaxation and cellular structure will permit to tailor heat treatment strategies to balance both the improved mechanical properties with knowledge on the evolution of the residual stress.

References

[1] P. Consulting, Additive Manufacturing, 2017. http://breakthrough.unglobalcompact.org/disruptive-technologies/additive-manufacturing/.

[2] M. Meboldt, M. Baertschi, Exploring new applications in additive manufacturing, in: E.T.H. Zürich, A. Network (Eds.) Swiss AM Guide, 2019.

[3] Y.M. Wang, T. Voisin, J.T. McKeown, J. Ye, N.P. Calta, Z. Li, Z. Zeng, Y. Zhang, W. Chen, T.T. Roehling, R.T. Ott, M.K. Santala, P.J. Depond, M.J. Matthews, A.V. Hamza, T. Zhu, *Additively manufactured hierarchical stainless steels with high strength and ductility*, Nat Mater, 17(1), (2018), 63-71, 10.1038/nmat5021.

[4] A.J. Birnbaum, J.C. Steuben, E.J. Barrick, A.P. Iliopoulos, J.G. Michopoulos, *Intrinsic strain aging, Σ3 boundaries, and origins of cellular substructure in additively manufactured 316L*, Addit. Manuf., 29, (2019), 10.1016/j.addma.2019.100784.

[5] K.M. Bertsch, G. Meric de Bellefon, B. Kuehl, D.J. Thoma, *Origin of dislocation structures in an additively manufactured austenitic stainless steel 316L*, Acta Mater., 199, (2020), 19-33, 10.1016/j.actamat.2020.07.063.

[6] T. Voisin, J.-B. Forien, A. Perron, S. Aubry, N. Bertin, A. Samanta, A. Baker, Y.M. Wang, *New insights on cellular structures strengthening mechanisms and thermal stability of an austenitic stainless steel fabricated by laser powder-bed-fusion*, Acta Mater., 203, (2021), 10.1016/j.actamat.2020.11.018.

[7] P. Krakhmalev, G. Fredriksson, K. Svensson, I. Yadroitsev, I. Yadroitsava, M. Thuvander, R. Peng, *Microstructure, Solidification Texture, and Thermal Stability of 316 L Stainless Steel Manufactured by Laser Powder Bed Fusion*, Metals, 8(8), (2018), 10.3390/met8080643.

[8] K.O. Bazaleeva, E.V. Tsvetkova, E.V. Balakirev, I.A. Yadroitsev, I.Y. Smurov, *Thermal stability of the cellular structure of an austenitic alloy after selective laser melting*, Russian Metallurgy (Metally), 2016(5), (2016), 424-430, 10.1134/s0036029516050062.

[9] J. Ferchow, Additive Manufacturing towards Industrial Series Production: Post-Processing Strategies and Design, ETH Zürich, 2021.

[10] T. DebRoy, H.L. Wei, J.S. Zuback, T. Mukherjee, J.W. Elmer, J.O. Milewski, A.M. Beese, A. Wilson-Heid, A. De, W. Zhang, *Additive manufacturing of metallic components – Process, structure and properties*, Progress in Materials Science, 92, (2018), 112-224, 10.1016/j.pmatsci.2017.10.001.

[11] P. Mercelis, J.P. Kruth, *Residual stresses in selective laser sintering and selective laser melting*, Rapid Prototyping J., 12(5), (**2006**), 254-265, 10.1108/13552540610707013.

[12] H.L. Wei, H.K.D.H. Bhadeshia, S.A. David, T. DebRoy, *Harnessing the scientific synergy of welding and additive manufacturing*, Science and Technology of Welding and Joining, 24(5), (**2019**), 361-366, 10.1080/13621718.2019.1615189.

[13] T. Fritsch, M. Sprengel, A. Evans, L. Farahbod-Sternahl, R. Saliwan-Neumann, M. Hofmann, G. Bruno, *On the determination of residual stresses in additively manufactured lattice structures*, J. Appl. Crystallogr., 54(1), (**2021**), 228-236, 10.1107/s1600576720015344.

[14] R.J. Williams, F. Vecchiato, J. Kelleher, M.R. Wenman, P.A. Hooper, C.M. Davies, *Effects of heat treatment on residual stresses in the laser powder bed fusion of 316L stainless steel: Finite element predictions and neutron diffraction measurements*, J. Manuf. Pro., 57, (**2020**), 641-653, 10.1016/j.jmapro.2020.07.023.

[15] L. Karlsson, Thermal Stresses, Thermal Stresses in Welding, North-Holland Publishing, Amsterdam, 1986, pp. 229-389.

[16] P. Bajaj, A. Hariharan, A. Kini, P. Kürnsteiner, D. Raabe, E.A. Jägle, *Steels in additive manufacturing: A review of their microstructure and properties*, Mat. Sci. Eng. A, 772, (**2020**), 10.1016/j.msea.2019.138633.

[17] J.C. Lippold, D.J. Kotecki, *Welding Metallurgy and Weldability of Stainless Steels* (**2005**),

[18] M.P. American Society for Metals, OH : HandbookCommittee, Metals Handbook. Vol. 13: Corrosion, ASM International, 1987.

[19] A.I.H. Committee, ASM Handbook: Heat Treating. Vol. 4, ASM International, 1990.

[20] J.J. Smith, R.A. Farrar, *Influence of microstructure and composition on mechanical properties of some AISI 300 series weld metals*, International Materials Reviews, 38(1), (**1993**), 25-51, 10.1179/imr.1993.38.1.25.

[21] A.L. Schaeffler, *Constitution Diagram for Stainless Steel Weld Metal*, Metal Progress, 56(11), (**1949**), 680,

[22] K.H. Lo, C.H. Shek, J.K.L. Lai, *Recent developments in stainless steels*, Materials Science and Engineering: R: Reports, 65(4-6), (**2009**), 39-104, 10.1016/j.mser.2009.03.001.

[23] J.W. Elmer, S.M. Allen, T.W. Eagar, *Microstructural development during solidification of stainless steel alloys*, Metallurgical Transactions A, 20(10), (**1989**), 2117-2131, 10.1007/BF02650298.

[24] D. Kong, X. Ni, C. Dong, L. Zhang, C. Man, J. Yao, K. Xiao, X. Li, *Heat treatment effect on the microstructure and corrosion behavior of 316L stainless steel fabricated by selective laser melting for proton exchange membrane fuel cells*, Electrochimica Acta, 276, (**2018**), 293-303, 10.1016/j.electacta.2018.04.188.

[25] T. Tancogne-Dejean, A.B. Spierings, D. Mohr, *Additively-manufactured metallic micro-lattice materials for high specific energy absorption under static and dynamic loading*, Acta Mater., 116, (**2016**), 14-28, 10.1016/j.actamat.2016.05.054.

[26] ISO/ASTM, ISO/ASTM 52900: Additive Manufacturing, General Principles - Terminology, The International Standardization Organisation GENEVA, 2022.

[27] D. Herzog, V. Seyda, E. Wycisk, C. Emmelmann, *Additive manufacturing of metals*, Acta Mater., 117, (**2016**), 371-392, 10.1016/j.actamat.2016.07.019.

[28] J.O. Milewski, Additive Manufacturing of Metals: From Fundamental Technology to Rocket Nozzles, Medical Implants, and Custom Jewelry, Springer International Publishing2017.

[29] W.E. Frazier, *Metal Additive Manufacturing: A Review*, J. Mater. Eng. Perform., 23(6), (**2014**), 1917-1928, 10.1007/s11665-014-0958-z.

[30] C. Kamath, B. El-dasher, G.F. Gallegos, W.E. King, A. Sisto, *Density of additively-manufactured, 316L SS parts using laser powder-bed fusion at powers up to 400 W*, The International Journal of Advanced Manufacturing Technology, 74(1-4), (**2014**), 65-78, 10.1007/s00170-014-5954-9.

[31] T. Mukherjee, T. DebRoy, *Printability of 316 stainless steel*, Science and Technology of Welding and Joining, 24(5), (**2019**), 412-419, 10.1080/13621718.2019.1607061.

[32] M. Ma, Z. Wang, X. Zeng, *A comparison on metallurgical behaviors of 316L stainless steel by selective laser melting and laser cladding deposition*, Mat. Sci. Eng. A, 685, (**2017**), 265-273, 10.1016/j.msea.2016.12.112.

[33] H. Choo, K.-L. Sham, J. Bohling, A. Ngo, X. Xiao, Y. Ren, P.J. Depond, M.J. Matthews, E. Garlea, *Effect of laser power on defect, texture, and microstructure of a laser powder bed fusion processed 316L stainless steel*, Materials & Design, 164, (**2019**), 10.1016/j.matdes.2018.12.006.

[34] M.S. Pham, C. Liu, I. Todd, J. Lertthanasarn, *Damage-tolerant architected materials inspired by crystal microstructure*, Nature, 565(7739), (**2019**), 305-311, 10.1038/s41586-018-0850-3.

[35] E. Maleki, S. Bagherifard, M. Bandini, M. Guagliano, *Surface post-treatments for metal additive manufacturing: Progress, challenges, and opportunities*, Addit. Manuf., 37, (**2021**), 101619, 10.1016/j.addma.2020.101619.

[36] T.M. Mower, M.J. Long, *Mechanical behavior of additive manufactured, powder-bed laser-fused materials*, Mat. Sci. Eng. A, 651, (**2016**), 198-213, 10.1016/j.msea.2015.10.068.

[37] S. Patel, A. Rogalsky, M. Vlasea, *Towards understanding side-skin surface characteristics in laser powder bed fusion*, J. Mater. Res., 35(15), (**2020**), 2055-2064, 10.1557/jmr.2020.125.

[38] T. DebRoy, T. Mukherjee, H.L. Wei, J.W. Elmer, J.O. Milewski, *Metallurgy, mechanistic models and machine learning in metal printing*, Nature Reviews Materials, 6(1), (**2020**), 48-68, 10.1038/s41578-020-00236-1.

[39] A. Fedorenko, B. Fedulov, Y. Kuzminova, S. Evlashin, O. Staroverov, M. Tretyakov, E. Lomakin, I. Akhatov, *Anisotropy of Mechanical Properties and Residual Stress in Additively Manufactured 316L Specimens*, Materials (Basel), 14(23), (**2021**), 10.3390/ma14237176.

[40] I. Tolosa, F. Garciandía, F. Zubiri, F. Zapirain, A. Esnaola, *Study of mechanical properties of AISI 316 stainless steel processed by "selective laser melting", following different manufacturing strategies*, The International Journal of Advanced Manufacturing Technology, 51(5-8), (**2010**), 639-647, 10.1007/s00170-010-2631-5.

[41] M. Ziętala, T. Durejko, M. Polański, I. Kunce, T. Płociński, W. Zieliński, M. Łazińska, W. Stępniowski, T. Czujko, K.J. Kurzydłowski, Z. Bojar, *The microstructure, mechanical properties and corrosion resistance of 316L stainless steel fabricated using laser engineered net shaping*, Mat. Sci. Eng. A, 677, (**2016**), 1-10, 10.1016/j.msea.2016.09.028.

[42] A. Saboori, M. Toushekhah, A. Aversa, M. Lai, M. Lombardi, S. Biamino, P. Fino, *Critical Features in the Microstructural Analysis of AISI 316L Produced By Metal Additive Manufacturing*, Metallography, Microstructure, and Analysis, 9(1), (**2020**), 92-96, 10.1007/s13632-019-00604-6.

[43] K.M. Bertsch, A. Nagao, B. Rankouhi, B. Kuehl, D.J. Thoma, *Hydrogen embrittlement of additively manufactured austenitic stainless steel 316 L*, Corrosion Science, 192, (**2021**), 10.1016/j.corsci.2021.109790.

[44] L. Palmeira Belotti, J.A.W. van Dommelen, M.G.D. Geers, C. Goulas, W. Ya, J.P.M. Hoefnagels, *Microstructural characterisation of thick-walled wire arc additively manufactured stainless steel*, Journal of Materials Processing Technology, 299, (2022), 10.1016/j.jmatprotec.2021.117373.

[45] L. Wang, J. Xue, Q. Wang, *Correlation between arc mode, microstructure, and mechanical properties during wire arc additive manufacturing of 316L stainless steel*, Materials Science and Engineering: A, 751, (2019), 183-190, 10.1016/j.msea.2019.02.078.

[46] J. Douthett, Heat treating, ASM Handbook, ASM International, 1991, pp. 1682-1708.

[47] H.L. Wei, J. Mazumder, T. DebRoy, *Evolution of solidification texture during additive manufacturing*, Sci Rep, 5, (2015), 16446, 10.1038/srep16446.

[48] W. Chen, T. Voisin, Y. Zhang, J.-B. Florien, C.M. Spadaccini, D.L. McDowell, T. Zhu, Y.M. Wang, *Microscale residual stresses in additively manufactured stainless steel*, Nat. Commun., 10(1), (2019), 4338, 10.1038/s41467-019-12265-8.

[49] A. Charmi, R. Falkenberg, L. Avila, G. Mohr, K. Sommer, A. Ulbricht, M. Sprengel, R. Saliwan Neumann, B. Skrotzki, A. Evans, *Mechanical anisotropy of additively manufactured stainless steel 316L: An experimental and numerical study*, Mat. Sci. Eng. A, 799, (2021), 10.1016/j.msea.2020.140154.

[50] Y.-D. Im, K.-H. Kim, K.-H. Jung, Y.-K. Lee, K.-H. Song, *Anisotropic Mechanical Behavior of Additive Manufactured AISI 316L Steel*, Metallurgical and Materials Transactions A, 50(4), (2019), 2014-2021, 10.1007/s11661-019-05139-7.

[51] T. Ronneberg, C.M. Davies, P.A. Hooper, *Revealing relationships between porosity, microstructure and mechanical properties of laser powder bed fusion 316L stainless steel through heat treatment*, Mater. Des., 189, (2020), 10.1016/j.matdes.2020.108481.

[52] L. Spieß, R. Schwarzer, H. Behnken, G. Teichert, Röntgendiffraktometrie für Materialwissenschaftler, Physiker und Chemiker, B.G. Teubner Verlag / GWV Fachverlage GmbH, Wiesbaden, 2005.

[53] K.A. Sofinowski, S. Raman, X. Wang, B. Gaskey, M. Seita, *Layer-wise engineering of grain orientation (LEGO) in laser powder bed fusion of stainless steel 316L*, Addit. Manuf., 38, (2021), 10.1016/j.addma.2020.101809.

[54] D. Kong, C. Dong, S. Wei, X. Ni, L. Zhang, R. Li, L. Wang, C. Man, X. Li, *About metastable cellular structure in additively manufactured austenitic stainless steels*, Addit. Manuf., 38, (2021), 10.1016/j.addma.2020.101804.

[55] M. Godec, S. Zaefferer, B. Podgornik, M. Šinko, E. Tchernychova, *Quantitative multiscale correlative microstructure analysis of additive manufacturing of stainless steel 316L processed by selective laser melting*, Mater. Charact., 160, (**2020**), 10.1016/j.matchar.2019.110074.

[56] M. Sabzi, S.M. Dezfuli, *Drastic improvement in mechanical properties and weldability of 316L stainless steel weld joints by using electromagnetic vibration during GTAW process*, Journal of Manufacturing Processes, 33, (**2018**), 74-85, 10.1016/j.jmapro.2018.05.002.

[57] J.L. Bartlett, X. Li, *An overview of residual stresses in metal powder bed fusion*, Addit. Manuf., 27, (**2019**), 131-149, 10.1016/j.addma.2019.02.020.

[58] P.J. Withers, H.K.D.H. Bhadeshia, *Residual stress Part 1 – Measurement techniques*, Mater. Sci. Technol., 17(4), (**2001**), 355-365, 10.1179/026708301101509980.

[59] E. Macherauch, H. Wohlfahrt, U. Wolfstieg, *Zur zweckmäßigen definition von eigenspannungen*, HTM Journal of Heat Treatment and Materials, 28(3), (**1973**), 201-211,

[60] I.C. Noyan, J.B. Cohen, Residual Stress: Measurement by Diffraction and Interpretation, Springer-Verlag New York, 1987.

[61] M.T. Hutchings, Introduction to the Characterization of Residual Stress by Neutron Diffraction, CRC Press, 2005.

[62] J. Repper, M. Hofmann, C. Krempaszky, B. Regener, E. Berhuber, W. Petry, E. Werner, *Effect of macroscopic relaxation on residual stress analysis by diffraction methods*, J. Appl. Phys. (Melville, NY, U. S.), 112(6), (**2012**), 10.1063/1.4752877.

[63] M.B. Prime, *Cross-sectional mapping of residual stresses by measuring the surface contour after a cut*, J Eng Mater-T Asme, 123(2), (**2001**), 162-168, Doi 10.1115/1.1345526.

[64] J.-P. Kruth, J. Deckers, E. Yasa, R. Wauthlé, *Assessing and comparing influencing factors of residual stresses in selective laser melting using a novel analysis method*, Proceedings of the Institution of Mechanical Engineers, Part B: Journal of Engineering Manufacture, 226(6), (**2012**), 980-991, 10.1177/0954405412437085.

[65] R.J. Williams, C.M. Davies, P.A. Hooper, *A pragmatic part scale model for residual stress and distortion prediction in powder bed fusion*, Addit. Manuf., 22, (**2018**), 416-425, 10.1016/j.addma.2018.05.038.

[66] J.L. Bartlett, B.P. Croom, J. Burdick, D. Henkel, X. Li, *Revealing mechanisms of residual stress development in additive manufacturing via digital image correlation*, Addit. Manuf., 22, (**2018**), 1-12, 10.1016/j.addma.2018.04.025.

[67] T. Mishurova, S. Cabeza, K. Artzt, J. Haubrich, M. Klaus, C. Genzel, G. Requena, G. Bruno, *An Assessment of Subsurface Residual Stress Analysis in SLM Ti-6Al-4V*, Materials (Basel), 10(4), (**2017**), 10.3390/ma10040348.

[68] P.J. Withers, M. Turski, L. Edwards, P.J. Bouchard, D.J. Buttle, *Recent advances in residual stress measurement*, Int. J. Pressure Vessels Piping, 85(3), (**2008**), 118-127, 10.1016/j.ijpvp.2007.10.007.

[69] J.M. Alegre, A. Díaz, I.I. Cuesta, J.M. Manso, *Analysis of the Influence of the Thickness and the Hole Radius on the Calibration Coefficients in the Hole-Drilling Method for the Determination of Non-uniform Residual Stresses*, Exp. Mech., 59(1), (**2018**), 79-94, 10.1007/s11340-018-0433-0.

[70] A.S.f. Testing, Materials, ASTM E837 - 13a: Standard Test Method for Determining Residual Stresses by Hole-drilling Strain-gage Method, ASTM2018.

[71] A. Salmi, E. Atzeni, L. Iuliano, M. Galati, *Experimental Analysis of Residual Stresses on AlSi10Mg Parts Produced by Means of Selective Laser Melting (SLM)*, Procedia CIRP, 62, (**2017**), 458-463, 10.1016/j.procir.2016.06.030.

[72] K. An, L. Yuan, L. Dial, I. Spinelli, A.D. Stoica, Y. Gao, *Neutron residual stress measurement and numerical modeling in a curved thin-walled structure by laser powder bed fusion additive manufacturing*, Mater. Des., 135, (**2017**), 122-132, 10.1016/j.matdes.2017.09.018.

[73] P. Staron, A. Schreyer, H. Clemens, S. Mayer, Neutrons and Synchrotron Radiation in Engineering Materials Science: From Fundamentals to Applications, Wiley2017.

[74] G. Bruno, R. Fernández, G. González-Doncel, *Gauge volume effects in residual stress determination by neutron diffraction: The strength differential effect in metal matrix composites*, Mat. Sci. Eng. A, 437(1), (**2006**), 100-108, 10.1016/j.msea.2006.04.064.

[75] T. Keller, N. Margadant, T. Pirling, M.a.J. Riegert-Escribano, W. Wagner, *Residual stress determination in thermally sprayed metallic deposits by neutron diffraction*, Mat. Sci. Eng. A, 373(1-2), (**2004**), 33-44, 10.1016/j.msea.2004.01.032.

[76] W.H. Bragg, W.L. Bragg, *The reflection of X-rays by crystals*, Proceedings of the royal society A, 88, (**1913**), 428-438, 10.1098/rspa.1913.0040.

[77] J.A. Kaduk, S.J.L. Billinge, R.E. Dinnebier, N. Henderson, I. Madsen, R. Černý, M. Leoni, L. Lutterotti, S. Thakral, D. Chateigner, *Powder diffraction*, Nature Reviews Methods Primers, 1(1), (**2021**), 10.1038/s43586-021-00074-7.

[78] O. Andreau, I. Koutiri, P. Peyre, J.-D. Penot, N. Saintier, E. Pessard, T. De Terris, C. Dupuy, T. Baudin, *Texture control of 316L parts by modulation of the melt pool morphology in selective laser melting*, J. Mater. Process. Technol., 264, (**2019**), 21-31, 10.1016/j.jmatprotec.2018.08.049.

[79] M.R. Daymond, M.A.M. Bourke, R.B. Von Dreele, B. Clausen, T. Lorentzen, *Use of Rietveld refinement for elastic macrostrain determination and for evaluation of plastic strain history from diffraction spectra*, J. Appl. Phys. (Melville, NY, U. S.), 82(4), (**1997**), 1554-1562, 10.1063/1.365956.

[80] N. Mavrikakis, C. Detlefs, P.K. Cook, M. Kutsal, A.P.C. Campos, M. Gauvin, P.R. Calvillo, W. Saikaly, R. Hubert, H.F. Poulsen, A. Vaugeois, H. Zapolsky, D. Mangelinck, M. Dumont, C. Yildirim, *A multi-scale study of the interaction of Sn solutes with dislocations during static recovery in α-Fe*, Acta Mater., 174, (**2019**), 92-104, 10.1016/j.actamat.2019.05.021.

[81] T. Thiede, S. Cabeza, T. Mishurova, N. Nadammal, A. Kromm, J. Bode, C. Haberland, G. Bruno, *Residual Stress in Selective Laser Melted Inconel 718: Influence of the Removal from Base Plate and Deposition Hatch Length*, Mater. Perform. Charact., 7(4), (**2018**), 10.1520/mpc20170119.

[82] T. Mishurova, I. Serrano-Muñoz, T. Fritsch, A. Ulbricht, M. Sprengel, A. Evans, A. Kromm, M. Madia, G. Bruno, A Critical Discussion on the Diffraction-Based Experimental Determination of Residual Stress in AM Parts, Structural Integrity of Additive Manufactured Materials & Parts2020, pp. 122-138.

[83] J. Schröder, A. Evans, T. Mishurova, A. Ulbricht, M. Sprengel, I. Serrano-Munoz, T. Fritsch, A. Kromm, T. Kannengießer, G. Bruno, *Diffraction-Based Residual Stress Characterization in Laser Additive Manufacturing of Metals*, Metals, 11(11), (**2021**), 10.3390/met11111830.

[84] V. Hauk, Structural and Residual Stress Analysis by Nondestructive Methods: Evaluation - Application - Assessment, Elsevier Science1997.

[85] B. Clausen, T. Lorentzen, T. Leffers, *Self-consistent modelling of the plastic deformation of f.c.c. polycrystals and its implications for diffraction measurements of internal stresses*, Acta Mater., 46, (**1998**), 3087-3098, 10.1016/S1359-6454(98)00014-7.

[86] M.R. Daymond, C.N. Tomé, M.A.M. Bourke, *Measured and predicted intergranular strains in textured austenitic steel*, Acta Mater., 48, (**2000**), 553-564, 10.1016/S1359-6454(99)00354-7.

[87] B. Clausen, T. Leffers, T. Lorentzen, *On the proper selection of reflections for the measurement of bulk residual stresses by diffraction methods*, Acta Mater., 51(20), (**2003**), 6181-6188, 10.1016/j.actamat.2003.07.002.

[88] T.M. Holden, A.P. Clarke, R.A. Holt, *Neutron diffraction measurements of intergranular strains in MONEL-400*, Metall. Mater. Trans. A, 28(12), (**1997**), 2565-2576, 10.1007/s11661-997-0014-9.

[89] D. Dye, H.J. Stone, R.C. Reed, *Intergranular and interphase microstresses*, Curr. Opin. Solid State Mater. Sci., 5, (**2001**), 31-37, 10.1016/S1359-0286(00)00019-X.

[90] B. Clausen, Lorentzen, T., Bourke, M.A.M., Daymond, M. R. , *Lattice strain evolution during uniaxial tensile loading of stainless steel*, Mat. Sci. Eng. A, 259, (**1999**), 17-24, 10.1016/S0921-5093(98)00878-8.

[91] M.R. Daymond, P.J. Bouchard, *Elastoplastic deformation of 316 stainless steel under tensile loading at elevated temperatures*, Metall. Mater. Trans. A, 37(6), (**2006**), 1863-1873, 10.1007/s11661-006-0129-4.

[92] D. Gonzalez, J.F. Kelleher, J. Quinta da Fonseca, P.J. Withers, *Macro and intergranular stress responses of austenitic stainless steel to 90° strain path changes*, Mat. Sci. Eng. A, 546, (**2012**), 263-271, 10.1016/j.msea.2012.03.064.

[93] J.R. Santisteban, M.R. Daymond, J.A. James, L. Edwards, *ENGIN-X: a third-generation neutron strain scanner*, J. Appl. Crystallogr., 39(6), (**2006**), 812-825, 10.1107/S0021889806042245.

[94] G.S. Pawley, *Unit-Cell refinement from powder diffraction scans*, J. Appl. Crystallogr., 14, (**1981**), 357-361, 10.1107/S0021889881009618.

[95] H. Choo, M.R. Koehler, L.P. White, Y. Ren, D. Morin, E. Garlea, *Influence of defect characteristics on tensile deformation of an additively manufactured stainless steel: Evolutions of texture and intergranular strain*, Mat. Sci. Eng. A, 791, (**2020**), 10.1016/j.msea.2020.139637.

[96] T. Mishurova, K. Artzt, J. Haubrich, S. Evsevleev, A. Evans, M. Meixner, I.S. Munoz, I. Sevostianov, G. Requena, G. Bruno, *Connecting Diffraction-Based Strain with Macroscopic Stresses in Laser Powder Bed Fused Ti-6Al-4V*, Metall. Mater. Trans. A, 51(6), (**2020**), 3194-3204, 10.1007/s11661-020-05711-6.

[97] V. Hauk, Problems of the X-ray Stress Analysis (RSA) and Their Solutions, in: V. Hauk, H. Hougardy, E. Macherauch (Eds.) Conference on Residual Stress, Deutsche Gesellschaft für Materialkunde, Darmstadt, 1990, pp. 1-20.

[98] J. Schröder, T. Mishurova, T. Fritsch, I. Serrano-Munoz, A. Evans, M. Sprengel, M. Klaus, C. Genzel, J. Schneider, G. Bruno, *On the influence of heat treatment on microstructure and mechanical behavior of laser powder bed fused Inconel 718*, Mat. Sci. Eng. A, 805, (**2021**), 10.1016/j.msea.2020.140555.

[99] M. Ghasri-Khouzani, H. Peng, R. Rogge, R. Attardo, P. Ostiguy, J. Neidig, R. Billo, D. Hoelzle, M.R. Shankar, *Experimental measurement of residual stress and distortion in additively manufactured stainless steel components with various dimensions*, Mat. Sci. Eng. A, 707, (**2017**), 689-700, 10.1016/j.msea.2017.09.108.

[100] W.-J. Lai, A. Ojha, Z. Li, C. Engler-Pinto, X. Su, *Effect of residual stress on fatigue strength of 316L stainless steel produced by laser powder bed fusion process*, Progress in Additive Manufacturing, (**2021**), 10.1007/s40964-021-00164-8.

[101] ISO, 21432: Non-destructive testing, Standard test method for determining residual stresses by neutron diffraction, 2019.

[102] Z. Wang, E. Denlinger, P. Michaleris, A.D. Stoica, D. Ma, A.M. Beese, *Residual stress mapping in Inconel 625 fabricated through additive manufacturing: Method for neutron diffraction measurements to validate thermomechanical model predictions*, Mater. Des., 113, (**2017**), 169-177, 10.1016/j.matdes.2016.10.003.

[103] D.W. Brown, J.D. Bernardin, J.S. Carpenter, B. Clausen, D. Spernjak, J.M. Thompson, *Neutron diffraction measurements of residual stress in additively manufactured stainless steel*, Mat. Sci. Eng. A, 678, (**2016**), 291-298, 10.1016/j.msea.2016.09.086.

[104] D. Gloaguen, B. Girault, B. Courant, P.-A. Dubos, M.-J. Moya, F. Edy, J. Rebelo Kornmeier, *Study of Residual Stresses in Additively Manufactured Ti-6Al-4V by Neutron Diffraction Measurements*, Metall. Mater. Trans. A, 51(2), (**2019**), 951-961, 10.1007/s11661-019-05538-w.

[105] F. Schmeiser, E. Krohmer, N. Schell, E. Uhlmann, W. Reimers, *Experimental observation of stress formation during selective laser melting using in situ X-ray diffraction*, Addit. Manuf., (**2019**), 10.1016/j.addma.2019.101028.

[106] D. Radaj, Eigenspannungen und Verzug beim Schweißen, Wärmewirkungen des Schweißens: Temperaturfeld, Eigenspannungen, Verzug, Springer Berlin Heidelberg, Berlin, Heidelberg, 1988, pp. 86-181.

[107] A. Scotti, *Five-bar and one-bar models for thermal stress generation in the FZ, HAZ, and BM during arc welding*, Welding International, 30(5), (**2016**), 329-337, 10.1080/09507116.2015.1096495.

[108] S. Pratihar, M. Turski, L. Edwards, P.J. Bouchard, *Neutron diffraction residual stress measurements in a 316L stainless steel bead-on-plate weld specimen*, International Journal of Pressure Vessels and Piping, 86(1), (**2009**), 13-19, 10.1016/j.ijpvp.2008.11.010.

[109] Y. Liu, Y. Yang, D. Wang, *A study on the residual stress during selective laser melting (SLM) of metallic powder*, The International Journal of Advanced Manufacturing Technology, 87(1-4), (**2016**), 647-656, 10.1007/s00170-016-8466-y.

[110] I. Yadroitsev, I. Yadroitsava, *Evaluation of residual stress in stainless steel 316L and Ti6Al4V samples produced by selective laser melting*, Virtual and Physical Prototyping, 10(2), (**2015**), 67-76, 10.1080/17452759.2015.1026045.

[111] T. Simson, A. Emmel, A. Dwars, J. Böhm, *Residual stress measurements on AISI 316L samples manufactured by selective laser melting*, Addit. Manuf., 17, (**2017**), 183-189, 10.1016/j.addma.2017.07.007.

[112] A. Salmi, E. Atzeni, *Residual stress analysis of thin AlSi10Mg parts produced by Laser Powder Bed Fusion*, Virtual and Physical Prototyping, (**2019**), 1-13, 10.1080/17452759.2019.1650237.

[113] K. Artzt, T. Mishurova, P.-P. Bauer, J. Gussone, P. Barriobero-Vila, S. Evsevleev, G. Bruno, G. Requena, J. Haubrich, *Pandora's Box–Influence of Contour Parameters on Roughness and Subsurface Residual Stresses in Laser Powder Bed Fusion of Ti-6Al-4V*, Materials, 13(15), (**2020**), 10.3390/ma13153348.

[114] R. Barros, F.J.G. Silva, R.M. Gouveia, A. Saboori, G. Marchese, S. Biamino, A. Salmi, E. Atzeni, *Laser Powder Bed Fusion of Inconel 718: Residual Stress Analysis Before and After Heat Treatment*, Metals, 9(12), (**2019**), 10.3390/met9121290.

[115] Y. Lu, S. Wu, Y. Gan, T. Huang, C. Yang, L. Junjie, J. Lin, *Study on the microstructure, mechanical property and residual stress of SLM Inconel-718 alloy manufactured by differing island scanning strategy*, Opt. Laser Technol., 75, (**2015**), 197-206, 10.1016/j.optlastec.2015.07.009.

[116] A. Ulbricht, S.J. Altenburg, M. Sprengel, K. Sommer, G. Mohr, T. Fritsch, T. Mishurova, I. Serrano-Munoz, A. Evans, M. Hofmann, G. Bruno, *Separation of the Formation Mechanisms of Residual Stresses in LPBF 316L*, Metals, 10(9), (**2020**), 10.3390/met10091234.

[117] M. Busi, N. Kalentics, M. Morgano, S. Griffiths, A.S. Tremsin, T. Shinohara, R. Logé, C. Leinenbach, M. Strobl, *Nondestructive characterization of laser powder bed*

fusion parts with neutron Bragg edge imaging, Addit. Manuf., 39, (**2021**), 10.1016/j.addma.2021.101848.

[118] A. Eliasu, S.H. Duntu, K.S. Hukpati, M.Y. Amegadzie, J. Agyapong, F. Tetteh, A. Czekanski, S. Boakye-Yiadom, *Effect of individual printing parameters on residual stress and tribological behaviour of 316L stainless steel fabricated with laser powder bed fusion (L-PBF)*, The International Journal of Advanced Manufacturing Technology, (**2022**), 10.1007/s00170-021-08489-y.

[119] A.S. Wu, D.W. Brown, M. Kumar, G.F. Gallegos, W.E. King, *An Experimental Investigation into Additive Manufacturing-Induced Residual Stresses in 316L Stainless Steel*, Metall. Mater. Trans. A, 45(13), (**2014**), 6260-6270, 10.1007/s11661-014-2549-x.

[120] M.F. Zaeh, G. Branner, *Investigations on residual stresses and deformations in selective laser melting*, Production Engineering, 4(1), (**2009**), 35-45, 10.1007/s11740-009-0192-y.

[121] L.A. Parry, I.A. Ashcroft, R.D. Wildman, *Geometrical effects on residual stress in selective laser melting*, Addit. Manuf., 25, (**2019**), 166-175, 10.1016/j.addma.2018.09.026.

[122] S. Santa-aho, M. Kiviluoma, T. Jokiaho, T. Gundgire, M. Honkanen, M. Lindgren, M. Vippola, *Additive Manufactured 316L Stainless-Steel Samples: Microstructure, Residual Stress and Corrosion Characteristics after Post-Processing*, Metals, 11(2), (**2021**), 10.3390/met11020182.

[123] P. Bian, J. Shi, Y. Liu, Y. Xie, *Influence of laser power and scanning strategy on residual stress distribution in additively manufactured 316L steel*, Opt. Laser Technol., 132, (**2020**), 10.1016/j.optlastec.2020.106477.

[124] A. Riemer, S. Leuders, M. Thöne, H.A. Richard, T. Tröster, T. Niendorf, *On the fatigue crack growth behavior in 316L stainless steel manufactured by selective laser melting*, Eng. Fract. Mech., 120, (**2014**), 15-25, 10.1016/j.engfracmech.2014.03.008.

[125] T. Mishurova, K. Artzt, J. Haubrich, G. Requena, G. Bruno, *Exploring the Correlation between Subsurface Residual Stresses and Manufacturing Parameters in Laser Powder Bed Fused Ti-6Al-4V*, Metals, 9(2), (**2019**), 10.3390/met9020261.

[126] A. Staub, A.B. Spierings, K. Wegener, *Correlation of meltpool characteristics and residual stresses at high laser intensity for metal lpbf process*, Adv. Mat. Pro. Tech., 5(1), (**2018**), 153-161, 10.1080/2374068x.2018.1535643.

[127] M. Yakout, M.A. Elbestawi, S.C. Veldhuis, S. Nangle-Smith, *Influence of thermal properties on residual stresses in SLM of aerospace alloys*, Rapid Prototyping J., ahead-of-print(ahead-of-print), (**2019**), 10.1108/rpj-03-2019-0065.

[128] I. Serrano-Munoz, A. Evans, T. Mishurova, M. Sprengel, T. Pirling, A. Kromm, G. Bruno, *The Importance of Subsurface Residual Stress in Laser Powder Bed Fusion IN718*, Adv. Eng. Mater., (2021), 10.1002/adem.202100895.

[129] F. Bayerlein, F. Bodensteiner, C. Zeller, M. Hofmann, M.F. Zaeh, *Transient development of residual stresses in laser beam melting – A neutron diffraction study*, Addit. Manuf., 24, (2018), 587-594, 10.1016/j.addma.2018.10.024.

[130] B. Vrancken, V. Cain, R. Knutsen, J. Van Humbeeck, *Residual stress via the contour method in compact tension specimens produced via selective laser melting*, Scripta Materialia, 87, (2014), 29-32, 10.1016/j.scriptamat.2014.05.016.

[131] P. Pant, S. Proper, V. Luzin, S. Sjöström, K. Simonsson, J. Moverare, S. Hosseini, V. Pacheco, R.L. Peng, *Mapping of residual stresses in as-built Inconel 718 fabricated by laser powder bed fusion: A neutron diffraction study of build orientation influence on residual stresses*, Addit. Manuf., 36, (2020), 10.1016/j.addma.2020.101501.

[132] C. Li, Z.Y. Liu, X.Y. Fang, Y.B. Guo, *Residual Stress in Metal Additive Manufacturing*, Procedia CIRP, 71, (2018), 348-353, 10.1016/j.procir.2018.05.039.

[133] Z.-C. Fang, Z.-L. Wu, C.-G. Huang, C.-W. Wu, *Review on residual stress in selective laser melting additive manufacturing of alloy parts*, Opt. Laser Technol., 129, (2020), 10.1016/j.optlastec.2020.106283.

[134] R. Acevedo, P. Sedlak, R. Kolman, M. Fredel, *Residual stress analysis of additive manufacturing of metallic parts using ultrasonic waves: State of the art review*, J. Mater. Res. Technol., 9(4), (2020), 9457-9477, 10.1016/j.jmrt.2020.05.092.

[135] R. Shrestha, N. Shamsaei, M. Seifi, N. Phan, *An investigation into specimen property to part performance relationships for laser beam powder bed fusion additive manufacturing*, Addit. Manuf., 29, (2019), 100807, 10.1016/j.addma.2019.100807.

[136] H.C. Taylor, E.A. Garibay, R.B. Wicker, *Toward a common laser powder bed fusion qualification test artifact*, Addit. Manuf., 39, (2021), 10.1016/j.addma.2020.101803.

[137] H. Ali, L. Ma, H. Ghadbeigi, K. Mumtaz, *In-situ residual stress reduction, martensitic decomposition and mechanical properties enhancement through high temperature powder bed pre-heating of Selective Laser Melted Ti6Al4V*, Mat. Sci. Eng. A, 695, (2017), 211-220, 10.1016/j.msea.2017.04.033.

[138] D. Buchbinder, W. Meiners, N. Pirch, K. Wissenbach, J. Schrage, *Investigation on reducing distortion by preheating during manufacture of aluminum components using selective laser melting*, Journal of Laser Applications, 26(1), (2014), 10.2351/1.4828755.

[139] P. Bleys, J.P. Kruth, B. Lauwers, B. Schacht, V. Balasubramanian, L. Froyen, J. Van Humbeeck, *Surface and Sub-Surface Quality of Steel after EDM*, Adv. Eng. Mater., 8(1-2), (**2006**), 15-25, 10.1002/adem.200500211.

[140] G. Mohr, K. Sommer, T. Knobloch, S.J. Altenburg, S. Recknagel, D. Bettge, K. Hilgenberg, *Process Induced Preheating in Laser Powder Bed Fusion Monitored by Thermography and Its Influence on the Microstructure of 316L Stainless Steel Parts*, Metals, 11(7), (**2021**), 10.3390/met11071063.

[141] C. Casavola, S.L. Campanelli, C. Pappalettere, *Preliminary investigation on distribution of residual stress generated by the selective laser melting process*, J. Strain Anal. Eng. Des., 44(1), (**2008**), 93-104, 10.1243/03093247jsa464.

[142] T. Mishurova, K. Artzt, J. Haubrich, G. Requena, G. Bruno, *New aspects about the search for the most relevant parameters optimizing SLM materials*, Addit. Manuf., 25, (**2019**), 325-334, 10.1016/j.addma.2018.11.023.

[143] L. Sun, X. Ren, J. He, Z. Zhang, *A bead sequence-driven deposition pattern evaluation criterion for lowering residual stresses in additive manufacturing*, Addit. Manuf., 48, (**2021**), 10.1016/j.addma.2021.102424.

[144] S. Catchpole-Smith, N. Aboulkhair, L. Parry, C. Tuck, I.A. Ashcroft, A. Clare, *Fractal scan strategies for selective laser melting of 'unweldable' nickel superalloys*, Addit. Manuf., 15, (**2017**), 113-122, 10.1016/j.addma.2017.02.002.

[145] D. Wang, S. Wu, Y. Yang, W. Dou, S. Deng, Z. Wang, S. Li, *The Effect of a Scanning Strategy on the Residual Stress of 316L Steel Parts Fabricated by Selective Laser Melting (SLM)*, Materials, 11, (**2018**), 10.3390/ma11101821.

[146] J. Robinson, I. Ashton, P. Fox, E. Jones, C. Sutcliffe, *Determination of the effect of scan strategy on residual stress in laser powder bed fusion additive manufacturing*, Addit. Manuf., 23, (**2018**), 13-24, 10.1016/j.addma.2018.07.001.

[147] J. Hajnys, M. Pagac, J. Mesicek, J. Petru, M. Krol, *Influence of Scanning Strategy Parameters on Residual Stress in the SLM Process According to the Bridge Curvature Method for AISI 316L Stainless Steel*, Materials, 13, (**2020**), 10.3390/ma13071659.

[148] J.H. Robinson, I.R.T. Ashton, E. Jones, P. Fox, C. Sutcliffe, *The effect of hatch angle rotation on parts manufactured using selective laser melting*, Rapid Prototyping J., 25(2), (**2019**), 289-298, 10.1108/rpj-06-2017-0111.

[149] I. Serrano-Munoz, T. Mishurova, T. Thiede, M. Sprengel, A. Kromm, N. Nadammal, G. Nolze, R. Saliwan-Neumann, A. Evans, G. Bruno, *The residual stress in as-built Laser Powder Bed Fusion IN718 alloy as a consequence of the scanning strategy induced microstructure*, Sci Rep, 10(1), (**2020**), 14645, 10.1038/s41598-020-71112-9.

[150] L. Hitzler, M. Merkel, W. Hall, A. Öchsner, *A Review of Metal Fabricated with Laser- and Powder-Bed Based Additive Manufacturing Techniques: Process, Nomenclature, Materials, Achievable Properties, and its Utilization in the Medical Sector*, Adv. Eng. Mater., 20(5), (**2018**), 10.1002/adem.201700658.

[151] L. Mugwagwa, D. Dimitrov, S. Matope, I. Yadroitsev, *Influence of process parameters on residual stress related distortions in selective laser melting*, Procedia Manufacturing, 21, (**2018**), 92-99, 10.1016/j.promfg.2018.02.099.

[152] L. Mugwagwa, I. Yadroitsev, S. Matope, *Effect of Process Parameters on Residual Stresses, Distortions, and Porosity in Selective Laser Melting of Maraging Steel 300*, Metals, 9(10), (**2019**), 10.3390/met9101042.

[153] S. Waqar, K. Guo, J. Sun, *FEM analysis of thermal and residual stress profile in selective laser melting of 316L stainless steel*, J. Manuf. Pro., 66, (**2021**), 81-100, 10.1016/j.jmapro.2021.03.040.

[154] Z. Xiao, C. Chen, H. Zhu, Z. Hu, B. Nagarajan, L. Guo, X. Zeng, *Study of residual stress in selective laser melting of Ti6Al4V*, Mater. Des., 193, (**2020**), 10.1016/j.matdes.2020.108846.

[155] J.P. Oliveira, T.G. Santos, R.M. Miranda, *Revisiting fundamental welding concepts to improve additive manufacturing: From theory to practice*, Progress in Materials Science, 107, (**2020**), 10.1016/j.pmatsci.2019.100590.

[156] P. Pant, S. Sjöström, K. Simonsson, J. Moverare, S. Proper, S. Hosseini, V. Luzin, R. Peng, *A Simplified Layer-by-Layer Model for Prediction of Residual Stress Distribution in Additively Manufactured Parts*, Metals, 11(6), (**2021**), 10.3390/met11060861.

[157] G. Mohr, S.J. Altenburg, K. Hilgenberg, *Effects of inter layer time and build height on resulting properties of 316L stainless steel processed by laser powder bed fusion*, Addit. Manuf., 32, (**2020**), 10.1016/j.addma.2020.101080.

[158] E.W. Lui, W. Xu, A. Pateras, M. Qian, M. Brandt, *New Development in Selective Laser Melting of Ti–6Al–4V: A Wider Processing Window for the Achievement of Fully Lamellar $\alpha + \beta$ Microstructures*, Jom, 69(12), (**2017**), 2679-2683, 10.1007/s11837-017-2599-9.

[159] B. Torries, S. Shao, N. Shamsei, S.M. Thompson, *Effect of inter-layer time interval on the mechanical behavior of direct laser deposited Ti-6Al-4V*, Solid Freeform Fabrication Symposium, (**2016**), 1272–1282,

[160] A. Yadollahi, N. Shamsaei, S.M. Thompson, D.W. Seely, *Effects of process time interval and heat treatment on the mechanical and microstructural properties of*

direct laser deposited 316L stainless steel, Mat. Sci. Eng. A, 644, (**2015**), 171-183, 10.1016/j.msea.2015.07.056.

[161] E.R. Denlinger, J.C. Heigel, P. Michaleris, T.A. Palmer, *Effect of inter-layer dwell time on distortion and residual stress in additive manufacturing of titanium and nickel alloys*, J. Mater. Process. Technol., 215, (**2015**), 123-131, 10.1016/j.jmatprotec.2014.07.030.

[162] L. Mugwaga, *A Methodology to Evluate the Influence of Part Geometry on Residual Stresses in Selective Laser Melting*,

[163] M.S.I.N. Kamariah, W.S.W. Harun, N.Z. Khalil, F. Ahmad, M.H. Ismail, S. Sharif, *Effect of heat treatment on mechanical properties and microstructure of selective laser melting 316L stainless steel*, IOP Conf. Ser.: Mater. Sci. Eng., 257, (**2017**), 10.1088/1757-899x/257/1/012021.

[164] M.L.M. Sistiaga, S. Nardone, C. Hautfenne, J. Van Humbeeck, *Effect of heat treatment of 316L stainless steel produced by Selective Laser Melting (SLM)*, Solid Freeform Fabrication Symposium, (**2016**),

[165] O.O. Salman, C. Gammer, A.K. Chaubey, J. Eckert, S. Scudino, *Effect of heat treatment on microstructure and mechanical properties of 316L steel synthesized by selective laser melting*, Mat. Sci. Eng. A, 748, (**2019**), 205-212,

[166] G. Totten, M. Howes, T. Inoue, *Handbook of Residual Stress and Deformation of Steel*, ASM International Publishers, USA, (**2002**), 417-444,

[167] J. Hoffmann, B. Scholtes, O. Voehringer, E. Macherauch, Relaxation of Residual Stresses of Various Sources by Annealing, in: E. Macherauch, V. Hauk (Eds.) Internation Conference on Residual Stresses, Deutsche Gesellschaft für Materialkunde, Garmisch-Partenkirchen, 1986.

[168] N.H. Tak, J.S. Kim, J.Y. Lim, *An Energy-Based Unified Approach to Predict the Low-Cycle Fatigue Life of Type 316L Stainless Steel under Various Temperatures and Strain-Rates*, Materials (Basel), 12(7), (**2019**), 10.3390/ma12071090.

[169] B.K. Choudhary, *Influence of Strain Rate and Temperature on Tensile Deformation and Fracture Behavior of Type 316L(N) Austenitic Stainless Steel*, Metall. Mater. Trans. A, 45(1), (**2013**), 302-316, 10.1007/s11661-013-1978-2.

[170] B. Diepold, S. Neumeier, A. Meermeier, H.W. Höppel, T. Sebald, M. Göken, *Temperature-Dependent Dynamic Strain Aging in Selective Laser Melted 316L*, Adv. Eng. Mater., (**2021**), 10.1002/adem.202001501.

[171] *Properties and Selection: Irons, Steels and High performance Alloys*, ASM Handbook, 1, (**1991**),

[172] M. Sprengel, A. Ulbricht, A. Evans, A. Kromm, K. Sommer, T. Werner, J. Kelleher, G. Bruno, T. Kannengiesser, *Towards the Optimization of Post-Laser Powder Bed Fusion Stress-Relieve Treatments of Stainless Steel 316L*, Metall. Mater. Trans. A, (**2021**), 10.1007/s11661-021-06472-6.

[173] F.R. Larson, J. Miller, *A time-temperature relationship for rupture and creep stresses* Trans. ASME, 74, (**1952**), 765-71,

[174] A.K. Koul, R. Castillo, K. Willett, *Creep Life Predictions in Nickel-based Superalloys*, Materials Science and Engineering, (66), (**1984**), 213-226,

[175] V. Cruz, Q. Chao, N. Birbilis, D. Fabijanic, P.D. Hodgson, S. Thomas, *Electrochemical studies on the effect of residual stress on the corrosion of 316L manufactured by selective laser melting*, Corros. Sci., 164, (**2020**), 10.1016/j.corsci.2019.108314.

[176] Q. Bai, H. Feng, L.-K. Si, R. Pan, Y.-Q. Wang, *A Novel Stress Relaxation Modeling for Predicting the Change of Residual Stress During Annealing Heat Treatment*, Metall. Mater. Trans. A, 50(12), (**2019**), 5750-5759, 10.1007/s11661-019-05454-z.

[177] X. Zhang, M.D. McMurtrey, L. Wang, R.C. O'Brien, C.-H. Shiau, Y. Wang, R. Scott, Y. Ren, C. Sun, *Evolution of Microstructure, Residual Stress, and Tensile Properties of Additively Manufactured Stainless Steel Under Heat Treatments*, Jom, 72(12), (**2020**), 4167-4177, 10.1007/s11837-020-04433-9.

[178] Screw thread tensile. https://www.isis.stfc.ac.uk/Pages/screw_thread_tensile10371.pdf.

[179] ISO, 11562: Geometrical product specification (GPS)-surface texture: profile method-metrological characteristics of phase correct filters, International Organization for Standardization Geneva, 1996.

[180] DIN, DIN EN ISO 4288:1998-04, Geometrical Product Specifications (GPS) - Surface texture: Profile method - Rules and procedures for the assessment of surface texture, 1998.

[181] M. Sprengel, G. Mohr, S.J. Altenburg, A. Evans, I. Serrano-Munoz, A. Kromm, T. Pirling, G. Bruno, T. Kannengiesser, *Triaxial Residual Stress in Laser Powder Bed fused 316L: Effects of Inter-Layer-Time and Scanning Velocity*, Adv. Eng. Mater., (**2021**), 10.1002/adem.202101330.

[182] E. Macherauch, B. Eigenmann, Röntgenographische Bestimmung elastischer Spannungen, in: F.H.W. Heuck, E. Macherauch (Eds.), Forschung mit Röntgenstrahlen: Bilanz eines Jahrhunderts (1895–1995), Springer Berlin Heidelberg, Berlin, Heidelberg, 1995, pp. 473-504.

[183] H. Wern, R. Johannes, H. Walz, *Dependence of the X-Ray Elastic Constants on the Diffraction Plane*, physica status solidi (b), 206(2), (**1998**), 545-557, 10.1002/(SICI)1521-3951(199804)206:2<545::AID-PSSB545>3.0.CO;2-J.

[184] T. Poeste, R.C. Wimpory, R. Schneider, *The New and Upgraded Neutron Instruments for Materials Science at HMI - Current Activities in Cooperation with Industry*, Mater. Sci. Forum, 524-525, (**2006**), 223-228, 10.4028/www.scientific.net/MSF.524-525.223.

[185] T. Pirling, G. Bruno, P.J. Withers, *SALSA—A new instrument for strain imaging in engineering materials and components*, Mat. Sci. Eng. A, 437(1), (**2006**), 139-144, 10.1016/j.msea.2006.04.083.

[186] C. Randau, U. Garbe, H.G. Brokmeier, *StressTextureCalculator: a software tool to extract texture, strain and microstructure information from area-detector measurements*, J. Appl. Crystallogr., 44(3), (**2011**), 641-646, 10.1107/s0021889811012064.

[187] D. Richard, M. Ferrand, G.J. Kearley, *Analysis and Visualisation of Neutron-Scattering Data*, Journal of Neutron Research, 4, (**1996**), 33-39, 10.1080/10238169608200065.

[188] C.M. Moreton-Smith, S.D. Johnston, F.A. Akeroyd, *Open GENIE—A Generic Multi-Platform Program for the Analysis of Neutron Scattering Data*, Journal of Neutron Research, 4, (**1996**), 41-47, 10.1080/10238169608200066.

[189] P. Rangaswamy, T.M. Holden, R.B. Rogge, M.L. Griffith, *Residual stresses in components formed by the laserengineered net shaping (LENS®) process*, J. Strain Anal. Eng. Des., 38(6), (**2003**), 519-527, 10.1243/030932403770735881.

[190] F.C. Pinto, L.S. Aota, I.R. Souza Filho, D. Raabe, H.R.Z. Sandim, *Recrystallization in non-conventional microstructures of 316L stainless steel produced via laser powder-bed fusion: effect of particle coarsening kinetics*, J. Mater. Sci., 57(21), (**2022**), 9576-9598, 10.1007/s10853-021-06859-1.

[191] C.-H. Yu, R.L. Peng, V. Luzin, M. Sprengel, M. Calmunger, J.-E. Lundgren, H. Brodin, A. Kromm, J. Moverare, *Thin-wall effects and anisotropic deformation mechanisms of an additively manufactured Ni-based superalloy*, Addit. Manuf., 36, (**2020**), 10.1016/j.addma.2020.101672.

[192] A. Leicht, U. Klement, E. Hryha, *Effect of build geometry on the microstructural development of 316L parts produced by additive manufacturing*, Mater. Charact., 143, (**2018**), 137-143, 10.1016/j.matchar.2018.04.040.

[193] N. Nadammal, S. Cabeza, T. Mishurova, T. Thiede, A. Kromm, C. Seyfert, L. Farahbod, C. Haberland, J.A. Schneider, P.D. Portella, G. Bruno, *Effect of hatch*

length on the development of microstructure, texture and residual stresses in selective laser melted superalloy Inconel 718, Mater. Des., 134, (**2017**), 139-150, 10.1016/j.matdes.2017.08.049.

[194] C.-H. Yu, M. Sprengel, J. Schröder, I. Serrano-Munoz, G. Mohr, A. Evans, A. Kromm, R. L. Peng, T. Kannengiesser, G. Bruno, J. Moverare, Distribution of subsurface residual stress as a function of wall thickness in stainless steel 316L LPBF structures, International Conference on Residual Stresses, Nancy, 2022.

[195] B.-Q. Li, Z. Li, P. Bai, B. Liu, Z. Kuai, *Research on Surface Roughness of AlSi10Mg Parts Fabricated by Laser Powder Bed Fusion*, Metals, 8(7), (**2018**), 10.3390/met8070524.

[196] D.W. Brown, D.P. Adams, L. Balogh, J.S. Carpenter, B. Clausen, G. King, B. Reedlunn, T.A. Palmer, M.C. Maguire, S.C. Vogel, *In Situ Neutron Diffraction Study of the Influence of Microstructure on the Mechanical Response of Additively Manufactured 304L Stainless Steel*, Metall. Mater. Trans. A, 48(12), (**2017**), 6055-6069, 10.1007/s11661-017-4330-4.

[197] A.K. Kanjarla, R.A. Lebensohn, L. Balogh, C.N. Tomé, *Study of internal lattice strain distributions in stainless steel using a full-field elasto-viscoplastic formulation based on fast Fourier transforms*, Acta Mater., 60(6-7), (**2012**), 3094-3106, 10.1016/j.actamat.2012.02.014.

[198] T. Yang, D. Xie, W. Yue, S. Wang, P. Rong, L. Shen, J. Zhao, C. Wang, *Distortion of Thin-Walled Structure Fabricated by Selective Laser Melting Based on Assumption of Constraining Force-Induced Distortion*, Metals, 9(12), (**2019**), 10.3390/met9121281.

[199] R.J. Moat, A.J. Pinkerton, L. Li, P.J. Withers, M. Preuss, *Residual stresses in laser direct metal deposited Waspaloy*, Mat. Sci. Eng. A, 528(6), (**2011**), 2288-2298, 10.1016/j.msea.2010.12.010.

[200] N. Takata, H. Kodaira, A. Suzuki, M. Kobashi, *Size dependence of microstructure of AlSi10Mg alloy fabricated by selective laser melting*, Mater. Charact., 143, (**2018**), 18-26, 10.1016/j.matchar.2017.11.052.

[201] Kromm, Residual Stresses in Selective Laser Melted Samples of a Nickel Based Superalloy, Residual Stresses 2018, 2018, pp. 259-264.

[202] P. Hou, S. Mooraj, V.K. Champagne, M.J. Siopis, P.K. Liaw, S. Gerasimidis, W. Chen, *Effect of Build Height on Temperature Evolution and Thermally Induced Residual Stresses in Plasma Arc Additively Manufactured Stainless Steel*, Metallurgical and Materials Transactions A, (**2021**), 10.1007/s11661-021-06538-5.

[203] P. He, C. Sun, Y. Wang, *Material distortion in laser-based additive manufacturing of fuel cell component: Three-dimensional numerical analysis*, Addit. Manuf., 46, (**2021**), 102188, 10.1016/j.addma.2021.102188.

[204] V. Luzin, N. Hoye, Stress in Thin Wall Structures Made by Layer Additive Manufacturing, in: T.M. Holden, O. Muránsky, L. Edwards (Eds.) International Conference on Residual Stresses 2016 ICRS-10, Sydney, 2017, pp. 497-502.

[205] J.E. Agapakis, K. Masubuchi, *Analytical Modeling of Thermal Stress Relieving in Stainless and Hight Strength Steel Weldments*, Welding Journal, 63, (**1984**), 187-196,

[206] A. Shaji Karapuzha, D. Fraser, D. Schliephake, S. Dietrich, Y. Zhu, X. Wu, A. Huang, *Microstructure, mechanical behaviour and strengthening mechanisms in Hastelloy X manufactured by electron beam and laser beam powder bed fusion*, Journal of Alloys and Compounds, 862, (**2021**), 10.1016/j.jallcom.2020.158034.

[207] S.J. Altenburg, N. Scheuschner, C. Maierhofer, G. Mohr, K. Hilgenberg, *Thermography in laser powder bed fusion of metals: time over threshold as feasible feature in thermographic data*, Conference Proceedings 15th Quantitative InfraRed Thermography conference, (**2020**),

[208] P.J. Withers, M. Preuss, A. Steuwer, J.W.L. Pang, *Methods for obtaining the strain-free lattice parameter when using diffraction to determine residual stress*, J. Appl. Crystallogr., 40, (**2007**), 891-904,

[209] B. Ahmad, S.O. van der Veen, M.E. Fitzpatrick, H. Guo, *Residual stress evaluation in selective-laser-melting additively manufactured titanium (Ti-6Al-4V) and inconel 718 using the contour method and numerical simulation*, Addit. Manuf., 22, (**2018**), 571-582, 10.1016/j.addma.2018.06.002.

[210] A.K. Syed, B. Ahmad, H. Guo, T. Machry, D. Eatock, J. Meyer, M.E. Fitzpatrick, X. Zhang, *An experimental study of residual stress and direction-dependence of fatigue crack growth behaviour in as-built and stress-relieved selective-laser-melted Ti6Al4V*, Mat. Sci. Eng. A, 755, (**2019**), 246-257, 10.1016/j.msea.2019.04.023.

[211] O. Muránsky, C.J. Hamelin, F. Hosseinzadeh, M.B. Prime, *Evaluation of a self-equilibrium cutting strategy for the contour method of residual stress measurement*, Int. J. Pressure Vessels Piping, 164, (**2018**), 22-31, 10.1016/j.ijpvp.2017.04.002.

[212] O. Muránsky, F. Hosseinzadeh, C.J. Hamelin, Y. Traore, P.J. Bendeich, *Investigating optimal cutting configurations for the contour method of weld residual stress measurement*, Int. J. Pressure Vessels Piping, 164, (**2018**), 55-67, 10.1016/j.ijpvp.2017.04.006.

[213] Y. Traore, F. Hosseinzadeh, P.J. Bouchard, *Plasticity in the Contour Method of Residual Stress Measurement*, Advanced Materials Research, 996, (**2014**), 337-342, 10.4028/www.scientific.net/AMR.996.337.

[214] P. Deng, H. Yin, M. Song, D. Li, Y. Zheng, B.C. Prorok, X. Lou, *On the Thermal Stability of Dislocation Cellular Structures in Additively Manufactured Austenitic Stainless Steels: Roles of Heavy Element Segregation and Stacking Fault Energy*, Jom, 72(12), (**2020**), 4232-4243, 10.1007/s11837-020-04427-7.

[215] R.W. Fonda, D.J. Rowenhorst, C.R. Feng, A.J. Levinson, K.E. Knipling, S. Olig, A. Ntiros, B. Stiles, R. Rayne, *The Effects of Post-processing in Additively Manufactured 316L Stainless Steels*, Metall. Mater. Trans. A, 51(12), (**2020**), 6560-6573, 10.1007/s11661-020-06039-x.

[216] Q. Chao, S. Thomas, N. Birbilis, P. Cizek, P.D. Hodgson, D. Fabijanic, *The effect of post-processing heat treatment on the microstructure, residual stress and mechanical properties of selective laser melted 316L stainless steel*, Mat. Sci. Eng. A, 821, (**2021**), 10.1016/j.msea.2021.141611.

List of Figures

List of Tables

Appendix

A.I: Correction of partially immersed measurement points

The correction of the partially immersed measurement points is two-fold. First the measurement position is corrected. During the experiment, the measurement position is the centre of the instrument. More specifically, the measurement position corresponds to the centre of scattering, for which the primary and secondary optics were calibrated for. Prior to the experiment the size of the gauge volume is determined by scanning through a copper foil (see A. 1 a). In this graph, the distance between the surface and measurement position is plotted against the position of the gauge volume. When the gauge volume is fully immersed, the distance from the specimen and position in the specimen corresponds to one another (linear part of the curve). Close to the surface, the position shifts as the centre of mass of the gauge volume is shifted. Furthermore, the theoretical intensity evolution when scanning through the specimen is calculated. This step considers the specimen geometry (path length), the absorption coefficient of the material and the instrument set-up. The measured intensity and corresponding measurement positions are then fitted to the theoretical intensity (see A. 1 b). These steps are necessary to correct the position of the centre of mass of the gauge volume.

When setting up the instrument, the secondary optics is aligned toward the scattering centre for the 2θ angle corresponding to the targeted reflection. This detector is position sensitive. Each neutron diffracted towards the detector is giving information on the diffraction angle. However, if the gauge volume centre is shifted due to the partial immersion, a shift in the peak position will occur (i.e. this is equivalent to a change in strain). Since the correct gauge position has been determined in the preliminary step, this shift can be corrected for.

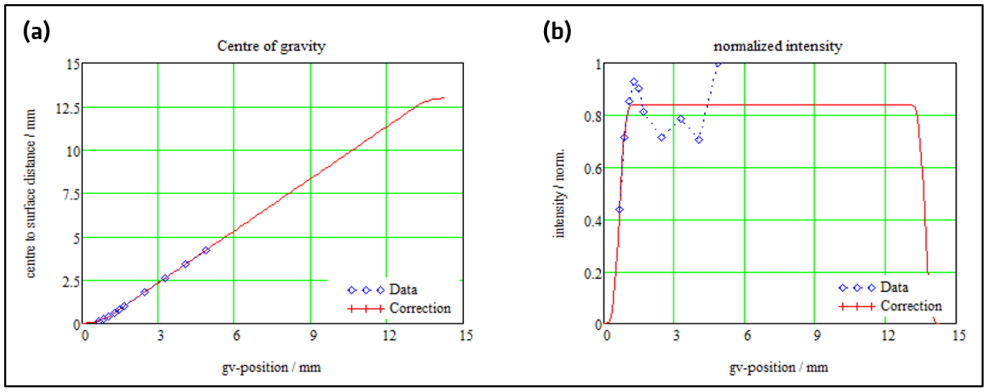

A. 1: a) Comparison of the measured and b) simulated gauge volume position.

The corrected values were provided by the instrument scientist. An example is given in Table A. 1. The error of the calculated strain in the same specimen and measurement orientation is in average 56 µm strain. The strains in this direction are in the order of multiples of 10^{-4} µstrain. The positions of the depth profile acquired using neutron diffraction are shown in Figure 3.18.

Table A. 1: Example of corrected measurement positions and associated strain difference in near surface neutron diffraction measurements

Measurement position in mm	Corrected Positions in mm	Position in sample in mm	Strain difference in µstrain
-2.6	-2.45	0.156	181
-2.4	-2.35	0.258	155
-2.2	-2.19	0.416	128
-2.0	-2	0.61	101
-1.8	-1.8	0.81	76

A.II : Additional microstructure and roughness analysis

The optical images of the microstructure shown in A. 2 show that the porosity is on a low level. The porosity of the wall specimens is assumed to be similar to the specimen with a volumetric energy density of 65 J.mm^{-3} and an ILT of 65 s (see A. 3), as the identical set of parameters was used.

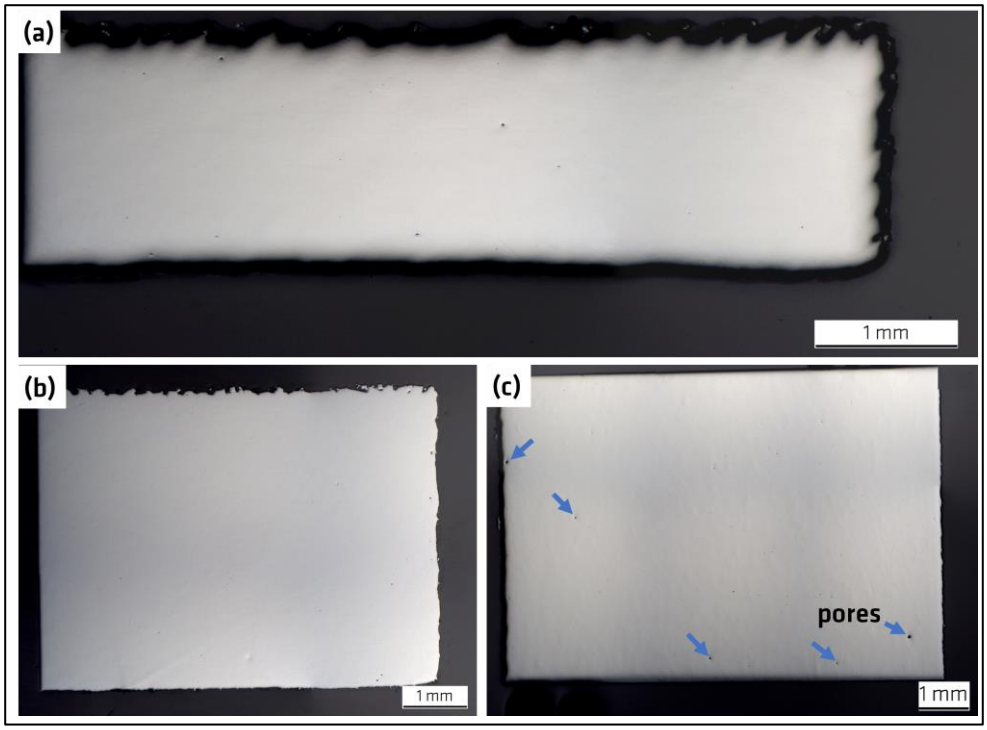

A. 2: a) Porosity in the X-Y plane of the wall specimens with a thickness of 2 mm, b) 5 mm and c) 9 mm. Blue arrows exemplarily show a few pores in the specimen with a thickness of 9 mm.

The porosity of the specimens of PBF-LB/M/316L tensile specimens sized 20 mm x 13 mm x 114.5 (length x length x height) manufactured with adapted process parameters for a layer thickness of 50 µm is shown in A. 3. The porosity corresponding to a volume energy density of 65 J.mm^{-3} and an ILT of 65 s was determined using X-ray computed tomography and found to be less than 0.01 % according to [49].

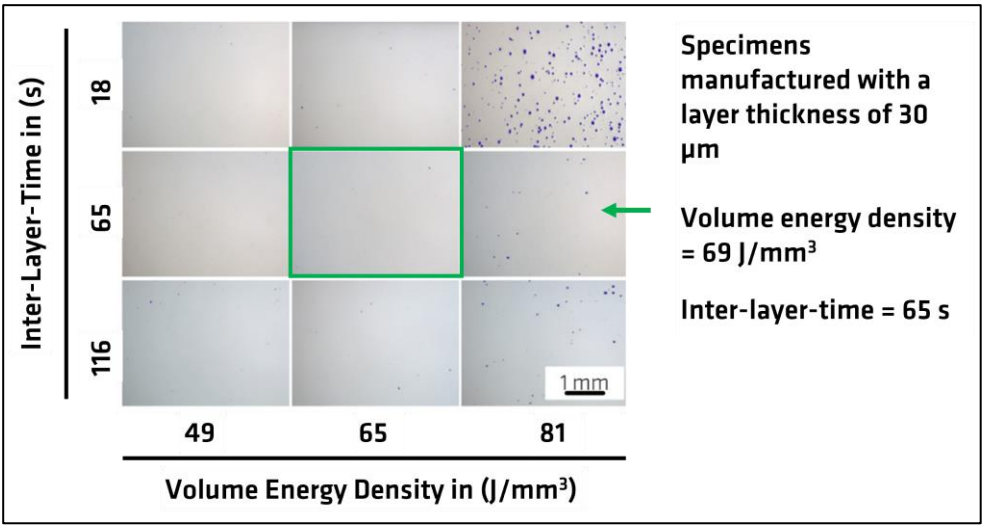

A. 3: Porosity of PBF-LB/M/316L specimens manufactured with a layer thickness of 50 µm and different Inter-layer-Times and Volume Energy Densities (adapted from [157]).

The length of the depth profiles is shown in A. 4. The depth profiles ended in the second track of a layer (laser spot size 80 µm) for the 2mm_26mm specimen and in the third track of a layer for the 5mm_26mm and the 9mm_26mm specimens.

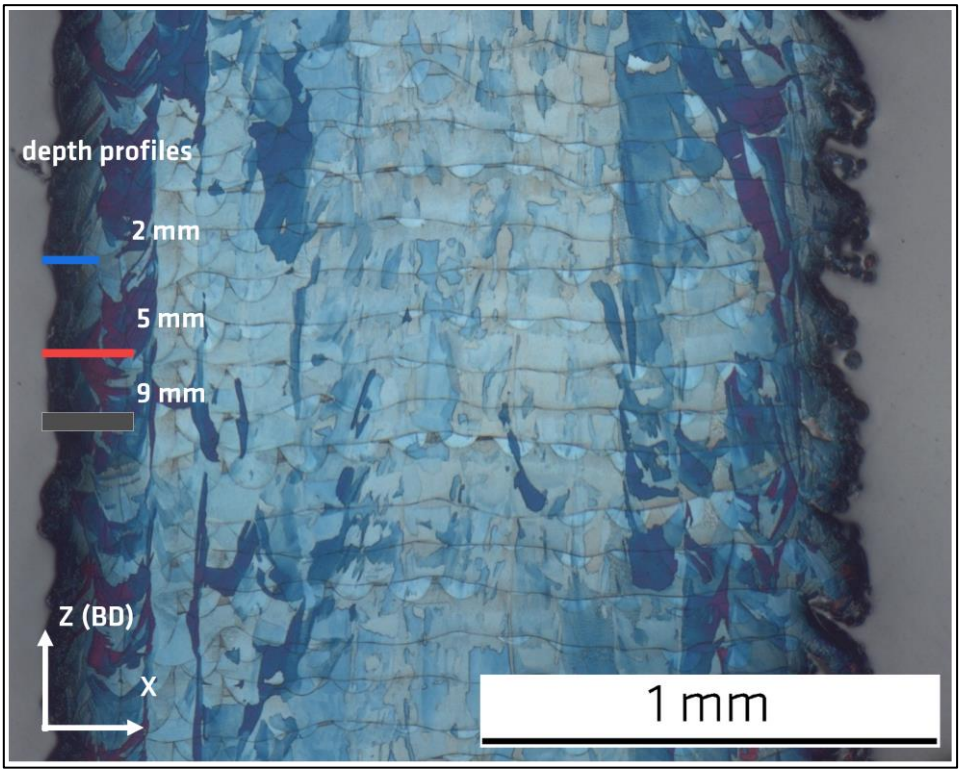

A. 4: Microstructure of the 2mm_13mm specimen and the highlighted lengths of the depth profiles.

A similar microstructure is observed in the material printed with a 30 µm compared to the 50 µm layer thickness as shown in A. 5. The microsections were extracted from a thin slice of a 80 mm x 80 mm x 80 mm wall (see A. 5 a). The checkerboard pattern is rotated by 45° as the scanning strategy is as well at an angle of 45° to the geometrical axes X and Y. This result supports the transferability of the outcome in chapter 4.2 addressing the approach for the determination of the residual stress in PBF-LB/M AISI 316L.

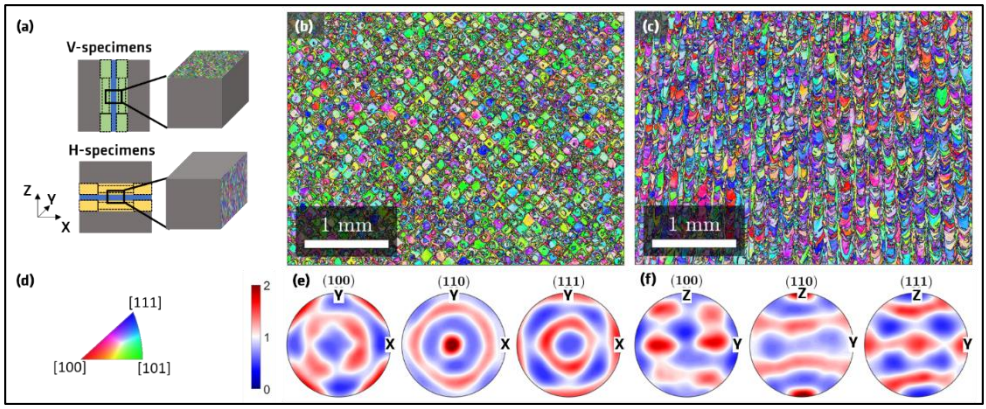

A. 5:a) Location and orientation of the EBSD pictures from the microstructure in the 30 µm PBF-LB/M walls, b) V-specimen texture and c) H-specimen texture. d) EBSD colour code, e) pole figure in the loading direction of the V-specimens and f) in the H-specimens. In a), the green specimens in wall 1 indicate the position of the V-specimens and the yellow specimens in wall 2 indicate the position of the H-specimens before extraction from the respective walls.

The Z profiles of the 2mm_26mm, the 5mm_26mm, and the 9mm_26mm specimens are shown in A. 6 a)-c) respectively. In the 2mm_26mm specimen the scale covers a range of 50 µm. In the 5mm_26mm specimen the scale covers a range of 75 µm and in the 9mm_26mm specimen the scale covers a range of 40 µm. These values are in the order of the roughness as shown in Figure 4.6.

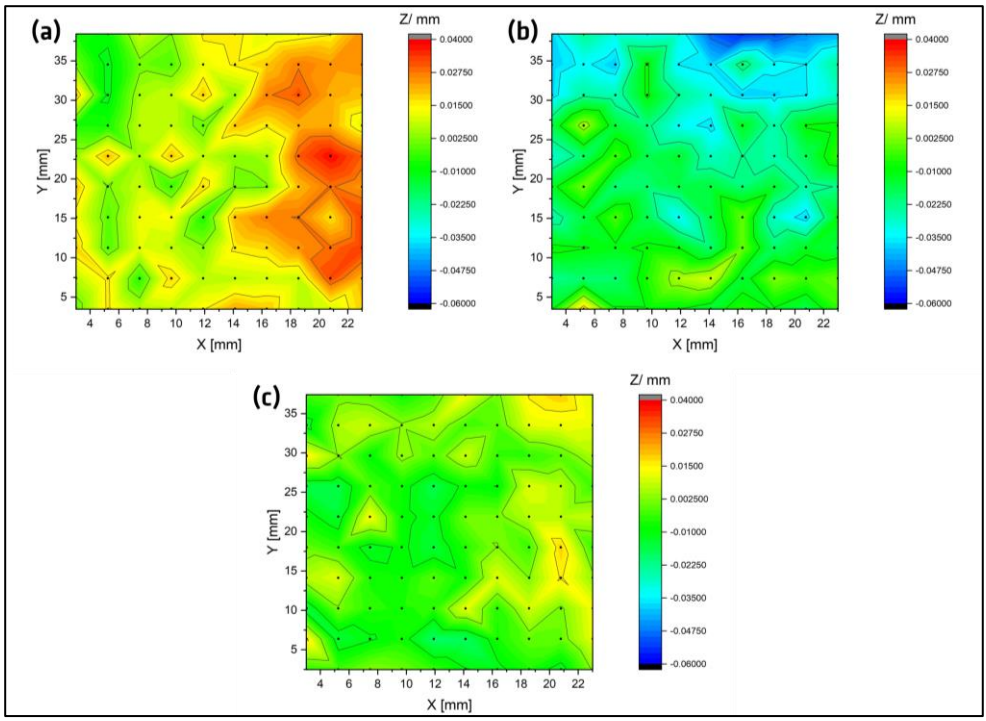

A. 6: a) Profile maps (Z) of the 2mm_26mm, b) the 5mm_26mm and c) the 9mm_26mm specimen.

A.III :In-situ tensile test experiment

The engineering stress – strain curves of the V-specimen and the H-specimen are shown in A. 7 a) and b) respectively.

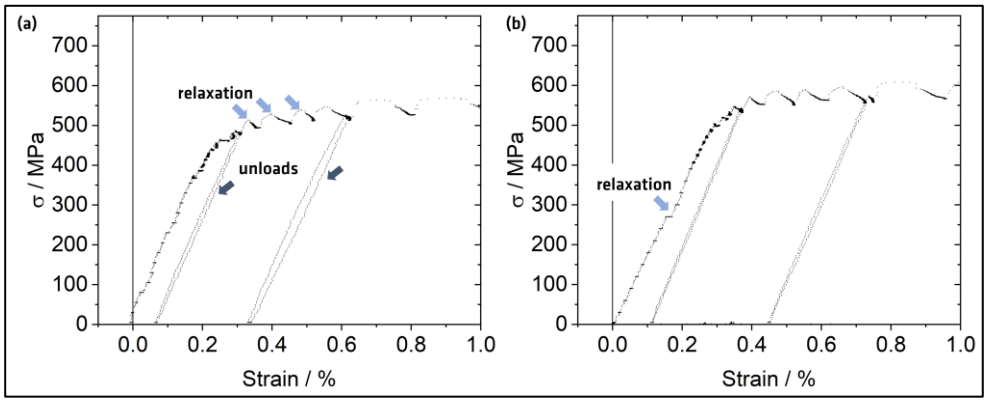

A. 7: a) Stress-strain data monitored by the tensile testing rig during the in-situ tensile test of the V-specimen and b) the H-specimen. Examples of relaxation during the acquisition of the diffraction pattern highlighted in (a) and example of the room temperature creep at an applied load of 270 MPa in (b).

A.IV : Python code for the determination of the yield strength

Python code to calculate the yield strength.

Created on Thu Nov 25 14:52:46 2021

This program calculates the yield strength:

```
import matplotlib.pyplot as plt

import numpy as np

#from numpy import Polynomial

import csv

import warnings

# constants used in this script

YIELD_STRAIN = 0.01

FILE_NAME = "Daymon_2006_macro_RT.txt"

strain = []

stress = []



def main():


    ### Avoid complex solutions for roots in function calc_intersection

    warnings.filterwarnings('ignore')

    fig, ax = plt.subplots(2,2, squeeze=False, figsize= (10,10))



    # First the file is opened and each line is read and stored in lines

    with open(FILE_NAME, 'r') as f:

        lines = csv.reader(f, delimiter='\t')

        for line in lines:

            strain.append(float(line[0]))

            stress.append(float(line[1]))

    ### plot data

    plt.sca(ax[0, 0])

    stress_strain(strain, stress)

    plt.sca(ax[0, 1])

    stress_strain(strain, stress)

    plt.sca(ax[1, 0])

    stress_strain(strain, stress)

    #plt.show()



    ### The user is asked to define the linear part of the curve

    x_min, x_max = data_range()



    #### A new data set with the above defined range is created

    strain_lin_range, stress_lin_range = fit_range(x_min, x_max, strain, stress)



    # Plot the data set of the linear part

    #stress_strain(strain_lin_range, stress_lin_range)



    ### Retrieve the slope and intercept of the linear part

    line = fit_line(strain_lin_range, stress_lin_range)
```

```
    ### Calculate the fitted line

    lin_x, lin_y = calc_line(line[0], line[1], strain)


    ### Plot the fitted line

    #stress_strain(lin_x, lin_y)


    ### Ask direction of inflection

    YIELD_STRAIN_NEW = inflection_direction(YIELD_STRAIN)

    print('This is the initial offset: ', YIELD_STRAIN, '\n')

    print('This is the new offset: ', YIELD_STRAIN_NEW, '\n')


    ### Shift the fitted line by the YIELD_STRAIN

    shift_x, shift_y = shift_line(line[0], line[1], strain, YIELD_STRAIN_NEW)


    ### Plot the shifted line

    plt.sca(ax[0, 1])

    stress_strain(shift_x, shift_y)


    ### Calculates the arguments of a x^2 polynomial

    curve = calc_poly(strain,stress)


    ### Retrieve the fitted curve

    poly_x, poly_y = fit_poly(curve,strain)


    ### Plot the fitted curve

    plt.sca(ax[1, 0])

    stress_strain(poly_x, poly_y)


    ### Plot the linear and poly fit

    plt.sca(ax[1, 1])

    stress_strain(shift_x, shift_y)

    stress_strain(poly_x, poly_y)


    ### Calculate the intersection

    yield_strength, x = calc_intersection(curve, line, YIELD_STRAIN_NEW)


    ### Output the result

    print('The yield strength is the next number that makes sense: ', yield_strength)

    #plt.plot(x[1],yield_strength[0])


def calc_intersection(curve, line, YIELD_STRAIN):

    p = [float(curve[0]),float(curve[1]),float(curve[2]
```

```
)-float(line[0]), float(curve[3])-float(line[1])+float(line[0])*float(YIELD_STRAIN)]

    intersection = np.roots(p)



    yield_strength = [float(line[0])*(float(intersection[0])-YIELD_STRAIN)+float(line[1]), float(line[0])*(float(intersection[1])-YIELD_STRAIN)+float(line[1])]

    return yield_strength, p



def fit_poly(curve, strain):

    y = []

    for x in strain:

        y_line = float(curve[0])*float(x)**3+float(curve[1])*float(x)**2+float(curve[2]*float(x) + float(curve[3]))

        y.append(y_line)

    return strain, y



def calc_poly(strain,stress):

    curve = np.polyfit(strain, stress, 3)

    return curve



def shift_line(slope, intercept, strain, YIELD_STRAIN):

    y= []

    for x in strain:

        y_line = float(slope)*float(x-YIELD_STRAIN) + float(intercept)

        y.append(y_line)

    return strain, y



def calc_line(slope, intercept, strain):

    y= []

    for x in strain:

        y_line = float(slope)*float(x) + float(intercept)

        y.append(y_line)

    return strain, y



def fit_line(strain_lin_range, stress_lin_range):

    line = np.polyfit(strain_lin_range, stress_lin_range, 1)

    return line



def stress_strain(strain, stress):

    plt.plot(strain, stress)

    #plt.show()



def fit_range(x_min, x_max, strain, stress):

    strain_lin_range = []
```

```
    stress_lin_range = []

    for a in strain:
        if x_min < a and x_max > a:
            strain_lin_range.append(a)

            # get index of the x value corresponding to a
            i = strain.index(a)
            stress_lin_range.append(stress[i])

    #print(strain_lin_range)
    #print(stress_lin_range)

    return strain_lin_range, stress_lin_range


def data_range():
    x_min = float(input('What is the lower x limit?: '))
    x_max = float(input('What is the upper x limit?: '))
    print('')
    return x_min, x_max


def inflection_direction(YIELD_STRAIN):
    direction = input('What is the direction of the inflection? (upward type left and downward type right): ')

    if direction == str('left'):
        YIELD_STRAIN = -YIELD_STRAIN
    else:
        YIELD_STRAIN = YIELD_STRAIN
    return YIELD_STRAIN


if __name__ == "__main__":
    main()
```